



**HAL**  
open science

# Modeling of Multiphysics Electromagnetic & Mechanical Coupling and Vibration Controls Applied to Switched Reluctance Machine

Man Zhang

► **To cite this version:**

Man Zhang. Modeling of Multiphysics Electromagnetic & Mechanical Coupling and Vibration Controls Applied to Switched Reluctance Machine. *Vibrations [physics.class-ph]*. Université Paris Saclay (COmUE), 2018. English. NNT: 2018SACLS287 . tel-02426016v2

**HAL Id: tel-02426016**

**<https://theses.hal.science/tel-02426016v2>**

Submitted on 23 Jan 2020

**HAL** is a multi-disciplinary open access archive for the deposit and dissemination of scientific research documents, whether they are published or not. The documents may come from teaching and research institutions in France or abroad, or from public or private research centers.

L'archive ouverte pluridisciplinaire **HAL**, est destinée au dépôt et à la diffusion de documents scientifiques de niveau recherche, publiés ou non, émanant des établissements d'enseignement et de recherche français ou étrangers, des laboratoires publics ou privés.

# Modeling of Multiphysics Electromagnetic & Mechanical Coupling and Vibration Controls Applied to Switched Reluctance Machine

Thèse de doctorat de l'Université Paris-Saclay  
préparée à l'Université Paris-Sud

École doctorale n°575: Electrical, Optical, Bio: Physics and  
Engineering (EOBE)  
Spécialité de doctorat : Génie électrique

Thèse présentée et soutenue à Gif sur Yvette, le 12 Septembre 2018 par

**Mme Man ZHANG**

Composition du Jury :

M. Malek GHANES Professeur des universités, Centrale Nantes (LS2N)	Président
M. Mickaël HILAIRET Professeur des universités, Université de Bourgogne Franche-Comté (FEMTO-ST)	Rapporteur
M. Vincent LANFRANCHI Professeur des universités, UTC (Roberval)	Rapporteur
M. Emmanuel GODOY Professeur des universités, CentraleSupélec (L2S)	Examineur
M. Johan GYSELINCK Professeur des universités, Université libre de Bruxelles (BEAMS)	Examineur
M. Xavier MININGER Professeur des universités, Université Paris-Sud (GeePs)	Directeur de thèse
Mme Imen BAHRI Maître de conférences, Université Paris-Sud (GeePs)	Encadrante
Mme Cristina VLAD Maître de conférences, CentraleSupélec (L2S)	Encadrante



## Acknowledgements

First of all, I would like to thank my supervisor M. Xavier MININGER, who gave me a chance to be a member of this laboratory GeePs and brought me to a new field. During the past three years, he not only helped me to understand how to be a researcher, but also how to enjoy the life. I really enjoyed working with you during these three years.

I would like to thank my co-supervisor Mme Imen BAHRI and Cristina VLAD, who always tried to work with me as if they were available. Their presence and involvement were invaluable to carry out this work.

I would like to thank the engineer M.Eric Berthelot, he was so nice that he was always there when I needed his help. I'd like to thank his time spent to help me with my experimental test.

I would also like to thank M. Claude MARCHAND, head of GeePs for his welcome within this team.

I would like to thank the reviewers of my thesis M. Vincent LANFRANCHI and M. Mickaël HILAIRET, who spent their holidays to evaluate my work. I also thank M. Malek GHANES for agreeing to be chair of my thesis jury, as well as the other jury members M. Emmanuel GODOY and M. Johan GYSELINCK for their acceptances to participate in the jury of my thesis.

Many thanks to my friend and also my colleague Mme Shuangfeng ZHANG who accompanied me to have a lively and interesting PhD life. Thank you for all the discussions and moments of relaxation we were able to share.

It is really my honor to work with all the faculty, staff, PhD students in GeePs. I will not forget those three years spent with you.

Finally, I also wish to dedicate this thesis to my husband M. Hongqin XIE, who knew me, support me and understood me, which enabled me to be here and be courage to move on.

## Tables of Content

List of figures .....	I
List of tables .....	VIII
Publications .....	IX
General Introduction .....	1
Contributions and Outline of the Thesis .....	6
Chapter 1 Vibration and Noise Reduction for Switched Reluctance Machine: State of the Art .....	9
1.1 Noise Sources of SRM.....	9
1.1.1 Electromagnetic Source .....	10
1.1.2 Mechanical Source .....	10
1.1.3 Aerodynamic Source .....	10
1.2 State of the Art regarding Noise Reduction .....	11
1.2.1 Geometric Design .....	11
1.2.2 Control Methods .....	14
1.2.3 Multi-physics Modeling Methods .....	16
1.2.4 Implementation of Control Methods.....	18
1.3 Conclusion .....	19
Chapter 2 Semi-analytical Electromagnetic/Structural Multi-Physics Model of SRM .....	20
2.1 Investigated SRM.....	21
2.2 Operating Principle of the SRM .....	22
2.3 Electromagnetic Model.....	23
2.3.1 Voltage Balance Equation .....	23
2.3.2 Flux-linkage Characteristics .....	24
2.3.3 Torque Production and Energy Conversion .....	25
2.3.4 Radial Force Characteristics .....	27
2.4 Structural Model .....	31
2.4.1 Modal Analysis .....	34
2.4.2 Harmonic Response Analysis .....	37
2.4.3 Modal Superposition Harmonic Analysis .....	39
2.5 Model Validation.....	42
2.6 Conclusion .....	46
Chapter 3 Vibration and Noise Reduction Control Strategies for SRM.....	47
3.1 Improved Variable Turn-off Angle Control (IVTC).....	47
3.1.1 Speed Controller Design .....	48
3.1.2 Current Controller Design.....	52
3.1.3 Vibration Reduction with IVTC.....	54
3.1.4 Simulation Results of IVTC.....	56

3.2 Direct Force Control with Reference Current Adapter (DFC & RCA) .....	60
3.2.1 Vibration Reduction with DFC .....	61
3.2.2 Reference Force Generator .....	64
3.2.3 Simulation Results: TMC vs DFC .....	66
3.2.4 Association of TMC and DFC .....	71
3.2.5 DFC with Reference Current Adaptor (DFC&RCA).....	75
3.2.6 Control Parameters Tuning for DFC& RCA .....	80
3.3 Efficiency and Torque Ripple Evaluation of the SRM .....	86
3.3.1 Losses and Efficiency .....	87
3.3.2 Simulation Results of IVTC.....	88
3.3.3 Simulation Results of DFC&RCA.....	89
3.4 Conclusion .....	98
Chapter 4 Experimental Validation of DFC&RCA: Application to SRM.....	100
4.1 Design Implementation of the Control Strategy .....	100
4.1.1 Influence of the Sampling Time.....	100
4.1.2 Development of the Hardware/Software Partitioning Control System....	101
4.1.3 Synchronous Signal Producer .....	106
4.2 Experimental Tests .....	107
4.2.1 Test Bench Set-up .....	107
4.2.2 Background Noise Measurement.....	108
4.2.3 Stable State Experiments .....	111
4.2.4 Transient State Experiments.....	116
4.3 Conclusion .....	124
General Conclusion and Prospective.....	126
Conclusions.....	126
Prospective.....	129
Bibliography.....	131
A. Characteristic Data of the Investigated SRM .....	137
B. Investigation on Current Harmonic Removal related to the Vibration Excitation .....	138
C. Losses and Efficiency Computation of SRM drive system .....	141
D. Résumé .....	146

## List of figures

Figure 1.1 Noise sources in electrical machines and drives.....	9
Figure 1.2 Four SRM structures: (a) Conventional SRM, (b) SR-SRM, (c) SS-SRM, (d) SSR-SRM. [29].....	12
Figure 1.3 (a) Types of frame/ribs for a 12/8 SRM. (b) Longitudinal cross-sectional view of axial, radial, and screw-type frames, respectively. [34] .....	13
Figure 1.4 Distributed airgap in the SRM stator .....	14
Figure 1.5 C-dump inverter for hybrid excitation method.[43] .....	15
Figure 2.1 Simulation model for SRM drive system for vibration analysis.....	20
Figure 2.2 Schematic block of a 4-phase 8/6 SRM.....	21
Figure 2.3 The states of the converter. ....	22
Figure 2.4 Inductance profile [17].....	23
Figure 2.5 Magnetic field distribution of SRM in FEM.....	24
Figure 2.6 Flux-linkage profile. ....	24
Figure 2.7 The definition of magnetic energy and magnetic co-energy. ....	26
Figure 2.8 Electromagnetic torque profile. ....	27
Figure 2.9 Radial force profile. ....	27
Figure 2.10 Schematic diagram of an SRM electromagnetic model.....	28
Figure 2.11 Applied phase current in the FEM simulation. ....	30
Figure 2.12 Radial Maxwell stress for an electric period in Pa. ....	30
Figure 2.13 Radial Maxwell stress 2D FFT in dB.....	30
Figure 2.14 Radial Maxwell stress harmonics distribution in the airgap for different temporal ranks .....	31
Figure 2.15 Viscous damped spring-mass system.....	32
Figure 2.16 Schematic diagram of the structural model for mode $n$ .....	33
Figure 2.17 Geometric shape of 8/6 SRM.....	36
Figure 2.18 Geometric model adopted in FEM.....	37
Figure 2.19 Natural Frequencies of the studied 8/6 SRM.....	37

Figure 2.20 Radial force applied on the stator teeth as loads.....	38
Figure 2.21 Transfer function of mode 0.....	40
Figure 2.22 Transfer function of mode 4.....	41
Figure 2.23 Flowchart of the Structural Modeling in Matlab. ....	42
Figure 2.24 Bode plot of the self-transfer function for P1 and P2. ....	42
Figure 2.25 Block diagram of the electromagnetic/mechanical multi-physics model. ....	43
Figure 2.26 Applied radial force (fundamental frequency is 200Hz) and its sketch.....	44
Figure 2.27 Comparisons results between semi-analytical model and FEM when the fundamental frequency of the applied radial force is 200Hz. ....	45
Figure 2.28 Comparisons results between semi-analytical model and FEM when the fundamental frequency of the applied radial force is 120Hz. ....	45
Figure 2.29 Spectrogram of vibration for speed-up test with a load of 2N·m.....	46
Figure 3.1 Block diagram of ATC. ....	47
Figure 3.2 Block diagram of the speed-loop with PI controller. ....	48
Figure 3.3 Block diagram of the speed-loop with IP controller. ....	48
Figure 3.4 Closed-loop system response using PI control and different damping ratio.....	50
Figure 3.5 Closed-loop system response using IP control and different damping ratio.....	51
Figure 3.6 Closed-loop system response: relationship between dynamic properties and damping ratio.....	51
Figure 3.7 Blok diagram of the discrete speed IP controller. ....	52
Figure 3.8 Block diagram of the current-loop with PI control. ....	53
Figure 3.9 Blok diagram of the discrete current PI controller.....	54
Figure 3.10 Bode plot of the self-transfer function between radial force and vibration acceleration.....	55
Figure 3.11 Acceleration for $\Omega = 600$ r/min, $T_L = 7$ N·m without speed controller: ATC vs VTC.....	56
Figure 3.12 Acceleration for $\Omega^* = 600$ r/min, $T_L = 7$ N·m without speed controller: ATC vs IVTC.....	57
Figure 3.13 Acceleration for $\Omega^* = 600$ r/min, $T_L = 7$ N·m with speed controller: ATC vs IVTC. .....	58

Figure 3.14 Comparison between ATC and IVTC for different operating points.....	59
Figure 3.15 IVTC: Acceleration for $\Delta\theta = 3^\circ$ (red line) and $\Delta\theta = 6^\circ$ (blue line) at $\Omega^* = 1300$ r/min and $T_L = 8$ N·m.....	59
Figure 3.16 Control structure of the DFC&RCA.....	61
Figure 3.17 Structure of direct force control.....	62
Figure 3.18 DFC: region division and control modes.....	63
Figure 3.19 Diagram of the hysteresis controllers.....	63
Figure 3.20 Torque profile.....	65
Figure 3.21 Radial force profile.....	65
Figure 3.22 Static characteristics between the overall torque and the total radial force.....	66
Figure 3.23 Total torque, total radial force, phase current, phase torque and phase radial force obtained with TMC at $\Omega^* = 600$ r/min and $T_L = 7$ N·m.....	67
Figure 3.24 Total torque, total radial force, phase current, phase torque and phase radial force obtained with DFC at $\Omega^* = 600$ r/min and $T_L = 7$ N·m.....	68
Figure 3.25 Spectrum of phase radial force and total torque of TMC at $\Omega^* = 600$ r/min and $T_L = 7$ N·m.....	68
Figure 3.26 Spectrum of phase radial force and total torque of DFC at $\Omega^* = 600$ r/min and $T_L = 7$ N·m.....	69
Figure 3.27 Acceleration of TMC at $\Omega^* = 600$ r/min and $T_L = 7$ N·m.....	69
Figure 3.28 Acceleration vibration of DFC at $\Omega^* = 600$ r/min and $T_L = 7$ N·m.....	70
Figure 3.29 Block diagram for the association of TMC and DFC.....	72
Figure 3.30 TMC + DFC: torque, total radial force, phase current and switching signals at $\Omega^* = 600$ r/min, $T_L = 7$ N·m.....	73
Figure 3.31 Comparison between the TMC and the association TMC + DFC: time-domain acceleration, frequency-domain acceleration at $\Omega^* = 600$ r/min and $T_L = 7$ N·m.....	74
Figure 3.32 Spectrum of phase radial force and total torque of TMC + DFC at $\Omega^* = 600$ r/min and $T_L = 7$ N·m.....	74
Figure 3.33 Total torque, total force, phase current, phase torque and phase radial force of	

TMC+DFC at $\Omega^* = 600$ r/min and $T_L = 7$ N·m.....	75
Figure 3.34 Structure of the proposed reference current adapter. ....	76
Figure 3.35 Current adapter algorithm .....	77
Figure 3.36 The DFC&RCA: total torque, total force, phase current and switching signal at $\Omega^* = 600$ r/min and $T_L = 7$ N·m. ....	78
Figure 3.37 Reference current adaption progress when $\Omega^*$ is 600 r/min with a load torque of 7N·m.....	78
Figure 3.38 Comparison between the TMC and the DFC&RCA: time-domain acceleration, frequency-domain acceleration at $\Omega^* = 600$ r/min and $T_L = 7$ N·m.....	79
Figure 3.39 Total torque, total force, phase current, phase torque and phase radial force of DFC&RCA at $\Omega^* = 600$ r/min and $T_L = 7$ N·m.....	79
Figure 3.40 The vibration energy with different torque variation limitation $\varepsilon_T$ .....	80
Figure 3.41 The torque ripple with different torque variation limitation $\varepsilon_T$ .....	80
Figure 3.42 Acceleration curve for different torque variations. ....	81
Figure 3.43 Phase current curve for different $\varepsilon_T$ at $\Omega^* = 600$ r/min and $T_L = 7$ N·m.....	82
Figure 3.44 Relationship between $\varepsilon_T$ and the reference current at $\Omega^* = 600$ r/min and $T_L = 7$ N·m.....	82
Figure 3.45 The vibration energy with different torque variation limitation $\varepsilon_F$ .....	83
Figure 3.46 The torque ripple with different torque variation limitation $\varepsilon_F$ .....	83
Figure 3.47 TMC: the torque variation $\sigma_T$ and force variation $\sigma_F$ for different operating points. ....	84
Figure 3.48 Contour of torque variation $\sigma_T$ .....	84
Figure 3.49 Contour of radial force variation $\sigma_F$ .....	84
Figure 3.50 Region division based on the torque variation bound and the force variation bound. ....	85
Figure 3.51 DFC&RCA performances for different bandwidths $\Delta F$ at $\Omega^* = 600$ r/min and $T_L = 7$ N·m.....	86
Figure 3.52 Comparison between the ATC and the IVTC: Total torque, phase current, phase torque and phase radial force obtained at $\Omega^* = 600$ r/min and $T_L = 7$ N·m.....	88
Figure 3.53 Investigated operating points on the torque-speed plane.....	89

Figure 3.54 TMC: total torque, total force, phase current, phase torque and phase radial force of TMC at $\Omega^* = 200$ r/min and $T_L = 16$ N·m. ....	91
Figure 3.55 DFC&RCA: total torque, total force, phase current, phase torque and phase radial force at $\Omega^* = 200$ r/min and $T_L = 16$ N·m. ....	92
Figure 3.56 Comparison between TMC and DFC&RCA: phase current and radial force spectrum at $\Omega^* = 200$ r/min and $T_L = 16$ N·m. ....	92
Figure 3.57 Comparison between TMC and DFC&RCA: phase flux linkage at $\Omega^* = 200$ r/min and $T_L = 16$ N·m. ....	93
Figure 3.58 Comparison between TMC and DFC&RCA acceleration spectrum at $\Omega^* = 200$ r/min and $T_L = 16$ N·m. ....	93
Figure 3.59 Total torque, total force, phase current, phase torque and phase radial force of TMC at $\Omega^* = 1500$ r/min and $T_L = 5$ N·m. ....	95
Figure 3.60 DFC&RCA: total torque, total force, phase current, phase torque and phase radial force at $\Omega^* = 1500$ r/min and $T_L = 5$ N·m. ....	95
Figure 3.61 Comparison between TMC and DFC&RCA: phase current and radial force spectrum at $\Omega^* = 1500$ r/min and $T_L = 5$ N·m. ....	96
Figure 3.62 Comparison between TMC and DFC&RCA: phase flux linkage at $\Omega^* = 1500$ r/min and $T_L = 5$ N·m. ....	96
Figure 3.63 Comparison between TMC and DFC&RCA: acceleration spectrum at $\Omega^* = 1500$ r/min and $T_L = 5$ N·m. ....	97
Figure 4.1 Structure of the vibration reduction controller -- DFC&RCA. ....	100
Figure 4.2 Simulation results for the DFC&RCA implemented with different sample times ( $T_{samp}$ ): (a) $200 \mu s$ , (b) $5 \mu s$ . ....	101
Figure 4.3 Architecture of the DFC&RCA system using hardware/software partitioning. ....	103
Figure 4.4 Schematic diagram of the factorization of the F-LUT3. ....	104
Figure 4.5 Schematic diagram of the square mean value calculator. ....	106
Figure 4.6 Structure of the triangle producer. ....	106
Figure 4.7 Setup of the test bench. ....	107
Figure 4.8 Measurement results of the background noise from the environment. ....	108
Figure 4.9 Measurement results of the background noise from the MPB + environment. ....	109

Figure 4.10 Set-up of power supply noise measurement .....	110
Figure 4.11 Measurement results of the background noise from power supply for different current values. ....	110
Figure 4.12 Experimental results at $\Omega^* = 600$ r/min and $T_L = 8$ N·m.....	111
Figure 4.13 Experimental results of the vibration acceleration at $\Omega^* = 600$ r/min and $T_L = 8$ N·m.....	112
Figure 4.14 Experimental results of acoustic noise at $\Omega^* = 600$ r/min and $T_L = 8$ N·m.....	112
Figure 4.15 Experimental results at $\Omega^* = 1000$ r/min and $T_L = 2$ N·m.....	113
Figure 4.16 Experimental results of vibration acceleration at $\Omega^* = 1000$ r/min and $T_L = 2$ N·m. ....	113
Figure 4.17 Experimental results of acoustic noise at 1000 r/min and $T_L = 2$ N·m. ....	114
Figure 4.18 Experimental results at $\Omega^* = 2000$ r/min and $T_L = 0.6$ N·m.....	114
Figure 4.19 Experimental results of vibration acceleration at $\Omega^* = 2000$ r/min and $T_L = 0.6$ N·m.....	115
Figure 4.20 Experimental results of acoustic at $\Omega^* = 2000$ r/min and $T_L = 0.6$ N·m. ....	115
Figure 4.21 Experimental results by control strategies commutating: sonogram of acoustic noise measured at $\Omega^* = 1000$ r/min and $T_L = 2$ N·m. ....	116
Figure 4.22 TMC: transient curves for a step-change in the reference speed from 200 r/min to 600 r/min and a load torque of 2 N·m. ....	117
Figure 4.23 DFC&RCA: transient curves for a step-change in the reference speed from 200 r/min to 600 r/min and a load torque of 2 N·m.....	118
Figure 4.24 Experimental sonogram of acoustic noise for a step-change in the reference speed from 200 r/min to 600 r/min and a load torque of 2 N·m.....	118
Figure 4.25 TMC: transient curve for a step-change in the reference speed from 200 r/min to 600 r/min and a load torque of 6 N·m. ....	119
Figure 4.26 DFC&RCA: transient curve for a step-change in the reference speed from 200 r/min to 600 r/min and a load torque of 6 N·m.....	119
Figure 4.27 Experimental sonogram of acoustic noise for a step-change in the reference speed from 200 r/min to 600 r/min and a load torque of 6 N·m.....	120
Figure 4.28 TMC: transient curves for a step-change in the load torque from 2 N·m to 6 N·m	

at constant reference speed $\Omega^* = 600$ r/min.....	121
Figure 4.29 DFC&RCA: transient curves for a step-change in the load torque from 2 N·m to 6 N·m at constant reference speed $\Omega^* = 600$ r/min.....	121
Figure 4.30 Experimental sonogram of acoustic noise for a step-change in the load torque from 2 N·m to 6 N·m at constant reference speed $\Omega^* = 600$ r/min.....	122
Figure 4.31 TMC: transient curves for a step-change in the load torque from 6 N·m to 2 N·m at constant reference speed $\Omega^* = 600$ r/min.....	123
Figure 4.32 DFC&RCA: transient curves for a step-change in the load torque from 6 N·m to 2 N·m at constant reference speed $\Omega^* = 600$ r/min.....	123
Figure 4.33 Experimental sonogram of acoustic noise at $\Omega^* = 600$ r/min with the load torque decreasing from 6 N·m to 2 N·m.....	124

## List of tables

Table 2-1 Coupling factors matrixes. ....	34
Table 3-1 Performance comparison of vibration energy between ATC and IVTC for different operating points .....	60
Table 3-2 Boundary values of different zones defined for $\sigma_T$ and $\sigma_F$ .....	84
Table 3-3 Performance comparison between ATC and IVTC for different operating points	89
Table 3-4 Definition of the investigated operating points. ....	90
Table 3-5 Losses comparison between TMC and DFC&RCA at $\Omega^* = 200$ r/min and $T_L = 16$ N·m. ....	91
Table 3-6 Losses comparison between TMC and DFC&RCA at $\Omega^* = 1500$ r/min and $T_L = 5$ N·m. ....	94
Table 3-7 Performance evaluation for different operating points.....	97
Table 4-1 Performance comparison for different reference speeds and a load torque of 2 N·m. ....	116
Table 4-2 Performance comparison for different loads and a reference speed of 600 r/min. ....	116

# **Publications**

## **Conference paper**

1. Zhang M, Mininger X, Bahri I and Vlad C. "Improvement of the variable turn-off angle control for SRM regarding vibration reduction". Electric Machines and Drives Conference (IEMDC), 2017 IEEE International. IEEE, 2017: 1-7.
2. Zhang M, Bahri I, Mininger X and Vlad C. "A new vibration reduction control strategy of switched reluctance machine". Electric Machines and Drives Conference (IEMDC), 2017 IEEE International. IEEE, 2017: 1-6.

## **Journal Paper**

1. Zhang M, Mininger X, Bahri I and Vlad C. "Vibration reduction strategy of switched reluctance machine", IEEE Transactions on Energy Conversion. Under revision.

## **Internship**

Internship to team BEAMS of Université libre de Bruxelles for one month.

# General Introduction

The global warming becomes more and more serious due to the increase of the Greenhouse Gases (GHG) emissions. In Europe, transport represents almost a quarter of the GHG emissions. Within this sector, road transport accounts for more than 70% of all the GHG, which is by far the biggest emitter [1]. To solve this problem, a resource-efficient and low-carbon economy is proposed by the European Union (EU) to reduce the GHG emissions, promoting greater energy security. A low-carbon economy means a much greater use of renewable sources of energy, energy-efficient building material, hybrid and electric cars and so on [2].

With the development of Electric Vehicles (EVs) and the support of government policies, EVs are showing a significant growth in EU, which makes EU the second largest EV market (Figure 1). Moreover, the new registrations of electric cars hit a new record in 2016, with over 750 thousand sales worldwide. The global electric car stock surpassed 2 million vehicles in 2016, after crossing the 1 million thresholds in 2015 (Figure 2) [3].

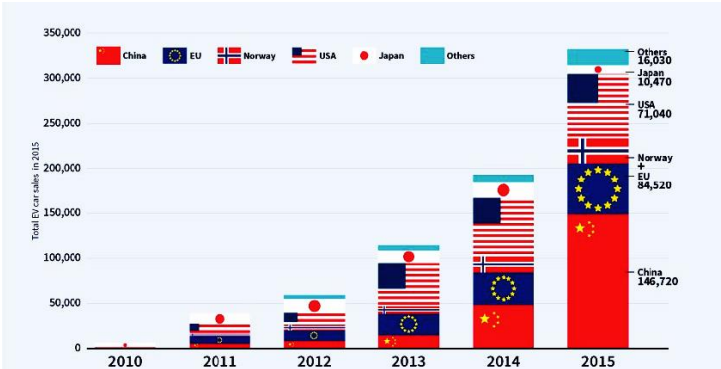


Figure 1 Total EV car sales of recent 5 years [3]

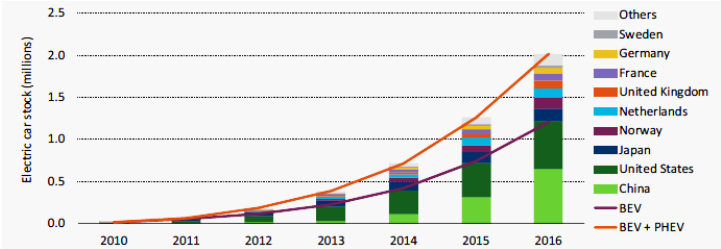


Figure 2 Evolution of the global electric car stock [3]

Besides, all across the globe, aggressive mandates are being set up to transition countries

away from petrol and diesel cars. For example, France, U.K, Netherlands and Norway plan diesel bans by 2040. The French government announced that it wants to end sales of gas and diesel-powered vehicles by 2040 to fight global warming. After that date, automakers will only be allowed to sell cars that run on electricity or other cleaner power, hybrid cars will also be permitted. U.K. said that it would ban sales of new gasoline and diesel cars starting in 2040 as part of a bid to clean up the country's air. In Norway, the government's transportation plan outlines a clear target: all new passenger cars and vans sold in 2025 should be zero-emission vehicles [4]. Dutch government presented its detailed plan: making all new cars emission-free by 2030 by virtually banning petrol and diesel-powered cars in favor of battery-powered vehicles [5].

The great potential of EVs has led to many researches on it. As the core component of EVs, the electric motor and drive is very important. Due to the peculiar operating modes and working conditions of the vehicle, it poses specific requirements for the electric motor and drive systems. The main requirements are as follows [6]-[8]:

- High torque and power densities,
- Wide speed operation range,
- Extended area of high efficiency (it should cover most of the operating regions),
- Large torque output at low speeds in order to dispose of enough torque when the vehicle starts or is climbing,
- Strong overload capability (i.e. the motor can output two-times the rated torque during a short time),
- Security and reliability (i.e. fault-tolerant configurations should be arranged),
- Low acoustic noise and torque ripple,
- Reasonable costs.

During the last decades, many types of electric motors have been analyzed and evaluated. There are mainly three kinds of electrical motors that are strong candidates for the drive system: the Induction Machine (IM), the Synchronous Machine (SM) and the Switched Reluctance Machine (SRM) [8]-[11].

IMs are robust, relatively low cost, and have well established manufacturing techniques.

Good dynamic torque control performance can be achieved by either vector control or direct torque control. For conventional IMs, the constant power range typically extends to 2–3 times the base speed. However, for traction machines, this is required to be extended to 4–5 times the base speed, which is generally desirable. Moreover, its efficiency is rather low when the load is light. On an urban driving cycle, a traction machine operates most frequently at light loads around the base speed. Therefore, in general, it should be designed to operate at high efficiency.

Among the SM, the main features of wound rotor synchronous machine (WR-SM) drives are high efficiency, high overload capability and good performance in the field weakening region. However, the existence of the brushes increases the cost to maintenance. Moreover, due to the existence of the winding on the rotor, special attention should be paid to the thermal design and the cooling system.

Permanent magnet synchronous machine (PMSM) is another type of SM. Since the magnetic field is produced by the PM, the weight and volume can be greatly reduced and because of the absence of the coils on the rotor, the copper losses have been decreased. So, among these electrical motors, PMSM has the best performance in power density and efficiency, which make PMSM to be the most popular electric motor for EVs. Nevertheless, the adoption of the permanent magnets (PMs) increases its cost, at the same time prevents it from being applied to the high temperature and harsh environment because of the demagnetization of the PM, which could make the machine out of control. Moreover, the price and supply of rare-earth materials have been recognized as one of the major problems for EV mass production.

Therefore, there are high demands for a rare-earth-free motor or a less rare-earth motor for the next-generation EVs. Several projects have been investigating substitute motors [12]-[16]. SRM is one of the possible solutions.

Due to its inherent advantages such as simple structure, high reliability and fault-tolerance, wide speed range and low cost, SRM has attracted much attention. There is neither PM nor copper winding on the SRM rotor, which increases its speed operation range and decreases the cost. The salient structure makes it easy to construct. The independent

connection among different phase windings brings in high fault-tolerance and reliability. However, its double salient structure leads to high nonlinearity and serious vibration and acoustic noise problems, which limit its use in the automotive industry, essentially because of the negative impact on the drivers' and passengers' comfort. For these reasons, SRMs still require further efforts to reduce the acoustic noise and the vibration. Table 1 gives the comparison results for the three machines adopted in the electric propulsion system.

Table 1 Electric propulsion systems comparison.

	IM	SM		SRM
		PMSM	WRSM	
Power density	*	***	***	**
Efficiency	*	***	***	**
Reliability	***	**	**	***
Maturity	***	**	***	**
Cost level	**	*	**	***
Noise level	***	***	***	**
Maintenance	***	***	**	***
Adopted automotive industrial examples	Tesla BMW	Toyota Honda Renault		Holden Land Rover (prototype)

The aim of this thesis is to improve the acoustic noise behavior of the SRM from the aspect of the control strategies for a prototype 8/6 SRM. For the SRM control, current or torque control is mainly used to obtain the desired bandwidth in torque and speed responses for electrical drive systems [17], [18]. There are two methods used for the torque control of the SRM based on current profiling, namely, Instantaneous Torque Control (ITC) and Average Torque Control (ATC). The ITC produces a reference current depending on the desired torque and rotor position at each sample time and controls the actual phase current to emulate the reference. The ATC imposes a square-wave current reference over one excitation period, which leads to small inherent torque fluctuations and high torque ripple during the phase commutation. The ATC is easily implementable but leads to important torque ripples compared to the ITC. However, for the ITC, the actual current is required to follow the reference value at every time instant, which is not possible with the increase of the speed. Indeed, the back electromotive force (EMF) increases with speed, which decreases the current rising rate due to the limited inverter voltage. Afterward, the motor enters the constant

power region (single-pulse mode), where the peak torque production is maintained by controlling the turn-on and conduction angles. Advanced angle commutation, necessary for the torque maximization at a given speed, is not possible with instantaneous torque control strategy [18]. Consequently, the capabilities of the motor are not fully used at every rotor speed unless the control algorithm switches to the ATC. Therefore, the second method is adopted in this work so that the SRM can operate in a wide speed operating range without switching between different control strategies [19].

The initial control strategy of SRM based on ATC is presented in Figure 3. Three fundamental control variables need to be adjusted: the reference current  $I_{ref}^*$ , the turn on angle  $\psi$  and the conduction angle  $\theta_p$ , whose definitions are presented in Figure 4. In fact, several sets of values of the control variables are able to make the SRM operate at a specific torque-speed point. However, one suitable combination for one speed-torque operating point should be chosen based on the desired optimization goals (e.g., efficiency, torque ripple or noise). The optimal values of the control parameters for each point of the operating range can be obtained by simulation. The lookup tables (LUTs) used in this thesis are generated off-line, for the entire torque-speed plane, using a software for the SRM simulation [20]. These control parameters are optimized according to different criteria: torque ripple and efficiency, which divide the torque-speed plane into three different areas as shown in Figure 5. In the first area, the torque ripple is minimized, whereas the second area is an area transiting to the second criteria – max global efficiency, which is considered in the third area [18]. The different parameters in these zones are used to make the SRM operate in wide-speed-range operation.

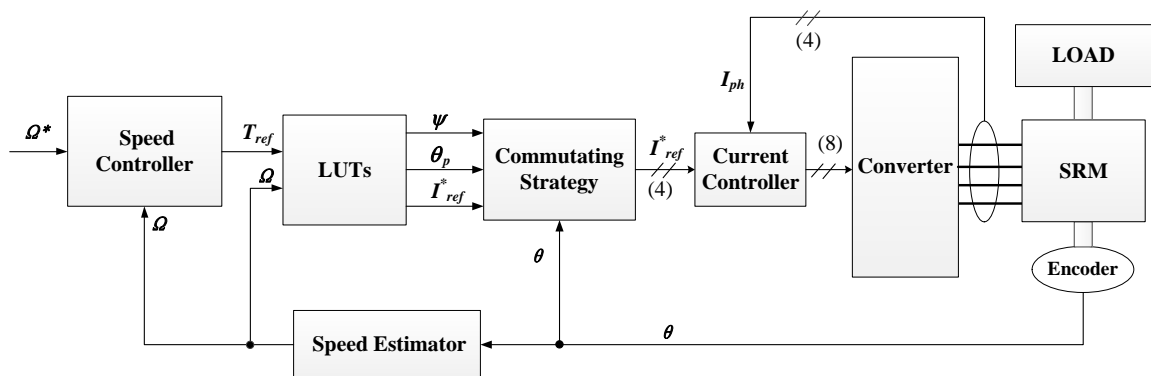


Figure 3 Block diagram of ATC.

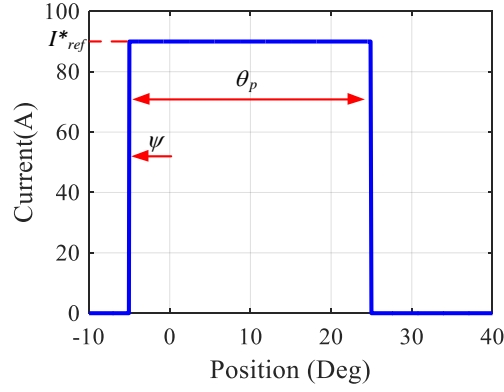


Figure 4 Definition of control variables.

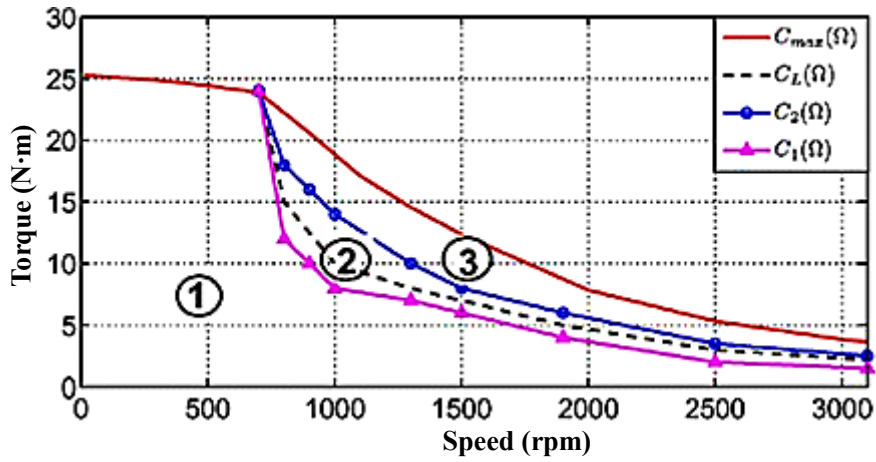


Figure 5 Definition of the three different area in ATC [18].

In this thesis, the control strategies proposed are continuous work of this basic control structure. The additional control blocks are added to the traditional control method so as to reduce the vibration and acoustic noise.

## Contributions and Outline of the Thesis

To improve the vibratory and acoustic behavior of SRMs, two vibration reduction control methods are proposed. The first one is an enhanced variable turn-off angle control since the turn-off angle is the key variable related to the vibration. It introduces a uniformly distributed random signal to the fixed-frequency sinusoidal-varying turn-off angle to avoid the local high vibration components near the frequency of the sinusoidal function. Then, the sinusoidal function frequency is determined based on the frequency response of the transfer function between the radial force and the acceleration. The second control strategy is based on the idea to reduce the variation of the radial force, which has a high impact on the vibration

performance. A hysteresis-based Direct Force Control (DFC) is adopted, which aims to obtain a smooth total radial force. However, this method has the disadvantage of increasing the torque ripple due to the absence of a current limitation. Thus, a reference current adapter is proposed to handle the vibration and the torque ripple reduction. It produces an auto-tuning reference current that limits the variation of the torque and the radial force such as to achieve a trade-off between torque ripple and vibration. In addition to the control method design, a hybrid implementation of the second control strategy is presented by adopting a software/hardware partitioning system. Experimental results are presented by comparing the proposed method with traditional control. The tests validate the effectiveness of the control approach and the contribution of the proposed hardware/software implementation.

Thus, this thesis is structured in four parts as follows:

Chapter 1 presents the main vibration and noise sources in the SRM system. Moreover, the vibration reduction methods of previous research are stated both from the aspects of geometrical optimization and control strategies. Besides, different experimental implementation controllers (software controller, hardware controller and hardware/software partitioning controller) are introduced based on the application requirements.

Chapter 2 introduces a semi-analytical vibration prediction model. At first, the electromagnetic model and the structural model are simulated using the Finite Element Method (FEM). Using the electromagnetic model, three profiles (flux linkage, torque and radial force profiles) are obtained. In the structural model, the natural frequency, and the damping ratio are computed for different modes. Based on these parameters, a semi-analytical electromagnetic/structural multi-physics model is built to estimate the vibration, where the radial force is the output of the electromagnetic model and the input for the structural model.

The main part of this thesis presents two vibration and noise reduction control strategies: Improved Variable Turn-off Control (IVTC) and Direct Force Control with Current Reference Adapter (DFC&RCA). Chapter 3 introduces the concept of these control methods and discusses the effects of the control parameters. Moreover, it investigates secondary aspects for the general applicability such as the efficiency and torque ripple performance by

means of simulation.

Chapter 4 presents the experimental implementation of DFC&RCA. The proposed control method is evaluated by experimental tests using a 8/6 SRM prototype. The control is applied using a hardware/software partitioning system developed by considering factors related to the system performance, the resource consumption and the design flexibility. In this implementation, a FPGA board is used combined with a DS1104 controller board equipped with a microprocessor. Experiments results are presented and discussed in comparison with results obtained with traditional control.

Chapter 5 summarizes the main conclusions of this work and provides an outlook on related future work challenges.

# Chapter 1 Vibration and Noise Reduction for Switched Reluctance Machine: State of the Art

This chapter provides a brief overview of the noise generation mechanisms of SRM in general and introduces an overview of solutions to SRM vibration and noise problems has talked in the literature. These solutions can be either structural focusing on the configuration of the machine or related to control strategies applied to the machine.

## 1.1 Noise Sources of SRM

Electrical drives emit various kinds of noise with inherent origins and transmission paths. One can distinguish between direct and indirect noise as shown in Figure 1.1, where the noise sources are divided into three broad categories: electromagnetic, mechanical, and aerodynamic noise [21]. The noise of the first two groups is transmitted indirectly. Direct noise is the airborne sound caused directly by cooling fans or moving machine parts, while indirect noise can be attributed to the mechanical vibrations (structure-borne sound) that radiate into the air.

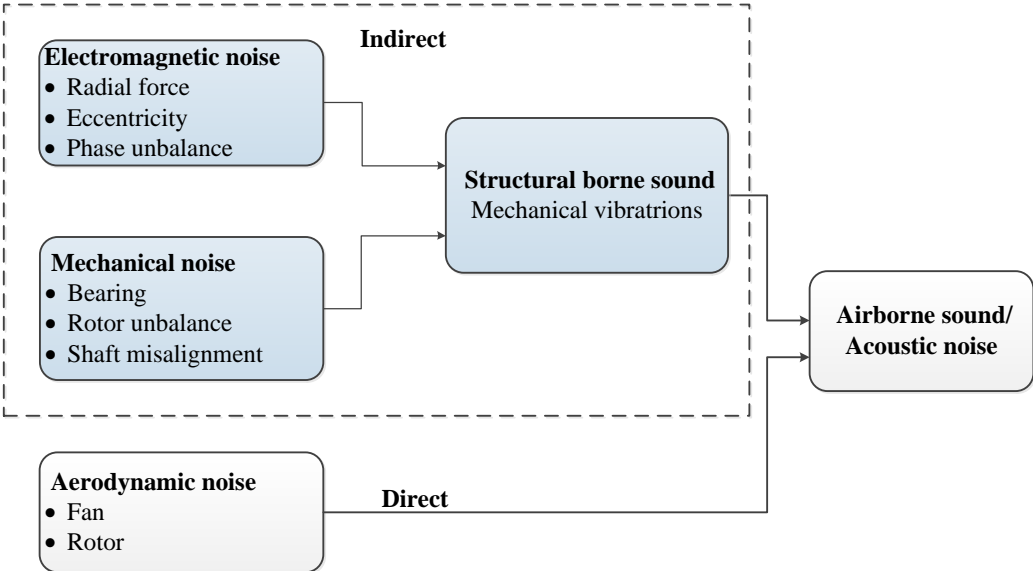


Figure 1.1 Noise sources in electrical machines and drives

### 1.1.1 Electromagnetic Source

The magnetic flux in the machine passes across the air gap. The corresponding magnetic flux density presents both radial and orthoradial components that depend on the rotor position. The induced magnetic force shows an orthoradial component related to the torque and a radial one related to vibrations. The stator-frame (or stator-enclosure) structure is the primary radiator of the machine noise. If the frequency of the radial force is close to or equal to any of the natural frequencies of the stator frame system, resonance occurs, leading to the stator system deformation, vibration, and acoustic noise [22], [23].

The fundamental frequency of the radial force is

$$f = \frac{n}{60} N_r \quad (1.1)$$

where  $n$  is the rotor speed and  $N_r$  the number of the rotor teeth.

### 1.1.2 Mechanical Source

Mechanical vibrations and noise are mainly due to bearings, their defects, sliding contacts, bent shaft, rotor unbalance, shaft misalignment, etc. The vibrations and noise produced by bearings depend on the roughness of the sliding surfaces, lubrication, stability manufacture process, quality, and installation. The rotor unbalance is mainly caused by the manufacture and installation. If there exists rotor unbalance, there will be centrifugal force between the bearing and the rotor when rotating. That causes rotor dynamic vibration which results in noise emissions from the stator, rotor, and rotor support structure. When the rotating speed of the motor is too high or too unstable, it will easily cause damage since the motor will not work properly, or it may even be damaged or runaway.

### 1.1.3 Aerodynamic Source

The main source of aerodynamic noise is the cooling fan in the motor. In a closed motor with no external fan, the aerodynamic noise is basically negligible. However, the SRM's unique salient pole rotor structure is the same as the "fan" when the motor rotates. Therefore, there will still be aerodynamic noise. During the rotation of the motor, the rotor poles

periodically act on the surrounding air mass, causing pressure pulses, which in turn generate rotational noise having the following frequency:

$$f_r = \frac{kN_r n}{60} \quad (1.2)$$

where  $k = 1, 2, 3 \dots$

Several studies have shown that the main vibration and noise source of the electrical machine is from the radial force produced by the interaction between the stator and the rotor poles [24], [25], [26], which induces resonant vibration with circumferential mode shapes of the stator. The noise due to deformation of rotor is limited because the rotor is much stiffer and hence less susceptible to forces [27].

## 1.2 State of the Art regarding Noise Reduction

During the past decades, many researchers have been involved in finding solutions for the vibration and acoustic noise problem of SRM. These issues can be mainly divided into two approaches: geometrical optimization, generally used for the design of the mechanical part of the machine, and (semi-active/active) control strategies that are able to limit the vibration independently of the design and sizing phases.

### 1.2.1 Geometric Design

In the design progress, apart from the electromagnetic performance satisfying the requirements on power density, torque density, temperature rise and so on, the vibration and noise aspects should also be considered. The electrical machine design problem is always a multi-objective optimization problem, which should take the electromagnetic part, the thermal part and the structural part into account. As it concerns the optimization-based design, several solutions have been proposed to improve vibration mainly focused on the radial force reduction [28]-[33], the motor natural frequency manipulation [34]-[37], and the stator damping effect improvement [38].

#### 1.2.1.1 Radial Force Reduction

Authors in [30] investigate the effect of skewing the stator and/or the rotor on the

vibration reduction. Different skewed combinations (as shown in Figure 1.2) are studied: a skewed stator-SRM (SS-SRM), a skewed rotor-SRM (SR-SRM) and a skewed stator and rotor-SRM (SSR-SRM). Different skewing angles are considered from the aspect of the radial force reduction. It points out that skewing the stator is more effective than skewing the rotor. However, the use of this solution is limited by the complicated fabrication with different stacks between two laminations.

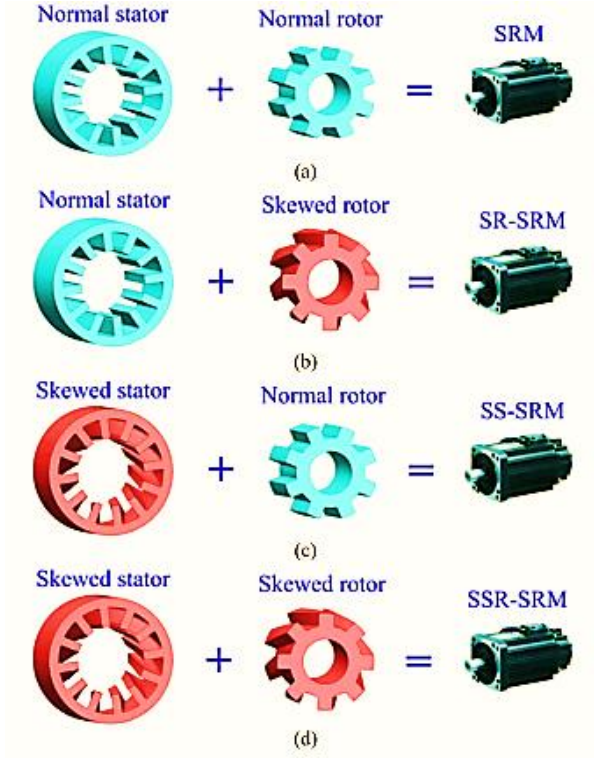


Figure 1.2 Four SRM structures: (a) Conventional SRM, (b) SR-SRM, (c) SS-SRM, (d) SSR-SRM. [30]

Different shapes of the stator poles and rotor poles are discussed in [31]. It points out that the sound pressure level depends on the maximum displacement of the stator and related to the value of the radial force. Based on that conclusion, it proposes a stator shape to increase the mechanical strength, combined with a rotor shape to reduce the radial force so as to improve the acoustic behavior. Authors in [32] propose to decrease the stator displacement by increasing the number of the stator and rotor poles to reduce the peak radial force. They make a comparison between 18/12 SRM and 24/16 SRM, which shows a decrease of noise by 2.3 dB at a speed of 2768 r/min and a load torque of 30 N·m. [33] investigated the effect of the stator poles shape on the vibration behavior of SRM and proposed a stator structure

with trapezoidal pole on the hexagon-round yoke to reduce the vibration, which has a reduction of 20% for the maximum vibration acceleration.

### 1.2.1.2 Natural Frequency Manipulation

Authors in [34] propose a new structure of SRM to make it less noisy while preserving a compromise between torque and copper losses. To this purpose, the machine structure is designed so that some of the natural frequencies of the SRM are beyond the audible spectrum. [35] investigates the effect of the frame on the acoustic noise and vibration of a high-speed and high-power switched reluctance machine. Different frame thicknesses, types of cooling ribs, and frame shapes are analyzed in five types of frame/ribs (as presented in Figure 1.3). A reduction up to 11.7 dB is estimated when changing from an axial frame toward a screw frame or a thicker frame.

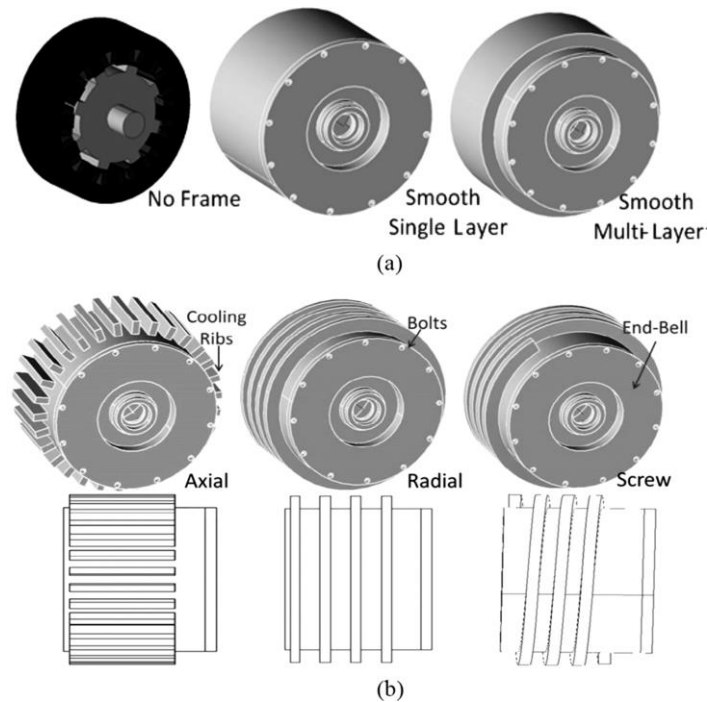


Figure 1.3 (a) Types of frame/ribs for a 12/8 SRM. (b) Longitudinal cross-sectional view of axial, radial, and screw-type frames, respectively. [35]

### 1.2.1.3 Stator Damping Improvement

Authors in [38] put forward that distributing the airgap in the SRM stator helps damping the vibration. They compare the electromagnetic and mechanical performance between the airgap placed in the stator tooth and the airgap in the stator yoke (Figure 1.4). It shows a

reduction of 14 dB when the airgap is in the stator yoke without compromising the torque. In terms of practicality of the method, the prototyping of the proposed method is difficult as the laser cutting time will increase excessively.



(a) Airgap in the stator tooth

(b) Airgap in the stator yoke

Figure 1.4 Distributed airgap in the SRM stator

In [39], the researchers propose a cylindrical-shape rotor aiming at reducing the winding losses and the acoustic noise at high rotational speed. The rotor poles are connected by thin ribs to obtain a cylindrical rotor surface. It makes a reduction of 11.4 dB at 7050 r/min.

## 1.2.2 Control Methods

### 1.2.2.1 Current Shaping

In the early stage of the research, the current shaping control method is usually adopted to reduce the SRM vibration and noise, such as the turn-on and turn-off angle advanced shift method [40], the random control angle method [41]; the two-stage [42] or three-stage commutation method. In [43], a new excitation method is proposed by adopting the C-dump inverter (shown in Figure 1.5) to decrease the change rate of the magnetic source at the commutation period so as to reduce the vibration and the acoustic noise. However, it weakens the fault-tolerant ability of the SRM due to the structure of C-dump converter. In [44], a three-phase full bridge inverter is adopted for a Y-type winding configuration SRM, based on which current-oriented control method is used, it improves the electromagnetic torque and cancels the third harmonic real power, which reduces the acoustic noise to some extent. In [45], it adopted the random frequency pulse width modulation (RPWM) to make the harmonics of the controlled current uniformly distribute to reduce the noise. To make this method more effective, a robust shaping technique [46] is employed in which a band-pass filter is added to

the control strategy to extract the current harmonics within a given range.

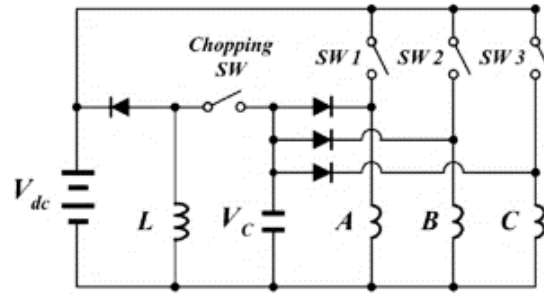


Figure 1.5 C-dump inverter for hybrid excitation method.[43]

### 1.2.2.2 PZT Actuator

Due to their piezoelectric properties, PZT (Lead Zirconate) actuators have become an alternative method for vibration reduction [47]-[51]. PZT actuators mounted between the stator teeth and the housing are used to actively dampen the vibrations caused by the radial forces. Different control methods are proposed based on the PZT used as an actuator or a sensor. A semi-active method named synchronized switch damping is introduced in [48] where the PZT is used as a sensor. This approach is compared to an active method based on the positive position feedback (PPF) [49] that uses the PZT as an actuator and points out that the active control has better performance but is more complex. Furthermore, the number and the placement of the piezoelectric actuators are optimized by using genetic algorithm to reduce the vibration further [50]. However, all the semi-active/active control solutions require additional components – PZTs.

### 1.2.2.3 Radial Force Shaping

Since the vibration of the machine is mainly due to the variation of the radial force, there are methods interested in maintaining a constant radial force. In [52], a new approach is proposed by controlling the radial force and electromagnetic torque simultaneously. To the end, the current of each stator pole is controlled independently. Based on the conventional torque control, two extra poles are adopted to compensate a desired radial force. However, this approach increases the cost because it uses more switching devices. Moreover, researches in [53]-[56] point out that the variation of the radial force has a high impact on the vibration

performance, which inspired the development of control methods aiming to obtain a smooth radial force. In [53], this objective is achieved by adopting the Direct Instantaneous Force Control (DIFC), along with a predictive controller used to compute the duty ratio of the PWM. However, this controller has the disadvantage of causing serious torque ripple. To solve the torque ripple problem in [53], authors in [54] propose a control method named direct instantaneous torque and force control (DIT&FC). It aims to keep constant both the overall torque and the overall radial force. However, the total losses have been increased up to 48% using this method, compared to the ones obtained with traditional current hysteresis control. In [55] and [56], the variation of the sum of radial forces has been minimized using a current profile control method. Yet, the methods are only suitable for three-phase SRM and can only work when the flux density is unsaturated.

In this thesis, a new control method is proposed, namely Direct Force Control with Reference Current Adapter (DFC&RCA) that is able to reduce the vibration of the SRM by handling the torque ripple and the radial force at the same time.

### **1.2.3 Multi-physics Modeling Methods**

The structural dynamic behavior of an electrical machine plays a key role in the noise generation process (see Figure 1.1). Therefore, it has to be assessed by acoustic analysis. Especially vibration or acoustic noise prediction methods need a mathematical representation of the machine structure that either can be derived from measurements or calculated using analytical or numerical approaches. Such modeling methods are needed to design an acoustically optimized machine in order to investigate the effect of the different control strategies.

#### **1.2.3.1 Analytical Methods**

Since it is usually not possible to set up the exact analytic equation of motion for a real electrical machine (or its solution), analytical approaches simplify the problem by treating the machine as an elementary shape. In [57], [58], a full analytical method that computes the radial force and the acoustic noise is presented and used for a SRM and an induction machine, separately. Both models consist of the electromagnetic section and the vibro-acoustic section

of each machine (established based on the machine geometry and material properties) and allow predicting the audible magnetic noise level radiated by the motor and the principal resonances occurring, which makes the noise optimization of the electrical machine more convenient to be realized. The model in [58] shows a good accuracy by comparing to the experimental results. In [59], a new analytical vibration model of SRM is proposed, in which an input-output model based on the mechanical impulse response is developed on the basis on the convolution theorem. The coefficients in the analytical model can be calculated with the vibration acceleration data measured from the experiments. However, large number of data need to be measured for different positions.

### **1.2.3.2 Numerical Methods**

One of the common numerical methods is the Finite Element Method (FEM). In [60], [61] a completely numerical modeling is presented to predict the acoustic noise for SRMs and PMSMs, respectively. FEM was adopted to obtain the electromagnetic and vibration behaviors of the machine. Both the Boundary Element Method (BEM) [60] and a point wise approximation [61] are adopted to simulate the acoustic noise of the machine. The effect of the damping ratio, the auxiliary element, and the constraints was discussed further in [61]. Both the two methods are compatible with the experimental results. However, the numerical method is time-consuming and it's very complex to implement the control strategies.

### **1.2.3.3 Combining Analytical and Numerical Method**

There are also literatures combines the numerical with the analytical method to predict the structural behaviors of electrical machines [62]-[65]. In [62], the vibration behavior of a Flux-Switching Permanent Magnet Motor (FSPM) is induced. An analytical model to simulate the stator deformation is built with the results of the FEM adopted to calculate the natural frequency of stators and the magnetic force, in which the deformation is in expression of Fouries series. In [63], an integrated approach to simulate the acoustic noise of SRM combing the means of field-circuit coupling and numerical simulation is proposed: the field-circuit coupling based on the temporary lumped-parameter model is adopted to obtain the field distribution, based on which the numerical analysis is completed with BEM. Based on

the analytical vibration model proposed in [59], the results of the vibration are adopted into the numerical method adopting the BEM to predict the acoustic noise in [64][65]. For this fixed model of simulation, it needs less time compared to the numerical method and improve the accuracy of the analytical method. The problem is also that it is complicated to validate different control strategies.

In this work, structural FEM is used to determine the transfer functions between the radial force and acceleration that can then be used in fast analytic models for control strategy investigation.

#### **1.2.4 Implementation of Control Methods**

From the control implementation aspect, the controllers are becoming more and more complicated in order to improve the performance of the drive system. Many of the control applications are implemented using a software controller due to its advantages such as low cost and design flexibility. However, the use of software solutions is limited because of serial operation caused by their internal architecture. The more sophisticated is the control algorithm, the more delay is introduced to the control loop, which affects the control performance [53]. Therefore, hardware solutions are proposed, among which the Field Programmable Gate Array (FPGA) has been proved a good candidate. Its high-speed computation ability with parallelism reduces the execution time and enhances the control performance [67], [68], which justifies its increasing quotient in the industrial applications [69], [70]. Moreover, some works use a combination of software and hardware solutions based on optimizing area, processing time or power consumption. In [71], authors propose a hardware/software codesign method considering both the control requirements and the architecture constraints for a sensorless AC machine drive system. It is implemented using a MicroBlaze soft processor and a FPGA fabric. In [72], it presents a system used to measure the stator inductance and the resistance in PMSM by combining of a microcontroller and a FPGA. The current control loop is implemented in the FPGA to reduce delay, and less time-sensitive control loops such as speed and position loop are implemented in the microcontroller. In [73], authors develop a digital Duty-Cycle-Space-Vector (DCSV) -based modulation strategy for the three- and four-leg matrix converter implemented in a DSP-FPGA

platform, aiming at reducing the calculation time of the modulation algorithm by splitting the computational load with Digital Signal Processor (DSP) and FPGA.

In this work, a hardware/software partitioning architecture of controller is adopted to implement the proposed vibration reduction control strategy considering the system performance, resource consumption and design flexibility.

### **1.3 Conclusion**

In this chapter, the main noise sources of SRMs are presented: structure-borne sound caused by the structural vibration and airborne sound attributed by cooling fans or rotor, which act on the surrounding air mass. Furthermore, an overview of vibration and noise reduction techniques is provided from two perspectives: geometric optimization and control. Next, the multi-physics modeling methods used to combine the electromagnetic and structural model are presented. Three different modeling methods, namely, analytical, numerical and analytical-numerical are introduced. Finally, different control application systems are introduced for the experimental implementation.

# Chapter 2 Semi-analytical Electromagnetic/Structural Multi-Physics Model of SRM

As investigated in Chapter 1, there are two kinds of noise in an electrical machine: indirect noise caused by the structural vibration and direct noise coming from cooling fans or moving machine parts. Accordingly, in this thesis, the noise reduction method will be studied from the aspects of vibration reduction. Then, an accurate structural model is required to verify the vibration and noise reduction method. There are mainly two ways to simulate the structural behavior of a SRM: the analytical method and the numerical method. The analytical method is simple and fast but not as accurate as the numerical one. However, the numerical method is time-consuming, especially for the transient simulations of the multi-physics model. Besides, it is more complicated to implement the control algorithm in FEM. So, in this work, a semi-analytical electromagnetic/structural multi-physics model is proposed, based on the simulation results of the static numerical computation. The electromagnetic/structural multi-physics model is composed of the electromagnetic and structural models, which are connected by the radial force.

The simulation model for SRM drive system for vibration analysis is shown in Figure 2.1. The blocks “Controller”, “Converter”, “Machine Model”, and “Load” are commonly used in time domain simulations of electrical machines. The Load model is not further discussed here. The blocks “Converter model”, “Machine Model”, “Force Model” and “Structural Model” are described in the following parts. The controller part will be investigated in Chapter 3.

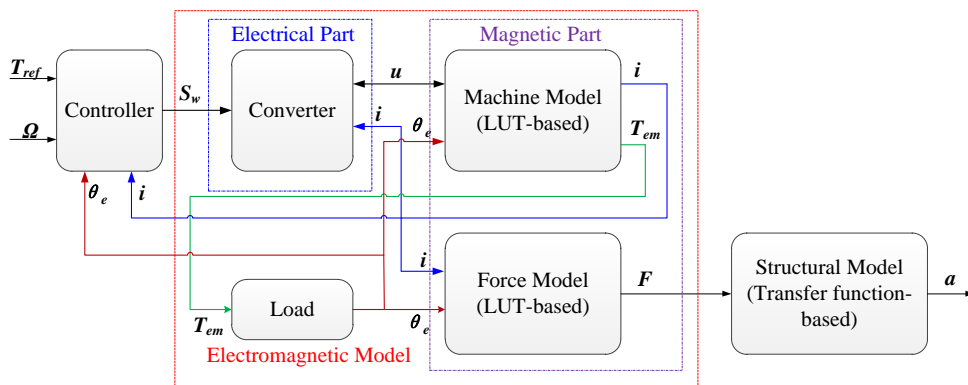


Figure 2.1 Simulation model for SRM drive system for vibration analysis.

## 2.1 Investigated SRM

SRM is a double-salient structure machine. Both its stator and rotor are made of laminated silicon steel. There are neither permanent magnets nor windings on its rotor, which enables it to work in a wide speed range and in harsh environment. Meanwhile, the simple structure of a SRM improves its robustness and lowers its cost. The machine investigated in this work is a 4-phase SRM with 8 stator teeth and 6 rotor teeth (its parameters are given in Appendix A). Its winding is connected to a traditional asymmetric half-bridge converter as shown in Figure 2.2.

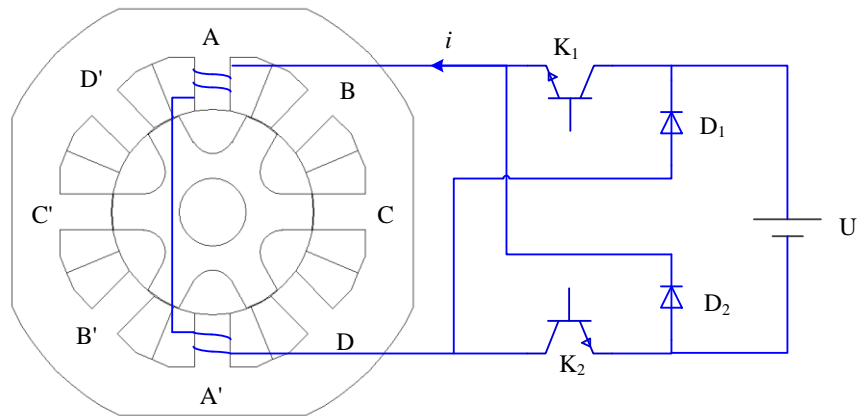


Figure 2.2 Schematic block of a 4-phase 8/6 SRM

The adopted converter has three different work states, which can provide positive, zero or negative terminal voltage to the phase winding of the SRM. The three states are achieved by controlling the status of the switches in the converter, the detail is given in Figure 2.3, here, the three different states of the converter are presented. When the state  $S_w = 1$ , both switches connected to the winding are turned on, and a positive voltage is applied to the phase winding of SRM. When the state  $S_w = 0$ , one of the switches is turned off, and the terminal voltage of the phase winding is zero. When the state  $S_w = -1$ , both switches are turned off, a negative voltage are supplied to the phase winding, the SRM starts to demagnetize.

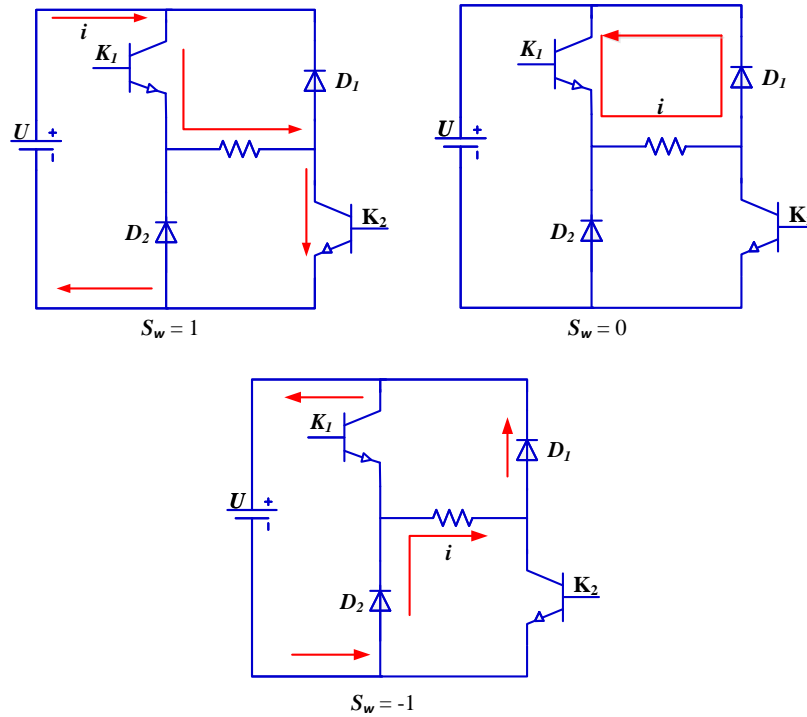


Figure 2.3 The states of the converter.

## 2.2 Operating Principle of the SRM

Unlike the traditional electrical machine relying on the interaction between magnetic fields generated by the stator and rotor windings (or permanent magnets), the SRM produces torque based on the principle of a magnetic circuit that tends to minimize its reluctance. Hence, the rotor will turn towards a position where the reluctance of the excited phase is lower, where the inductance  $L$  is higher. The position with maximum inductance  $L_a$  is called aligned position, whereas the position with minimum inductance  $L_u$  is called unaligned position. The definitions of aligned and unaligned positions are illustrated in Figure 2.4.

As presented in Figure 2.2, if the phase windings are excited as A-B-C-D successively, the rotor will rotate counterclockwise. Or it rotates clockwise when phases are excited in a sequence of D-B-C-A. By commutating the excitation from one phase to another before the aligned position is reached, a unidirectional overall torque can be achieved.

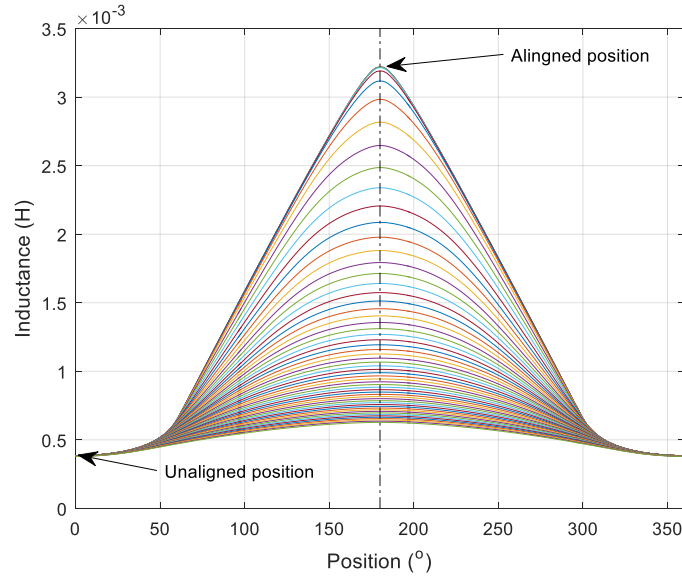


Figure 2.4 Inductance profile [18].

## 2.3 Electromagnetic Model

Electrical machines are electromechanical energy converters. They convert electrical energy into mechanical energy (and vice versa) via magnetic energy. To model an electrical machine in terms of its feeding voltages and currents (electrical part) and electromagnetic torque (magnetic part), one needs three basic “ingredients”: the voltage balance equation, the flux linkage characteristics, and the torque expression. To build a structural model, the radial force from the electromagnetic field is also needs to be calculated. From these four expressions, the simulation model of the machine is derived in this chapter and so is the control in Chapter 3.

### 2.3.1 Voltage Balance Equation

The voltage balance equation connects the winding terminal voltage  $u$  with the winding phase current  $i$  and phase flux linkage  $\lambda(\theta_e, i)$ :

$$u(t) = Ri(t) + \frac{d\lambda(\theta_e, i)}{dt} \quad (2.1)$$

where  $R$  is the phase resistor,  $\theta_e$  is the electrical position. This equation can be understood as a description of electric behavior.

The relationship between the mechanical position  $\theta_m$  and the electrical position  $\theta_e$  is:

$$\theta_e = N_r \theta_m \quad (2.2)$$

where  $N_r$  is the rotor pole number, which is equals to 6 for the investigated SRM.

### 2.3.2 Flux-linkage Characteristics

The flux-linkage characteristics describe the magnetic behavior of SRM. Since a SRM is always operated in saturation to improve the energy utilization, and has a double-salient structure, the phase flux linkage  $\lambda(\theta_e, i)$  is dependent on both position  $\theta_e$  and phase current  $i$ . Figure 2.5 illustrates the magnetic field distribution obtained with FEM when the rotor is in three different positions, when one phase is excited with a constant current. By changing the rotor position and the excitation current, the flux-linkage profile is obtained as shown in Figure 2.6.

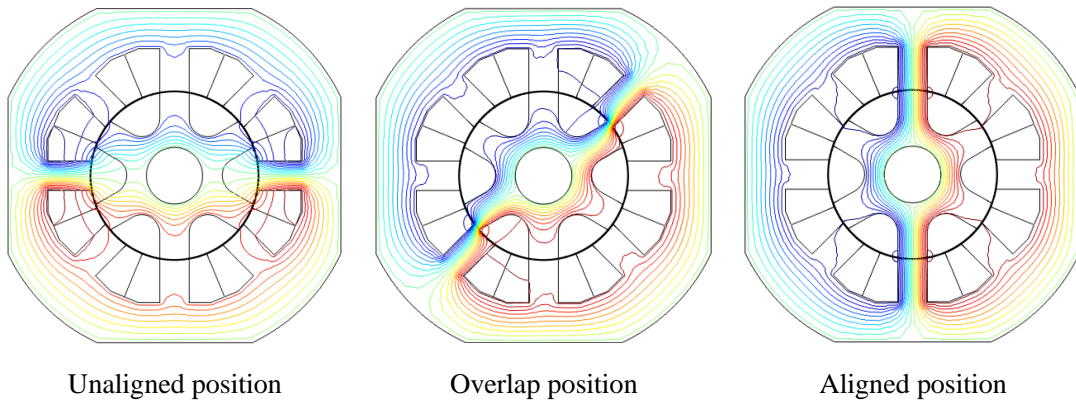


Figure 2.5 Magnetic field distribution of SRM in FEM

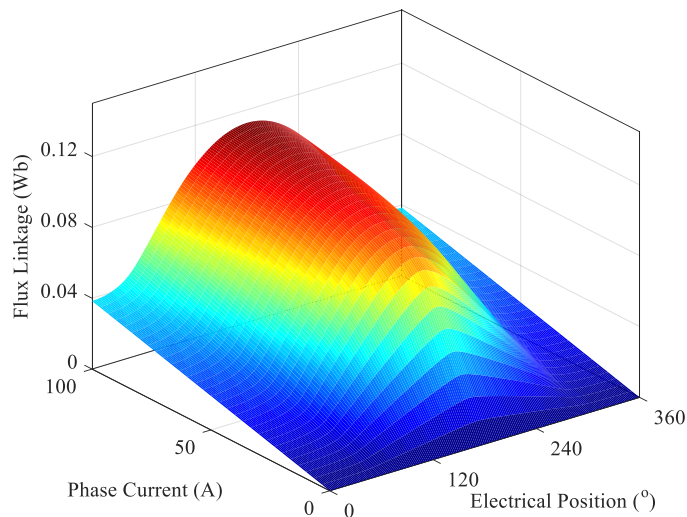


Figure 2.6 Flux-linkage profile.

### 2.3.3 Torque Production and Energy Conversion

Despite the fact that SRMs have a different working principle from AC machines and DC machines, a general compact torque expression can be derived that is valid for all electrical machines. Here, we will start with the energy balance equation [74].

The energy conversion of SRM can be expressed as:

$$W_{el} = W_{mag} + W_{mec} + W_J \quad (2.3)$$

The input electrical energy  $W_{el}$  is equal to the sum of magnetic energy stored in the machine  $W_{mag}$ , mechanical energy converted into mechanical  $W_{mec}$  and copper losses consumed by the phase windings  $W_J$ .

For incremental changes, eq. (2.3) is written as:

$$dW_{el} = dW_{mag} + dW_{mec} + dW_J \quad (2.4)$$

On the electrical supply side,  $dW_{el}$  depends on the product of input voltage and current:

$$dW_{el} = u \cdot idt \quad (2.5)$$

Combing eq. (2.1) with eq. (2.5), then

$$dW_{el} = \left( Ri + \frac{d\lambda}{dt} \right) \cdot idt = Ri^2 dt + id\lambda \quad (2.6)$$

Thus, eq. (2.4) becomes

$$id\lambda = dW_{mec} + dW_{mag} \quad (2.7)$$

For a rotating motor, the mechanical energy can be expressed as:

$$dW_{mec} = T_{em} d\theta_m \quad (2.8)$$

where  $T_{em}$  is the electromagnetic torque ignoring the magnetic losses and mechanical losses.

In rotation, the stored magnetic energy is expressed by:

$$W_{mag} = \int_0^\lambda id\lambda \quad (2.9)$$

So,

$$i = \frac{\partial W_{mag}}{\partial \lambda} \quad (2.10)$$

And the differential magnetic field stored energy  $dW_{mag}$  can be split in its  $\lambda$ - and its  $\theta$ -

dependent parts as:

$$dW_{mag} = \frac{\partial W_{mag}}{\partial \lambda} d\lambda + \frac{\partial W_{mag}}{\partial \theta_m} d\theta_m \quad (2.11)$$

Combing equations(2.7)(2.8) with eq.(2.11), then

$$T_{em} = -\frac{\partial W_{mag}}{\partial \theta_m} \quad (2.12)$$

Generally, the magnetic co-energy  $W'_{mag}$  (Figure 2.7) is introduced to express the  $T_{em}$ .

It is a function depending on the current  $i$  and mechanical position  $\theta_m$  as:

$$W'_{mag}(\theta_m, i) = \int_0^i \lambda(\theta_m, i) di \quad (2.13)$$

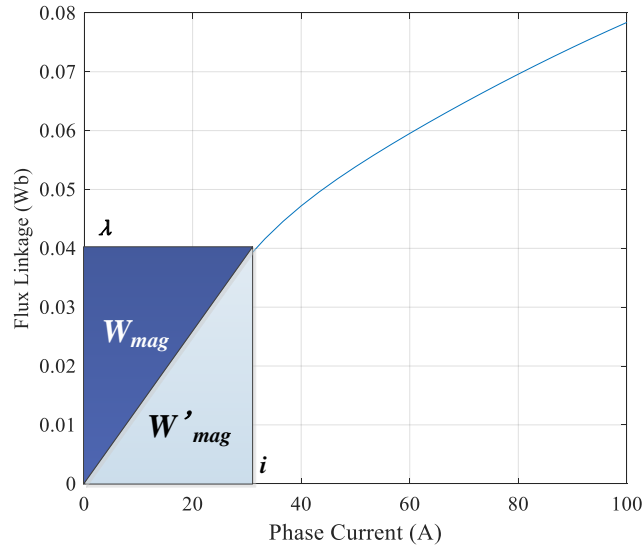


Figure 2.7 The definition of magnetic energy and magnetic co-energy.

Thus,

$$T_{em} = \frac{\partial W'_{mag}(\theta_m, i)}{\partial \theta_m} = \frac{\partial \left( \int_0^i \lambda(\theta_m, i) di \right)}{\partial \theta_m} \quad (2.14)$$

With eq.(2.14) the electromagnetic torque can be computed in non-linear cases following the virtual work principle or deduced from the flux linkage in FEM. The calculation result is presented in Figure 2.8.

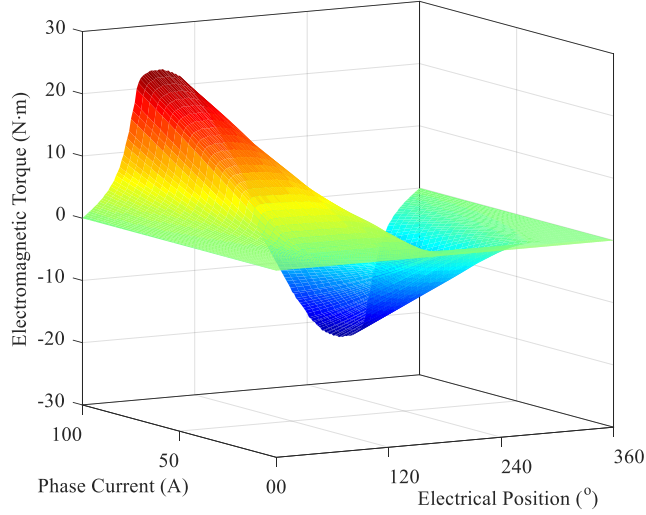


Figure 2.8 Electromagnetic torque profile.

### 2.3.4 Radial Force Characteristics

There are many ways [75] to calculate the radial force in of one the stator teeth, the two main solutions are: virtual work method in a similar way of the method adopted in the previous part [76] and Maxwell stress tensor method [77]. In this work, the second method is adopted, and the Maxwell stress tensor  $T^M$  is expressed as:

$$T^M = \vec{H} \otimes \vec{B} - \frac{1}{2} \vec{H} \cdot \vec{B} \delta \quad (2.15)$$

where  $\vec{H}$  is the magnetizing field and  $\vec{B}$  is the magnetic field,  $\otimes$  is the dyadic product, and  $\delta$  is the Kronecker symbol.

Then, the radial force on one tooth (its profile is given in Figure 2.9) can be computed:

$$F = \text{div}T^M \quad (2.16)$$

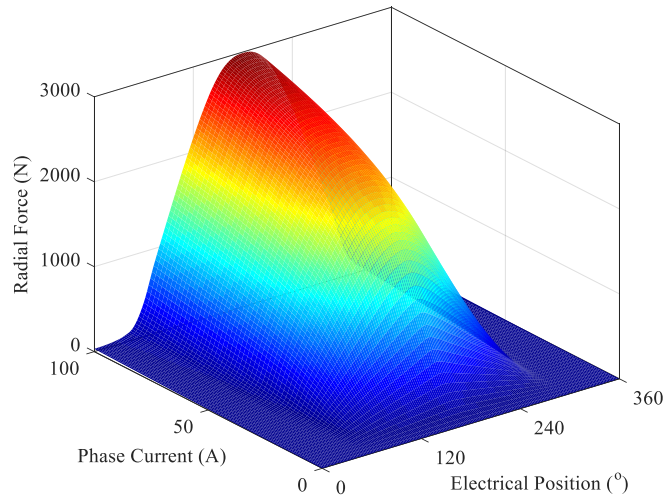


Figure 2.9 Radial force profile.

After performing the FEM, a Simulink model can be built based on the voltage balance equation (2.1) and the torque balance equations as follows:

$$T_s = T_L + J \frac{d\Omega}{dt} + K_t \Omega \quad (2.17)$$

where  $T_L$  is the load torque;  $J$  is the inertia;  $K_t$  is the friction coefficient; The value of the  $J$  and  $K_t$  is from the work of Hala in [78].

The electromagnetic model has a voltage input since voltage source converter supplies the machine. Within the context of this work, the aim is to determine the torque, force and the currents of the machine under arbitrary operating conditions. The electromagnetic force excitation as origin of the vibration is subsequently determined from the machine currents and the rotor position. The model built in Simulink is an inverse magnetization model for the current prediction, where the current is obtained as a function of flux linkage (presented in Figure 2.6). The FEM data, which delivers flux linkage as function of current, is inverted when parametrizing the model. In the model, Look-Up Tables (LUTs) using linear interpolation are adopted to predict the dynamic performances of the considered SRM such as current, torque and radial force based on the FEM data. The system simulation model contains no differentiator but only a integrator. The schematic diagram of the electromagnetic model for a SRM is given in Figure 2.10. Since the phases of an SRM can usually be regarded as magnetically independent, only one phase needs to be simulated and the results can be duplicated with adequate time shifts for the others. The SRM drive system model is implemented in MATLAB/Simulink environment, which eases the analysis of the dynamic behavior of the machine (compared to the FEM environment) and reduces the simulation time. The dynamic performance of SRM is also a multiphysics problem combining the electrical part with the magnetic part as shown in Figure 2.1.

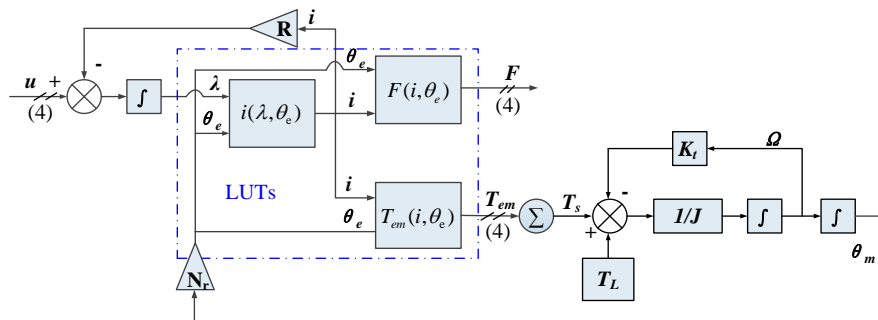


Figure 2.10 Schematic diagram of an SRM electromagnetic model.

Figure 2.12 presents the radial Maxwell stress under single pulse mode obtained by applying the current (shown in Figure 2.11) from the model in Figure 2.10 for an electric period (from the unaligned position to the aligned position) in the airgap. As presented in the figure, the stator teeth are under the influence of the rotor poles during the rotation. The area of the stress tensor increases during the rotation. And two points (with a spatial distance of one stator pole pitch) in the air gap are excited with the same force with a time difference of one stroke.

Thus, the radial Maxwell stress can be decomposed into circumferential spatial and temporal harmonic components  $(o_m, r_n)$  by the two-dimensional Fast Fourier Transformation (2D FFT), where  $o_m$  is the spatial orders and  $r_n$  is the temporal harmonics rank. Figure 2.13 shows the 2D FFT of the radial Maxwell stress. It can be seen that the circumferential spatial order  $o_m$  is equal to the integer multiples of 2 due to the excitation way, which at least two poles are excited simultaneously. So, its lowest nonzero spatial order is two. The difference between two temporal harmonic rank  $r_n$  components with high amplitude is equals to 4, which is attributed to machine phases, as four phases are excited each electrical period. A resonance would occur if and only if there is a match both between the circumferential spatial order of the force harmonic and the circumferential mode number of the stator, and an agreement between the frequency of the force harmonic and the natural frequency of the stator mode [79]. Thus, only the modes which are integer multiples of 2 are available for this investigated 8/6 SRM. And only a few temporal harmonics of the stress are able to excite the vibration modes as shown in Figure 2.13. For example, mode 0 can be excited by the 4<sup>th</sup> temporal harmonic, the 1<sup>st</sup> temporal harmonic is able to excite mode 2 and the 2<sup>nd</sup> and 6<sup>th</sup> temporal harmonics will excite mode 4. All of these phenomena are caused by the stress distribution of different temporal ranks in the air-gap shown in Figure 2.14. For different temporal harmonics of stress, their corresponding circumferential spatial distributions in the airgap might be various, so that they may lead to different relevant modes. Moreover, some harmonics are efficient to excite certain modes, but some are not. So, a control method may be interesting to remove certain harmonics of the force that are able to excite the corresponding modes, such as the 1<sup>st</sup>, 5<sup>th</sup>, 9<sup>th</sup> harmonics which excite mode 2. Some

preliminary works have been done based on this idea, using notch filter (details are given in Appendix B).

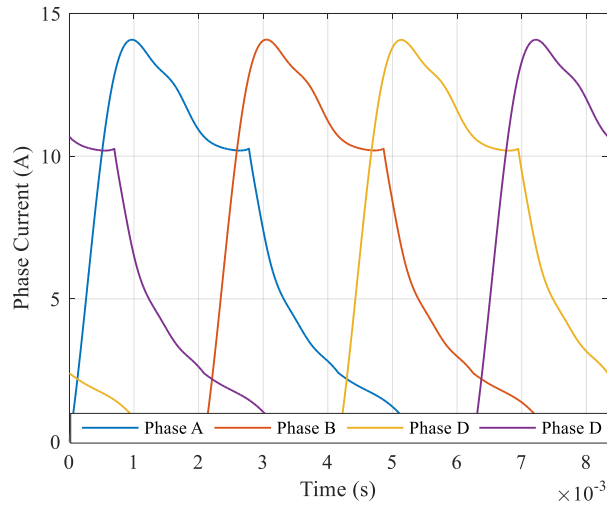


Figure 2.11 Applied phase current in the FEM simulation.

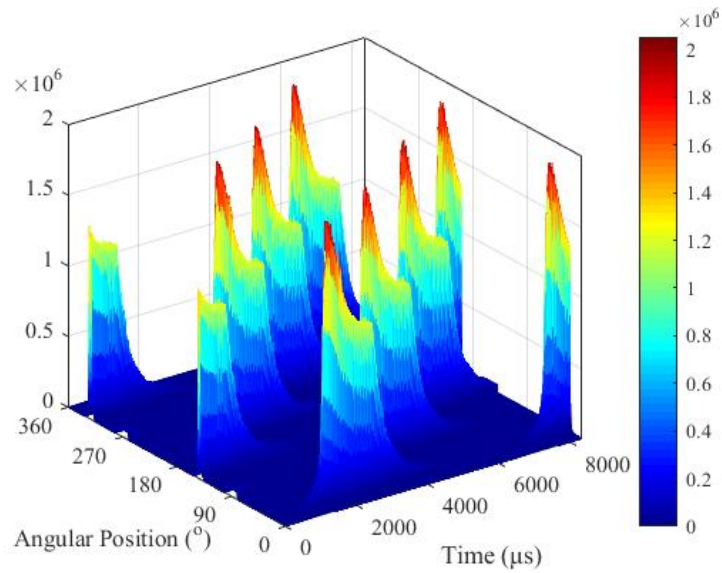


Figure 2.12 Radial Maxwell stress for an electric period in Pa.

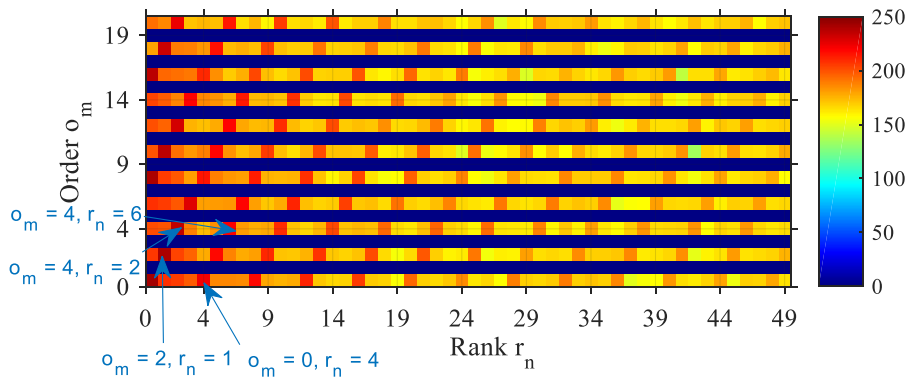


Figure 2.13 Radial Maxwell stress 2D FFT in dB.

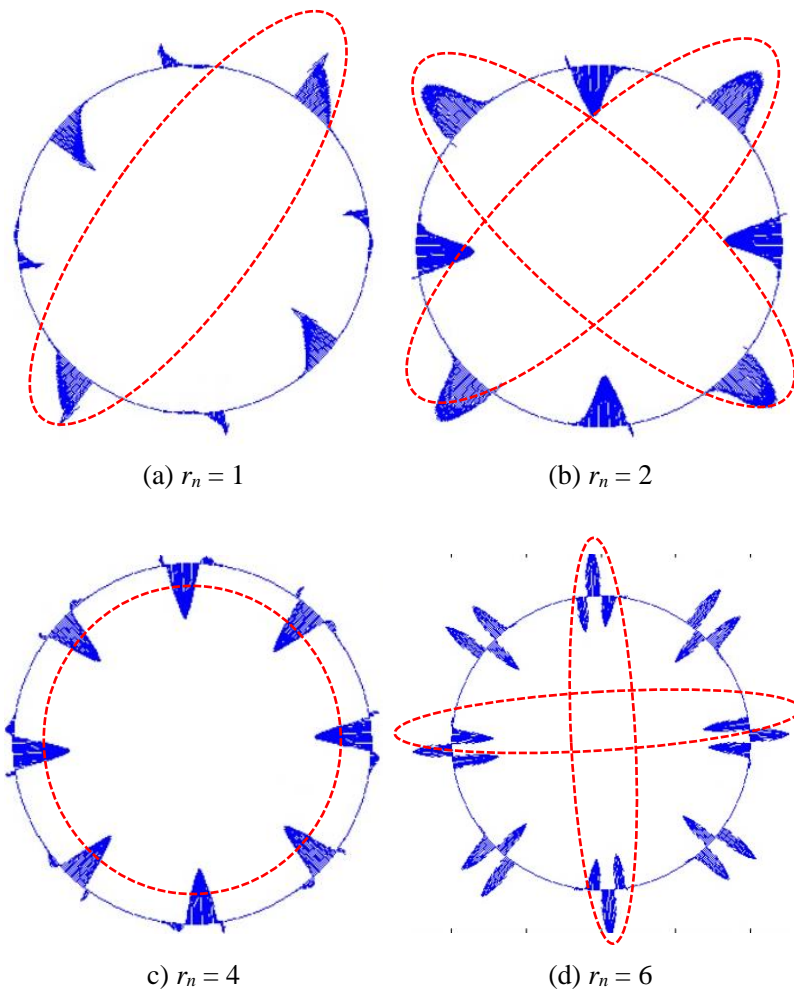


Figure 2.14 Radial Maxwell stress harmonics distribution in the airgap for different temporal ranks

## 2.4 Structural Model

The time domain analysis in FEM can be used to predict the vibration acceleration by applying the radial force obtained from the electromagnetic analysis to the stator poles. However, the multi-physics simulation with FEM is very time-consuming since the numerical method considers many degrees of freedom. In this work, a semi-analytical structural model to predict vibration is developed in MATLAB based on the results deduced by FEM.

The structural dynamic behavior of an object describes its reactions to dynamic external forces and is determined by its mass and stiffness distribution and damping. A detailed description of structural dynamic behavior is presented in [80]. SRM is a complex nonlinear Multi-Degree-of-Freedom (MDOF) system from the mechanical point of view, which can be simplified as the linear superposition of several Single-Degree-of-Freedom (SDOF) systems.

From the perspective of vibration, a SODF system can be simplified as a viscous damped spring-mass system (shown in Figure 2.15) [81]:

$$m\ddot{x} + c\dot{x} + kx = F \quad (2.18)$$

where  $m$  is the mass,  $\ddot{x}$  is the acceleration,  $\dot{x}$  is the velocity,  $x$  is the displacement,  $c$  is the damping coefficient of the viscous damper,  $k$  is the stiffness, and  $F$  is the applied force.

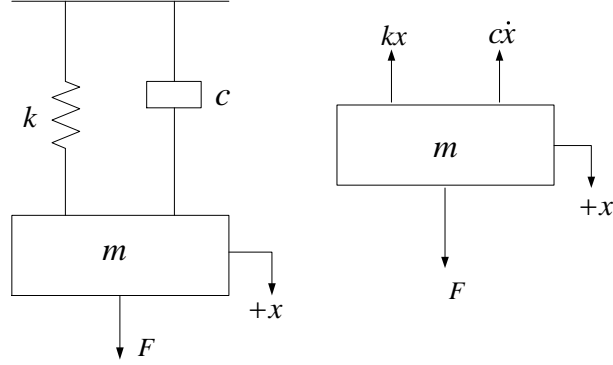


Figure 2.15 Viscous damped spring-mass system

Considering the undamped natural frequency  $\omega_n = \sqrt{\frac{k}{m}}$  and the damping ratio  $\xi = \frac{c}{2m\omega_n}$ , the Laplace transform applied to eq. (2.18) finally gives the transfer function of mode  $n$  from the radial force  $F$  to the vibration acceleration  $a$ :

$$H(s) = \frac{a(s)}{F(s)} = \frac{s^2}{m(s^2 + 2\xi\omega_n s + \omega_n^2)} = \frac{\frac{1}{m}s^2}{s^2 + 2\xi\omega_n s + \omega_n^2} = \frac{A_n s^2}{s^2 + 2\xi\omega_n s + \omega_n^2} \quad (2.19)$$

This expression can be used to model one vibration mode of the stator structure. In fact, there is more than one mode for a SRM stator. Thus, the transfer function of several different modes for the acceleration on one excited phase can be expressed as:

$$H(s) = \frac{a(s)}{F(s)} \cong \sum_{i=1}^{i=N} A_i \frac{s^2}{s^2 + 2\xi_i \omega_i s + \omega_i^2} \quad (2.20)$$

where,  $A_i$ ,  $\xi_i$ ,  $\omega_i$  ( $\omega_i = 2\pi f_i$ ,  $f_i$  is the natural frequency for the  $i^{th}$  mode) are respectively, the gain of the transfer function, the damping ratio, and the natural angular frequency for the  $i^{th}$  mode,  $N$  is the number of modes considered.

Furthermore, for a multi-phase SRM, more than one phase can be excited simultaneously. In this case, the radial force can be produced at different locations. Consequently, the vibration of the different excitation poles should be superimposed. The

impact of the excited phase  $i$  on the acceleration at the phase  $j$  is deduced from coupling factors. The coupling factors of different phases for different configurations of the symmetrical SRM have been indicated in [82]. They are obtained using the spatial Fourier components. The coupling factors can be calculated for each mode  $n$  by:

$${}_j B_n = \sum_{i=1}^{N_{ph}} {}_i B_n \cos(2n\pi(j-i)/N_s) \quad (2.21)$$

where  ${}_j B_n$  is the vibration acceleration at the  $j^{\text{th}}$  stator pole for mode  $n$ ,  $N_{ph}$  is the number of the phases;  ${}_i B_n$  is the vibration acceleration at the phase  $i$  excited by phase  $i$ ,  $n$  is the  $n^{\text{th}}$  mode, and  $N_s$  is the number of the stator poles.

Thus, the superimposed vibration acceleration for a 8/6 SRM at each pole can be expressed as a coupling matrix as follows:

$$\begin{bmatrix} {}_1 B_n \\ {}_2 B_n \\ {}_3 B_n \\ {}_4 B_n \end{bmatrix} = \begin{bmatrix} {}_{11} b_n & \cdots & {}_{N_{ph}1} b_n \\ \vdots & \ddots & \vdots \\ {}_{1N_{ph}} b_n & \cdots & {}_{N_{ph}N_{ph}} b_n \end{bmatrix} \begin{bmatrix} {}_{11} B_n \\ {}_{22} B_n \\ {}_{33} B_n \\ {}_{44} B_n \end{bmatrix} \quad (2.22)$$

where the  ${}_{ij} b_n$  in the matrix is equals to  $\cos(2n\pi(j-i)/N_s)$ .

Thus, the schematic diagram of the structural model is presented in Figure 2.16. In which,  $F_1$  to  $F_4$  and the  ${}_1 H_n(s)$  to  ${}_4 H_n(s)$  are the radial force and transfer function (its expression is in eq.(2.19)) of mode  $n$  for four different phases, respectively.  $a_n$  is the acceleration of mode  $n$  considering the superimposition of phases.

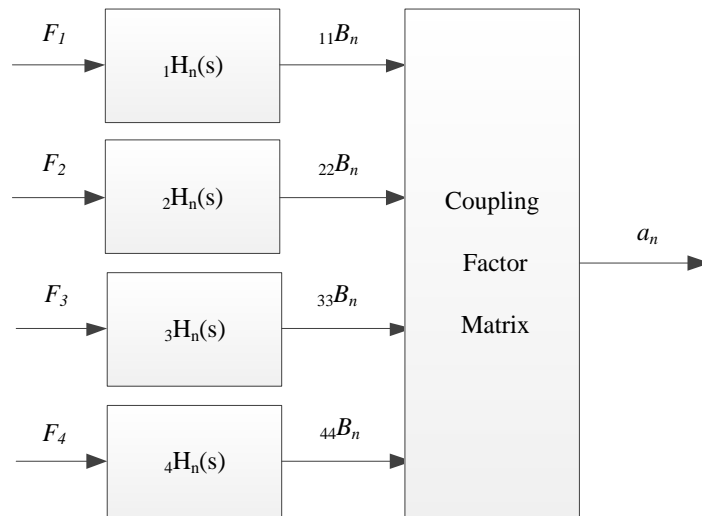


Figure 2.16 Schematic diagram of the structural model for mode  $n$

The coupling factors matrixes for each mode are given in Table 2-1. It shows that the coupling factors of mode 2 are zero for the adjacent phases, which means that they contribute independently to the vibrations and will not affect each other. As investigated in Section 2.3.4, the match between the spatial order of the force harmonic and the circumferential mode number of the stator is a prerequisite for causing considerable vibration. Thus, for the studied 8/6 SRM, not every mode of the SRM is an effective mode. Only the multiples of 2 modes are considered as effective modes because of the symmetrically loaded radial forces. Besides, only these modes within audible frequency range are considered.

Table 2-1 Coupling factors matrixes.

Mode Order	Coupling Matrix
2 <sup>nd</sup>	$\begin{bmatrix} 1 & 0 & -1 & 0 \\ 0 & 1 & 0 & -1 \\ -1 & 0 & 1 & 0 \\ 0 & -1 & 0 & 1 \end{bmatrix}$
0 <sup>th</sup>	$\begin{bmatrix} 1 & 1 & 1 & 1 \\ 1 & 1 & 1 & 1 \\ 1 & 1 & 1 & 1 \\ 1 & 1 & 1 & 1 \end{bmatrix}$
4 <sup>th</sup>	$\begin{bmatrix} 1 & -1 & 1 & -1 \\ -1 & 1 & -1 & 1 \\ 1 & -1 & 1 & -1 \\ -1 & 1 & -1 & 1 \end{bmatrix}$

Then based on (2.20) and (2.22) the structural model can be built. However, the natural frequency, the damping ratio and the gain of the transfer functions of each mode have to be determined. At first, the natural frequencies of the modes should be determined, which are obtained with modal analysis using FEM.

### 2.4.1 Modal Analysis

When it comes to simulating the structural behavior and hence the resonances, one can distinguish two different approaches: analytic and numeric methods. All analytic approaches have in common that they require only very low computation time. Hence, they are suitable to compare many different design variations in the early stage of the design process. However, their accuracy is extremely limited. So, FEM is adopted in this thesis.

The basic idea of the structural FEM is that a given complex structure, for which the equation of motion cannot be solved directly, is discretized into many simple elements, for which the equation of motion can be solved. The elements are connected at the nodes. Each possible movement of such a node is referred to as a DOF. Due to the large number of nodes, such a system is also called NDOF system, compared to a mass-spring-damper system that has only one DOF [83]. The initial balance equation is:

$$\text{div } \sigma + F = \rho \frac{\partial^2 x}{\partial t^2} \quad (2.23)$$

Considering the associated weak formulation, the equation of motion describing the discretized problem can be summarized in matrix form as:

$$M\ddot{x} + C\dot{x} + Kx = F \quad (2.24)$$

where the vector  $x$  contains the displacements of all DOFs,  $M$  is the mass matrix,  $K$  is the stiffness matrix and  $C$  is the damping matrix.  $F$  is the vector of exciting force acting on the DOFs.

In this work, the modal analysis is performed to determine the natural frequency of the SRM, where the vibration is free, without damping and additional boundary conditions. It assumes that when the damping is low, the eigenfrequencies (natural frequencies) are independent of the damping coefficient. This assumption holds for low damping values that are usual for electrical machines [84].

Thus, (2.24) becomes:

$$M\ddot{x} + Kx = 0 \quad (2.25)$$

Replacing  $x$  with  $\hat{x} \sin(\omega t)$ , thus equation can be rewritten as:

$$-\omega^2 M\hat{x} + K\hat{x} = 0 \quad (2.26)$$

This system of equations has only one no-trivial solution if the determinant is zero.

$$\det[K - \lambda M] = 0 \quad (2.27)$$

With  $\lambda = \omega^2$ , this leads to a polynomial of the order  $N_{\text{DOF}}$ , where  $N_{\text{DOF}}$  is the number of DOFs of the system. Its solution yields the eigenvalues  $\lambda_n$  (with  $n$  ranging from 1 to  $N_{\text{DOF}}$ ), hence the natural frequencies  $f_n = \sqrt{\lambda_n}/2\pi$ . With equation (2.26) a deflection shape  $\hat{x}_n$  can be computed for every eigenvalue by substituting  $\omega$ .

The first step to build a structural finite element model is creating a geometrical

description of the objects to be simulated. The actual geometric shape of the considered 8/6 SRM is presented in Figure 2.17.

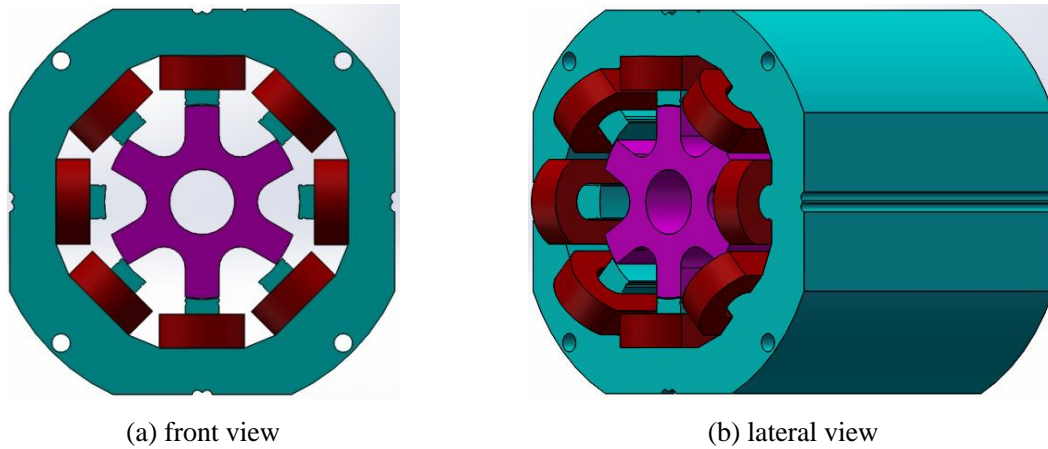


Figure 2.17 Geometric shape of 8/6 SRM.

However, for the FEM simulation, some simplifications are made concerning small geometrical details like grommets to reduce the required mesh density and therewith the computation time considerably. The rotor is omitted since it does not contribute significantly to the relevant mode shapes because the rotor structure is extremely stiff compared to the stator [85]. The mass and the stiffness of the concentrated windings of switched reluctance machines compensate each other and thus the coils could be omitted completely [86]. Finally, only the stator core is considered in the structural simulation, whose geometry model is shown in Figure 2.18. A 2-D model is simulated because of the uniformly distributed radial force along the axial direction. The simulation results are shown in Figure 2.19. It can be seen there are two modes 2, with a difference of 304 Hz between their natural frequencies caused by the asymmetric profile of the geometry.

Then the damping ratio of the mode can be determined by the corresponding natural frequency calculated with an empirical expression for small and medium sized electrical machines below [84]:

$$\xi_i = \frac{(2.76 \times 10^{-5} \times f_i + 0.062)}{2\pi} \quad (2.28)$$

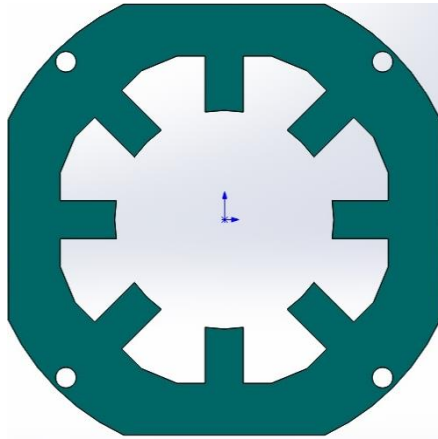


Figure 2.18 Geometric model adopted in FEM.

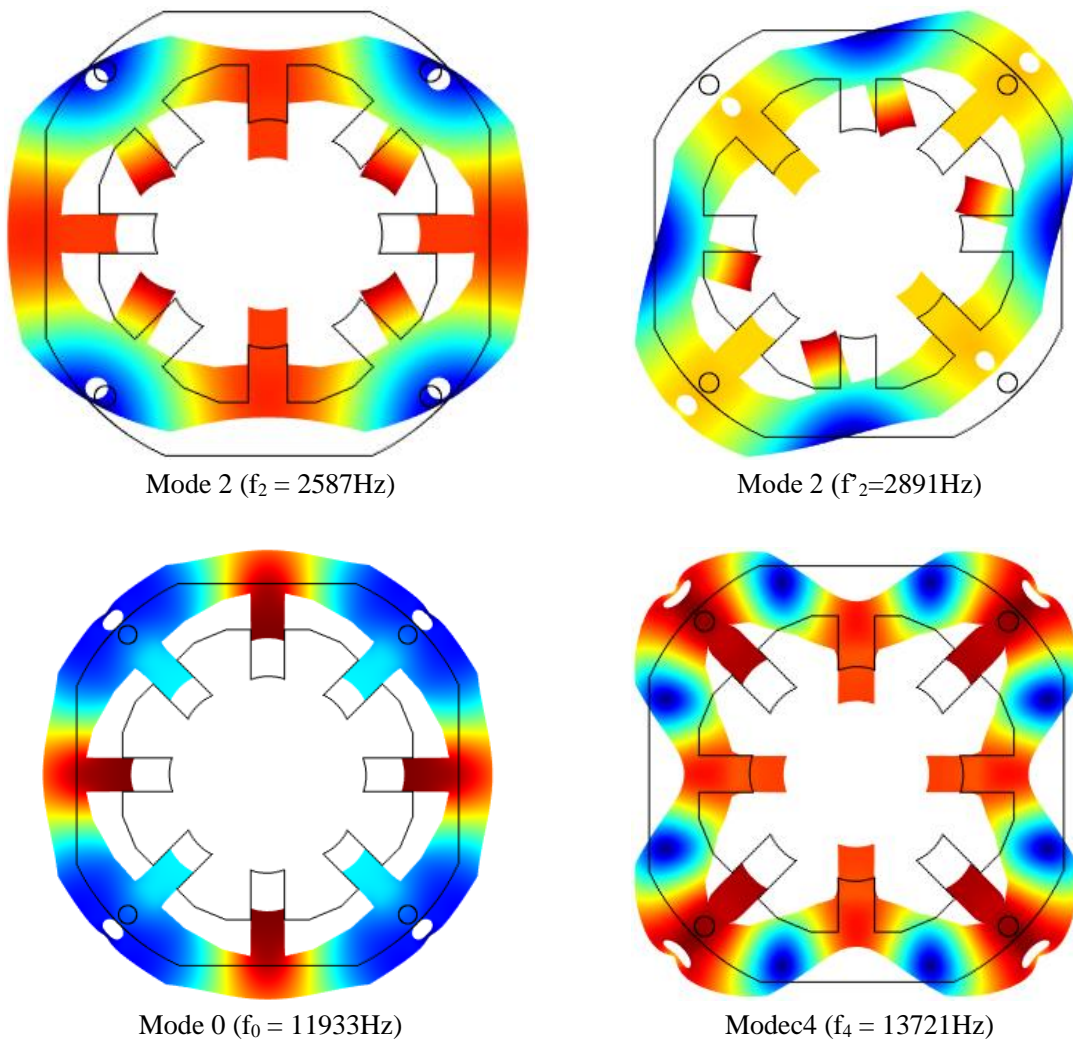


Figure 2.19 Natural Frequencies of the studied 8/6 SRM

### 2.4.2 Harmonic Response Analysis

The harmonic response analysis is used to compute the gain of the transfer function

between the radial force and the vibration. This analysis is implemented in COMSOL, in which the damping type is the *Rayleigh damping*, where two damping coefficients  $\alpha_{dK}$  and  $\beta_{dM}$  are specified. This type of damping is a viscous damping proportional to a linear combination of mass and stiffness expressed as [87]:

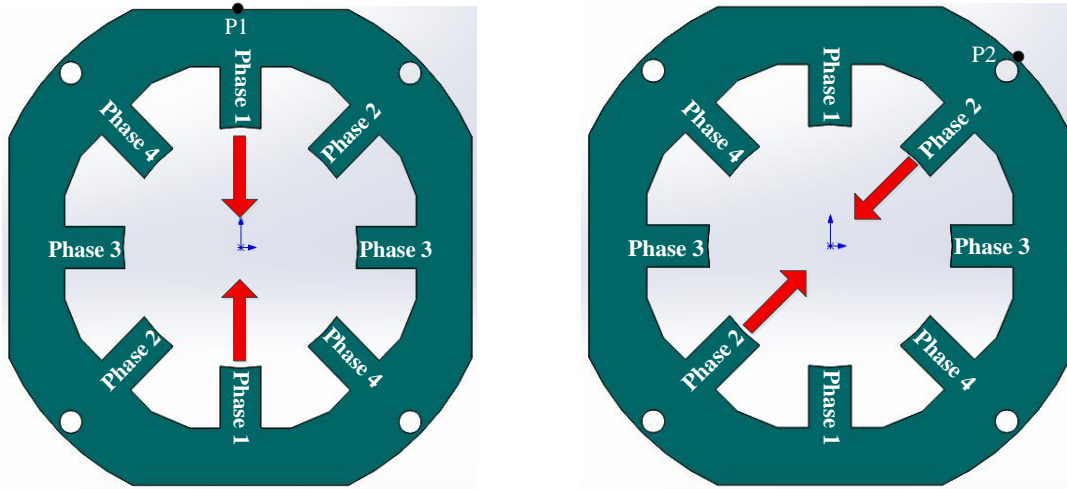
$$c = \beta_{dM}m + \alpha_{dK}k \quad (2.29)$$

Combining  $\xi = \frac{c}{2m\omega_n}$  with eq.(2.28), the two factors can be determined as:

$$\begin{cases} \beta_{dM} = \frac{(f_m \xi_m - f_n \xi_n)}{\pi(f_m^2 - f_n^2)} \\ \alpha_{dK} = 4\pi f_m \xi_m - 4\pi^2 \beta_{dM} f_m^2 \end{cases} \quad (2.30)$$

where  $\xi_m, \xi_n$  are the damping ratios of considered upper  $m$  mode and lower  $n$  mode respectively, whose corresponding frequencies are  $f_m$  and  $f_n$ .

In this analysis, the radial force  $F_0 \sin(\omega_n t)$  changes sinusoidally with a given frequency  $\omega_n$ . The sinusoidal radial force is applied as a load to the stator teeth as shown in Figure 2.20. Due to the asymmetrical structure of the stator, the harmonic response for Phases 1&3 is different from that for Phases 2&4. So, the radial force is applied to Phase 1 and Phase 2, respectively.



(a) Radial force applied on Phase 1

(b) Radial force applied on Phase 2

Figure 2.20 Radial force applied on the stator teeth as loads

The harmonic response analysis in FEM provides the vibration accelerations  ${}_{ii}B_n$  (the vibration acceleration at the phase  $i$  excited by phase  $i$ ) and  ${}_{ij}B_n$  (the vibration acceleration at

the phase  $i$  excited by phase  $j$ ,  $i \neq j$ ) at the two points P1 and P2 illustrated in Figure 2.20 that are generated in response to the applied radial force. They are then used to calculate the gain  $A_n$  of the transfer function in eq. (2.19).

Replacing  $s$  with  $j\omega_n$  in eq. (2.19), it is rewritten as:

$$H(j\omega_n) = \frac{a(j\omega_n)}{F(j\omega_n)} = \frac{-A_n\omega_n^2}{-\omega_n^2 + 2j\zeta\omega_n^2 + \omega_n^2} = \frac{-A_n}{2j\zeta} \quad (2.31)$$

Thus, the amplitude of the frequency response eq. (2.31) is

$$|H(j\omega_n)| = \frac{|a(j\omega_n)|}{|F(j\omega_n)|} = \frac{A}{2\zeta} \quad (2.32)$$

The gain  $A_n$  of the transfer function can be determined using the relation  $A_n = 2\zeta \frac{|a(j\omega)|}{|F(j\omega)|}$ , in which the numerator is the simulated vibration acceleration  ${}_{ii}B_n$  ( ${}_{ij}B_n$ ) and the denominator is the applied radial force  $F_0$ .

Based on the *Rayleigh* damping, the other damping ratios in the frequency range  $[f_n, f_m]$  can be calculated by:

$$\zeta_i = \frac{(\zeta_m - \zeta_n)(f_i - f_n)}{(f_m - f_n)} + \zeta_n \quad (2.33)$$

### 2.4.3 Modal Superposition Harmonic Analysis

After all, the transfer function between the radial force and the vibration acceleration can be determined. However, because of the asymmetrical structure of the studied machine stator, the equation (2.21) used to calculate the coupling factor matrix for different modes requires to be modified as follows:

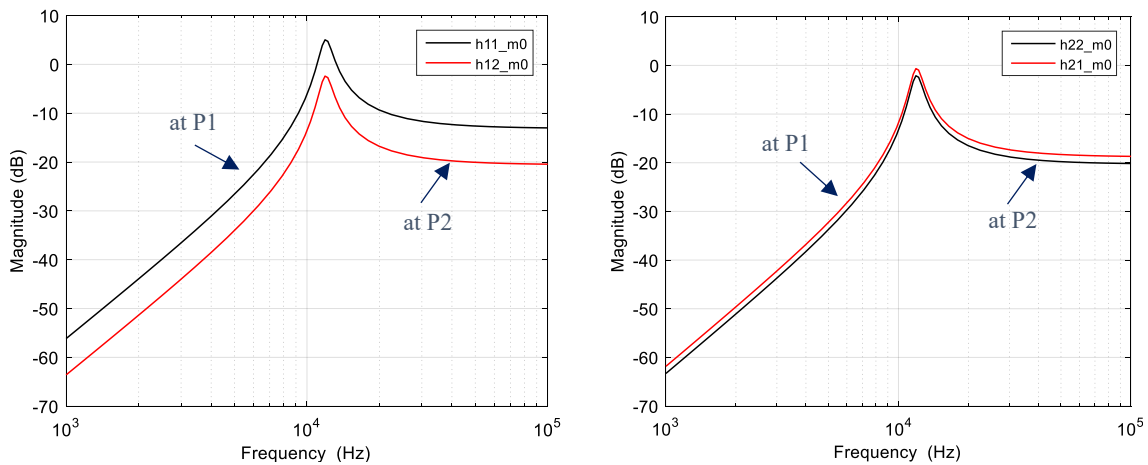
$${}_jB_n = \sum_{i=1}^{N_{ph}} {}_{ij}B_n \cos(2n\pi(j-i)/N_s) \quad (2.34)$$

For this asymmetrical structure of stator,  ${}_{ii}B_n$  (the vibration acceleration at the phase  $i$  excited by phase  $i$ ); is not equal to  ${}_{ji}B_n$  (the vibration acceleration at the phase  $i$  excited by phase  $j$ ) for mode 0 and mode 4 when the phases are adjacent.

Thus, in this thesis, there are two types of transfer functions between the radial force and the vibration acceleration: self-transfer function and mutual-transfer function. The self-

transfer function describes the relationship between the radial force applied at phase  $i$  and the vibration acceleration generated at phase  $i$ . However, the mutual-transfer function gives the relationship between the radial force applied at phase  $j$  and the vibration acceleration generated at phase  $i$  ( $i \neq j$ ).

Figure 2.21 gives the comparison between the self-transfer function and the mutual-transfer function of mode 0. Figure 2.21 (a) illustrates the transfer function of mode 0 when exciting Phase 1. In the figure,  $h_{11\_m0}$  stands for the self-transfer function of mode 0 between the radial force of phase 1 and vibration responded at point P1, whereas  $h_{12\_m0}$  represents the mutual-transfer function of mode 0 between the radial force of Phase 1 and vibration responded at point P2. Figure 2.21 (b) illustrates the transfer function of mode 0 when exciting Phase 2. In the figure,  $h_{22\_m0}$  and  $h_{21\_m0}$  are respectively, the self-transfer function of mode 0 between the radial force of phase 2 and vibration responded at point P2, and the mutual-transfer function of mode 0 between the radial force of Phase 2 and vibration responded at point P1.

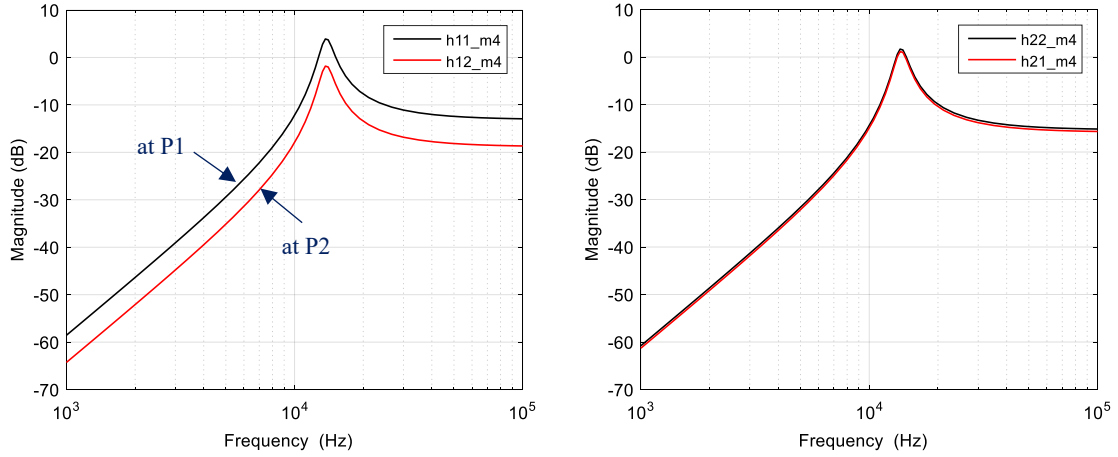


(a) Transfer function of mode 0 when exciting Phase 1. (b) Transfer function of mode 0 when exciting Phase 2.

Figure 2.21 Transfer function of mode 0.

According to the comparisons, the self-transfer function is different from the mutual-transfer function when Phase 1 is excited: there is a 8-dB difference at the natural frequency of mode 0. However, the difference is very small when Phase 2 is excited. Comparing Figure 2.21 (a) to Figure 2.21 (b), the self-transfer functions of mode 0 at P1 ( $h_{11\_m0}$ ) and P2 ( $h_{22\_m0}$ ) are different and so are the mutual-transfer functions  $h_{12\_m0}$  and  $h_{21\_m0}$ .

Figure 2.22 presents the comparison results between self-transfer function and mutual-transfer function of mode 4. The self-transfer function is different from the mutual-transfer function when Phase 1 is excited: there is a 6 dB difference at the natural frequency of mode 4. However, the difference is very small when Phase 2 is excited.



(a) Transfer function of mode 4 when exciting Phase 1. (b) Transfer function of mode 4 when exciting Phase 2.

Figure 2.22 Transfer function of mode 4.

Considering the asymmetrical structure of this machine, the structural model becomes more complicated and the different mutual transfer functions need be considered for investigation.

To sum up, the details of this structural modeling process are given in Figure 2.23. At first, the modal analysis is completed to calculate the natural frequency of different modes in FEM. Then, adopting equations (2.28) and (2.30), the damping parameters  $\alpha_{dK}$  and  $\beta_{dM}$  are determined with the calculated  $f_m$  and  $f_n$  for the mode  $m$  ( $m=4$ ) and the mode  $n$  ( $n=2$ ). After that, the damping ratio  $\xi_i$  for the other modes can be estimated with (2.33). Thus, the gain of the transfer functions  $A_i$  in (2.20) can be obtained with the harmonic response analysis in COMSOL. Next, applying the same radial force obtained from the electromagnetic model to the semi-analytical model and finite element model, the transient curve of vibration accelerations  $a_{FEM}$  (acceleration predicted with FEM) and  $a_s$  (acceleration predicted with the semi-analytical model) are compared. Some additional tests are added to determine the adapted upper mode frequency. Finally, the model to predict the vibration is obtained.

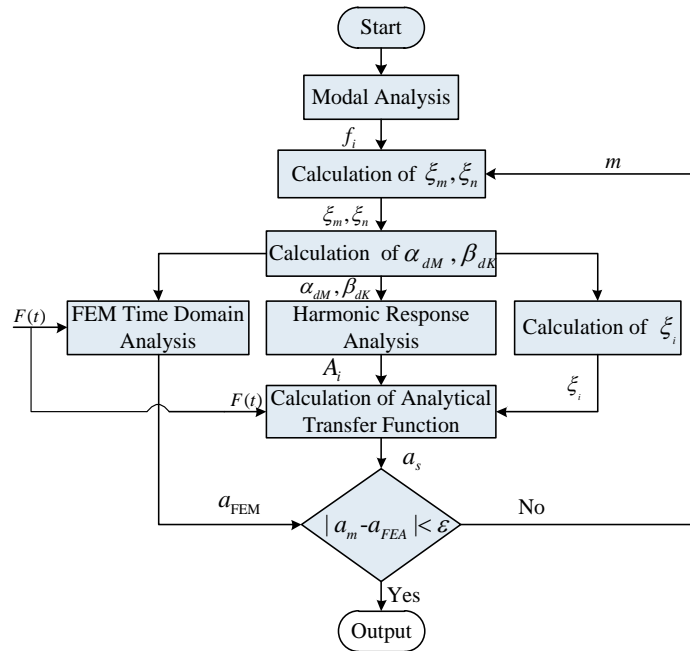


Figure 2.23 Flowchart of the Structural Modeling in Matlab.

Thus, the Bode plot of the self-transfer function between radial force and vibration acceleration considering mode 2, mode 0 and mode 4 for P1 and P2 are presented in Figure 2.24. It can be seen that the gain of the self-transfer function of P1 is bigger than P2 at the corresponding natural frequencies, which means that the vibration acceleration of P1 is more serious than P2 when the corresponding force harmonic are the same.

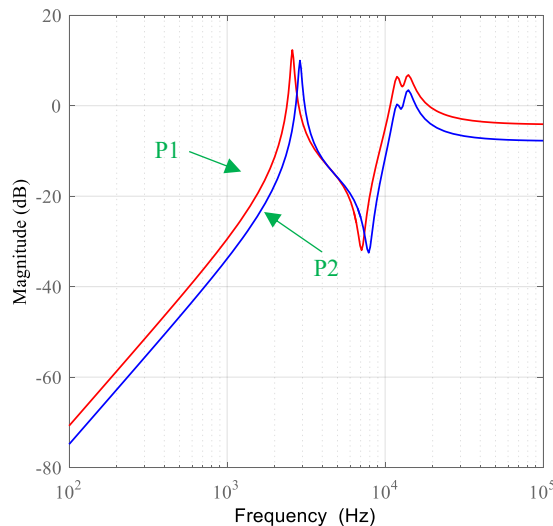


Figure 2.24 Bode plot of the self-transfer function for P1 and P2.

## 2.5 Model Validation

The electromagnetic/structural multi-physics model is used to connect the

electromagnetic model to the structural model by radial force. It is proposed to predict the vibration acceleration for a given operating point ( $\Omega$ ,  $T_L$ ). The details of the estimation are illustrated in Figure 2.25. For the electromagnetic model, the phase current and the rotor position are given to get the magnetic field distribution of the machine. Then, the phase flux linkage, the electromagnetic torque and the radial force profiles are calculated using the flux density obtained. With the flux-linkage profile, LUT is adopted to build an inverse magnetization model to express the current. Thus, the transient radial force and electromagnetic torque curves can be obtained using another two LUTs (a LUT for the radial force and a LUT for the electromagnetic torque, both dependent on the phase current and the rotor position). For the structural model, the natural frequencies are computed with modal analysis. Then, harmonic response analysis is adopted to obtain the unknown parameters from the transfer function. Using the radial force from electromagnetic model as the input of the transfer function, the vibration acceleration is obtained.

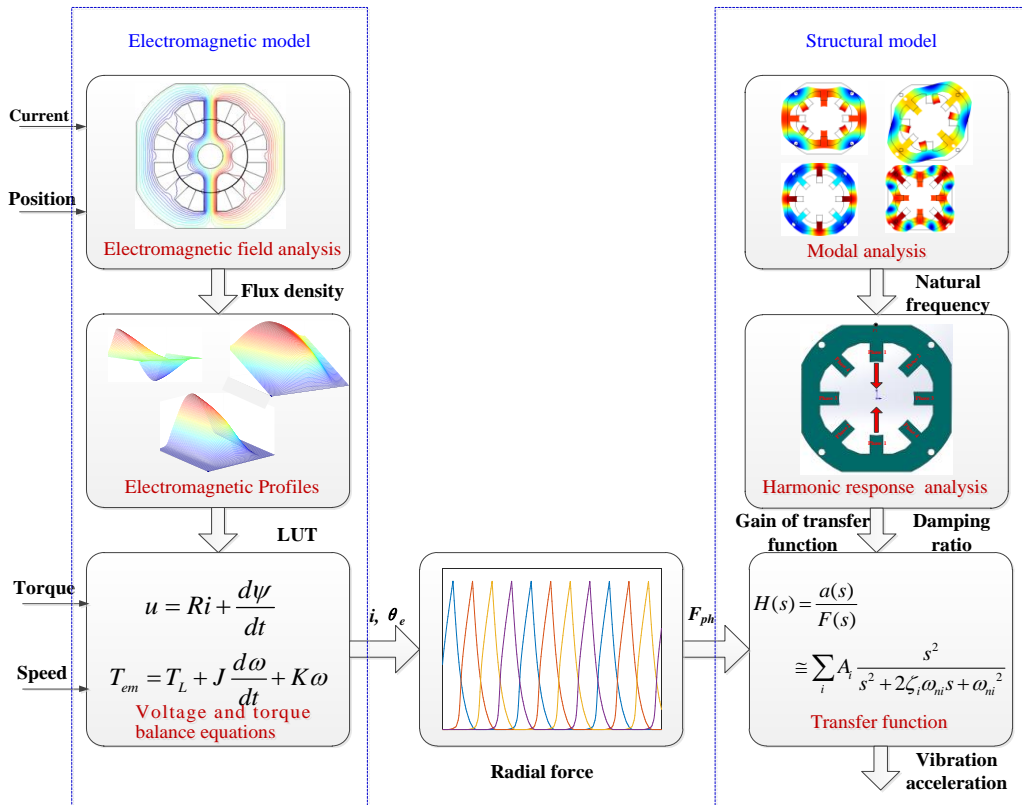


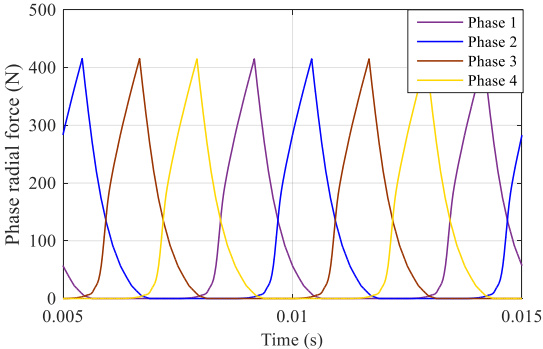
Figure 2.25 Block diagram of the electromagnetic/mechanical multi-physics model.

To validate the accuracy of the proposed model, simulation results of this semi-analytical model and the finite element model are compared. In the simulations, the four

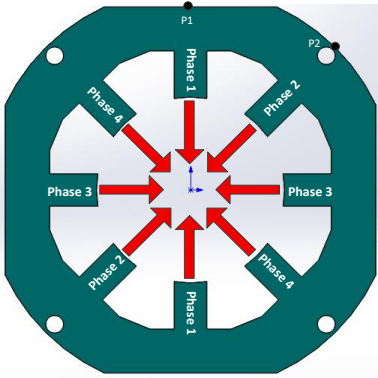
phases are excited one-by-one in the following sequence 1-2-3-4-1. The curves in Figure 2.26 (a) represent the radial force loaded to the stator poles, which is excited as shown in Figure 2.26 (b). In this case, the four phases are excited one by one with a 90° electrical angle phase shift and the fundamental frequency of the force is 200Hz (speed is 2000 r/min).

Figure 2.27 illustrates the vibration acceleration in the time and frequency domains at points P1 and P2. The results show that the semi-analytical model agrees well with finite element model. Moreover, it should be noted that the time cost of semi-analytical model is 0.67s, which is far less than the 2 hours required for simulating of FEM.

Figure 2.28 presents another vibration acceleration comparison result in frequency domains at point P1 and P2. The fundamental frequency of the force is 120Hz (speed is 1200 r/min). The results from both simulation models are identical, which validate the accuracy of the semi-analytical model further.

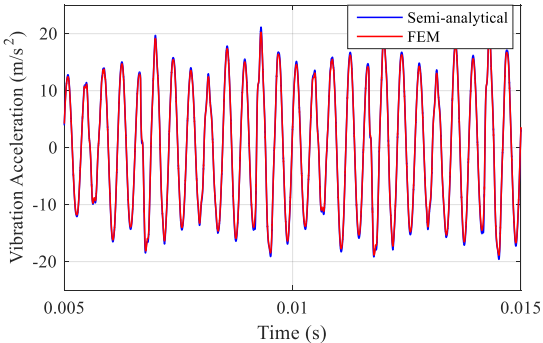


(a) Applied radial force.

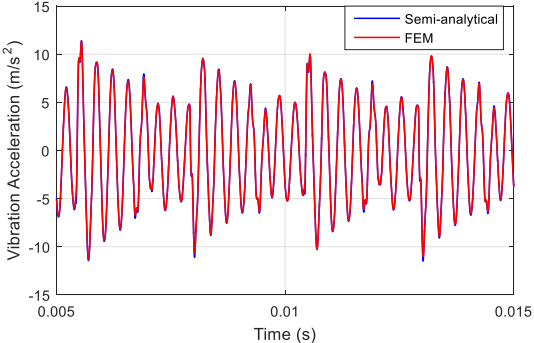


(b) Sketch of the applied Radial Force.

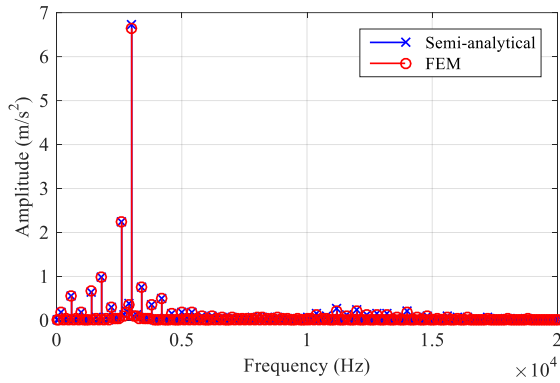
Figure 2.26 Applied radial force (fundamental frequency is 200Hz) and its sketch.



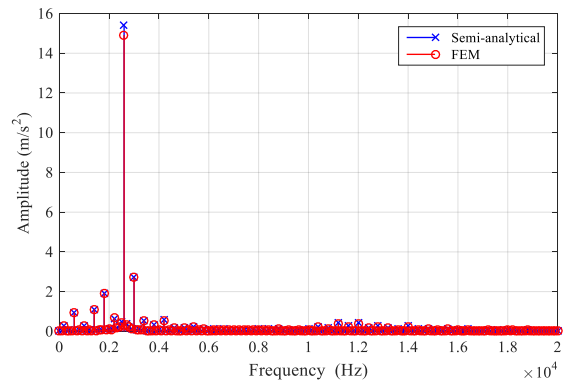
(a) Comparison of transient vibration acceleration at P1.



(b) Comparison of transient vibration acceleration at P2.

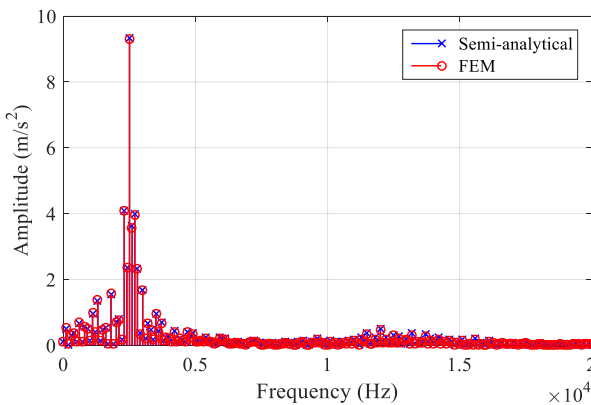


(c) Comparison of vibration acceleration spectrum at P1.

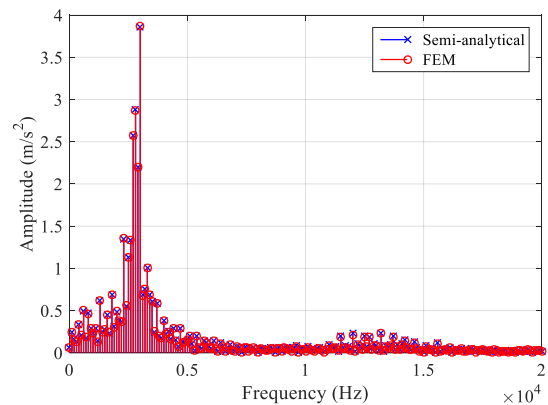


(d) Comparison of vibration acceleration spectrum at P2.

Figure 2.27 Comparisons results between semi-analytical model and FEM when the fundamental frequency of the applied radial force is 200Hz.



(a) Comparison of vibration acceleration spectrum at P1.



(b) Comparison of vibration acceleration spectrum at P2.

Figure 2.28 Comparisons results between semi-analytical model and FEM when the fundamental frequency of the applied radial force is 120Hz.

Figure 2.29 shows the vibration spectrogram of the SRM for speed-up test (from 100 r/min to 3000 r/min) with a constant load of 2 N·m using the multi-physics model developed in this chapter. It can be seen that the vibration is very serious near the mode 2, and the odd harmonic is more important for the vibration excitation. The 21<sup>th</sup> order harmonic of speed 1200 r/min has a high amplitude, because this temporal harmonic of radial force excites circumferential spatial order 2 (corresponding to the mode 2 shape) and this frequency is near the natural frequency of mode 2. Such conditions lead to the stator vibrations, as it has been pointed out with the 2-D FFT described in Section 2.3.4.

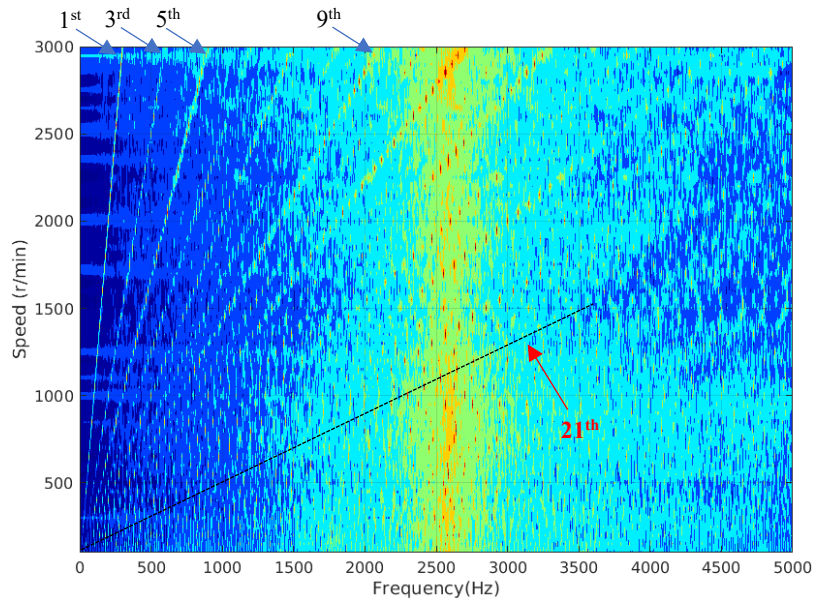


Figure 2.29 Spectrogram of vibration for speed-up test with a load of  $2\text{N}\cdot\text{m}$ .

## 2.6 Conclusion

This chapter introduces a semi-analytical electromagnetic/mechanical model. At first, the operating principle of SRM is introduced. Next, an electromagnetic model based on voltage balance equation and torque balance equation is built with three profiles named flux linkage profile, torque profile and radial force profile. Then, the mechanical model is deduced, in which the SRM mechanical system is simplified as the superposition of several SDOF systems. The structural model is realized based on the transfer function between the radial force and the vibration acceleration, where the radial force is the output of the electromagnetic model and the input for the mechanical model. Besides, due to the asymmetrical structure of the studied machine, the transfer functions are categorized as self-transfer function and mutual-transfer function to improve the accuracy of the model. Finally, the simulation results from the semi-analytical model are compared with those in FEM, which validate the accuracy of this model. The model will be used to evaluate the proposed control strategies in the next chapter.

# Chapter 3 Vibration and Noise Reduction Control Strategies for SRM

In this chapter, two vibration reduction methods are introduced, namely, the Improved Variable Turn-off Control (IVTC) and Direct Force Control with Reference Current Adapter (DFC&RCA). IVTC is presented via random-varying turn-off angle control, which is based on the mechanical property of the switched reluctance machine. In this method, a sinusoidal function with a random-variation-frequency is adopted to make the turn-off angle vary with time. The DFC & RCA is proposed by introducing a RCA to handle the torque ripple increase caused by the DFC. Both two methods are evaluated and validated in simulation, using the multi-physics model presented in the previous chapter, and experimentally, the results of second method being presented in Chapter 4.

## 3.1 Improved Variable Turn-off Angle Control (IVTC)

The proposed methods in this thesis are based on the traditional control method ATC, whose block diagram is shown in Figure 3.1. There are two controllers: the speed controller of the outer loop and the current controller of the inner loop. LUTs store the optimized control parameters. By using the reference torque and actual rotor speed as inputs, the control parameters  $I_{ref}^*$ ,  $\psi$  and  $\theta_p$  are then constantly updated. Thus, the error between the reference current  $I_{ref}^*$  and the phase current  $I$  is used by the current control to compute a variable duty ratio such that the phase current tracks the reference value. In the next sections, the design of the speed and current controllers are introduced.

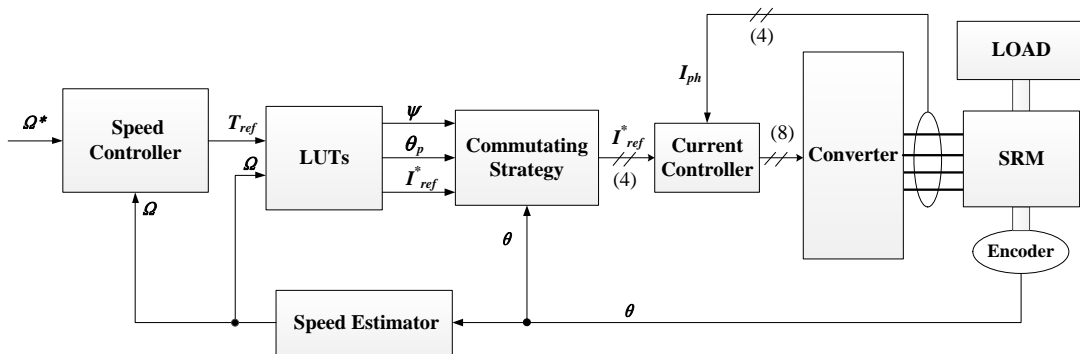


Figure 3.1 Block diagram of ATC.

### 3.1.1 Speed Controller Design

The Proportional Integral (PI) controller is a conventional control that has been widely used by different electrical machines [88]-[90]. The major features of the PI controller are the zero steady state error for step references and disturbances and the easy implementation on microprocessors. However, because of the trade-off between overshoot and disturbances rejection [91]-[94], the use of PI control in electric vehicle (EV) applications is limited (EVs are often subject to high variations of the load torque). Therefore, the Integral Proportional (IP) controller is adopted in this work for the speed loop. The zero introduced by the PI control in the controller transfer function is avoided in the case of IP control, and thus the overshoot can be reduced [95].

Both the PI and IP controllers consist of a proportional component and an integral component. The difference is that the proportional action of PI controller is in the forward path as shown in Figure 3.2, whereas, it is moved to the feedback path (Figure 3.3) for the IP controller. In these two figures,  $\Omega^*(s)$  is the reference speed (the input of the close-loop system),  $\Omega(s)$  is the actual speed (system output),  $\varepsilon(s)$  is the error between the reference and feedback of the system and  $T_L(s)$  is the load torque disturbance.  $K_p$  and  $K_i$  are the proportional and the integral control parameters, respectively.  $J$  represents the motor moment of inertia and  $K_t$  stands for the friction coefficient.

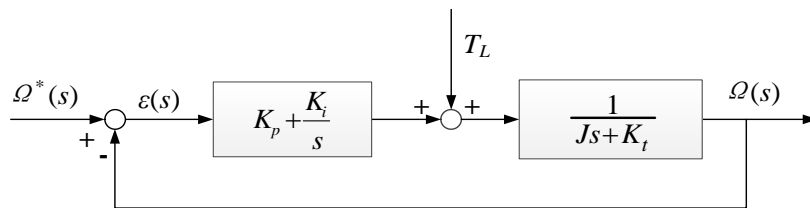


Figure 3.2 Block diagram of the speed-loop with PI controller.

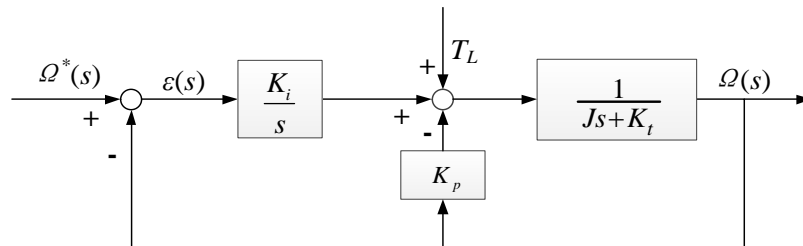


Figure 3.3 Block diagram of the speed-loop with IP controller.

Thus, the closed-loop transfer function  $G_{PI}(s)$  of the PI controller between the input  $\Omega^*(s)$  and the output  $\Omega(s)$  is the following:

$$G_{PI}(s) = \frac{\Omega(s)}{\Omega^*(s)} = \frac{K_p s + K_i}{Js^2 + (K_t + K_p)s + K_i} \quad (3.1)$$

By making  $\omega_c^2 = K_i/J$ ,  $2\xi\omega_c = (K_t + K_p)/J$ , and  $b = K_i/K_p$ , where  $\xi$  is damping ratio and  $\omega_c$  is the natural frequency. Eq.(3.1) then becomes:

$$G_{PI}(s) = \frac{\Omega(s)}{\Omega^*(s)} = \frac{(\omega_c^2/b)(s+b)}{s^2 + 2\xi\omega_c s + \omega_c^2} \quad (3.2)$$

On the other hand, the transfer function  $D_{PI}(s)$  between the disturbance load torque  $T_L(s)$  and the output  $\Omega(s)$  is expressed as:

$$D_{PI}(s) = \frac{\Omega(s)}{T_L(s)} = \frac{s/J}{s^2 + 2\xi\omega_c s + \omega_c^2} \quad (3.3)$$

Meanwhile, for the IP controller, the closed-loop transfer function  $G_{IP}(s)$  between the input  $\Omega^*(s)$  and output  $\Omega(s)$  is:

$$G_{IP}(s) = \frac{\Omega(s)}{\Omega^*(s)} = \frac{\omega_c^2}{s^2 + 2\xi\omega_c s + \omega_c^2} \quad (3.4)$$

The corresponding disturbance transfer function  $D_{IP}(s)$  between the load torque  $T_L(s)$  and the output  $\Omega(s)$  is:

$$D_{IP}(s) = \frac{\Omega(s)}{T_L(s)} = \frac{s/J}{s^2 + 2\xi\omega_c s + \omega_c^2} \quad (3.5)$$

Comparing equations (3.4) with (3.2), it can be seen that the zero introduced by the PI controller in the closed speed loop transfer function is missing when a IP controller is used, and thus the overshoot with an IP controller is expected to be reduced. According to equations (3.3) and (3.5), the transfer functions between the disturbance and the output for the two controllers are exactly the same with both controllers.

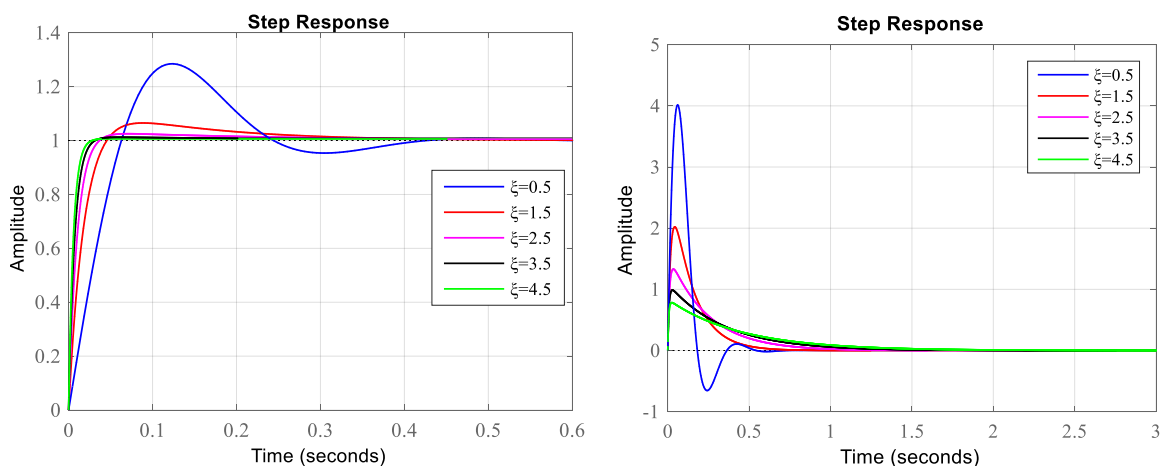
Figure 3.4 and Figure 3.5 present the step response of the PI and IP controllers for different damping ratio, respectively. As it can be noticed in the figures, the overshoot of the IP controller is always smaller than that of the PI controller for the same value of the damping ratio. According to the relationship between dynamic properties and damping ratio shown in

Figure 3.6, the following conclusions are formulated:

- ✓ both the rising time and the settling time of the input signal decrease with the increase of the damping ratio when the PI controller is used;
- ✓ the rising time of the input signal increases with the increase of the damping ratio when the IP controller is used;
- ✓ the overshoot of the input signal decreases with the increase of the damping ratio for both PI and IP controllers;
- ✓ for the IP control, the settling time of the input signal decreases with the damping ratio increase as long as  $\zeta < 1$ . The dependence is reversed for damping ratio values  $\zeta > 1$  as shown in Figure 3.6 (b). The same behavior can be observed for the settling time to a unit-step disturbance with both PI and IP controllers.

Thus, when the PI control is used the overshoot can be reduced by increasing the damping ratio. However, it will increase the settling time of the disturbance. This means that for a sudden change of the load torque, the zero steady state error will be achieved with a rather slow dynamic. Meanwhile, the overshoot can be completely removed without increasing the settling time to step inputs and step disturbances by using an IP controller.

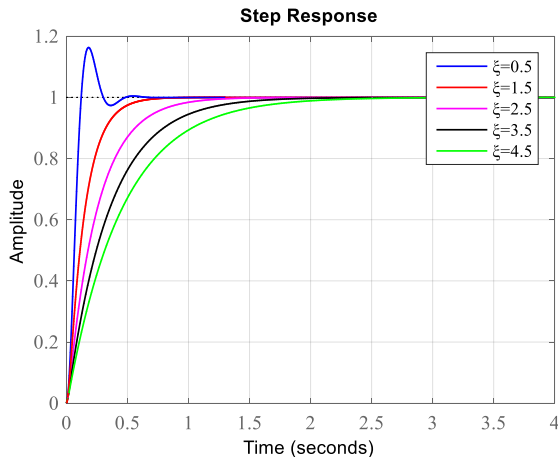
In EV applications, the torque load varies fast based on the driving conditions (urban, rural, motorway) and the traffic. The load variations are frequent and steep in urban traffic conditions. So, both good input response and disturbance response are required. Therefore, the IP controller is adopted for the speed control loop.



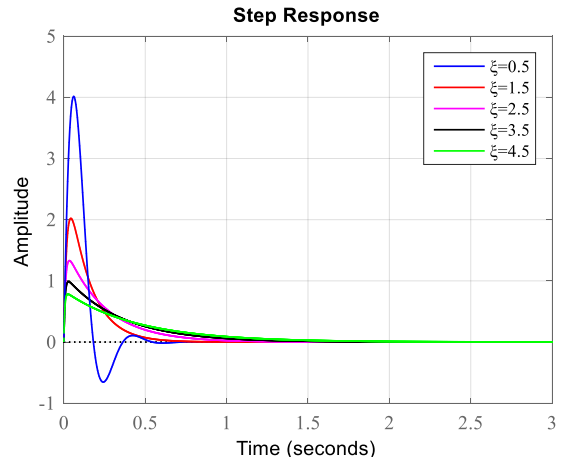
(a) System response to unit-step input signal.

(b) System response to unit-step disturbance.

Figure 3.4 Closed-loop system response using PI control and different damping ratio.

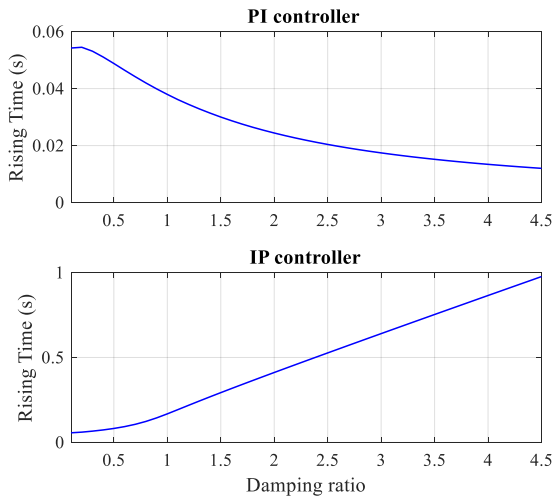


(a) System response to unit-step input signal.

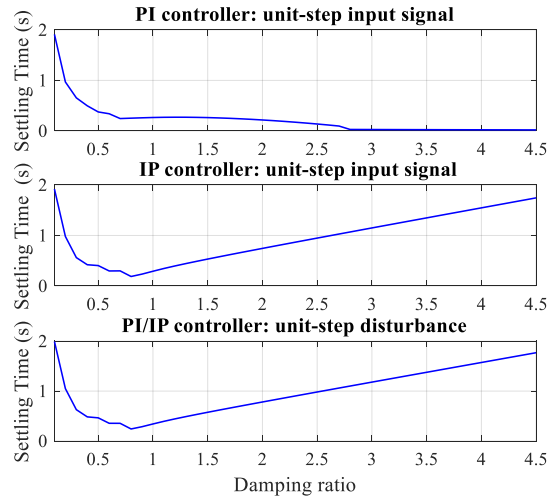


(b) System response to unit-step disturbance.

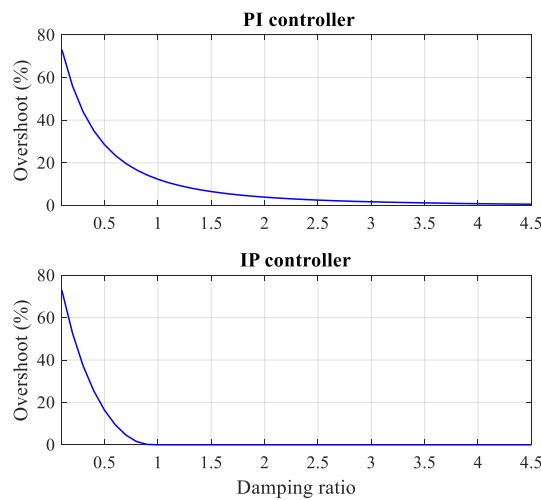
Figure 3.5 Closed-loop system response using IP control and different damping ratio.



(a) Relationship between rising time and damping ratio for a unit-step input signal.



(b) Relationship between settling time and damping ratio.



(c) Relationship between overshoot and damping ratio for a unit-step input signal.

Figure 3.6 Closed-loop system response: relationship between dynamic properties and damping ratio.

The discrete IP controller obtained by discretizing the continuous-time IP controller with the sampling time  $T_{samp}$  is presented in Figure 3.7. The integrator is approximated using Euler's method:  $S(k) = S(k-1) + K_i T_{samp}$ . An anti-wind-up action is placed at the output of the controller to limit the output reference torque maximum value (which is 25 N·m in this thesis) depending on the torque characteristics of the machine [96].

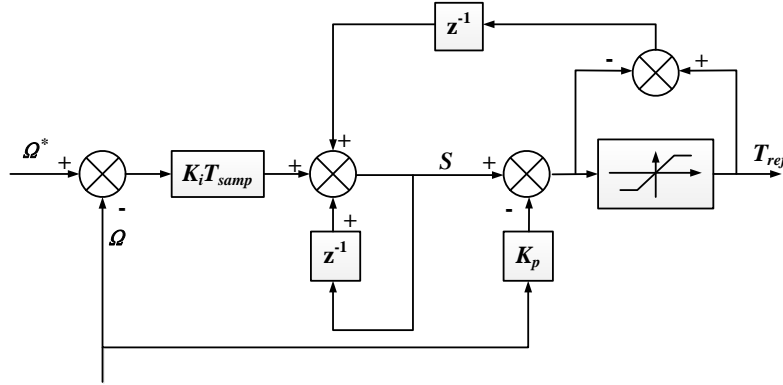


Figure 3.7 Blok diagram of the discrete speed IP controller.

### 3.1.2 Current Controller Design

The most commonly used method for the inner loop is the hysteresis controller, which is robust, easy to implement and does not require any model of the system. However, too narrow bandwidth will cause high switching losses and variable switching frequency may cause a subsonic noise in SRMs [97]. The alternative solution is a PWM (Pulse Width Modulation) fixed switching frequency controller.

According to the investigation in Section 3.1.1, increasing the damping ratio can reduce the overshoot and settling time, which improves the dynamic performance of the speed-loop with PI control to input signals at the cost of penalizing the disturbance response. For the current loop, the disturbance signal is the back-EMF ( $\text{back-EMF} = i\omega \frac{\partial L(\theta, i)}{\partial \theta}$ ), which depends on the rotor speed  $\omega$ , the current  $i$  and the self-inductance variation  $\frac{\partial L(\theta, i)}{\partial \theta}$ . Due to the inertia of the rotor, sudden changes of the speed are not possible, and neither of the current because of the inductance. Therefore, there are only slow variations of the EMF that lower the requirements of the current controller to the disturbance response. Therefore, the PI controller is adopted for the current loop as shown in Figure 3.8. In the figure,  $R$  is the

resistor.

In order to take into account the magnetic saturation phenomenon and its dependence on the rotor position and the current, a PI controller with variable gains is adopted [98]. This controller compensates the inductance variation and maintains the dynamics of the closed-loop system constant. The transfer function between the reference current  $I_{ref}^*(s)$  and the actual phase current  $I(s)$  is as follows:

$$\frac{I(s)}{I_{ref}^*(s)} = \frac{K_p s + K_i}{s^2 + K_p s + K_i} \quad (3.6)$$

where,

$$\begin{cases} K_p = 2\xi'\omega'_c L_{inc}(\theta, i) - R \\ K_i = L_{inc}(\theta, i)\omega'_c{}^2 \end{cases} \quad (3.7)$$

where,  $\xi'$  and  $\omega'_c$  are the damping ratio and the natural frequency of the closed-current loop,  $L_{inc}$  stands for incremental inductance, whose expression is:

$$L_{inc} = L(\theta, i) + i \frac{\partial L(\theta, i)}{\partial i} \quad (3.8)$$

where the  $L(\theta, i)$  is the self-inductance,  $i$  is the phase current. Because of its highly non-linear electromagnetic characteristics, the incremental inductance  $L_{inc}$  of the SRM is a function that depends on the position and the current.

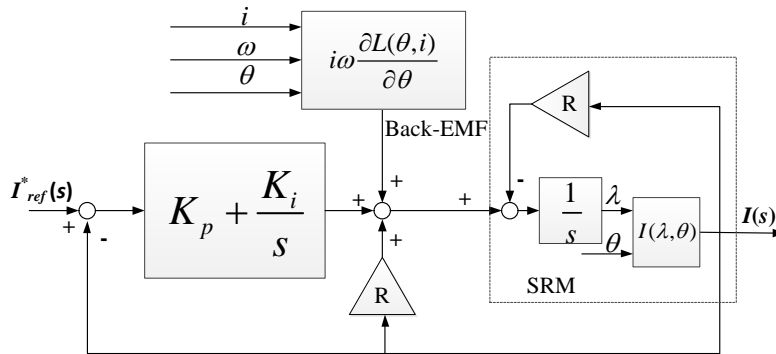


Figure 3.8 Block diagram of the current-loop with PI control.

Therefore, both coefficients  $K_p$  and  $K_i$  are parameters depending on the incremental inductance  $L_{inc}$  and resistor  $R$  when the natural frequency and damping ratio of this current controller are given. Figure 3.9 presents the discrete PI controller with an additional initialization block of the integrator which is used whenever the reference current reverts to

zero to avoid the accumulated error [96].

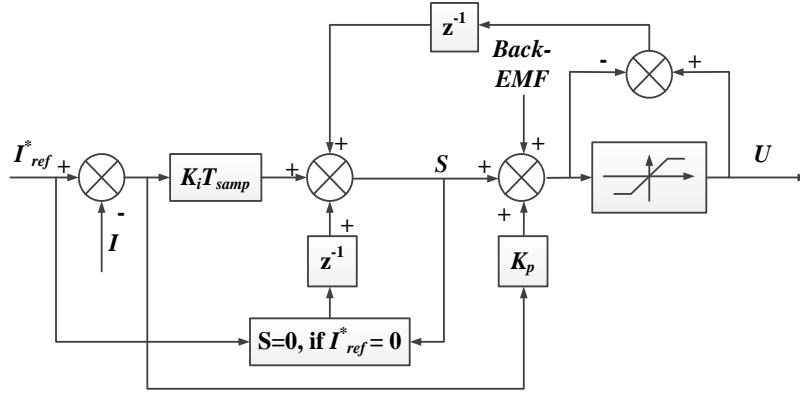


Figure 3.9 Blok diagram of the discrete current PI controller.

### 3.1.3 Vibration Reduction with IVTC

The main drawback of the ATC is that the vibration aspect is not considered in the control design. The current controller uses a constant turn-off angle, defined as the sum of the turn-on angle  $\psi$  and conduction angle  $\theta_p$ , over one excitation period. In fact, the turn-off angle has a big influence on the vibration, because when the rotor approaches the aligned position, the radial force increases rapidly.

In [41], a variable turn-on and turn-off angle control (VTC) is proposed, where the turn-off (turn-on) angle is expressed as:

$$\theta'_{off} = \theta_{off} + \Delta\theta r(t) \quad (3.9)$$

$$r(t) = \sin(2\pi f_{sin} t) \quad (3.10)$$

where  $\theta_{off}$  is the constant average turn-off angle;  $\Delta\theta$  is the magnitude of the turn-off angle variation; and  $f_{sin}$  is the frequency of the sinusoidal function  $r(t)$ . Since the turn-off angle is the key variable related to the vibration, only a variable turn-off angle is considered in this work.

The frequency  $f_{sin}$ , defining the variation of the turn-off angle, needs to be properly chosen to avoid the excitation of the mechanical vibrations, and a reasonable  $\Delta\theta$  is required to avoid the torque sacrifice. In [41], the authors propose to optimize the control parameters,  $\Delta\theta$  and  $f_{sin}$ , to maximize the vibration reduction for the mode 2 of the machine. However, optimizing two parameters simultaneously is a rather complex and time-consuming process.

In this thesis, a concept based on the property of the transfer function between the radial force and the acceleration is proposed to determine the frequency  $f_{\sin}$  of the sinusoidal function  $r(t)$ . Figure 3.10 shows the frequency response of the self-transfer function. There is a local minimum value at the frequency  $f=7100$  Hz, meaning that the response of this radial force harmonics to the vibration has the minimum value. Thus, the frequency of the sinusoidal function is chosen as  $f_{\sin} = 7100$  Hz. Then, this idea is applied to the model built in last chapter. In order to analyze the influence of the control variables in simulation, the speed controller is not included. This means that the rotational speed and the reference torque (inputs of the LUTs in Figure 3.1) are maintained constant. Moreover, the measurement noise introduced by the current sensors is modeled by a normally distributed white noise with a standard deviation of 0.15 A (this value roughly matches the conditions from the test bench). It is important to consider the measurement noise in simulation because it affects the performance of the current controller.

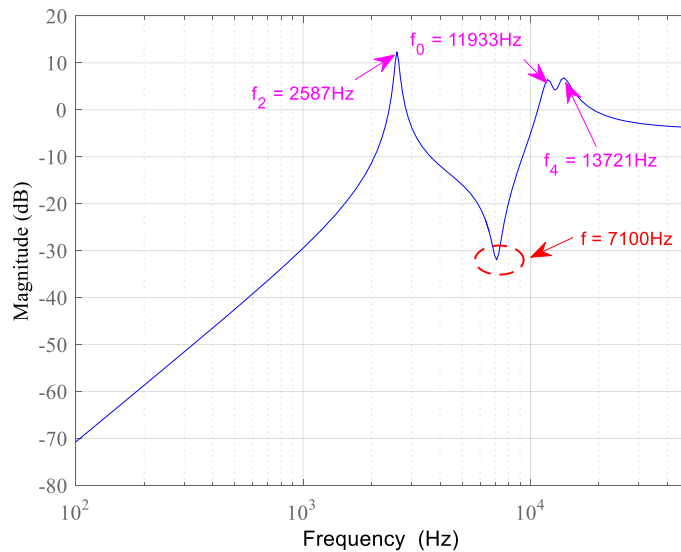


Figure 3.10 Bode plot of the self-transfer function between radial force and vibration acceleration.

The results obtained with ATC and VTC ( $f_{\sin} = 7100$  Hz) are compared in Figure 3.11. The magnitude variation  $\Delta\theta$  of the turn-off angle is fixed at  $3^\circ$ . It can be seen that the mode 2 ( $f_2 = 2587$  Hz) is the dominant mode for the investigated SRM for this operation point. Also, there exists a peak near the PWM carrier frequency ( $f_{PWM} = 20$  kHz). The vibration near mode 2 has been successfully reduced. The maximum vibration acceleration near the mode 2 is reduced up to 72.5% compared to the case when a constant turn-off angle is used.

However, the vibration near the given sinusoidal function frequency (7100Hz) and its multiple 2 (14200 Hz) has been increased. Thus, an Improved VTC (IVTC) is proposed in the following part.

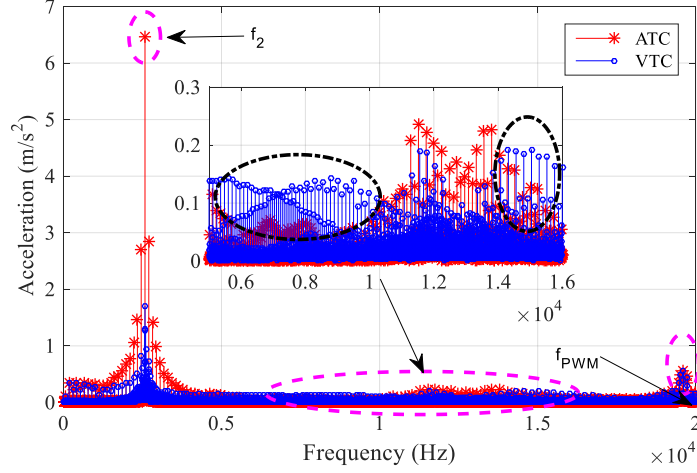


Figure 3.11 Acceleration for  $\Omega = 600$  r/min,  $T_L = 7$  N·m without speed controller: ATC vs VTC.

Thus, an improved VTC (IVTC) is proposed to remove the vibration amplification at the fixed frequency  $f_{sin}$  and its multiple, a uniformly distributed random function is added in order to uniformly distribute the vibration harmonics around  $f_{sin}$  and its multiple. Then, the new frequency of the sinusoidal function is expressed as:

$$f_s = f_{sin} + r_f(t)\Delta f \quad (3.11)$$

where  $r_f(t)$  is a uniformly distributed random function in the range of  $[-1, +1]$  and  $\Delta f$  represents the frequency variation range.  $\Delta f$  is the difference between the frequency whose magnitude is at most 3dB higher than of the frequency  $f_{sin} = 7100$ Hz and frequency  $f$ . Thus, the sinusoidal function  $r(t)$  that gives the evolution of the turn-off angle is computed as:

$$r(t) = \sin(2\pi f_s t) \quad (3.12)$$

For the investigated SRM in the thesis,  $\Delta f$  is equal to 200Hz.

### 3.1.4 Simulation Results of IVTC

Figure 3.12 presents the vibration acceleration obtained using both ATC and IVTC. The results show that the IVTC removes the harmonics near the fixed frequency  $f_{sin}$  (7100 Hz) and its multiple 2 (14200 Hz) by updating the frequency of the sinusoidal function  $r(t)$  using a random distributed function  $r_f(t)$ .

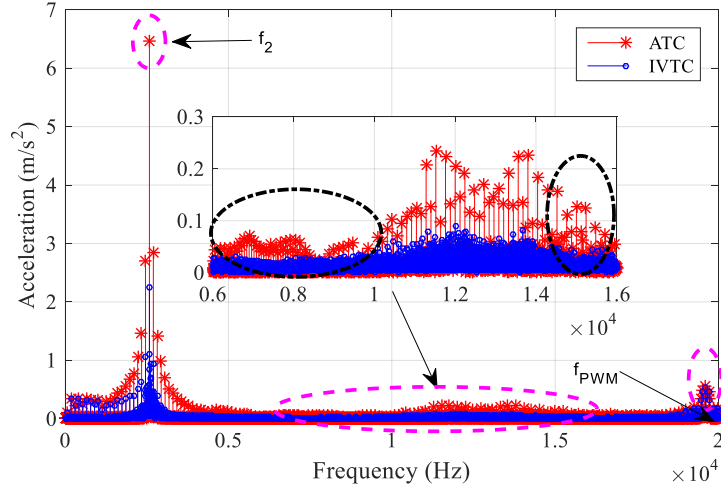


Figure 3.12 Acceleration for  $\Omega^* = 600$  r/min,  $T_L = 7$  N·m without speed controller: ATC vs IVTC.

Then, the proposed IVTC is validated with the speed control-loop. Figure 3.13 presents the simulation results obtained for the speed of 600 r/min and the load of 7 N·m. As expected, the maximum vibration near the mode 2 has been reduced up to 66.2% without increasing the harmonic component near the given sinusoidal function frequency (7100 Hz) and its multiple 2 (14200 Hz).

To assess the performance of the control strategy in a wide range of frequency, a criterion for evaluation has been adopted [99] with the total energy  $W$  gives a quantity related to the vibration behavior of all spectrum (all audible frequencies). The total energy  $W$  is deduced from the energy spectral density as follows:

$$W = \int_0^{f_{\max}} a(f)a^*(f)df \quad (3.13)$$

where,  $a(f)$  is the value of the acceleration FFT at the frequency  $f$ ;  $a^*(f)$  is the complex conjugate of  $a(f)$ .

The total energy  $W$  has been computed for the vibration acceleration obtained with each control method, IVTC and ATC, respectively. The vibration energy has been reduced with a 59.3% decrease with IVTC comparing to initial ATC for this operating point.

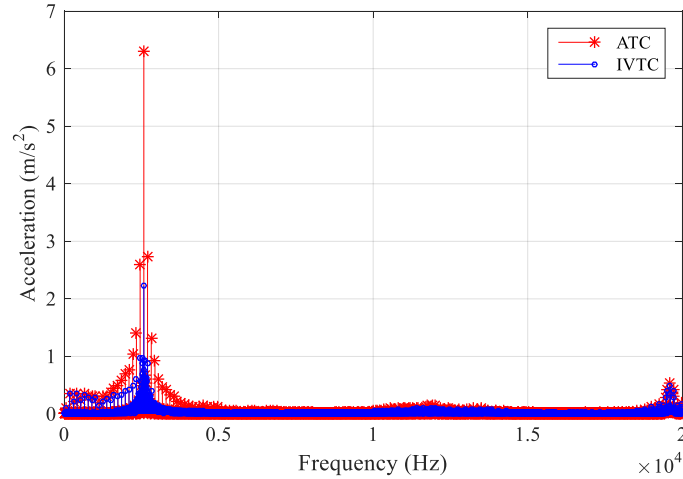
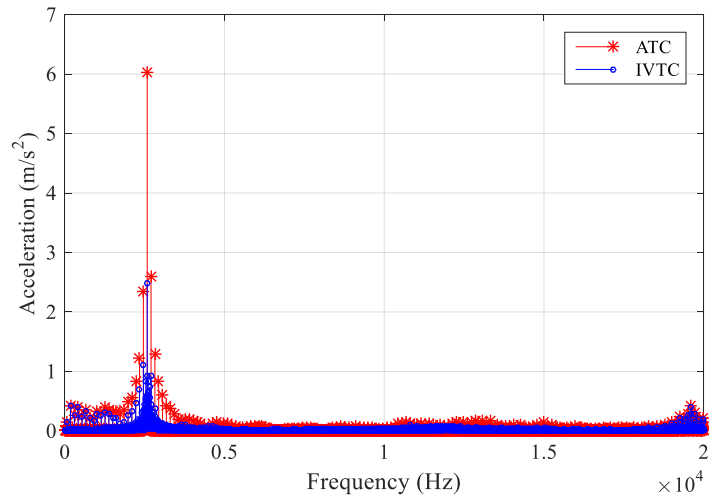


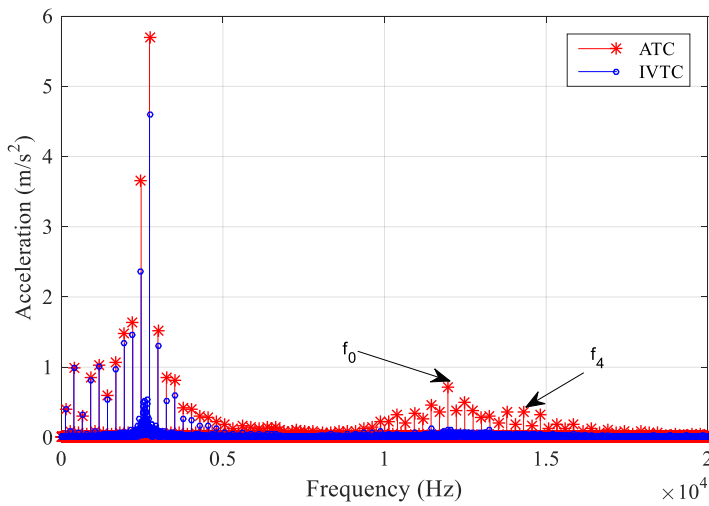
Figure 3.13 Acceleration for  $\Omega^* = 600$  r/min,  $T_L = 7$  N·m with speed controller: ATC vs IVTC.

To further investigate the performance of the IVTC, simulations are run for two other operating points characterized by low speed high torque ( $\Omega^* = 600$  r/min,  $T_L = 16$  N·m) and high-speed average torque ( $\Omega^* = 1300$  r/min,  $T_L = 8$  N·m). Moreover, for the second operating point, the acceleration is determined for different values of the turn-off angle magnitude:  $\Delta\theta = 3^\circ$  and  $\Delta\theta = 6^\circ$ . Figure 3.14 shows the acceleration spectrum obtained with both ATC and IVTC for each operating point and Table 3-1 gives the corresponding vibration energy reduction.

As shown in Figure 3.14 (b), although the vibration harmonics of modes 0 and 4 become important at high speed with an average load torque, the dominant vibration mode is still mode 2. Compared to the IVTC performance at low speed, the vibration reduction is less significant (32.5% for  $\Omega^* = 1300$  r/min). However, this can be improved by increasing the magnitude of the turn-off angle variation  $\Delta\theta$ . Figure 3.15 shows the simulation results using the IVTC for two different values of  $\Delta\theta$ . The vibration near mode 2 has been reduced further by increasing the  $\Delta\theta$  from  $3^\circ$  to  $6^\circ$ , and the vibration energy for the whole audible range has been reduced by 29% more.



(a) Acceleration for  $\Omega^* = 600$  r/min and  $T_L = 16$  N·m: ATC vs IVTC.



(b) Acceleration for  $\Omega^* = 1300$  r/min and  $T_L = 8$  N·m: ATC vs IVTC.

Figure 3.14 Comparison between ATC and IVTC for different operating points.

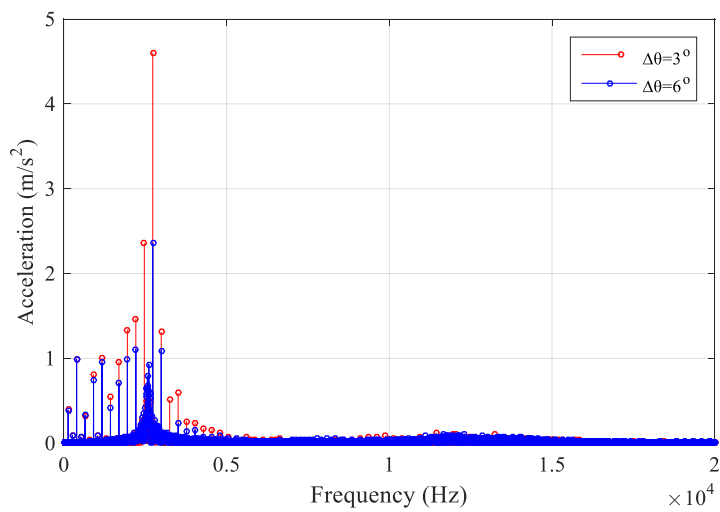


Figure 3.15 IVTC: Acceleration for  $\Delta\theta = 3^\circ$  (red line) and  $\Delta\theta = 6^\circ$  (blue line) at  $\Omega^* = 1300$  r/min and  $T_L = 8$  N·m.

Table 3-1 Performance comparison of vibration energy between ATC and IVTC for different operating points

Operating point	Variation magnitude	Vibration energy reduction
$\Omega^* = 600 \text{ r/min}, T_L = 7 \text{ N}\cdot\text{m}$	$\Delta\theta = 3^\circ$	59.3 %
$\Omega^* = 600 \text{ r/min}, T_L = 16 \text{ N}\cdot\text{m}$	$\Delta\theta = 3^\circ$	60.5 %
$\Omega^* = 1300 \text{ r/min}, T_L = 8 \text{ N}\cdot\text{m}$	$\Delta\theta = 3^\circ$	32.5 %
	$\Delta\theta = 6^\circ$	61.5 %

In this section, a vibration reduction method based on the principle of varying turn-off angle has been proposed. This method has been developed by introducing a variable frequency sinusoidal signal to the turn-off angle so that the turn-off angle is updated in time rather than keeping it constant over one excitation period. The basic frequency of this sinusoidal signal is located at the local minimum magnitude of the transfer function between the radial force and the vibration acceleration. Besides, a random distributed signal is introduced to the basic frequency of the sinusoidal signal to avoid vibration amplification at this frequency. This method works well when the speed is low. However, the performance is limited when the speed is high with a fixed turn-off angle variation magnitude  $\Delta\theta$ . It can be improved by increasing  $\Delta\theta$ . Nevertheless, the effect of  $\Delta\theta$  depending on the operating points needs to be investigated further. The torque ripple and efficiency effects have to be considered, and they will be investigated in Section 3.3.2.

### 3.2 Direct Force Control with Reference Current Adapter (DFC & RCA)

Another control approach for reducing vibration is to control the radial force directly, since the variation of the radial force has a large impact on the vibratory performance. However, this can have a negative impact on the torque ripple as the torque variations are not controlled. Thus, a reference current adapter is included in order to handle the trade-off between the vibration reduction and the torque ripple reduction.

The proposed Direct Force Control (DFC) & Reference Current Adapter (RCA) vibration reduction control strategy for the switched reluctance machine is presented in Figure 3.16. The torque ripple minimization controller, referred in the figure as TMC, is a traditional ATC that uses LUTs to minimize the torque ripple at each operating point (see

Figure 3.1 in previous part). The main idea of this control structure that will be detailed in the following parts is to combine the TMC and the DFC, each controller being active depending on the level of torque variation and force variation. Each part of the proposed control structure is described in the following sections: TMC, DFC, signal combination--AND and RCA.

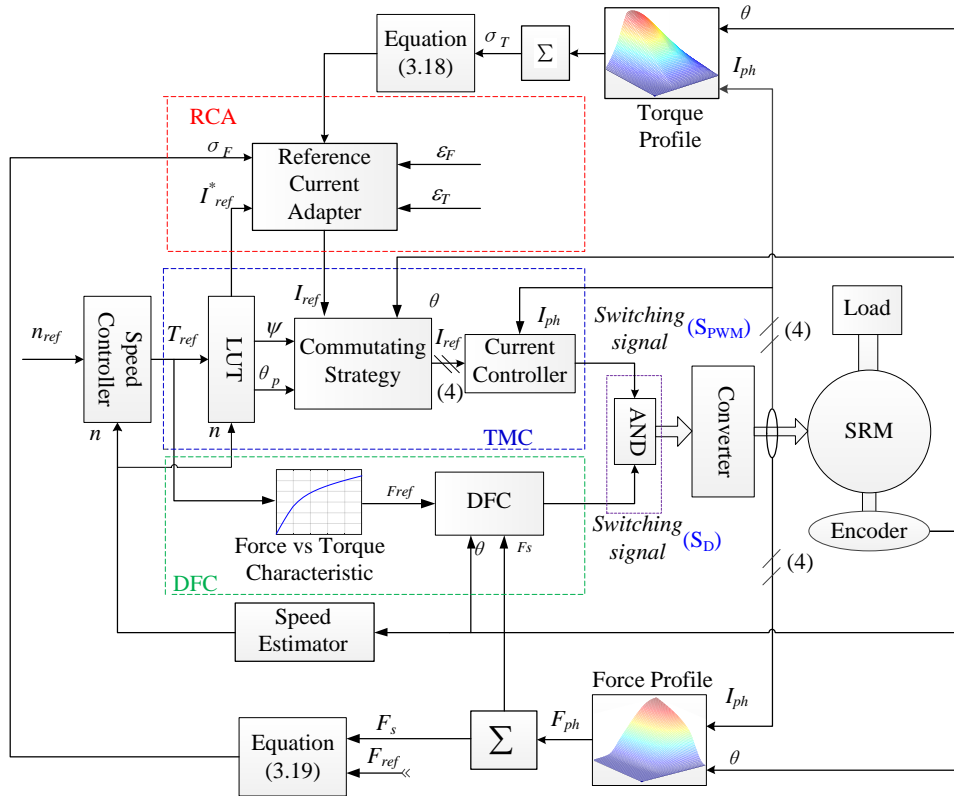


Figure 3.16 Control structure of the DFC&RCA.

First, the principle of DFC is introduced (Section 3.2.1) and its integration in the speed loop with a reference force generation (Force vs. Torque Characteristic block of Figure 3.16) is detailed. Next, the AND signal combination is introduced so as to combine the TMC with the DFC. Finally, Section 3.2.5 will give the interest of the addition of a RCA.

### 3.2.1 Vibration Reduction with DFC

In this part, only the DFC control is considered (no TMC or AND blocks). The DFC is a control strategy based on Direct Instantaneous Torque Control (DITC) [100], whose objective is to control the phase torques to get an overall torque as constant as possible. The aim of the adopted DFC is then to obtain a smooth overall radial force by controlling the

converter switches so that the sum of radial forces amplitude (not a vectoral sum), generated in the stator phases, reaches a desired value  $F_{ref}$  at each moment and then stays as constant as possible so as to limit the mechanical excitation. It is expected that the consequence is the reduction of the radial force variation, which is the main vibration cause pointed out in [53]-[55]. The control scheme of the SRM based on DFC is illustrated in Figure 3.17.

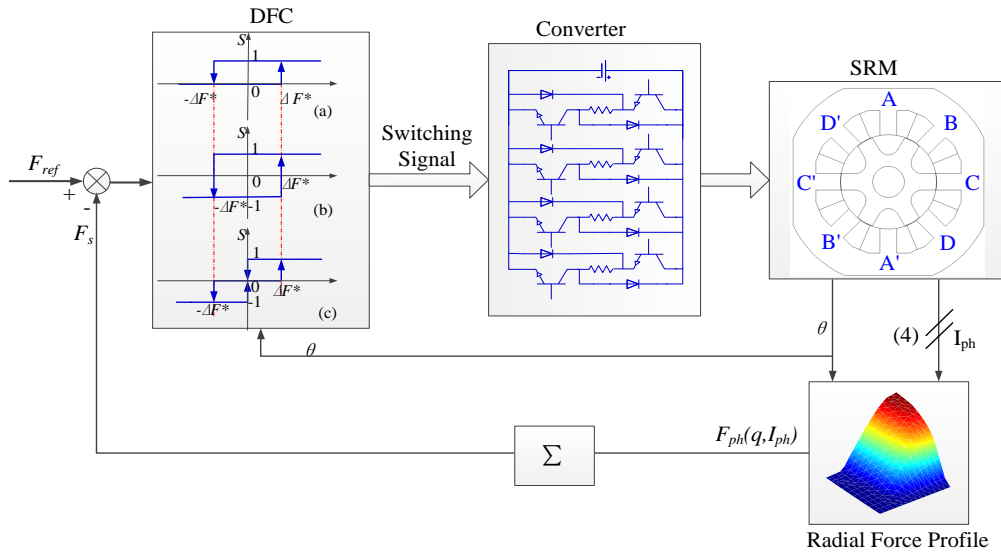


Figure 3.17 Structure of direct force control.

The switching signals of the power converter are generated by the DFC block in order to reduce  $\Delta F$  ( $F_{ref} - F_s$ ), defined as the difference between the desired total radial force  $F_{ref}$  and the actual sum of the radial forces of each phase  $F_s$ . Due to its asymmetric half-bridge structure, the adopted converter can provide three different terminal voltages (positive, zero, negative) to the connected phase winding.

Based on the same principle as the DITC [100], the DFC consists of three hysteresis controllers that produce the switching signals for each phase of the SRM, the main difference with DITC is that the signal to be controlled is the total force instead of the total torque. Depending on the position of the rotor, the controlling process is divided into three periods, as depicted in Figure 3.18 and the switching rules of the hysteresis-controller are illustrated in Figure 3.19. The force shape shown in Figure 3.18 does not reveal the actual one, but the one used as an illustration for the DFC principle. The hysteresis bands are defined within the intervals  $[-\Delta F^*, \Delta F^*]$ , where  $\Delta F^*$  is the hysteresis band chosen by the user. Taking phases A, B and D for example, the three periods are defined as follows:

- ✓ period I: the outgoing phase (phase D) and the current phase (phase A) are excited simultaneously.
- ✓ period II: only the current phase (phase A) is excited.
- ✓ period III: the current phase (phase A) and the incoming phase (phase B) are excited simultaneously.

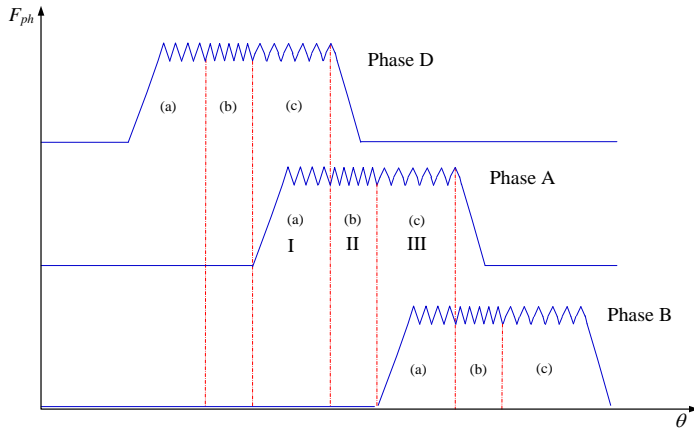


Figure 3.18 DFC: region division and control modes.

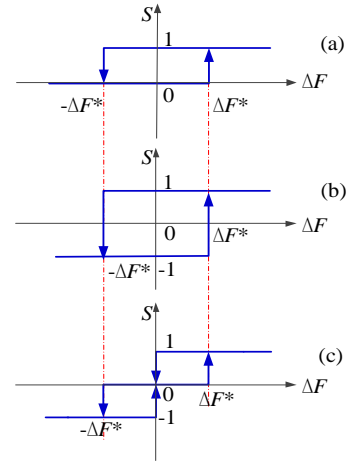


Figure 3.19 Diagram of the hysteresis controllers.

Therefore, considering the excitation states, there are two possible control modes for one period: *commutation mode* or *single excitation mode*. In *commutation mode*, two adjacent phases are excited at the same time (periods I and III in Figure 3.18). In this case, the switching states  $S$  of the outgoing phase (phase D, period I or phase A, period III) and the incoming phase (phase A, period I or phase B, period III) follow the rules in Figure 3.19 (c) and Figure 3.19 (a), respectively. In *single excitation mode*, just one phase is excited (phase A, period II) following the rules in Figure 3.19 (b). During the *commutation mode*, the DFC is achieved by controlling both excited phases. When the *single excitation mode* is activated, the sum of the radial force is tuned using the single excited phase.

Considering that the *commutation mode* (periods I and III) is active, when the control input  $\Delta F$  is smaller than the lower bound  $-\Delta F^*$  of the hysteresis band (total radial force too high), phase D is demagnetized, and phase A keeps freewheeling. As a result,  $F_s$  decreases and  $\Delta F$  increases up to zero, which triggers phase D to switch to freewheeling. While  $\Delta F$  keeps increasing, the switches of phase A and phase D turn on when  $\Delta F$  reaches the upper

bound  $\Delta F^*$  of the band. While exciting both phase A and phase D,  $\Delta F$  starts to decrease. Thus, when  $\Delta F = 0$ , phase D switches into freewheeling, while keeping phase A being excited. If the sum of radial forces keeps increasing until  $\Delta F \leq -\Delta F^*$ , then phase D is demagnetized, and phase A switches to freewheeling. By using these commands above, the variation of the sum radial force can be reduced during the commutation periods I and III.

During the *single excitation mode* (period II), phase A is excited with a classic hysteresis control and phase D has been turned off. Supposing that the total radial force  $F_s$  is smaller than the reference value  $F_{ref}$ , and that  $\Delta F$  goes beyond the upper bound  $\Delta F^*$ , phase A is magnetized until  $\Delta F \leq -\Delta F^*$ , when phase A is turned off to prevent the overall radial force increasing further. By demagnetizing phase A, the total radial force begins to decrease, and phase A is magnetized as soon as  $\Delta F \geq -\Delta F^*$ .

In the DFC, different hysteresis controllers are adopted in different regions, the hysteresis controllers used in this work are designed considering the output torque performance, the efficiency and the vibration of the machine. In part I, the force from phase A of the SRM is smaller than the one of phase D, and then hysteresis (a) allows a limited switching rate and a fast increase of the current in order to provide the requested output torque. In part II, a high dynamic is required, so that the actual total force can emulate the reference value, which can be obtained by hysteresis (b). In part III, the force of phase A is high (near aligned position) and hysteresis (c) has shown to allow a restricted variation of the force around  $F_{ref}$  to limit the vibration during the commutation period.

### 3.2.2 Reference Force Generator

According to Figure 3.17, a reference radial force  $F_{ref}$  is required by the DFC. However, the output of the speed controller is the reference torque  $T_{ref}$  used to control the speed. Thus, a relationship between reference torque and reference radial force is necessary. Therefore, a static characteristic  $F_{ref} = f(T_{ref})$  is introduced, that allows to obtain the equivalent mean radial force value on half electrical period based on the equivalent mean torque value on one half electrical period. It is well-known that the torque and the radial force profiles of the SRM present a highly nonlinear behavior which is related to the phase current and rotor position (as shown in Figure 3.20 and Figure 3.21).

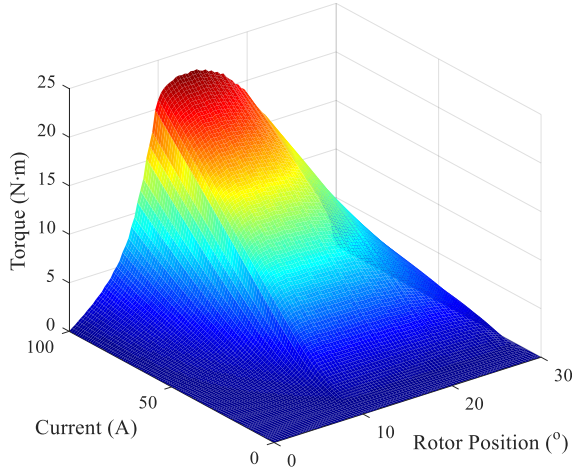


Figure 3.20 Torque profile.

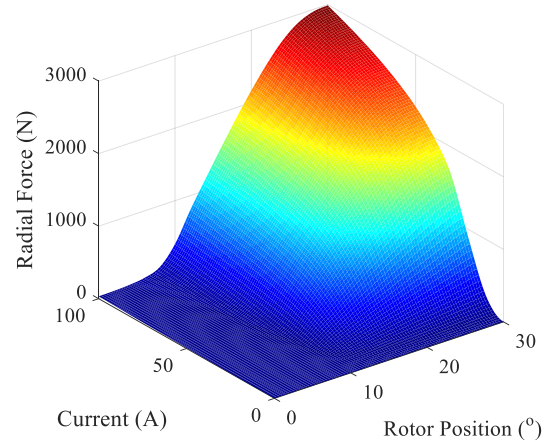


Figure 3.21 Radial force profile.

Based on these profiles, the equivalent mean values of both torque and radial force during a half electrical period can be calculated, for each current. Actually, the mean values of these quantities depend on the speed, as the optimized parameters for the current reference depend on it. As the force and torque are small near the unaligned position presented in Figure 3.20 and Figure 3.21, we assume that the integration can be done on all the half period to get the mean value, instead of only on the conduction period. The considered expressions are then the following:

$$T_m(I) = \frac{1}{\pi} \int_0^{\pi} T(I, \theta) d\theta \Big|_{I=const} \quad (3.14)$$

$$F_m(I) = \frac{1}{\pi} \int_0^{\pi} F(I, \theta) d\theta \Big|_{I=const} \quad (3.15)$$

Therefore, the relationship between the mean torque and radial force is obtained as illustrated in Figure 3.22. Based on these static characteristics related to the considered SRM only, the reference mean torque and mean radial force are estimated simultaneously.

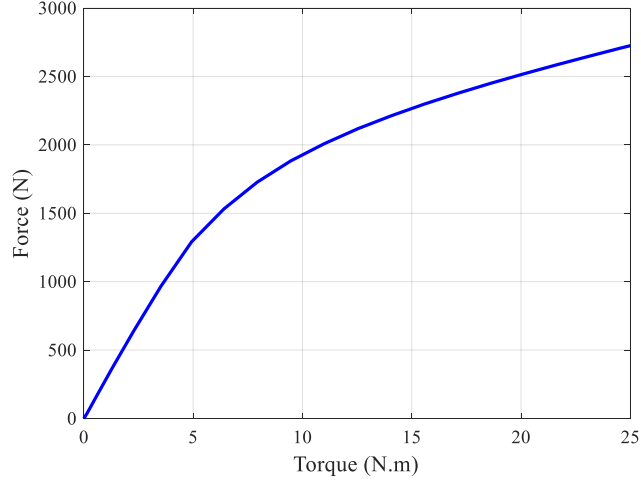


Figure 3.22 Static characteristics between the overall torque and the total radial force.

Using such DFC alone for the control of the SRM, the current amplitude is modified (compared to the amplitude obtained with TMC) to control the total force and to improve the vibratory behavior of the SRM. Nevertheless, there is no more limitation for the current amplitude. Consequently, it deteriorates the torque ripple: it introduces a peak current, which leads to a peak value in the phase torque that increases the torque ripple. To state this problem clearly, simulation results will be given in the next section.

### 3.2.3 Simulation Results: TMC vs DFC

To verify the performance of the DFC, this control method is tested in simulation with the multi-physics model built in last chapter. The inputs of this model are the reference speed  $\Omega^*$  of 600 r/min and the load torque  $T_L$  of 7 N·m. Then, both electromagnetic properties (including current, torque and radial force) and structural property (vibration acceleration) can be obtained. Figure 3.23 and Figure 3.24 present the simulation results of the total torque ( $T_s$ ), total radial force ( $F_s$ ), phase current ( $I_{ph}$ ), phase torque ( $T_{ph}$ ), and phase radial force ( $F_{ph}$ ) for TMC and DFC, respectively.

As shown in Figure 3.23, a quasi-square phase current is obtained using TMC. The turn-on angle is before the unaligned position so as to produce a negative torque (shown within the red dash circle) to compensate the peak torque (shown within the green dash circle). Thus, the torque ripple can be reduced. The shape of the radial force is triangular, the value is rather small near the unaligned position (shown within blue circle) even though the phase current has caught up with the reference value and is stable. That is because when the rotor is near

the unaligned position, the inductance is very small, as the air-gap is very large. The phase radial force increases with the rotor approaching the aligned position, the phase current being constant until this phase is turned off. Thus, DFC requires a high current when the rotor is near to unaligned position to produce a smooth total radial force as shown in Figure 3.24. However, the phase current peak leads to a peak value of phase torque (shown within purple dash circle), which increases the torque ripple and generates an oscillation of the total radial force  $F_s$ . Because of the serious torque ripple introduced by the DFC, the actual speed fluctuates around the reference speed that gives an oscillating reference torque  $T_{ref}$ . Since the reference force  $F_{ref}$  is a function based on  $T_{ref}$ , the reference force varies also with the  $T_{ref}$ .

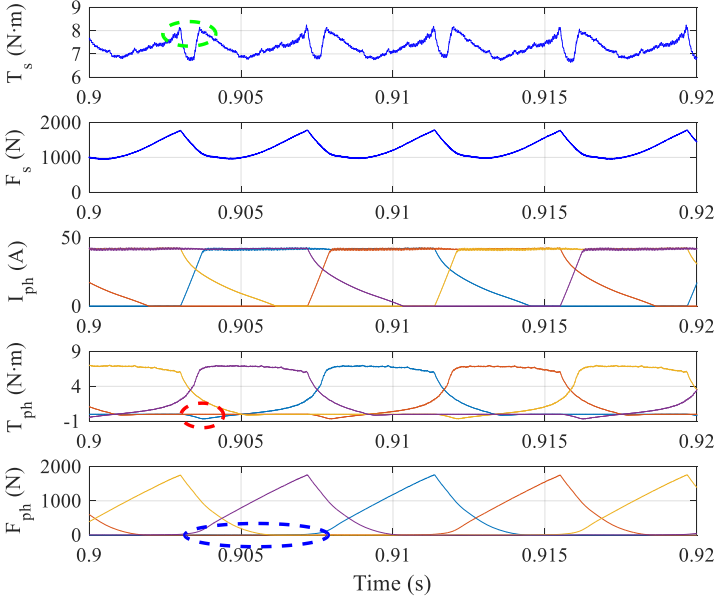


Figure 3.23 Total torque, total radial force, phase current, phase torque and phase radial force obtained with TMC at  $\Omega^* = 600$  r/min and  $T_L = 7$  N·m.

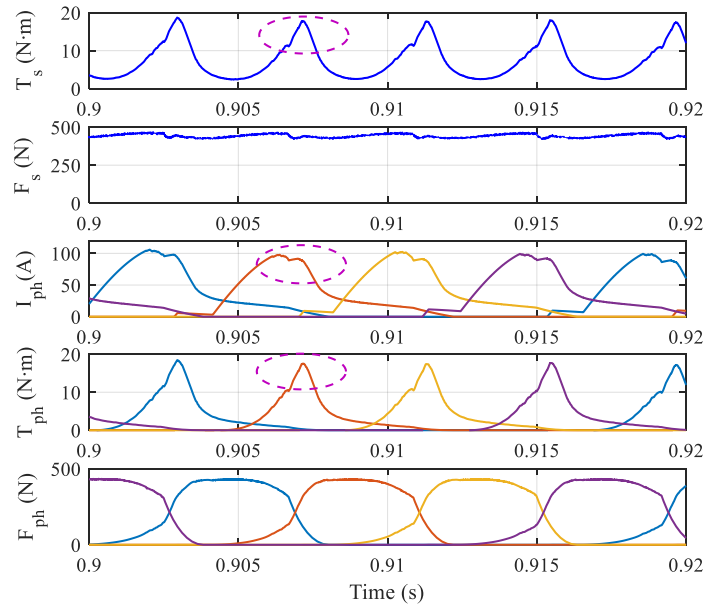


Figure 3.24 Total torque, total radial force, phase current, phase torque and phase radial force obtained with DFC at  $\Omega^* = 600$  r/min and  $T_L = 7$  N·m.

Figure 3.25 and Figure 3.26 present the FFT spectrum of the phase radial force  $F_{ph}$  and total torque  $T_s$ . As presented in the figures, both the low-order harmonics and the harmonics near the natural frequency  $f_2$  (frequency of mode 2) have been reduced. This leads to a reduction of vibration acceleration up to 68.7% (TMC --  $6.3$  m/s<sup>2</sup> vs. DFC --  $1.97$  m/s<sup>2</sup>) near  $f_2$  (mode 2) as shown in Figure 3.27 and Figure 3.28.

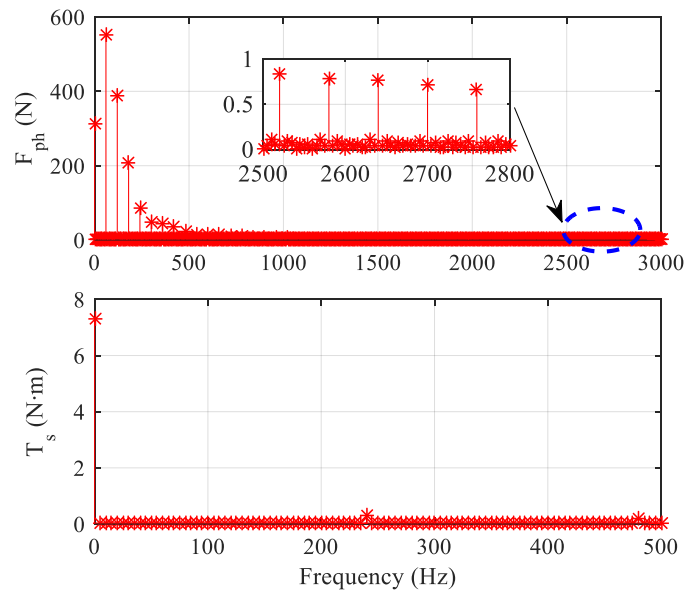


Figure 3.25 Spectrum of phase radial force and total torque of TMC at  $\Omega^* = 600$ r/min and  $T_L = 7$  N·m.

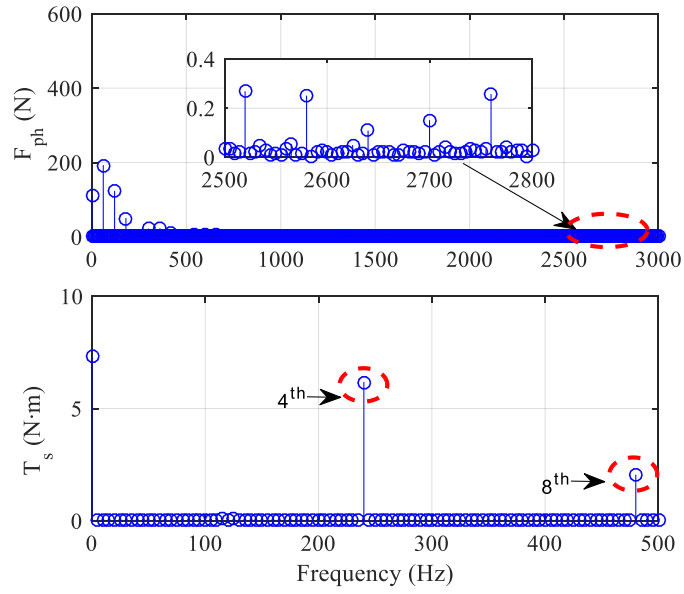


Figure 3.26 Spectrum of phase radial force and total torque of DFC at  $\Omega^* = 600\text{r/min}$  and  $T_L = 7\text{ N}\cdot\text{m}$ .

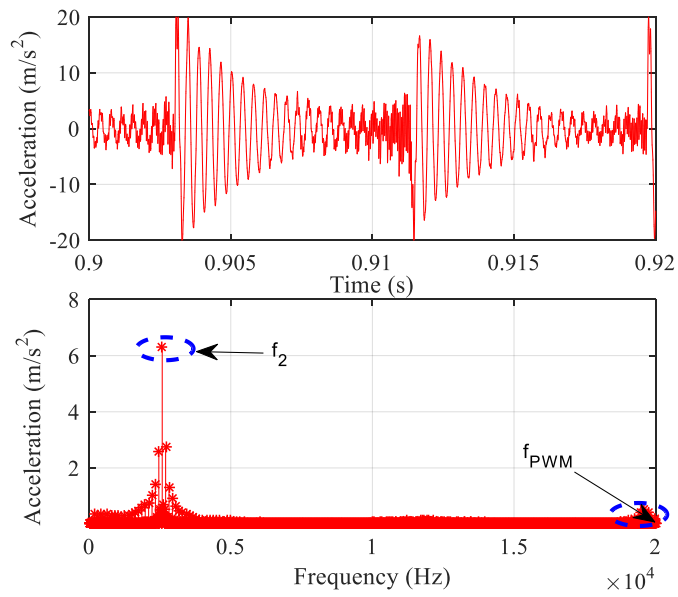


Figure 3.27 Acceleration of TMC at  $\Omega^* = 600\text{r/min}$  and  $T_L = 7\text{ N}\cdot\text{m}$ .

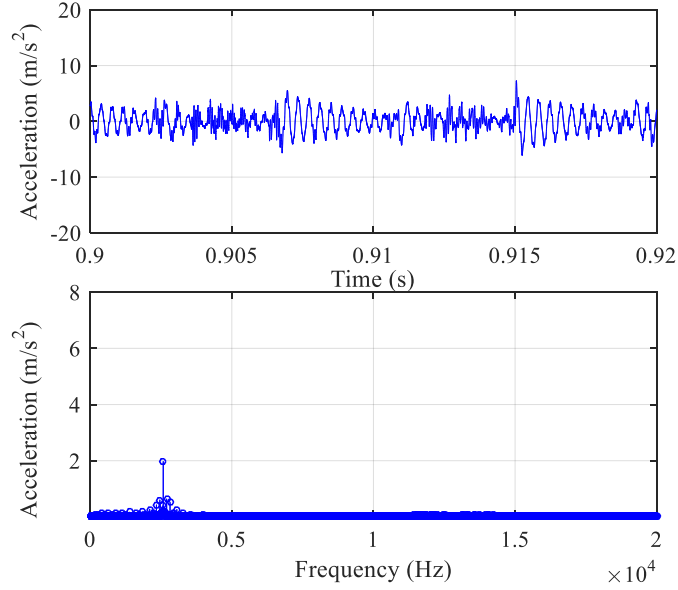


Figure 3.28 Acceleration vibration of DFC at  $\Omega^* = 600\text{r/min}$  and  $T_L = 7\text{ N}\cdot\text{m}$ .

The vibration energy computed with equation (3.13) has been reduced up to 89.1% (TMC -- 349 vs. DFC -- 38).

Nevertheless, the torque ripple has also to be considered for the proposed method. The torque ripple is computed as follows:

$$\gamma = 100\% * (T_{\max} - T_{\min}) / T_{\text{avg}} \quad (3.16)$$

where  $T_{\max}$  and  $T_{\min}$  are respectively the maximum and minimum torque in one electrical period.

The problem with the adopted controller is here that the torque ripple is increased by 200.2% (TMC--22.5% vs. DFC--222.7%), meaning that the torque ripple of DFC is almost ten times of that of TMC. As presented in Figure 3.25 and Figure 3.26, the DFC increases the 4<sup>th</sup> and 8<sup>th</sup> harmonic of the total torque, which worsens the torque ripple. The torque ripple will make the drivability of electric vehicle at risk at very low speed (e.g. at driveaway or during curb climbing), as the main torsional resonances of the whole drive train can be found in the range of a few Hertz. The excitation is either due to the torque ripple of the machine, the transmission error of the gear or an external disturbance (e.g. while curb climbing). The latter can only be tackled with an outer anti-jerk control loop [101], which will not be considered in this thesis. In SRM, the torque ripple can be very large so that it usually

becomes the main source of oscillation. The fundamental torque harmonic of an SRM can be calculated as

$$f_T = N_{ph} N_r f_m \quad (3.17)$$

where  $f_m$  is the mechanical frequency,  $N_{ph}$  and  $N_r$  are the number of phases and rotor teeth, respectively.

The second adverse effect of the torque ripple is that it can excite vibrations of the gearbox. Therefore, the torque ripple problem is necessary to be considered. Thus, an association of TMC and DFC is introduced in the following part to consider the advantages of the two controllers.

### 3.2.4 Association of TMC and DFC

The control structure of the association of TMC and DFC is presented in Figure 3.29. The association of the two controllers is simply a logical AND with the two switching signals as inputs. In this part, the RCA (in Figure 3.16) is not yet presented. The idea is the following:

- ✓ When the total force is small enough, only the output of the TMC is switching, and the DFC tries to impose a closed condition. As a consequence, the output of the AND block is similar to the output of TMC (TMC AND 1 = TMC).
- ✓ When the total force reaches  $F_{ref}$ , the DFC starts to impose switching signals in order to control the total radial force. The main changes comparing to TMC alone is that the output of the AND block is then equal to 0 when DFC tries to impose 0 and TMC tries to impose 1. Therefore, the resulting mean torque will be slightly lower comparing to the case with TMC alone. This gives an additional parameter to manage the trade-off between torque ripple and force harmonics.

In the Figure 3.29, the switching signal  $S_T$  and  $S_D$  represent the switching control signal from TMC and DFC, respectively.

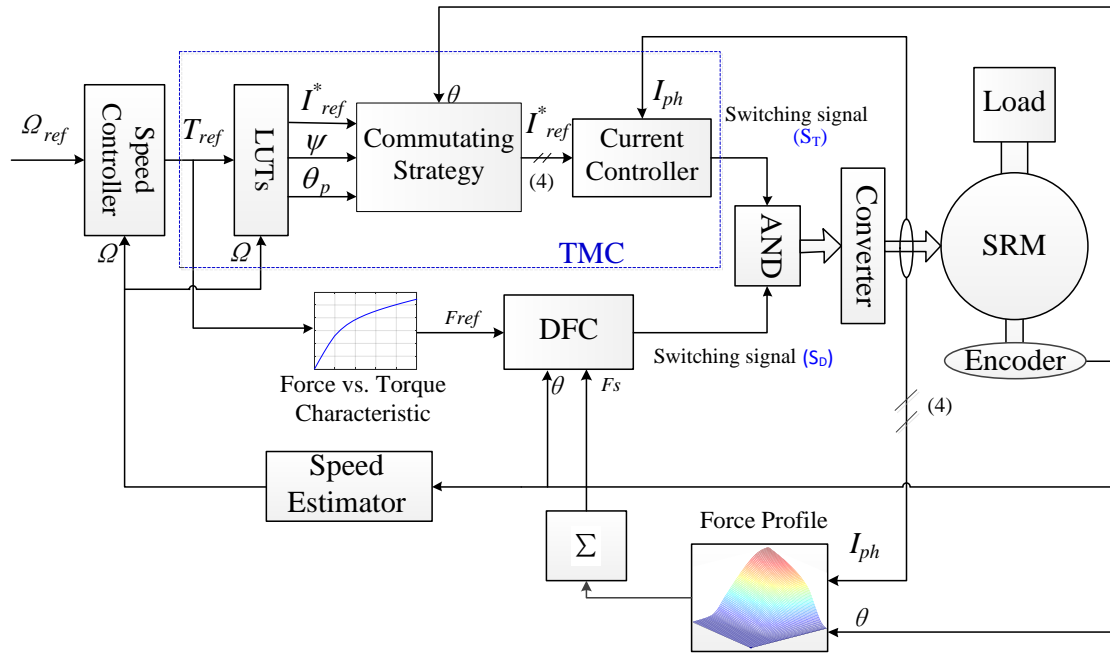


Figure 3.29 Block diagram for the association of TMC and DFC.

Figure 3.30 presents the torque, the total radial force, phase current and switching signals of one excited phase sent to the converter, obtained with the association of TMC and DFC. In the figure,  $S_{PWM}$  is the switching signal from the PWM-based current controller of the TMC,  $S_{DU}$  and  $S_{DL}$  are the switching signals sent to the upper and lower MOSFET of the excited phase, respectively. As expected, when the force is small enough, the switching signal ( $S_{DU}$  and  $S_{DL}$ ) for TMC+DFC is the same with the signal from the signal ( $S_{PWM}$ ) from the current controller of TMC during the period (a) and (c). When the total radial force reaches  $F_{ref}$ , and the actual phase current  $I_{ph}$  is slightly smaller than the reference current, the TMC and DFC are both active illustrated during the period (b). The total force is then controlled, but the main radial force and the torque output are from the outgoing phase. During the period (d), the total radial force reaches  $F_{ref}$  again, and the main radial force and the torque output are from the current phase. Since the switching signal of TMC is 1, only the DFC is active during this period. The impact of the DFC clearly appears (green-dashed circle).

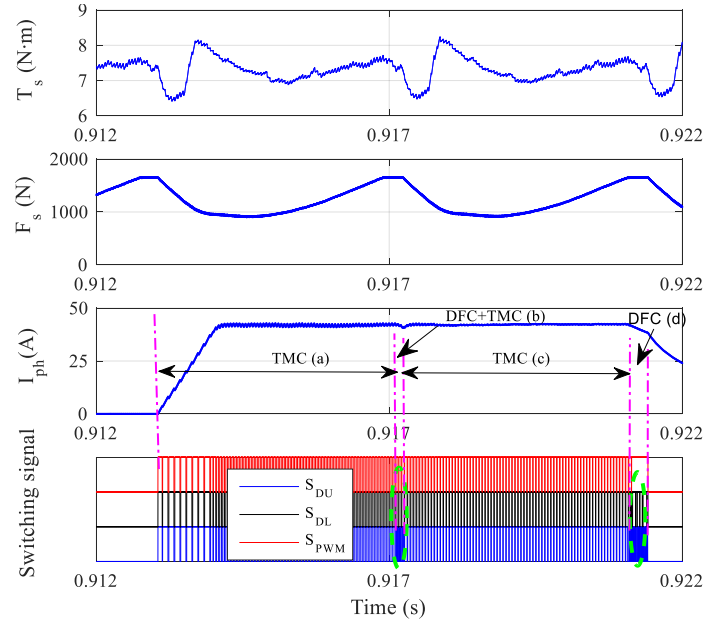


Figure 3.30 TMC + DFC: torque, total radial force, phase current and switching signals at  $\Omega^* = 600$  r/min,  $T_L = 7$  N·m.

Figure 3.31 shows the acceleration obtained in both cases (TMC+DFC vs. TMC). These results show that the TMC+DFC leads to a vibration acceleration reduction of 15.7 % (TMC- $-6.3$  m/s<sup>2</sup>, TMC+DF-- $5.31$  m/s<sup>2</sup>) near the  $f_2$  (mode 2) and the vibration energy reduction is about 30 % compared to TMC, and the torque ripple has been increased from 22.5 % to 26.1 %. However, the torque ripple is reduced by 196.6% compared to the case when only DFC is used. This is because the 4<sup>th</sup> and 8<sup>th</sup> harmonics of the total torque  $T_s$  have been removed (Figure 3.32) compared to DFC (Figure 3.26). The vibration reduction is less significant while combining the TMC with the DFC, because of the current limitation that allows the DFC to work for a short time (within the red dash circle shown in Figure 3.33). Thus, if the current is allowed to increase the DFC can be active for a longer time, so that the force variation can be reduced for a longer period to reduce vibration. However, if the current is too high, it will lead to serious torque ripple. Therefore, a reference current adapter is proposed to handle this compromise.

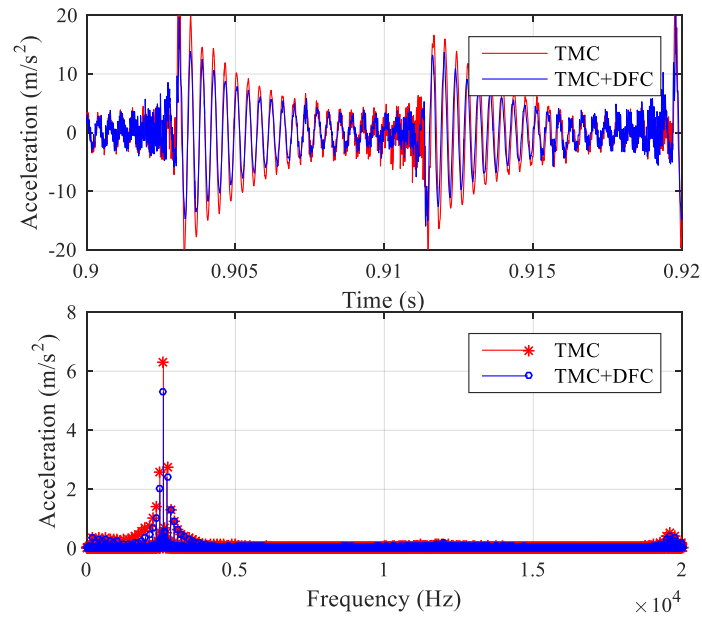


Figure 3.31 Comparison between the TMC and the association TMC + DFC: time-domain acceleration, frequency-domain acceleration at  $\Omega^* = 600$  r/min and  $T_L = 7$  N·m.

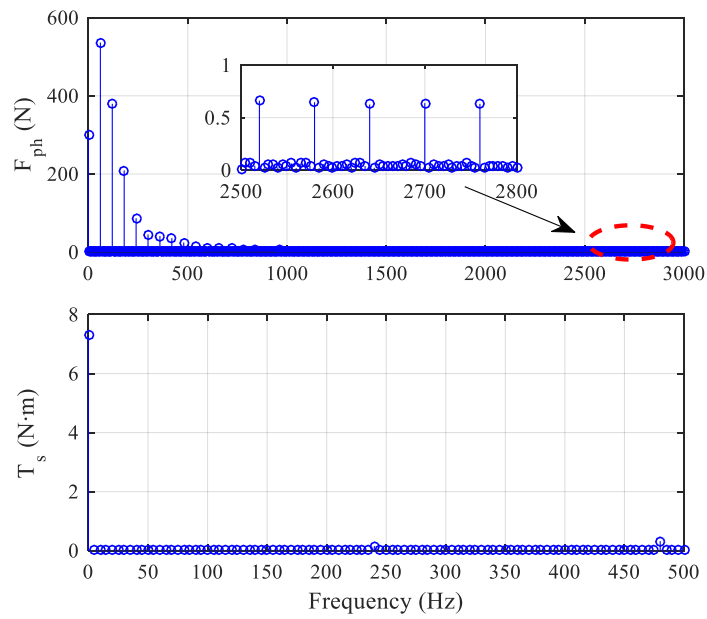


Figure 3.32 Spectrum of phase radial force and total torque of TMC + DFC at  $\Omega^* = 600$  r/min and  $T_L = 7$  N·m.

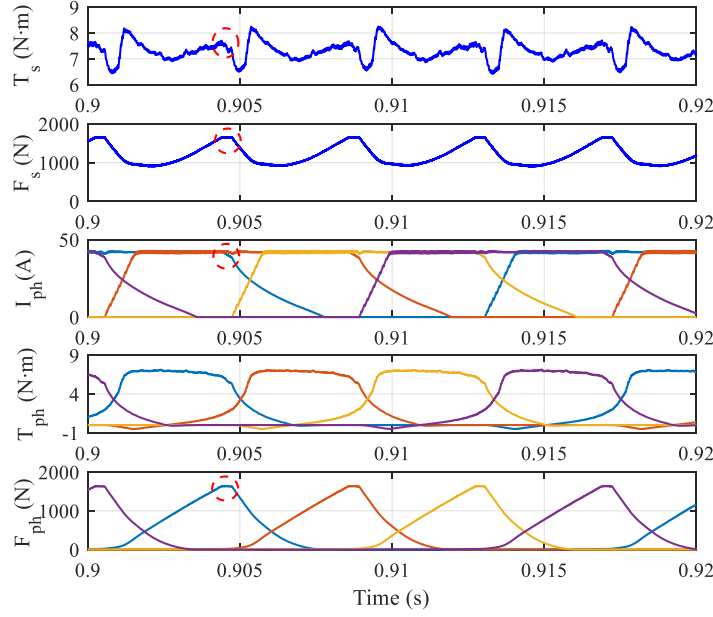


Figure 3.33 Total torque, total force, phase current, phase torque and phase radial force of TMC+DFC at  $\Omega^* = 600$  r/min and  $T_L = 7$  N·m.

### 3.2.5 DFC with Reference Current Adaptor (DFC&RCA)

The purpose of a reference current adaptor is to manage the tradeoff between the two objectives: torque ripple minimization and vibration reduction by updating the current reference. The value of the current reference is constantly adapted based on the variations of the torque and radial force within an electrical period, noted  $\sigma_T$  and  $\sigma_F$  respectively. These criteria are calculated using the following expressions:

$$\sigma_T = \sqrt{\int_0^{T_c} (T(t) - T_{avg})^2 dt / (T_{avg}^2 T_c)} \quad (3.18)$$

$$\sigma_F = \sqrt{\int_0^{T_c} (F(t) - F_{ref})^2 dt / (F_{ref}^2 T_c)} \quad (3.19)$$

where,  $T(t)$ ,  $F(t)$  are the transient total torque and total radial force, respectively;  $T_{avg}$ ,  $F_{ref}$  are the mean value of the total torque and the total radial force reference during one electrical period, respectively;  $T_c$  is the cycle time of one electrical period.

The structure of the reference current adaptor is illustrated in Figure 3.34.  $I_{ref}[k]$  is the output of the reference current adaptor at time  $k$ .  $I_{new}[k]$  is the intermediate current reference value at time  $k$ .  $\delta I$  is the current increment of the current adaptor that can be positive or negative depending on condition.  $I_{ref}^*[k]$  is the reference current obtained from the optimized LUT in usual TMC. Details of this current adaptor algorithm are presented in Figure 3.35.

The main idea is to adapt the initial  $I_{ref}^*$  so as to amplify the effect of the DFC.

The parameters  $\varepsilon_F$  and  $\varepsilon_T$  are the upper limits for the radial force variations and the torque variation. The values of  $\varepsilon_F$  and  $\varepsilon_T$  are chosen to ensure an acceptable trade-off between torque ripple minimization and vibration reduction.  $\Delta I$  is a constant value that can also be tuned by the user: a too small value will slow down the adaptation process, a too big value will drive the system unstable. In this thesis,  $\Delta I$  is equals to 0.5A, and the effect of other parameters ( $\varepsilon_F$ ,  $\varepsilon_T$  and  $\Delta F$ ) will be investigated in the next few sections.

Firstly, at each sampling instant,  $\sigma_T$  and  $\sigma_F$  are determined and compared to constant value of  $\varepsilon_T$  and  $\varepsilon_F$  in order to compute the intermediate current reference  $I_{new}[k]$ . Since the main objective of this work is to reduce the vibration, the force variation limitation of  $\varepsilon_F$  should be met at first. Actually, the condition  $\sigma_F > \varepsilon_F$  is obtained when the total force is smaller than the reference force. Then, the current adapter increases the reference current as long as the force variation  $\sigma_F$  exceeds the limitation  $\varepsilon_F$ . If  $\sigma_F \leq \varepsilon_F$  (vibration criterion validated), then the torque criterion is considered. If  $\sigma_T > \varepsilon_T$ , that means that the torque has to be reduced to avoid a peak torque value, so the reference current is reduced. If both variations of torque and radial force are inside their allowed range, the intermediate current reference  $I_{new}[k]$  is equal to the pervious output  $I_{ref}[k-1]$ . The reference current  $I_{ref}^*[k]$  is used to ensure the speed-up of the machine. Finally, the output of the reference current adapter is equal to the biggest value between  $I_{ref}^*[k]$  and  $I_{new}[k]$ . The output of the current adapter is then always superior or equal to  $I_{ref}^*$  to compensate the small decrease of the torque due to the DFC.

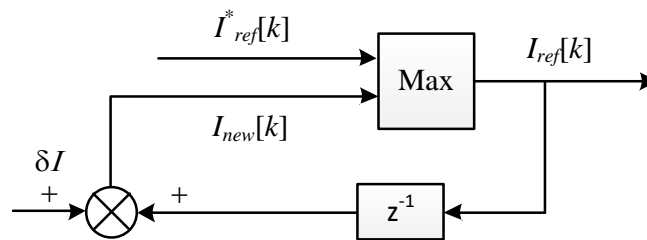


Figure 3.34 Structure of the proposed reference current adapter.

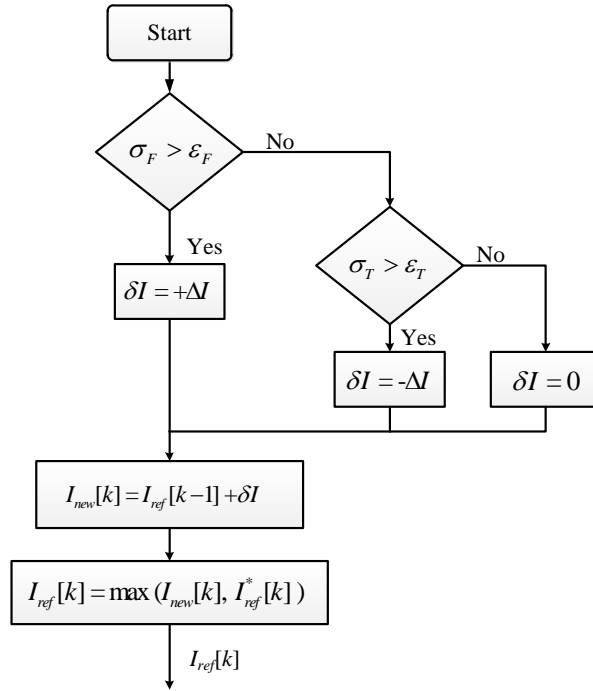


Figure 3.35 Current adapter algorithm

Figure 3.36 presents the torque, the total force, the phase current and switching signals of excited phase applied to the converter, obtained with DFC&RCA ( $\varepsilon_F = 0.5$ ,  $\varepsilon_T = 0.12$ ,  $\Delta F = 5$  and  $\Delta I = 0.5$ ). Comparing the switching signal of DFC&RCA with that of TMC+DFC in Figure 3.30, the DFC in DFC&RCA works in a wider region than in TMC+DFC, which yields a higher vibration reduction.

The adaption process handled by the reference adapter is shown in Figure 3.37. The reference current  $I_{ref}$  increases at the beginning (region (a)) to reduce the force variation  $\sigma_F$  and to meet the requirement of  $\varepsilon_F$ . When  $\sigma_F \leq \varepsilon_F$ ,  $I_{ref}$  starts to decrease (region (b)) in order to reduce the torque ripple until  $\sigma_T$  satisfies the requirement of  $\varepsilon_T$  (region (c)). Within region (c), where  $\sigma_F \leq \varepsilon_F$  and  $\sigma_T \leq \varepsilon_T$ , the adaption process is made up of two parts: region (c.1) and region (c.2). Inside the region (c.1), the controller works in the mode of TMC+DFC (when  $I_{ref} = I_{ref}^*$ ). The reference current  $I_{ref}^*$  from the LUT starts to decrease slowly because the difference between the actual speed  $\Omega$  and reference speed  $\Omega^*$  is reducing, which leads to the reduction of the reference torque  $T_{ref}$  (output of the speed controller). As the actual speed  $\Omega$  approaches the reference speed  $\Omega^*$ , the reference current  $I_{ref}^*$  decreases faster and becomes smaller than the  $I_{ref}$ , the reference current adapter stops updating and enters the region (c.2)

where the current is constant. We recall that the RCA output is the maximum between  $I_{ref}^*$  and  $I_{ref}$ .

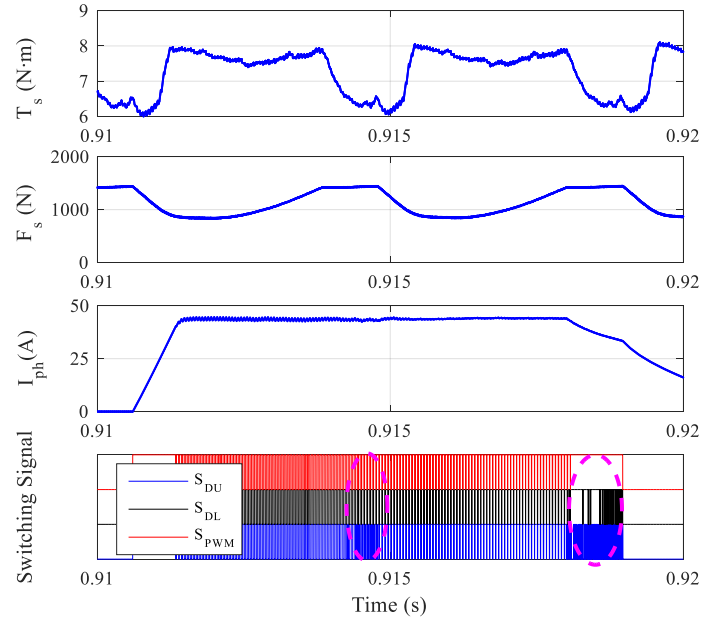


Figure 3.36 The DFC&RCA: total torque, total force, phase current and switching signal at  $\Omega^* = 600$  r/min and  $T_L = 7$  N·m.

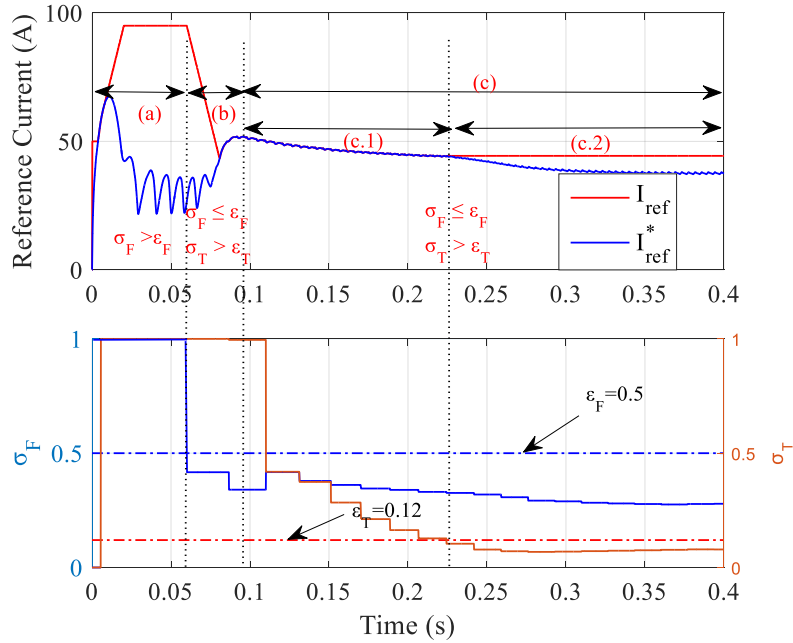


Figure 3.37 Reference current adaption progress when  $\Omega^*$  is 600 r/min with a load torque of 7N·m.

Figure 3.38 shows the acceleration obtained with both controllers (the traditional TMC and DFC&RCA). The vibration energy is reduced up to 81.7% compared to the TMC. The vibration acceleration is also reduced by 73.2% (TMC--6.3  $m/s^2$ , DFC&RCA--1.69  $m/s^2$ ) near the mode 2 frequency  $f_2$ . Nonetheless, the torque ripple is slightly increased by 7.3 %

compared to TMC, because of the DFC. In the period, the DFC works to control the radial force so that to emulate the reference radial force  $F_{ref}$ , which reduces the output phase torque  $T_{ph}$  within the red-dash circle region shown in Figure 3.39. From Figure 3.39, we see that the current shape is modified, and presents a smooth decrease within the red-dash circle region.

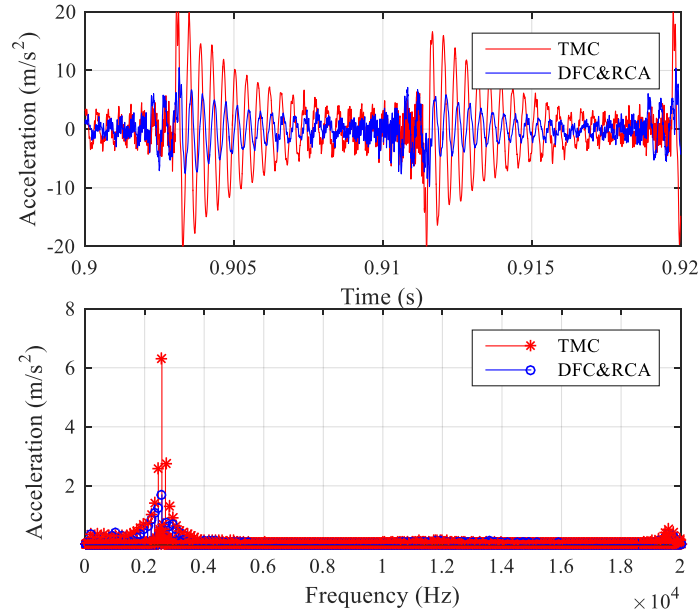


Figure 3.38 Comparison between the TMC and the DFC&RCA: time-domain acceleration, frequency-domain acceleration at  $\Omega^* = 600$  r/min and  $T_L = 7$  N·m

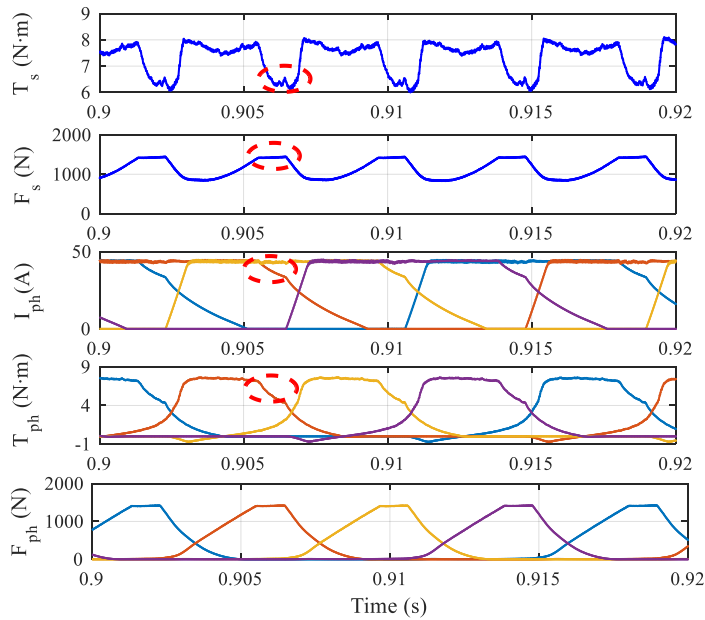


Figure 3.39 Total torque, total force, phase current, phase torque and phase radial force of DFC&RCA at  $\Omega^* = 600$  r/min and  $T_L = 7$  N·m.

### 3.2.6 Control Parameters Tuning for DFC& RCA

In this section, the control parameters (the bandwidth of the hysteresis controllers  $\Delta F$ , the force variation bound  $\varepsilon_F$ , torque variation bound  $\varepsilon_T$ ) tuning is investigated in simulation. All of which have effect on the performance of the proposed control approach.

The proposed reference current adapter is used to manage the tradeoff between the two objectives: torque ripple minimization and vibration reduction. The current update is based on two parameters, namely, the torque variation  $\sigma_T$  and the force variation  $\sigma_F$  per electrical period by following these rules introduced in Section 3.2.5. The effect of the force variation bound  $\varepsilon_F$  and the torque variation bound  $\varepsilon_T$  are then investigated firstly in the following sections.

#### 3.2.6.1 Effect of the Torque Variation Bound

At first, the effect of the torque variation bound  $\varepsilon_T$  is studied with a fixed force variation bound  $\varepsilon_F = 0.5$ . Five different values of  $\varepsilon_T$  are tested in simulation for the operating point defined by the reference speed  $\Omega^*$  of 600 r/min and the load torque of 7N·m. Figure 3.40 and Figure 3.41 show the vibration energy and the torque ripple for different values of the upper bound  $\varepsilon_T$ .

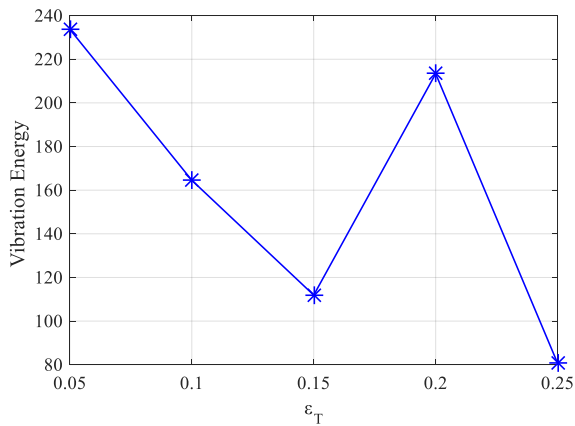


Figure 3.40 The vibration energy with different torque variation limitation  $\varepsilon_T$

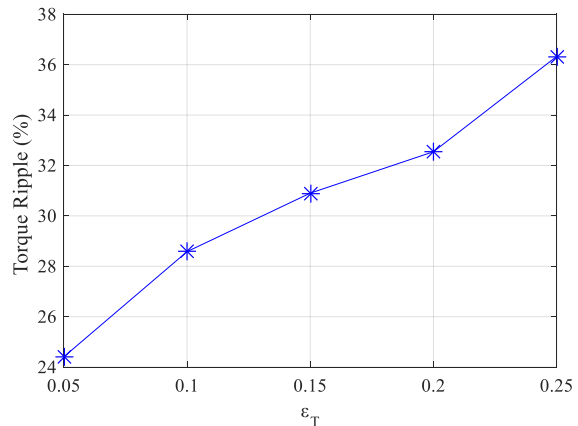


Figure 3.41 The torque ripple with different torque variation limitation  $\varepsilon_T$

According to the results, the vibration is minimum when the torque variation bound  $\varepsilon_T = 0.25$ . In addition, there is a high difference between the minimum and the maximum values of the vibration energy (the maximum value is almost three times the minimum value). It can

be seen that the vibration energy mainly decreases with the increase of the torque variation bound  $\varepsilon_T$  except for  $\varepsilon_T=0.2$ . As expected, the torque ripple is increased when the  $\varepsilon_T$  is high.

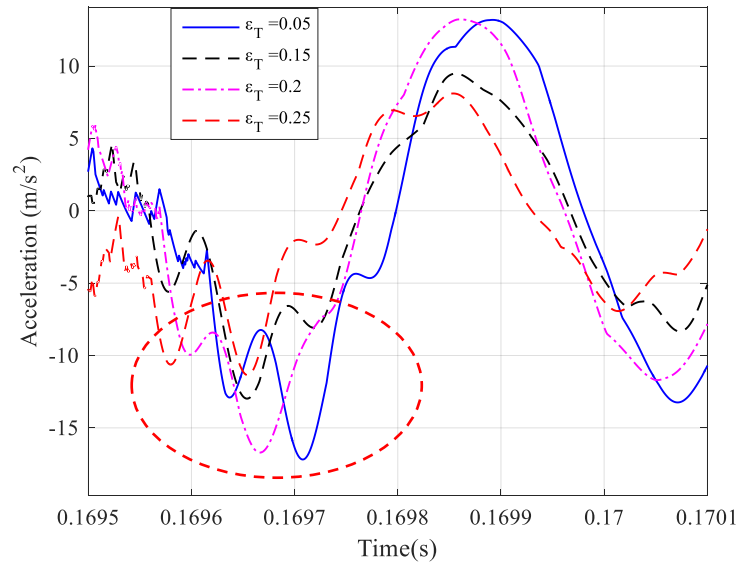
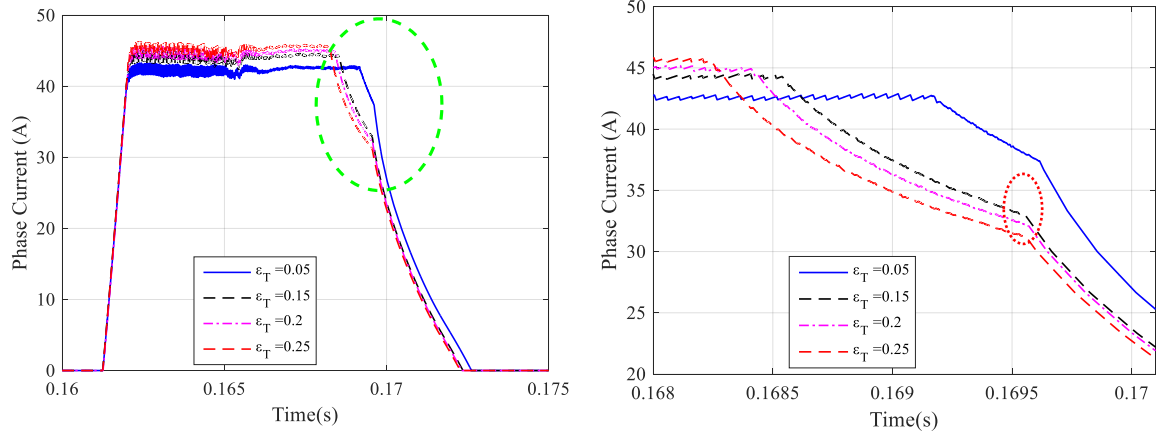


Figure 3.42 Acceleration curve for different torque variations.

Figure 3.42 shows the corresponding acceleration near the turn-off position (shown within red-dash circle). It can be seen that for  $\varepsilon_T \in \{0.05, 0.2\}$  the turn-off angles are more important than the ones for the other two values (0.15 and 0.25) of  $\varepsilon_T$ , which causes serious vibration when switching off at these positions. Because the closer the turn off position is to the aligned position, the force variation is bigger. Comparing the results of  $\varepsilon_T = 0.15$  and  $\varepsilon_T = 0.25$ , their turn-off angles are the same but the vibration of  $\varepsilon_T = 0.25$  is a little smaller than that of  $\varepsilon_T = 0.15$ . This is because for  $\varepsilon_T = 0.25$  the DFC works for a longer period of time due to the increase of the reference current. Thus, the current of  $\varepsilon_T = 0.25$  is smaller than that of  $\varepsilon_T = 0.15$  on the turned-off position (shown in Figure 3.43), which results in a smaller force variation at that moment.

The relationship between the torque variation bound  $\varepsilon_T$  and reference current  $I_{ref}$  are presented in Figure 3.44. The reference current  $I_{ref}$  increase with the increase of the torque variation bound  $\varepsilon_T$ .



(a) Phase current for different torque variation limitation  $\varepsilon_T$ . (a.1) Corresponding zoom of phase current.

Figure 3.43 Phase current curve for different  $\varepsilon_T$  at  $\Omega^* = 600$  r/min and  $T_L = 7$  N·m.

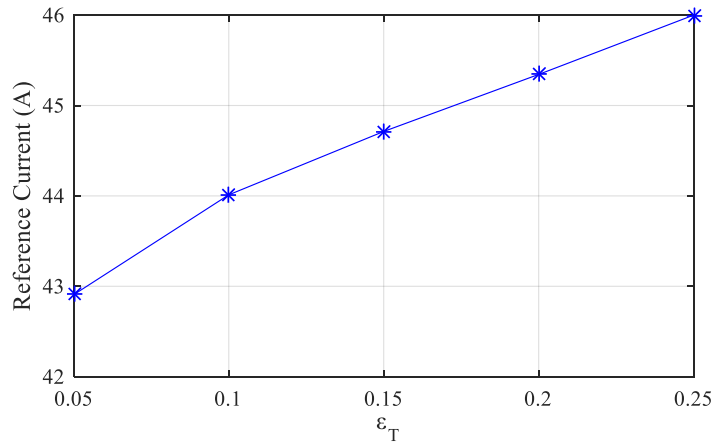


Figure 3.44 Relationship between  $\varepsilon_T$  and the reference current at  $\Omega^* = 600$  r/min and  $T_L = 7$  N·m.

### 3.2.6.2 Effect of the Force Variation Bound

The effect of the force variation bound  $\varepsilon_F$  is investigated with a fixed torque variation bound  $\varepsilon_T = 0.5$  that gives a wider force variation possibility than the range referred in the previous part. Simulation are run for the same operating point as before ( $\Omega^* = 600$  r/min,  $T_L = 7$  N·m) using five different values of  $\varepsilon_F \in \{0.3, 0.35, 0.4, 0.45, 0.5\}$ . Simulation results of the vibration energy and the torque ripple for different values of the upper bound  $\varepsilon_F$  are shown in Figure 3.45 and Figure 3.46.

According to the simulation results, when the force variation bound  $\varepsilon_F$  is 0.3 or 0.35, the control performances are the same, because the reference current produced by the RCA is the same, a reference current of 95 A is required to satisfy such a low limitation of the radial

force variation. Then, the vibration energy increases with the increase of the force variation bound  $\varepsilon_F$  in the range of  $[0.3, 0.45]$ . The vibration energy for  $\varepsilon_F = 0.4$  and  $\varepsilon_F = 0.45$  are equal, because the force variation cannot reach 0.5 in an electrical cycle. Comparing Figure 3.41 and Figure 3.46, the torque ripple (58.1%) obtained with the pairs bounds ( $\varepsilon_F = 0.5, \varepsilon_T = 0.5$ ) is bigger than the one (36.3%) obtained for ( $\varepsilon_F = 0.5, \varepsilon_T = 0.25$ ), which is expected since the allowed torque variation is greater.

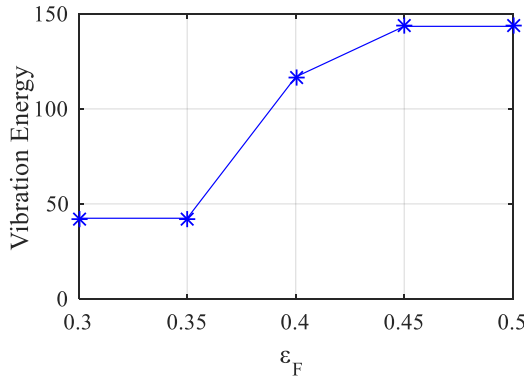


Figure 3.45 The vibration energy with different torque variation limitation  $\varepsilon_F$

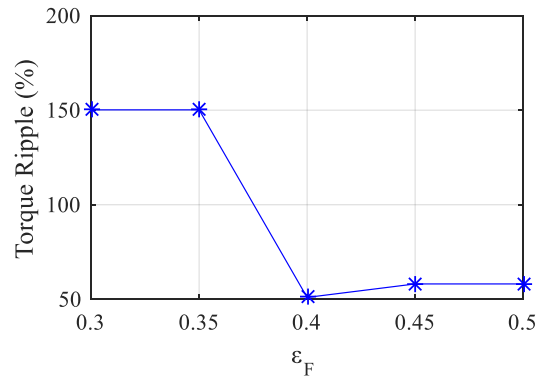
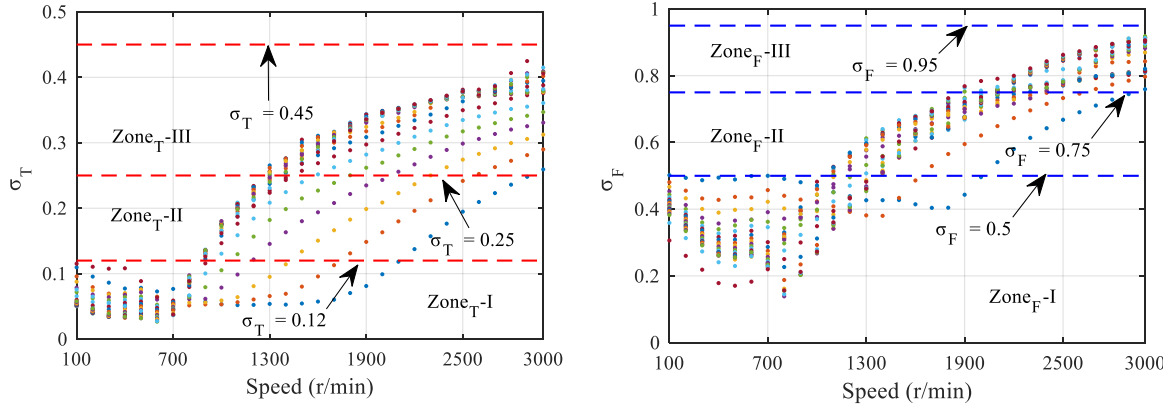


Figure 3.46 The torque ripple with different torque variation limitation  $\varepsilon_F$

In conclusion, the vibratory behavior of the SRM with DFC&RCA depends mostly on the force variation bound  $\varepsilon_F$ : it increases if this bound ( $\varepsilon_F$ ) is increased, but there exist upper and lower limitations for it. The torque ripple is more related to the torque variation bound  $\varepsilon_T$ : the torque ripple variation  $\sigma_T$  increases with the increase of this limitation  $\varepsilon_T$ . A too small force variation bound  $\varepsilon_F$  will generate high torque ripple (in Figure 3.46, when  $\varepsilon_F = 0.3$ , the torque ripple is up to 150%). A too small torque variation bound  $\varepsilon_T$  will worsen the vibration performance (in Figure 3.40, the vibration energy for  $\varepsilon_T = 0.05$  is three times the one obtained for  $\varepsilon_T = 0.25$ ). In this thesis, the bounds of the torque and force variations are chosen as  $\varepsilon_T = 0.12$  and  $\varepsilon_F = 0.5$  for the considered operating point ( $\Omega^* = 600$  r/min,  $T_L = 7$  N·m), as they offer an acceptable trade-off between the torque ripple minimization and the vibration reduction. With these two values, the vibration energy equals 64 and the torque ripple is of 29.8%.

In fact, the torque variation  $\sigma_T$  and the force variation  $\sigma_F$  change depending on the SRM operating point. In Figure 3.47, the TMC is employed to compute the torque and force variations for different values of speed (range:  $[100, 3000]$  r/min) and torque (range:  $[1, 25]$

N·m). It can be seen that both torque variation and force variation are relatively small when the speed is below 800 r/min. Beyond this value, they increase with the increase of speed (or torque).



(a) Torque variation  $\sigma_T$  for different operating points (b) Force variation  $\sigma_F$  for different operating points

Figure 3.47 TMC: the torque variation  $\sigma_T$  and force variation  $\sigma_F$  for different operating points.

Based on these results, both the torque and the force variation are divided into three zones (as shown in Table 3-2) as follows:

Table 3-2 Boundary values of different zones defined for  $\sigma_T$  and  $\sigma_F$

Zone	Zone <sub>T</sub>	Zone <sub>F</sub>
I	$\sigma_T \leq 0.12$	$\sigma_F \leq 0.5$
II	$0.12 < \sigma_T \leq 0.25$	$0.5 < \sigma_F \leq 0.75$
III	$0.25 < \sigma_T \leq 0.45$	$0.75 < \sigma_F \leq 0.95$

Figure 3.48 and Figure 3.49 illustrate the contour of torque and radial force variation on the torque-speed plane and the corresponding zone distribution on the plane.

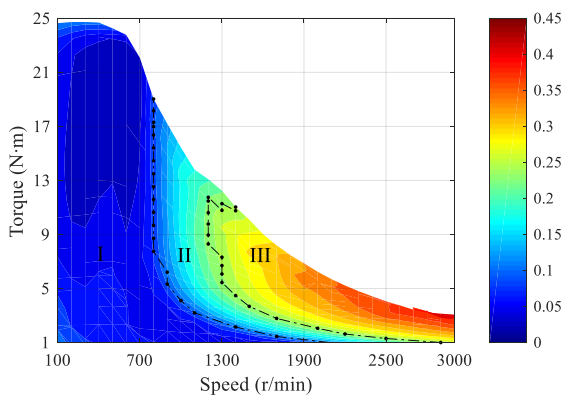


Figure 3.48 Contour of torque variation  $\sigma_T$

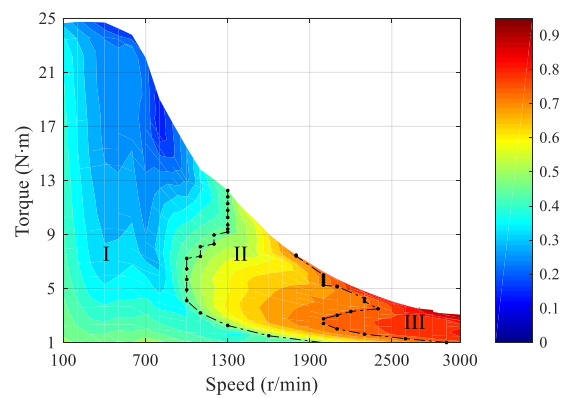


Figure 3.49 Contour of radial force variation  $\sigma_F$

As shown in Figure 3.48, both the torque variation and the force variation of low torque

are higher than that of high torque in the Zone-I because of the increase of mean value. And they increase with the speed at the same electromagnetic torque in the low-torque region because of the Electromotive Force (EMF). Thus, the speed-torque plane is divided into different zones according to rules as follows.

The upper limitation values in Zone<sub>T-I</sub> and Zone<sub>F-I</sub> are the maximum value of the low-speed and low-torque region. In second zone, the upper limitation values are the maximum value of the high-speed and low-torque region. In third zone, the upper limitation values are the maximum value of the three regions. Then, the boundaries of these regions are used as limitations of the torque variation and the force variation to define different regions on the plane torque-speed as shown in Figure 3.50. Since there are three zones for each parameter, theoretically there are nine combinations ( $\varepsilon_F, \varepsilon_T$ ). However, four of them are unfeasible (e.g.  $\varepsilon_F = 0.5$  and  $\varepsilon_T = 0.45$ ). Therefore, based on the feasible combinations of these two bounds,  $\varepsilon_F$  and  $\varepsilon_T$ , the torque-speed plane is divided into five operating regions.

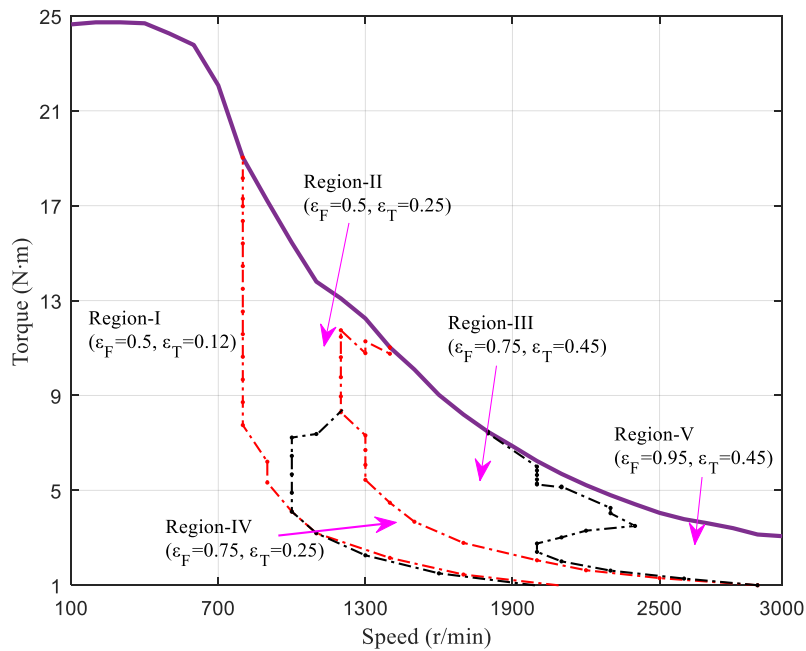
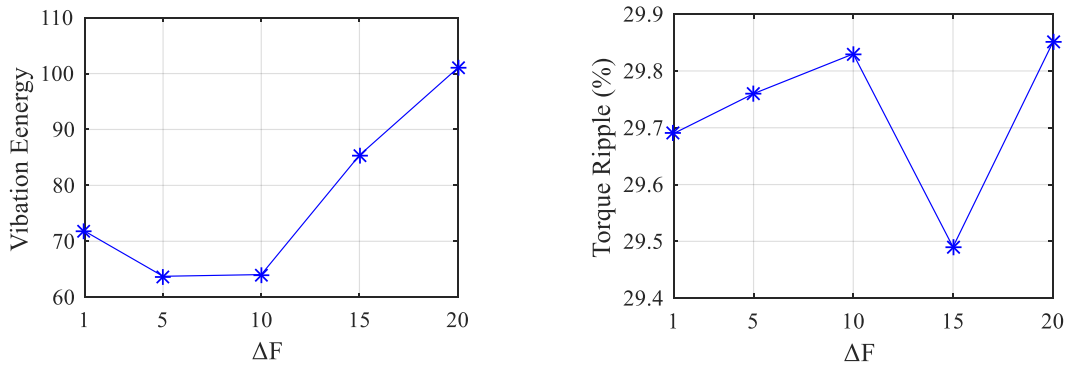


Figure 3.50 Region division based on the torque variation bound and the force variation bound.

### 3.2.6.3 Bandwidth Tuning

The DFC performance is highly related to the bandwidth of the hysteresis controllers. Therefore, in this section, different bandwidths  $\Delta F$  within the range of [1, 20] are tested in simulation. Five different values are considered for the operating point ( $\Omega^* = 600$  r/min,  $T_L$

= 7 N·m) and the results are shown in Figure 3.51. The bandwidths value has a very small effect on the torque ripple, the difference between the maximum and minimum value is just 0.36 % due to the fast dynamics of the DFC. In addition, there is a small decrease in the vibration energy when  $\Delta F < 10$  N, which is due to the white noise introduced to the simulation model. For  $\Delta F$  values greater than 10, the vibration energy increases with the bandwidth increases. This is because the vibration is mainly caused by the force variation, the higher bandwidth means bigger force variation within that limitation. Considering the switching losses of converter caused by a narrow bandwidth, the bandwidth  $\Delta F$  in this thesis is set to 5N.



(a) Vibration energy for different bandwidths  $\Delta F$ .

(b) Torque ripple for bandwidth  $\Delta F$ .

Figure 3.51 DFC&RCA performances for different bandwidths  $\Delta F$  at  $\Omega^* = 600$  r/min and  $T_L = 7$  N·m.

### 3.3 Efficiency and Torque Ripple Evaluation of the SRM

The general concept of IVTC and DFC&RCA was introduced in the previous sections. However, the system efficiency needs to be investigated before judging whether the new control scheme is suitable to be applied to SRM-based traction drives. The main interest for using SRMs in traction applications is certainly its cost efficiency. Nevertheless, the cost savings on the machine side are moot if they are overcompensated by additional battery costs due to excessive efficiency shortcomings of the drive unit. Besides, torque ripple is a frequently stressed point in the literature when it comes to SRMs. In traction applications, torque ripple can potentially excite the downstream power train, which can lead to undesirable jerking of the vehicle or secondary noise radiating as gear whine from the transmission.

### 3.3.1 Losses and Efficiency

Four major loss types determine the efficiency of SRMs drive system. The mechanical losses caused by bearing friction or air drag, and the air friction are especially important due to the doubly-salient structure of the SRM. However, the mechanical losses are only important in the high-speed range of the machine since the air-drag power increases disproportionately with the speed. Moreover, mechanical losses are independent of the torque level and the control so that they are not considered in this thesis.

The second type of losses is represented by the copper losses, that can be divided into DC copper losses and AC copper losses. The DC ones are caused by the ohmic resistance. However, this ohmic resistance can be increased by the alternating magnetic fields, which cause the skin and the proximity effect [102]. The latter can be particularly severe in SRMs because the main flux can penetrate the top layers of the coils if they are close to the air gap. This potentially causes significant losses. For the investigated machine, AC copper losses are expected to play a minor role since its coils are placed relatively far from the air gap. The copper loss is significant when the load torque is heavy, which are affected by the control methods.

The third type of losses is the iron losses. These losses are also induced by the alternating magnetic fields, which cause hysteresis losses and eddy-current losses in the metal stack of the machine. The controller typically does not change the fundamental frequency of the SRM. However, it can affect the harmonic content and the flux amplitudes. Thus, iron losses are essential for evaluating the efficiency performance of a control strategy.

The fourth major source of losses is the converter loss. These losses are classified into conduction losses and switching losses of the power-electronic devices. Conduction losses are similar to the DC copper losses in the machine. They primarily occur in the silicon of the MOSFETs and the diodes, which are required in an asymmetric half bridge. The switching losses of the power-electronic devices arise during the transition from conducting to blocking state and vice versa. Conduction losses are especially significant at high torque as it also applies to DC copper losses in the machine. Switching losses, however, are crucial over the complete torque-speed map.

All the considered losses computation is detailed in Appendix C.

### 3.3.2 Simulation Results of IVTC

From the definitions of the torque ripple and efficiency previously given, the IVTC for the operating point at  $\Omega^* = 600$  r/min and  $T_L = 7$  N·m shows to give torque ripple increased by slightly 4% compared to the ATC, and the efficiencies are identical, which are 56.6 % (IVTC) and 56.4% (ATC), respectively.

Figure 3.52 presents the comparison results between the ATC and IVTC of the total torque ( $T_s$ ), phase current ( $I_{ph}$ ), phase torque ( $T_{ph}$ ), and phase radial force ( $F_{ph}$ ). The torque ripple of the IVTC is bigger than the traditional ATC because the turn-off angle of the IVTC is smaller than the ATC, so that the IVTC switches off earlier. This leads to the fast decrease of the phase torque as shown in Figure 3.52 (c), which causes a deeper concave part (within pink-dash line) in Figure 3.52 (a) that increases the torque ripple. Meanwhile, the vibration is reduced because the excited phase switches off earlier and has a smoother radial force variation near the turn-off position as shown in Figure 3.52 (d). As illustrated in Figure 3.52 (b), the conduction angle of the ATC is bigger than the IVTC but smaller stable amplitude value so that to guarantee the torque output.

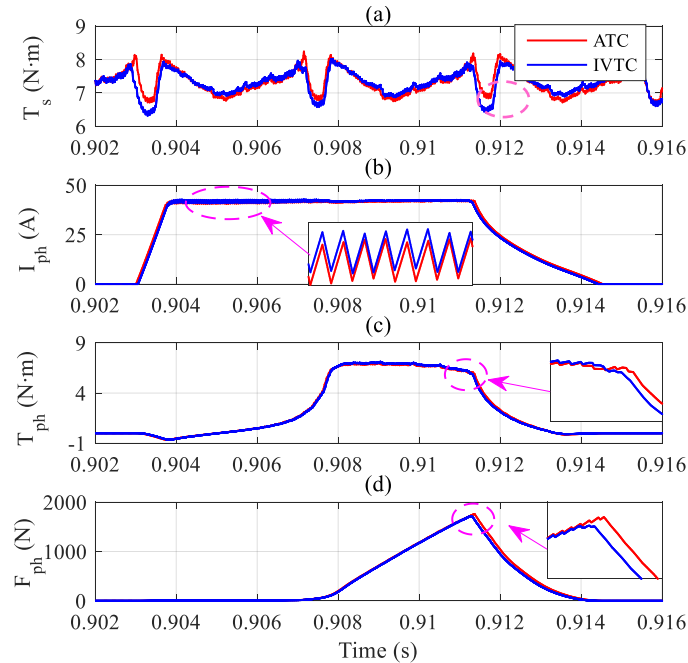


Figure 3.52 Comparison between the ATC and the IVTC: Total torque, phase current, phase torque and phase radial force obtained at  $\Omega^* = 600$  r/min and  $T_L = 7$  N·m.

Different operating points are investigated summarized in Table 3-3.

Table 3-3 Performance comparison between ATC and IVTC for different operating points

Operating point	Variation magnitude	Vibration energy reduction	Torque ripple increase	Efficiency increase
$\Omega^* = 600 \text{ r/min}, T_L = 7 \text{ N}\cdot\text{m}$	$\Delta\theta = 3^\circ$	59.3 %	+4 %	-0.2 %
$\Omega^* = 600 \text{ r/min}, T_L = 16 \text{ N}\cdot\text{m}$	$\Delta\theta = 3^\circ$	60.5 %	+6.5 %	+0.2 %
$\Omega^* = 1300 \text{ r/min}, T_L = 8 \text{ N}\cdot\text{m}$	$\Delta\theta = 3^\circ$	32.5 %	+4.4 %	0%
	$\Delta\theta = 6^\circ$	61.5 %	+8 %	0%

It can be concluded that for such kind of controller the torque ripple is increased due to the variation of the turn-off angle each period and the efficiency are identical for the considered operating points.

### 3.3.3 Simulation Results of DFC&RCA

To investigate the closed-loop system efficiency using the DFC&RCA, different operating points are simulated with the multi-physics model built in last chapter. Seven working points are analyzed, which are distributed in five different regions shown in Figure 3.53. Table 3-4 gives the definition of the seven investigated operating points.

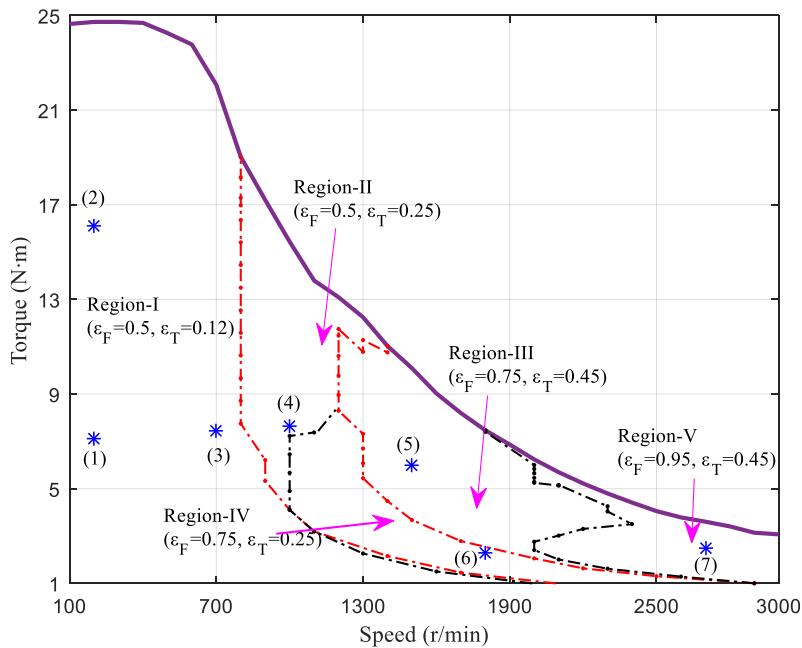


Figure 3.53 Investigated operating points on the torque-speed plane.

Table 3-4 Definition of the investigated operating points.

	(1)	(2)	(3)	(4)	(5)	(6)	(7)
Speed (r/min)	200	200	700	1000	1500	1800	2700
Load Torque (N·m)	7	16	7	7	5	1.1	0.7

Operating point (1) at 200 r/min and 7 N·m represents a low-speed and low-torque operating point. The drive system efficiency is known to be quite limited in this area. On the other hand, only a relatively little amount of power is converted and efficiency of its converter is also low.

Operating point (2) at 200 r/min and 16 N·m denotes a low-speed but heavy-load operating point. The Ohmic DC losses in the machine and the inverter are supposed to be dominant here since the RMS phase current is up to 46 A.

Operating point (3) at 700 r/min and 7 N·m is a point the vibration energy is the maximum for  $\Omega < 700$  r/min.

Operating point (4) at 1000 r/min and 7 N·m is a point representing a average speed and average load operating point. It is a partial load condition, where the machine usually works.

Operating point (5) at 1500 r/min and 5 N·m is a point with maximum vibration energy when the speed is 1500 r/min. Since it is also a partial-load operating point (similar to (3)).

Operating points (6) and (7) are points with high speed, and low torque. Since the friction is considered in the machine model, for these two points the output electromagnetic torque is of 2 N·m. The switching losses of the inverter become important.

Here only two points are detailed, and the evaluation for all the points will be given later.

#### **Operating point (2): low speed high torque**

Figure 3.54 shows the TMC performance for low speed - heavy load conditions that correspond to the operating point (2) with  $\Omega^* = 200$  r/min and  $T_L = 16$  N·m. The turn-on angle is after the unaligned position to avoid producing negative output torque. However, due to the identical current shape near the commutation period (shown within the red-dash circle), there is a torque peak during that period. Meanwhile, when DFC&RCA is used (Figure 3.55), the peak torque is removed because the DFC is active in that period reducing the phase current and torque of the outgoing phase. The *torque ripple* is reduced from 22.7% (TMC) to 11% (DFC&RCA).

With respect to the *efficiency*, it has been increased by 0.7%. The different losses obtained with both control strategies are given in Table 3-5. It can be seen that the dominant

losses at this operating point are the copper losses and the converter losses because of the high RMS current value that generates high the high output torque.

Table 3-5 Losses comparison between TMC and DFC&RCA at  $\Omega^* = 200$  r/min and  $T_L = 16$  N·m.

	$P_{iron}$ (W)	$P_{copper}$ (W)	$P_{conv}$ (W)	Efficiency (%)
TMC	21.5	430	213.8	33.6%
DFC&RCA	19.6	425	201	34.3%

The iron losses ( $P_{iron}$ ), the copper losses ( $P_{copper}$ ) and the converter losses ( $P_{conv}$ ) are all reduced. Although the difference between the peak values of the phases currents is of 1A, the RMS current value obtained with the DFC&RCA is 0.27 A smaller than the RMS value obtained with the TMC (TMC -- 46.37A, DFC&RCA -- 46.1A). This reduces the DC component of both copper and converter losses. The RMS current value is decreased because the DFC works during the commutation period, which reduces the phase current. The iron losses are reduced mainly because the high-order harmonics of the phase current have been reduced (Figure 3.56) and the DFC&RCA peak value of the phase flux linkage ( $\lambda_{ph}$ ) is smaller than that of the TMC peak value as presented in Figure 3.57.

Considering the vibration acceleration, the results are presented in Figure 3.58. The maximum value of the acceleration near the mode 2 is reduced up to 52.4% due to the decrease of the radial force harmonic near the mode 2 (Figure 3.56), and the vibration energy within the audible frequency is decreased by 51%.

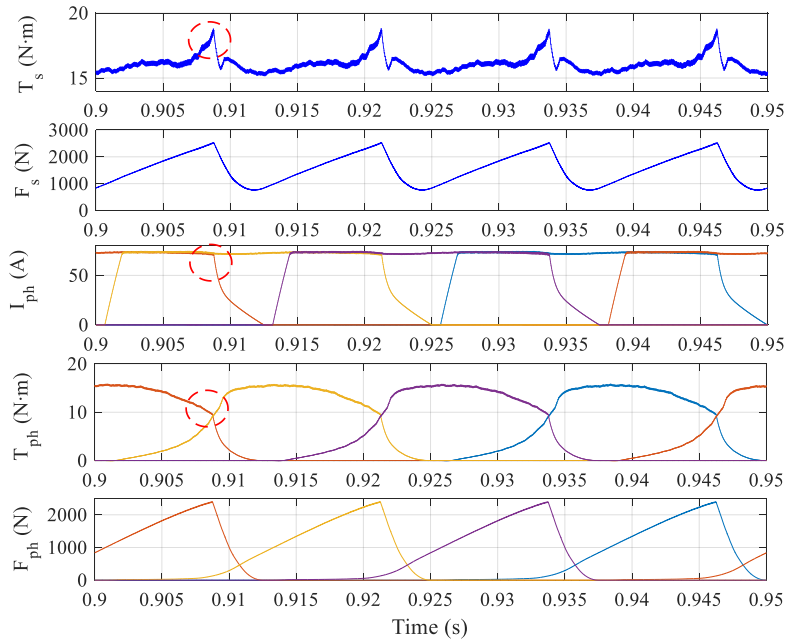


Figure 3.54 TMC: total torque, total force, phase current, phase torque and phase radial force of TMC at  $\Omega^* = 200$  r/min and  $T_L = 16$  N·m.

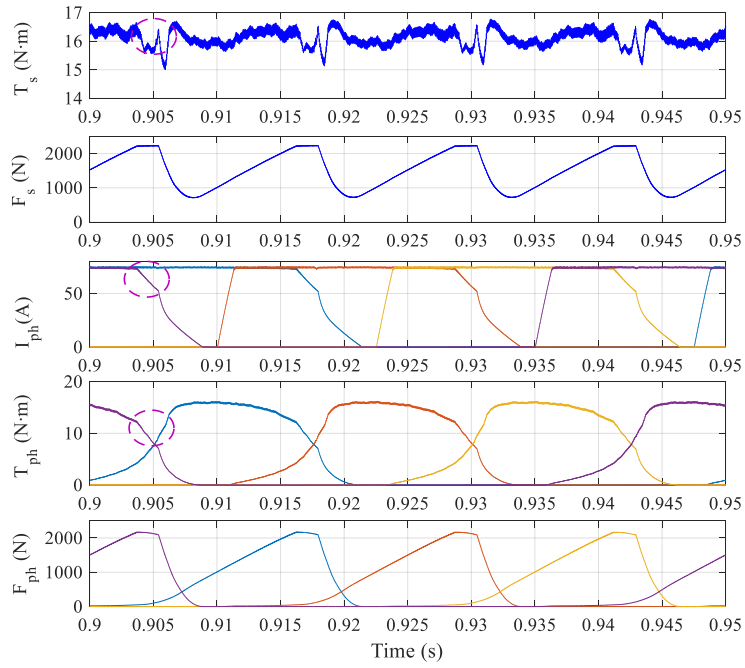


Figure 3.55 DFC&RCA: total torque, total force, phase current, phase torque and phase radial force at  $\Omega^* = 200$  r/min and  $T_L = 16$  N·m.

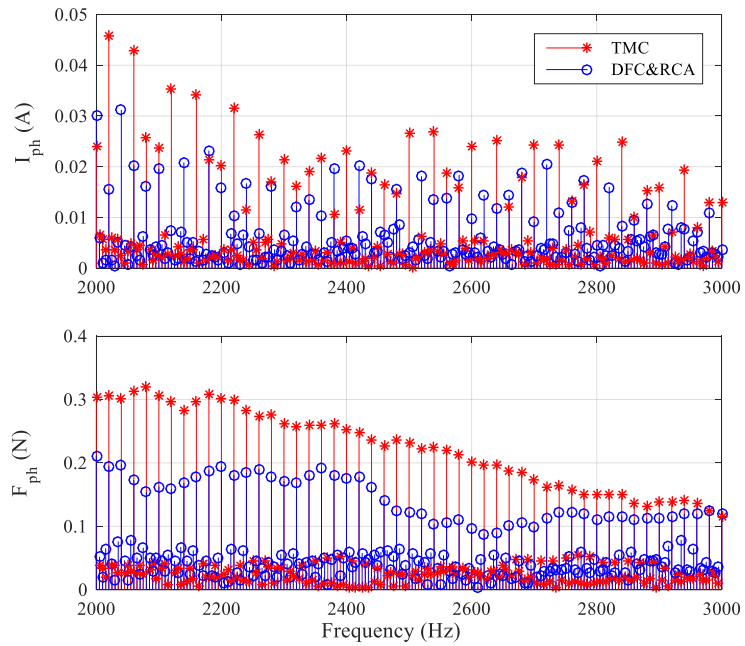


Figure 3.56 Comparison between TMC and DFC&RCA: phase current and radial force spectrum at  $\Omega^* = 200$  r/min and  $T_L = 16$  N·m.

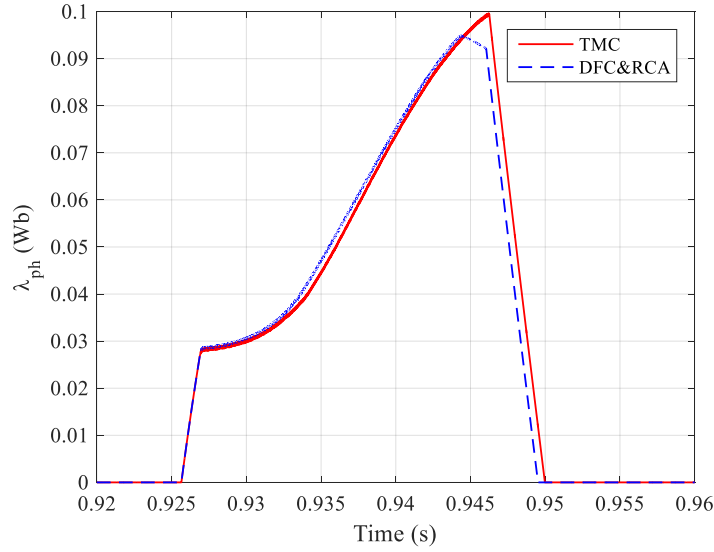


Figure 3.57 Comparison between TMC and DFC&RCA: phase flux linkage at  $\Omega^* = 200$  r/min and  $T_L = 16$  N·m.

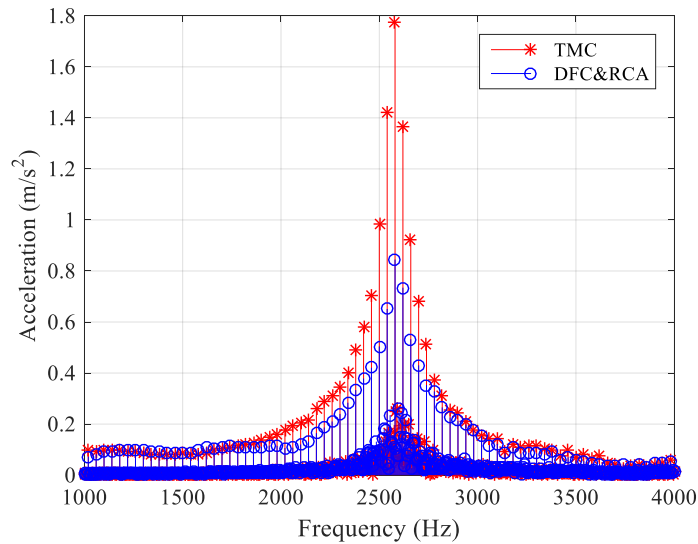


Figure 3.58 Comparison between TMC and DFC&RCA acceleration spectrum at  $\Omega^* = 200$  r/min and  $T_L = 16$  N·m.

### Operating point (5): high speed and middle torque

Figure 3.59 shows the TMC performance for high speed - average load conditions that correspond to the operating point (5) with  $\Omega^* = 1500$  r/min and  $T_L = 5$  N·m. The turn-on angle is before the unaligned position to produce a negative phase torque to compensate the phase torque peak of outgoing phase. However, due to the high EMF (consequence of the high speed), the current starts to decrease (within the purple-dash circle) even though the turn-off angle has not been reached, which reduces the phase torque. The high EMF also

slows down the increase of the incoming phase current, which limits the negative torque output of the incoming phase. The high EMF results in a slow current increase of incoming phase and a fast-current decrease of outgoing phase, which causes serious torque ripple. Meanwhile, when the DFC&RCA is used (Figure 3.60), this problem is aggravated because of the DFC is active (within the green-dash circle) within the commutation period, which reduces the phase torque further. Thus, comparing DFC&RCA with the TMC, the torque ripple is increased by 18.6 % at this operation point. However, at high speed the torque ripple has a high frequency and can be filtered by the moment of inertia of the drive train [18].

With respect to the efficiency, it has been increased by 0.6%. The losses are given in Table 3-6 for both control strategies. It can be seen that the dominant losses at this operating point are still the copper losses and the converter loss because of the high current values required to provide enough power. Again, the iron loss ( $P_{iron}$ ), the copper loss ( $P_{conv}$ ) and the converter losses ( $P_{conv}$ ) are all decreased.

Table 3-6 Losses comparison between TMC and DFC&RCA at  $\Omega^* = 1500$  r/min and  $T_L = 5$  N·m.

	$P_{iron}$ (W)	$P_{copper}$ (W)	$P_{conv}$ (W)	Efficiency (%)
TMC	40.6	198.2	153.9	69.8%
DFC&RCA	38.5	195.8	146.8	70.4%

Although the difference between the peak values of the phases currents is of 3A, the RMS current value obtained with the DFC&RCA is 0.19 A smaller than the RMS value obtained with the TMC (TMC--31.48 A, DFC&RCA--31.29 A). Thus, the DC component of both copper and converter losses is reduced. The RMS current value is decreased because the DFC works during the commutation period, which reduces the phase current. The iron losses are reduced mainly because with DFC&RCA the peak value of the phase flux linkage ( $\lambda_{ph}$ ) is smaller than the value obtained with the TMC (Figure 3.62) and the flux-linkage shape is smoother.

The results for the vibration acceleration are presented in Figure 3.63. The maximum value near the mode 2 is reduced up to 63%. However, the vibration at the frequency of 2850 Hz is higher with the DFC& RCA. This is caused by the low-order harmonics of the phase current shown in Figure 3.61 (green-dash circle). Within the pink-dash circle, the harmonics amplitude is higher for the DFC&RCA compared with the TMC. Since the current is

restricted by the RCA, the increase is limited. Thus, for this operation point the vibration energy is reduced by 72.2 %.

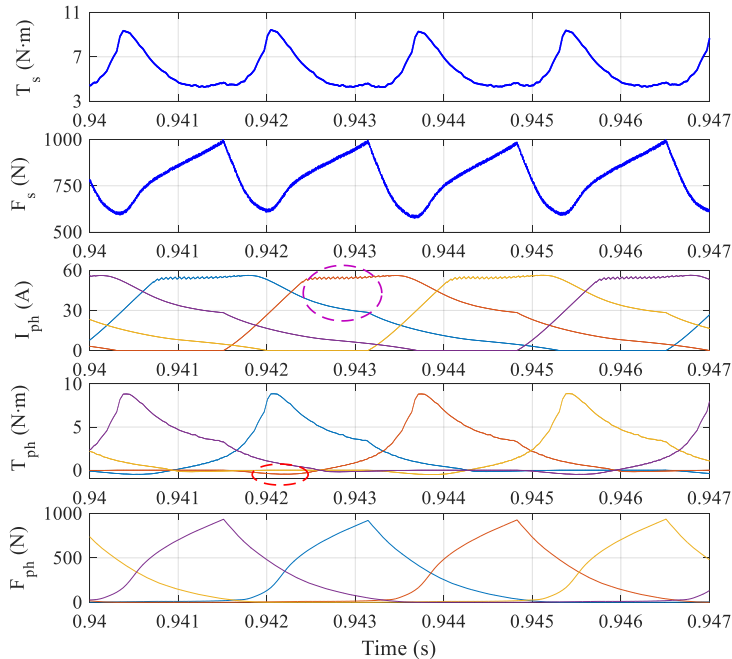


Figure 3.59 Total torque, total force, phase current, phase torque and phase radial force of TMC at  $\Omega^* = 1500$  r/min and  $T_L = 5$  N·m.

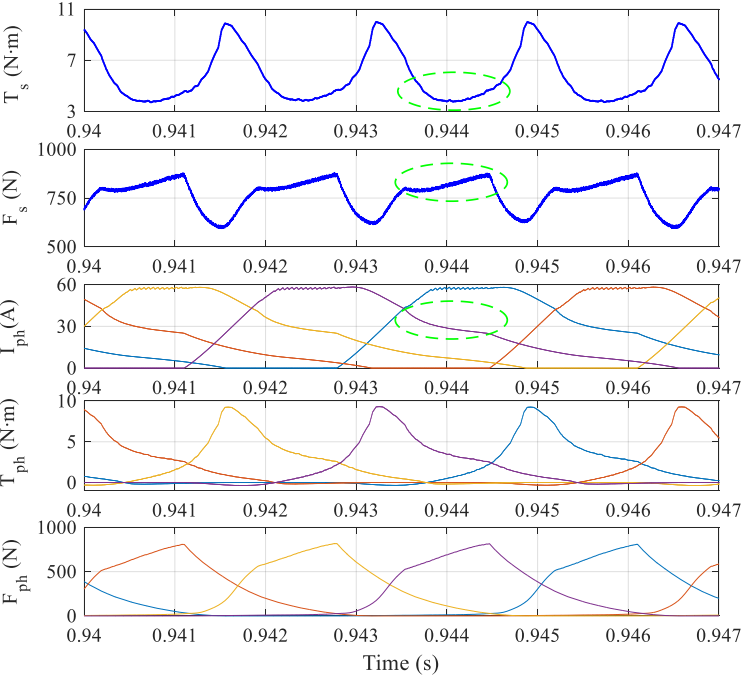


Figure 3.60 DFC&RCA: total torque, total force, phase current, phase torque and phase radial force at  $\Omega^* = 1500$  r/min and  $T_L = 5$  N·m.

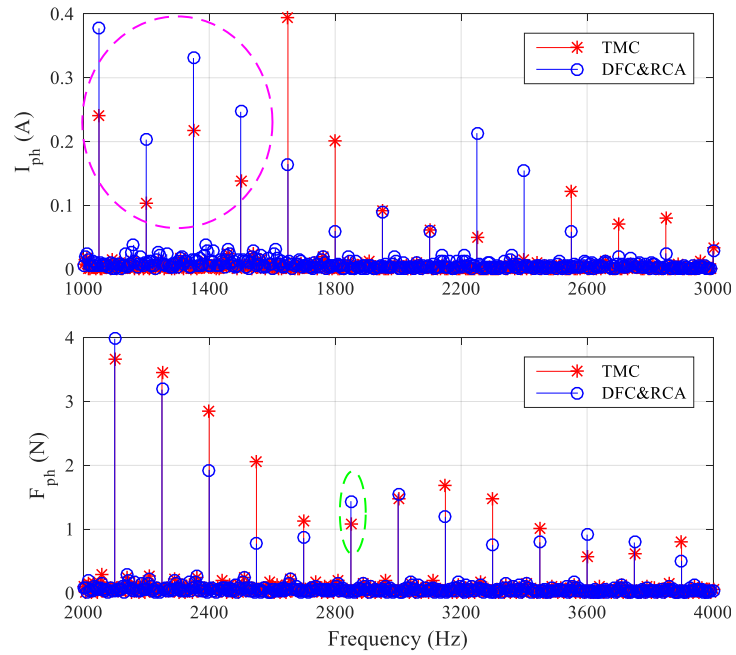


Figure 3.61 Comparison between TMC and DFC&RCA: phase current and radial force spectrum at  $\Omega^* = 1500$  r/min and  $T_L = 5$  N·m.

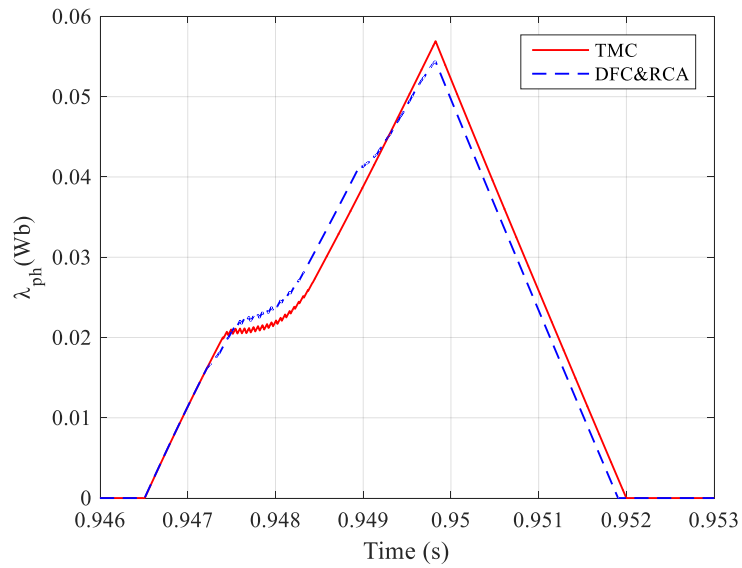


Figure 3.62 Comparison between TMC and DFC&RCA: phase flux linkage at  $\Omega^* = 1500$  r/min and  $T_L = 5$  N·m.

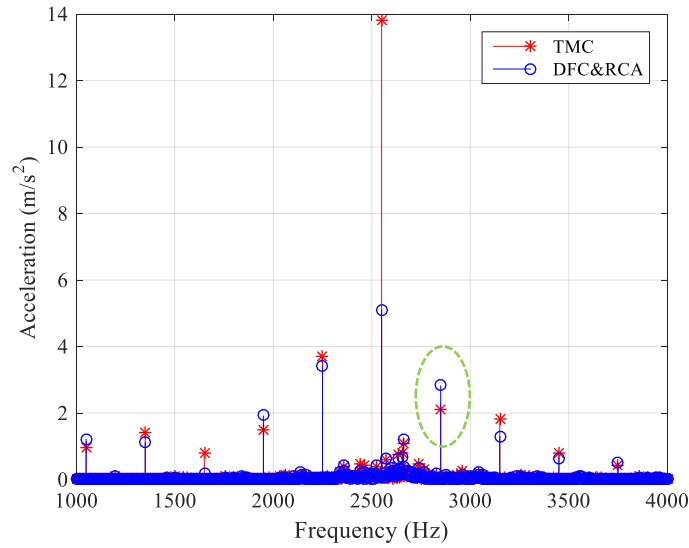


Figure 3.63 Comparison between TMC and DFC&RCA: acceleration spectrum at  $\Omega^* = 1500$  r/min and  $T_L = 5$  N·m.

Table 3-7 Performance evaluation for different operating points.

Operating Point	$P_{iron}$ (W)		$P_{copper}$ (W)		$P_{conv}$ (W)		Efficiency (%)		$\Delta \gamma$ (%)	$\Delta W$ (%)
	TMC	DFC&RCA	TMC	DFC&RCA	TMC	DFC&RCA	TMC	DFC&RCA		
200 r/min, 7 N·m	17.9	15.5	135.2	135.3	102.8	110.3	36.8	36.3	-7.6	51.9
200 r/min, 16 N·m	21.5	19.6	430	425	213.8	201	33.6	34.3	-11	51
700 r/min, 7 N·m	39.7	32.9	175.6	182.9	143.3	150	60.1	59.6	+7.8	43.7
1000 r/min, 7 N·m	43.1	38.9	218.2	229.5	161.6	181.1	65.1	63.7	+10.8	65.2
1500 r/min, 5 N·m	40.6	38.5	198.2	195.8	153.9	146.8	69.8	70.4	+18.6	72.2
1800 r/min, 1.1 N·m	30.8	28.4	58.3	58.1	71.4	77.3	70.6	70.1	+7.8	50.2
2700 r/min, 0.7 N·m	32.5	31.6	66.9	69.9	76.6	78	77.2	76.9	+11.5	34

Table 3-7 compares the TMC and the DFC&RCA performances for the investigated operating points using different criteria: losses, efficiency, torque ripple and energy vibration. The following conclusions are drawn:

- The iron losses for DFC&RCA are always smaller than the ones for TMC for all the considered points, which is more obvious in the middle speed and middle torque

(there is a reduction of 17.1% for  $\Omega^* = 700\text{r/min}$  and  $T_L = 7\text{ N}\cdot\text{m}$ ).

- The DC copper losses are almost similar due to the RCA, which limits the current level. However, the converter losses are increased except the operating points (2) and (5). The main cause is the relatively high switching frequency of the DFC&RCA.
- The DFC&RCA has a small effect on the efficiency.
- The torque ripple is reduced when the speed is low because the DFC reduces the phase torque output of the outgoing phase, which removes the peak torque. However, the torque ripple is increased when the speed is high. This happened also because the DFC reduces the phase torque output of the outgoing phase. However, it makes the concave part of the total torque deep, which deteriorates the torque ripple. The main difference between the two conditions is the generated total torque: when the speed is low, the excited phases can provide a higher total torque than the load torque during the commutation period. On the other hand, when the speed is high, the current starts to decrease before the turn-off position due to the EMF, which limits the provided phase torque. In this case, the excited phases fail to provide a total torque equals to the load torque. Thus, when the total torque is higher than the load torque, the DFC reduces the outgoing phase torque to reduce the torque ripple. Nevertheless, the DFC deteriorates the torque ripple when the total torque is lower than the load torque, because the DFC always reduces the outgoing phase torque during the commutation period.

### 3.4 Conclusion

Two different vibration reduction control strategies have been introduced in this chapter. The first one is an enhanced vibration reduction method with an improved turn-off angle control (IVTC): it introduces a uniformly random distributed signal to the sinusoidal-varying turn-off angle to reduce the harmonic components near the frequency and its multiple of the sinusoidal function. The frequency of the sinusoidal function is determined based on the mechanical property of switched reluctance machine. Simulation results show that this

method can reduce the vibration energy up to 60.5% when the speed is low without sacrificing the efficiency and penalizing the torque ripple too much. Nevertheless, its performance decays when the speed is high. However, this can be compensated by increasing the magnitude of turn-off angle variation.

The second control method presented in this chapter is the DFC&RCA. It is an improved control method based on DFC, which is proposed as a solution for the vibration reduction aiming to provide a smooth sum of radial forces. However, the DFC cannot be used alone because it increases the torque ripple due to the absence of the current limitation. Thus, a reference current adapter is proposed to assess the torque and radial force variations in order to obtain an auto-tuning current reference. Then, the effect of the control parameters in the DFC&RCA is investigated to offer a basic tuning procedure for this control strategy. Next, the DFC&RCA is evaluated from the aspects of efficiency and torque ripple. It shows that the DFC&RCA can reduce the torque ripple when the speed is low but deteriorates the torque ripple when the speed is high because the DFC works during the commutation periods. For seven investigated operating points, the DFC&RCA reduces the iron losses compared to the TMC, because the DFC&RCA naturally yields lower amplitudes of flux linkage. Regarding the efficiency, the DFC&RCA is competitive with the TMC, the DFC&RCA even increases the machine efficiency at low speed with heavy load. Besides, the maximum vibration energy reduction is up to 72.2% that proves the potential of the proposed control strategy.

# Chapter 4 Experimental Validation of DFC&RCA: Application to SRM

In this chapter, the new vibration reduction control, named DFC&RCA (as shown in Figure 4.1), which was presented and analyzed through simulations in Chapter 3, is validated experimentally on a 8/6 pole 4-phase SRM. An architecture based on a hardware/software partitioning is proposed to make full use of both microprocessor and Field-Programmable Gate Array (FPGA) resources. The less time-sensitive controller (speed controller) and the complex arithmetic operations (divisions and square roots) are implemented using a microprocessor, whereas the controllers requiring high sampling time and fast dynamic response (i.e. the current controller and DFC) are implemented in an FPGA.

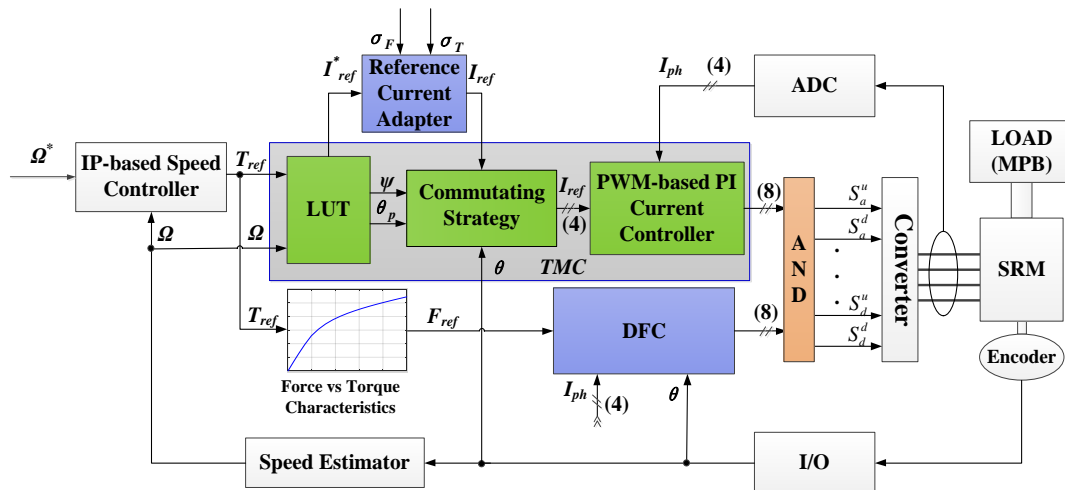


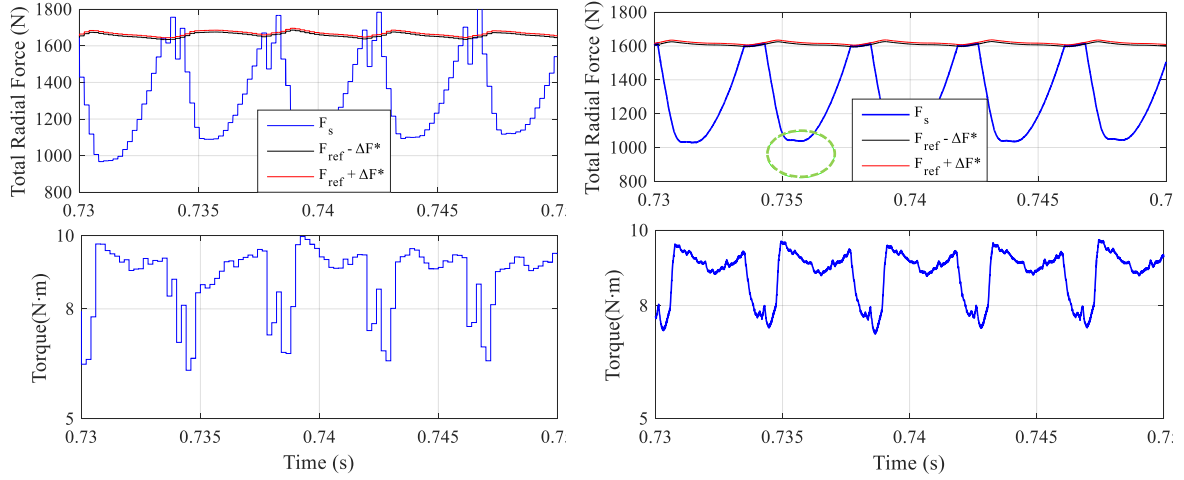
Figure 4.1 Structure of the vibration reduction controller -- DFC&RCA.

## 4.1 Design Implementation of the Control Strategy

### 4.1.1 Influence of the Sampling Time

To evaluate the impact of sampling period on control performance, at first, the DFC&RAC is simulated with two different sampling times of  $5 \mu s$  and  $200 \mu s$ , respectively. Because of its complex structure and large-scale data saved in the LUT, the maximum sampling time of the microprocessor is  $200 \mu s$ . However, it is possible to implement the same

control with a sampling time of  $5 \mu\text{s}$  in the case of FPGA implementation due to its high-speed computation ability with parallelism. The simulation results are shown in Figure 4.2.



(a) Microprocessor implementation with a sampling time of  $200 \mu\text{s}$  (b) FPGA implementation with a sampling time of  $5 \mu\text{s}$

Figure 4.2 Simulation results for the DFC&RCA implemented with different sample times ( $T_{samp}$ ): (a)  $200 \mu\text{s}$ , (b)  $5 \mu\text{s}$ .

In Figure 4.2 (a) and (b), the upper figures present the total radial force  $F_s$ , and the lower ones give the electromagnetic torque  $T_s$ . According to the results, the total radial force  $F_s$  in Figure 4.2 (a) always exceeds the hysteresis bandwidth due to the high computation time of the software implementation. Meanwhile, the radial force in Figure 4.2 (b) emulates the reference  $F_{ref}$  properly within the bandwidth  $[-\Delta F^*, \Delta F^*]$ . It should be noted that, the concave region in the green dot line in Figure 4.2 (b) is caused by the current limitation used to reduce the torque ripple. With this controller, the vibration and torque ripple reduction are balanced as introduced in Chapter 3. Comparing the results of lower figures in Figure 4.2 (b) and Figure 4.2 (a), the torque ripple has been reduced up to 16%. The interest of the  $5 \mu\text{s}$  sampling time is then obvious.

## 4.1.2 Development of the Hardware/Software Partitioning Control System

### 4.1.2.1 DFC&RCA Control System Partitioning

According to the simulation results shown in Section 4.1.1, the performance of the control system implemented in FPGA with a sampling time of  $5 \mu\text{s}$  is better than that implemented in microprocessor: the torque ripple is reduced, and the hysteresis controller

(DFC) can work properly within the given bandwidth. However, the implementation of the whole control system in FPGA is resource-consuming. Moreover, if the control objective changes, the LUT in Figure 4.1 needs to be replaced (here, the look-up table stores control parameters that minimize the torque ripple for different operating points). Updating the stored LUT in the FPGA is also time-consuming. Besides, the mechanical time constant is higher than the electrical time constant for an electric machine. Hence, it is more suitable to implement the speed controller and the look-up table in a microprocessor. Thus, a hardware/software partitioning control system is proposed considering the system performance, the resource consumption and the design flexibility. The LUT used for torque ripple minimization and the speed controller are implemented in the microprocessor, meanwhile, the current controller and DFC are implemented in FPGA. Therefore, the controller is decomposed into three blocks with different sampling times as shown in Figure 4.3.

- The first block estimates the rotor speed  $n$  from the measured position  $\theta$ . Then, it computes the reference current  $I_{ref}^*$  and the angles  $(\psi, \theta_p)$  with LUT1, and predicts the parameters  $(K_i, K_p)$  of the PI current controller for each phase with LUT2. These parameters  $(K_i, K_p)$  are adapted as they are dependent on the position and the phase current, as shown in Section 3.1.2. Finally, the block calculates the variations  $\sigma_T$  and  $\sigma_F$  of the torque and radial forces using equations (3.18) and (3.19). Based on the values of  $\sigma_T$  and  $\sigma_F$ , the current reference  $I_{ref}$  is updated following the rules introduced in Section 3.2.5. In this block, all the computations are performed with a sampling time equal to  $200 \mu s$ , which is the limitation of the Microprocessor system.
- The second block is represented by the current controller. It supplies the voltage reference to be compared to the PWM signal in order to generate control signals for the converter so that the actual current  $I_{ph}$  can emulate the reference value  $I_{ref}$ . The sampling time is  $50 \mu s$  considering both the stability and the current regulation performance.
- In the third block, the data acquired from the current sensor and the position encoder

are sent to the F-LUT3 (LUT of radial force) to estimate the total radial force  $F_s$ . The inner structure of the F-LUT3 is shown in Figure 4.4 (some details are given in the next section to explain the factorization of the LUT3). Then, the force reference  $F_{ref}$  computed in the microprocessor and the estimation of the total radial force  $F_s$  from FPGA are compared to implement the DFC. The sampling time of this block is of  $5 \mu s$  considering the current disturbance from the MOSFET switching and the bandwidth requirements of the DFC.

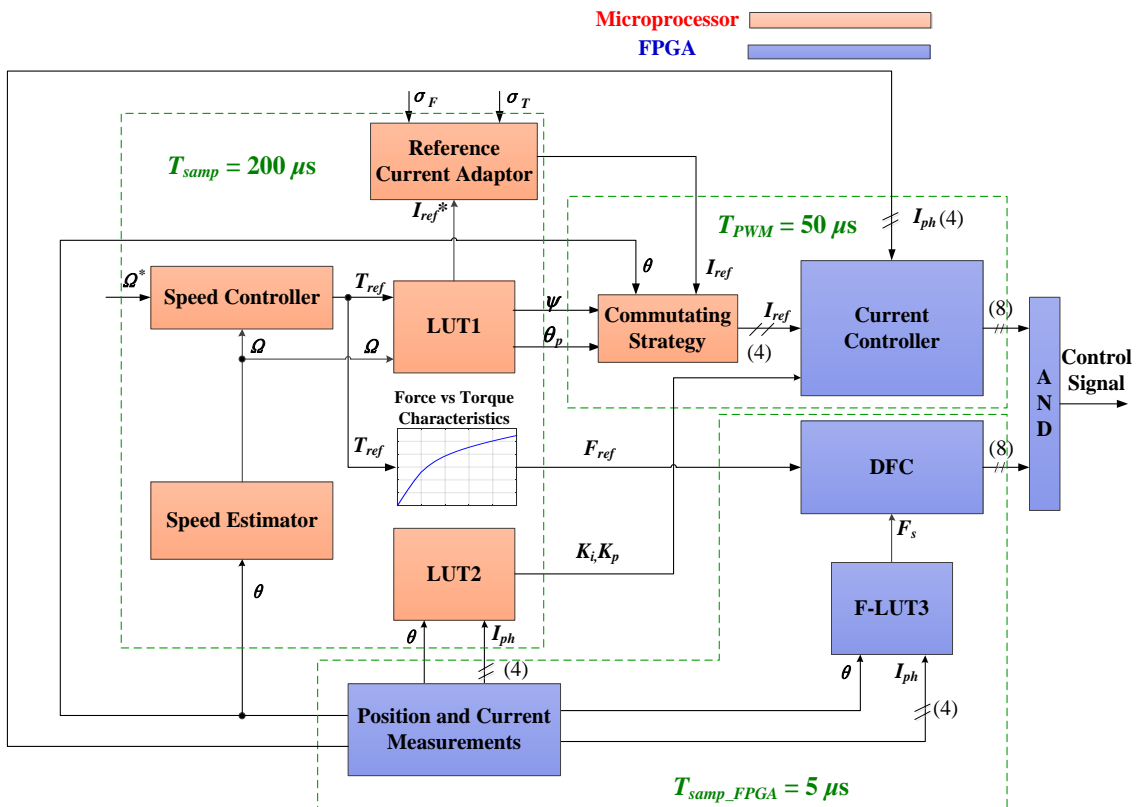


Figure 4.3 Architecture of the DFC&RCA system using hardware/software partitioning.

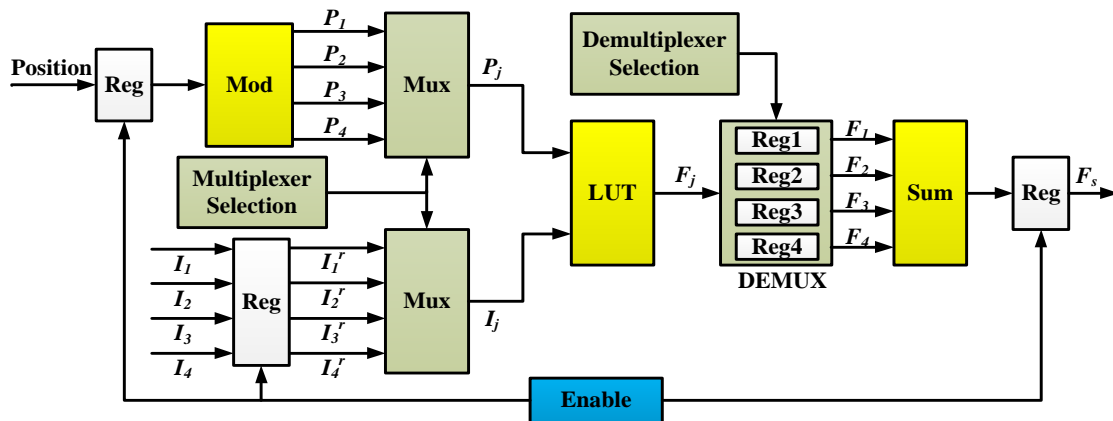


Figure 4.4 Schematic diagram of the factorization of the F-LUT3

#### 4.1.2.2 Implementation of the Hardware/Software Solution

a) Software Part:

In order to simplify the control implementation process, the speed estimation, the speed controller, the current reference adapter and the look-up tables LUT1 and LUT2 are implemented in the microprocessor because of their slow dynamic requirements and design flexibility. Moreover, the complex arithmetic operations such as division and square root are also executed in the microprocessor to reduce the resource consumption in FPGA.

b) Hardware Part

The anti-windup PI current controller is implemented in FPGA. The coefficients  $K_i$ ,  $K_p$  of the PWM-based PI controller are adapted due to the highly non-linear behavior of the SRM inductance. It adopts a carrier-based PWM to generate switching signal to drive the current to its reference value.

In addition, LUTs estimating the total torque and the radial force are built in FPGA by means of linear interpolation. The Block RAM in FPGA is used to store the data of radial force and torque profiles obtained from FEM. One LUT has two 61x81 matrices with 11041 elements. Since there are four phases for this SRM and two LUTs are required for each phase to get the total torque and radial force, 88328 elements should be saved in the RAM. To reduce the resource consumption in FPGA, a factorized architecture is proposed to calculate the sum of the forces (the same procedure is used for the torque computation) with just one LUT for four phases as shown in Figure 4.4. The factorization allows to reduce the consumed resources on the RAM in FPGA by 75%. In Figure 4.4, the position encoder gives only one position at each sampling time. The modulus function is then adopted to generate four different relative positions  $P_1, P_2, P_3, P_4$ . Both four position signals and the current signals are selected by the multiplexer selection signal, which is carried out by a 2-bit counter counting from 0 to 3. Thus, one of the inputs from 1 to 4 is selected at each time instant. Then, the chosen signals  $P_j$  and  $I_j$  are sent to the LUT to compute the corresponding phase radial force  $F_j$ . With the demultiplexer selection signal, the input signal  $F_j$  is split into four output signals ( $F_1, F_2, F_3, F_4$ ) using four registers. In fact, the demultiplexer selection signal is a

group of trigger signals used to enable data saved in these registers to be updated. To synchronize the entire progress, a register is placed in front of each input and output signal and is controlled by an enable signal.

Equations (3.18) and (3.19) are also implemented in FPGA for a better computation accuracy. A method to compute the mean value and mean square value by numerical integration is proposed, that is based on the position signal. The mean value of torque can be expressed as:

$$T_{avg} = \frac{1}{T_c} \int_0^{T_c} T_s(t) dt \quad (4.1)$$

Since the electrical cycle time  $T_c$  changes with speed, it is more convenient to use the position signal to replace the time dependence. Then equation (4.1) can be rewritten as:

$$T_{avg} = \frac{1}{\theta_e} \int_0^{\theta_e} T_s(\theta) d\theta \quad (4.2)$$

where  $\theta_e$  is the electrical position period, with  $\theta_e = 6\theta_m$ , and  $\theta_m$  is the mechanical position period. Following the rectangular method of numerical integration, equation (4.2) is calculated as:

$$T_{avg} = \frac{1}{N_p} \sum T_s(N_\theta) \quad (4.3)$$

where  $N_p$  is the total number of positions per electrical cycle. Since the resolution of adopted position encoder is of  $0.1^\circ$ ,  $N_p$  equals 600,  $N_\theta$  is the rank of the estimated position that varies from 0 to 599.

Thus, the structure of this calculator is shown in Figure 4.5. The estimated torque is sent to an accumulator to get the sum of the torque  $T_s$  in an electrical cycle. The multiplier (the Gain block in Figure 4.5) is updated when one cycle is completed (i.e. when  $N_\theta$  is equal to 599). The mean square value can also be calculated with the blocks in Figure 4.5 by replacing  $T_s$  with  $T_s^2$ .

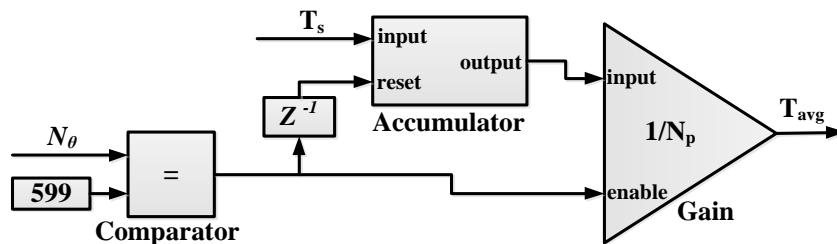


Figure 4.5 Schematic diagram of the square mean value calculator

In terms of FPGA resources consumption, the hardware part occupies 23% of the slices, 29% of the Block RAM and 7% of the DSP48Es.

### 4.1.3 Synchronous Signal Producer

Since the DFC&RCA is implemented in a hybrid way, there are three blocks with different sampling times. Thus, it is necessary to synchronize the signals from different blocks. However, due to the absence of an internal clock signal for FPGA, a counter is used, whose sampling time  $T_{sf}$  is  $10^{-8}$  s.

As referred in Section 4.1.2.2, a carrier-based PWM is adopted using a triangle signal of 20kHz (it is equal to the frequency of the PWM,  $f_{PWM}$ ) as carrier signal. This triangle is produced by two counters, a constant, a comparator and a multiplexer as shown in Figure 4.6. There is one increasing counter (Counter1) and one decreasing counter (Counter2). Comparing the signal of Counter1 to a constant signal, whose value is equal to  $1/(2T_{sf}f_{PWM}) - 1$ , a selection signal is produced and sent to the multiplexer. Moreover, a PI synchronous producer is designed to activate the PI controller with a frequency of 20 kHz.

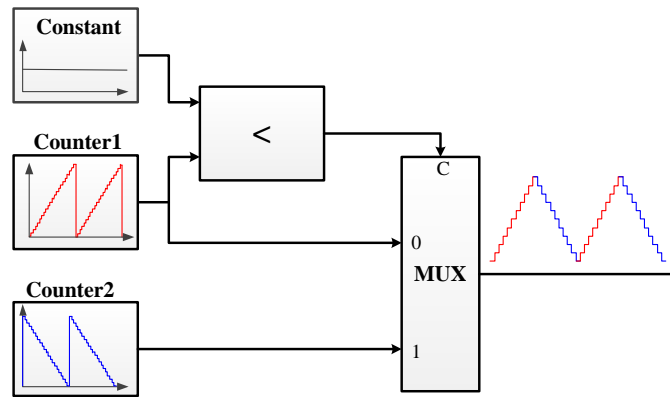


Figure 4.6 Structure of the triangle producer.

There are six A/D channels on the FPGA board adopted. Four channels are used to obtain the digital phase currents from the analog current sensors. Moreover, the A/D synchronous producers are able to work at a frequency of 200 kHz.

Because a block containing less time-sensitive systems and complex calculation process is implemented in the microprocessor, an interrupt synchronous signal is required to enable

transmit data between the microprocessor and FPGA with a frequency of 5 kHz.

## 4.2 Experimental Tests

### 4.2.1 Test Bench Set-up

Once the implementation design is completed, the proposed vibration reduction control strategy (DFC&RCA) is evaluated by experimental tests using a 8/6 SRM prototype. The FPGA board is used combined with the DS1104 controller board equipped with a Power PC750GX Microprocessor produced by IBM. The FPGA board features the Xilinx Virtex-5 FPGA running at 100 MHz, with 6 ADC and 16 digital I/O channels. The microprocessor has a CPU frequency of 1 GHz and level-2 cache of 1MB. The FPGA board is connected to the processor board via PHS (Physical High Speed) bus. An optical fiber cable connects the PC and the dSPACE processor board. An incremental encoder is mounted on the rotor shaft to detect the rotor position. The phase current is measured by Hall-effect current sensor. Both signals (position and current measurements) are sent to FPGA to be used for DFC and the current control, and then transmitted to the microprocessor to select the corresponding PI parameters based on LUT2. The load is applied using a magnetic particle brake (MPB), which can be controlled via ControlDesk. The test bench is presented in Figure 4.7. The acceleration data is acquired with an accelerometer (PZT) located over A-phase tooth, in the middle of the axial lamination (see Figure 4.7). The accelerometer is MMF KS76C IEPE (102.11 mV/g) with MMF M32 conditioner. The noise is measured with a microphone which is placed near the test bench at a distance close to 20 cm.

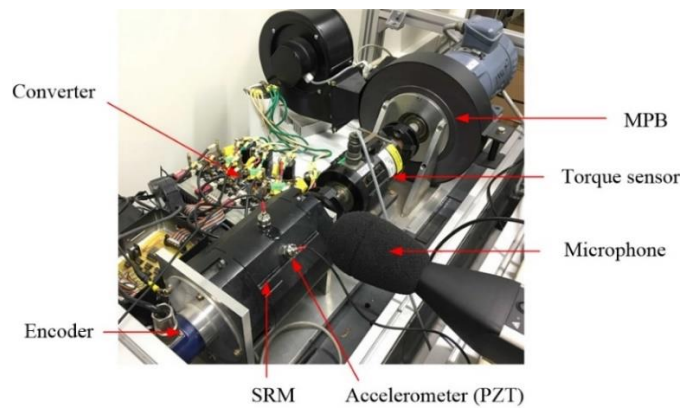


Figure 4.7 Setup of the test bench.

## 4.2.2 Background Noise Measurement

Actually, the noise measured from the machine is composed by noise from the SRM itself and background noise (e.g. noise from the power supply, MPB and environment). All of these sources of noise have an influence on the noise measurements. To distinguish the background noise, it is measured firstly when the SRM is stanstill.

### 4.2.2.1 Environment Noise Measurement

When measuring the background noise from the environment, the MPB and power supply are turned off, and the SRM is static. The microphone is placed the same position where to measure the noise of the SRM. The test results are presented in Figure 4.8. It can be seen that this kind of noise is mainly distributed in a low frequency range, below 70 Hz. The measured Sound Pressure Level (SPL) is about 33.6 dB.

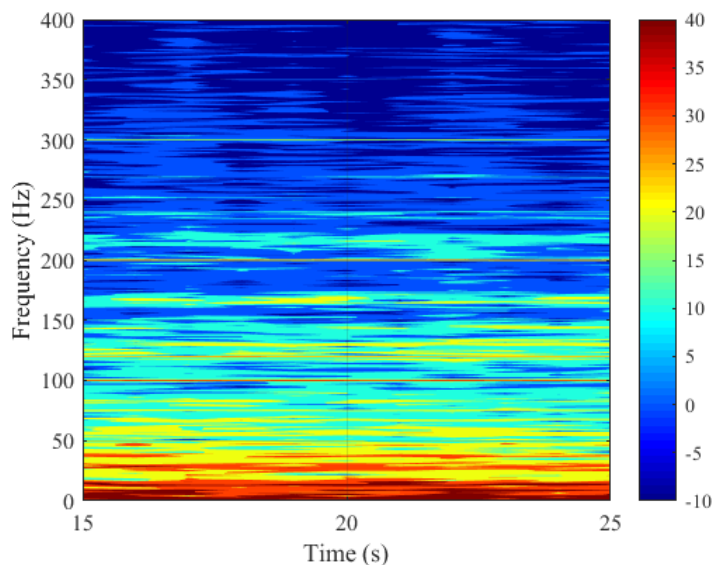


Figure 4.8 Measurement results of the background noise from the environment.

### 4.2.2.2 MPB Noise Measurement

When the noise from MPB is measured, only the MPB is turned on and the SRM does not run yet. The test results are presented in Figure 4.9. According to the experimental results, there exist two dominant frequencies for MPB, which are of 540 Hz and 670 Hz, respectively. Furthermore, the noise from MPB is mainly distributed in the range from 400 Hz to 700 Hz. The measured SPL is 48 dB. Therefore, the acoustic noise increases by 14.4 dB because of

the MPB.

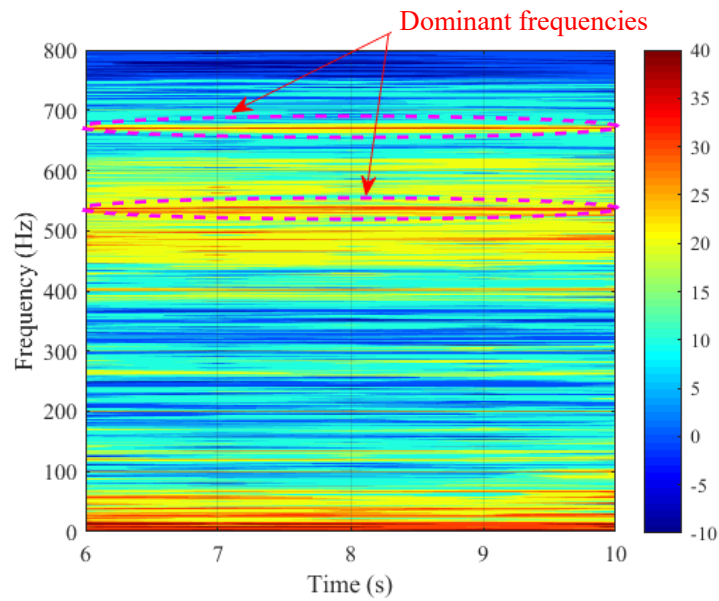


Figure 4.9 Measurement results of the background noise from the MPB + environment.

### 4.2.2.3 Power Supply Noise Measurement

Regarding the noise from the power supply, it is more complicated to measure than the previous two types of noise, because it varies with the output power. Since the SRM is supplied with a constant voltage of 24 V, the output power of the power supply changes with the current. To investigate the effect of the current variation on the noise, a resistor load is connected to the power supply (as shown in Figure 4.10) so that the current is controllable without introducing additional noise. The experimental results of different current values ( $I_{sup}$ ) are given in Figure 4.11. From these results, it is obvious that, there is a dominant noise frequency for power supply. Moreover, this dominant frequency value increases (400 Hz - 420 Hz - 470 Hz) with the increase of the current output. That is because while the current increases, the fan from the power supply rotates faster to cool the system. Besides, the noise from the power supply distributes in a wide frequency range and is significant when the current is high. As shown in Figure 4.11 (c), the SPL is up to 58 dB near its dominant frequency when the supplied current  $I_{sup}$  is 37 A.



Figure 4.10 Set-up of power supply noise measurement

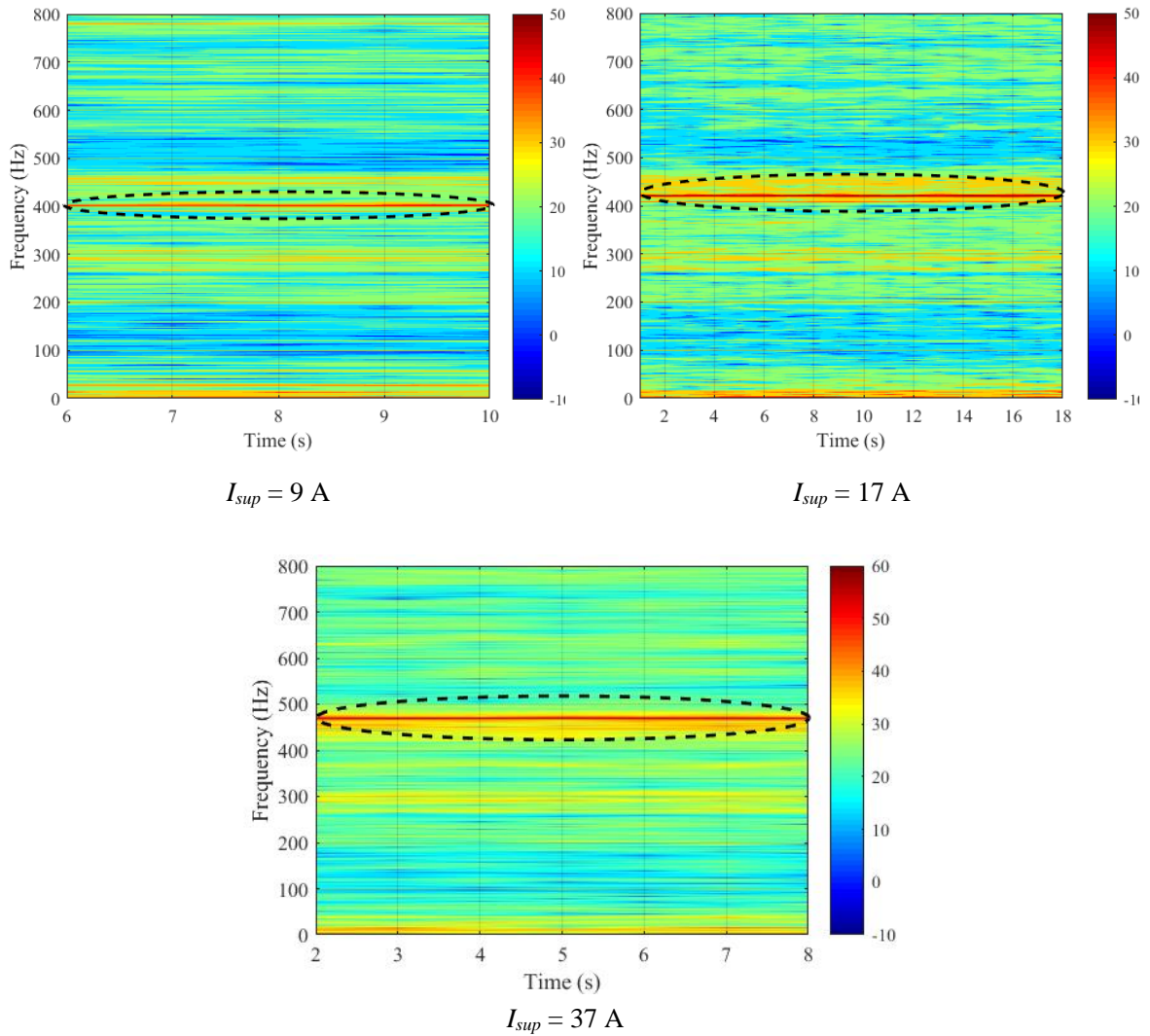


Figure 4.11 Measurement results of the background noise from power supply for different current values.

### 4.2.3 Stable State Experiments

Firstly, TMC and DFC&RCA are implemented respectively. The experimental results are compared when the speed is stable, which means that the actual speed is equal to the reference speed. The transient curve of the current is measured by the current sensor, the vibration is measured by the accelerometer and the curves of the total radial force and torque are estimated in FPGA. All of them are sent to a four-channel oscilloscope for saving.

The experimental results of the closed-loop system, the phase current, the sum of radial forces and the electromagnetic torque are illustrated in Figure 4.12 for a reference speed  $\Omega^*$  of 600 r/min with a load torque  $T_L$  of 8 N·m. According to the results, the currents of DFC&RCA and TMC have close root mean square values: 30.5 A (TMC) and 30.8 A (DFC&RCA), which means their DC copper losses are identical. In Figure 4.12 (c), the proposed control method generates a smaller minimum torque than the TMC due to DFC, which increases the torque ripple of 2.55%. However, both control strategies produce the same mean torque. Moreover, the efficiencies of the two methods both are 56.7%.

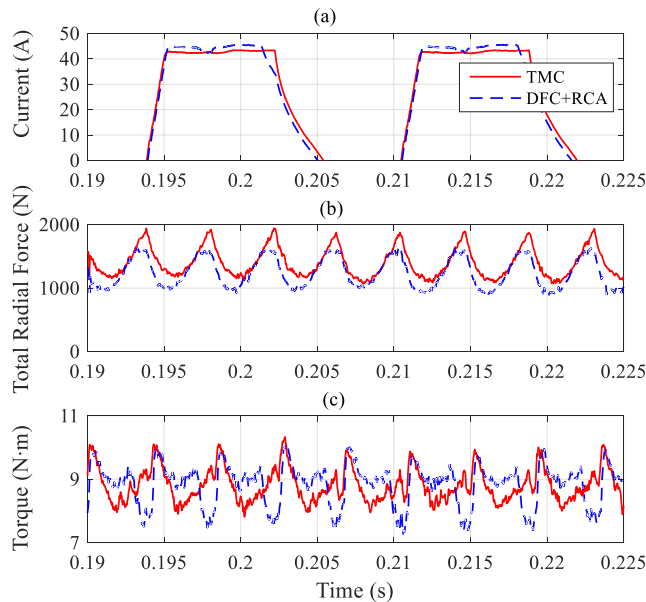


Figure 4.12 Experimental results at  $\Omega^* = 600$  r/min and  $T_L = 8$  N·m.

Figure 4.13 shows the corresponding experimental results for the vibration acceleration spectrum. The spectral analysis shows a significant vibration reduction. The maximum vibration value near its natural frequency has been reduced by 8.4 dB. Moreover, the

vibration has been reduced in a wide range since the vibration energy has decreased up to 56.08%. Figure 4.14 shows the spectrum of the measured SPL. The acoustic noise has been reduced by 7.1 dB near the natural frequency. As presented in Chapter 3, the dominant mode of the investigated SRM is mode 2, whose frequency is near 2600Hz, so only the results in the frequency range of [500, 5000]Hz is shown here.

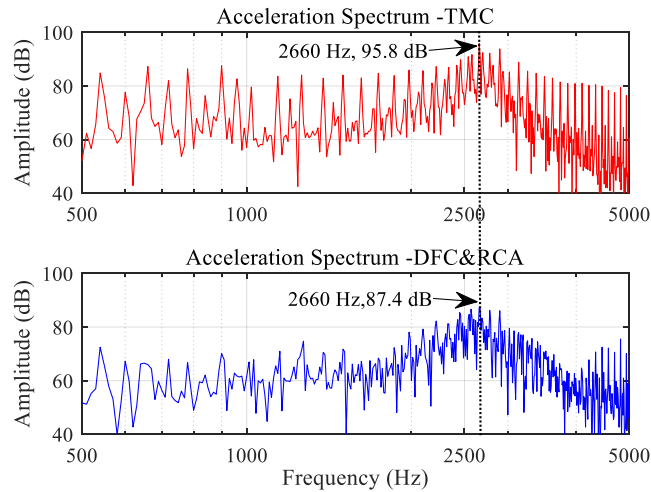


Figure 4.13 Experimental results of the vibration acceleration at  $\Omega^* = 600$  r/min and  $T_L = 8$  N·m.

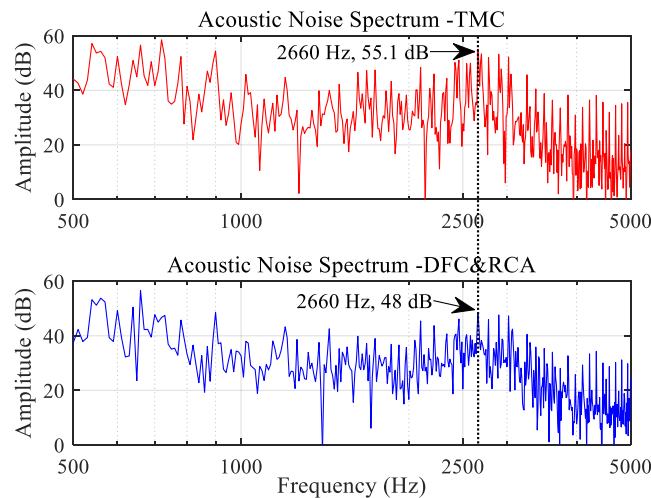


Figure 4.14 Experimental results of acoustic noise at  $\Omega^* = 600$  r/min and  $T_L = 8$  N·m.

Figure 4.15 presents the SRM performance for a reference speed  $\Omega^*$  of 1000 r/min and a load torque  $T_L$  of 2 N·m. The currents of DFC&RCA and TMC have close root mean square values, 16.7 A (TMC) and 16.9 A (DFC&RCA), so that the copper losses are quite identical. The torque ripple has been increased by 6% because the DFC causes a concave part of the torque shown in Figure 4.15 (c). Besides, the system efficiencies with both methods are 76.2%.

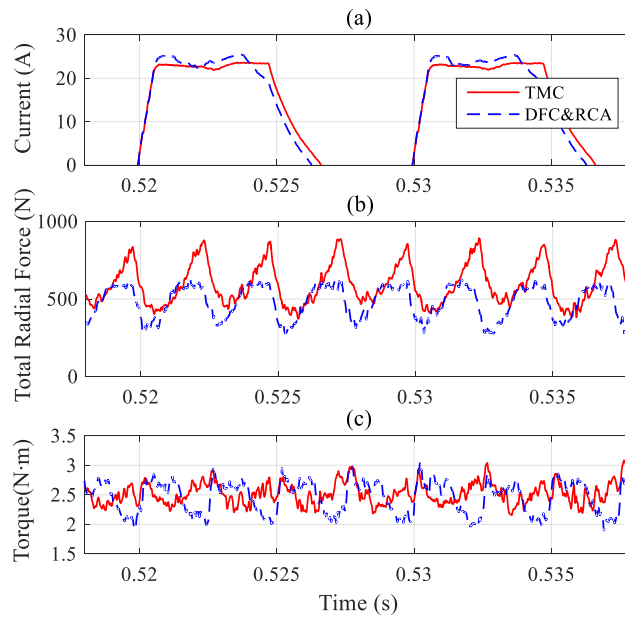


Figure 4.15 Experimental results at  $\Omega^* = 1000$  r/min and  $T_L = 2$  N·m.

In Figure 4.16, the corresponding vibration acceleration spectrum is presented. The maximum vibration value near its natural frequency presents a reduction of 17.9 dB. Moreover, the vibration has been reduced in a wide frequency range according to the comparisons. It shows a vibration energy reduction of 59.3%. The spectrum of the measured SPL is presented in Figure 4.17 showing a reduction of 13.7 dB near the natural frequency.

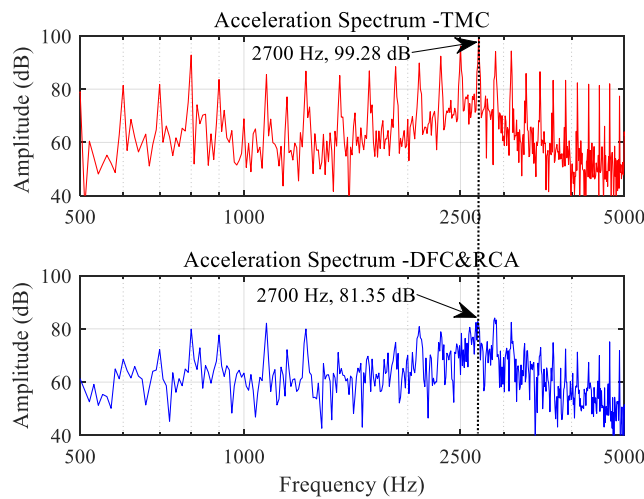


Figure 4.16 Experimental results of vibration acceleration at  $\Omega^* = 1000$  r/min and  $T_L = 2$  N·m.

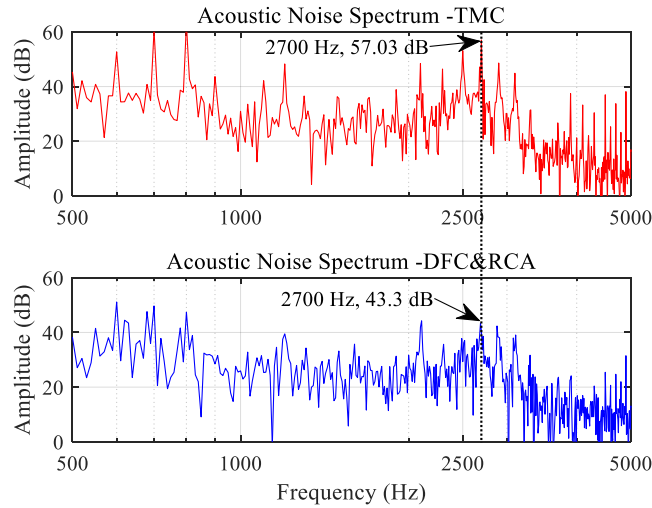


Figure 4.17 Experimental results of acoustic noise at 1000 r/min and  $T_L = 2 \text{ N}\cdot\text{m}$ .

Figure 4.18 illustrates the SRM behavior for a reference speed  $\Omega^*$  of 2000 r/min and a load torque  $T_L$  of 0.6 N·m. The peak value of the current is still bigger than the one generated by TMC. However, the current of DFC&RCA within the green dash circle (shown in Figure 4.18 (a)) is smaller than that of TMC because DFC aims to obtain a smooth total radial force. Thus, for both control approaches, the RMS values are identical (TMC -- 9.8 A, DFC&RCA -- 9.8 A). Moreover, the measured drive system efficiencies are both of 56.1%.

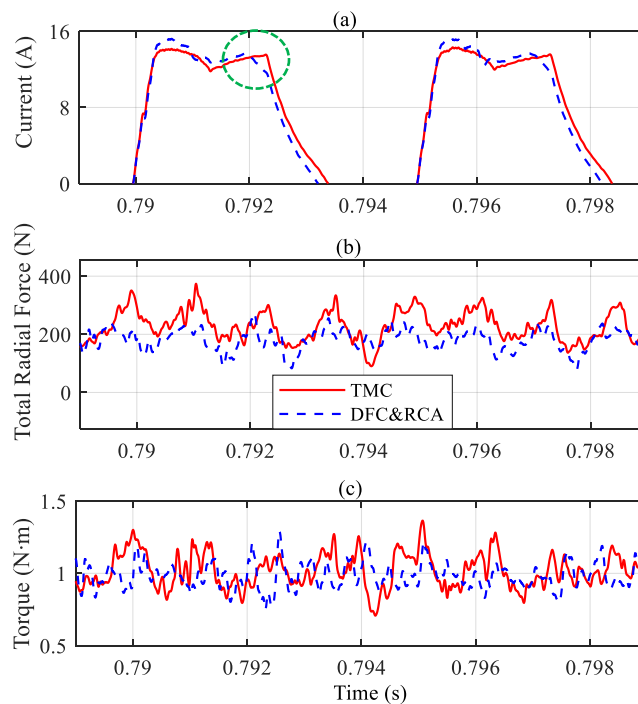


Figure 4.18 Experimental results at  $\Omega^* = 2000 \text{ r/min}$  and  $T_L = 0.6 \text{ N}\cdot\text{m}$ .

The relevant vibration acceleration spectrum is shown in Figure 4.19. The maximum

vibration value near its natural frequency has a reduction of 4.6 dB. The vibration reduction is not as significant as in the previous two cases because the speed is too high. In this case, the turn-on and turn-off angles sent by the microprocessor present a delay of  $2.4^\circ$ , which limits the interest of the proposed control. Figure 4.20 shows the acoustic noise results with a reduction of 4.3 dB is achieved near the natural frequency.

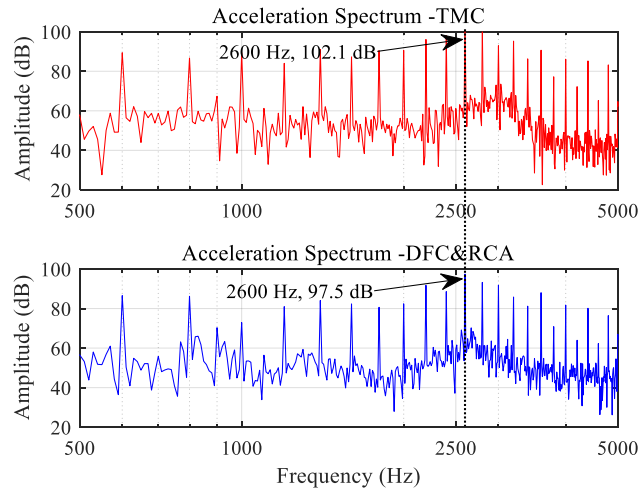


Figure 4.19 Experimental results of vibration acceleration at  $\Omega^* = 2000$  r/min and  $T_L = 0.6$  N·m.

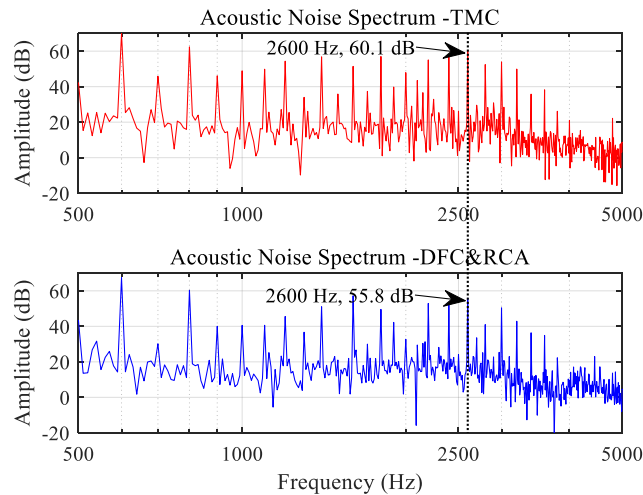


Figure 4.20 Experimental results of acoustic at  $\Omega^* = 2000$  r/min and  $T_L = 0.6$  N·m.

Besides, Figure 4.21 shows the sonogram of a speed of 1000 r/min with a load of 2 N·m. The control strategy switches from traditional TMC to proposed DFC&RCA at 12 s. The harmonics of the speed are visible at multiples of  $f_d = 100$  Hz ( $f_d = 1000/60 \times 6$  rotor poles). And only odd noise harmonics exist near the 2nd mode. It is seen that the acoustic noise has been reduced in a wide frequency range when the control is switched to DFC&RCA.

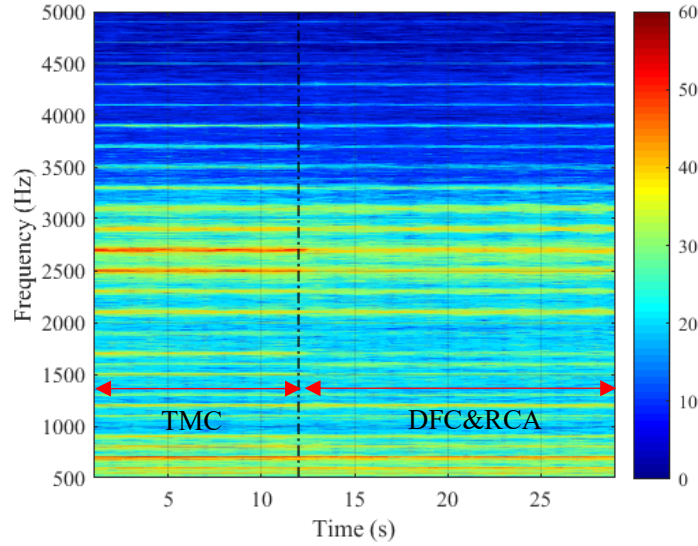


Figure 4.21 Experimental results by control strategies commutating: sonogram of acoustic noise measured at  $\Omega^* = 1000$  r/min and  $T_L = 2$  N·m.

Furthermore, the performances of the proposed control strategy have been evaluated for different reference speeds with a load torque of 2 N·m and for different loads with the reference speed of 600 r/min. The vibration energy and the torque ripple, respectively, are shown in Table 4-1 and Table 4-2. According to the results, the energy reduction for DFC&RCA is above 35% with a maximum torque ripple increase of 6.07%. Moreover, the efficiency for the two control methods are the same for all the considered operating points.

Table 4-1 Performance comparison for different reference speeds and a load torque of 2 N·m.

Reference Speed	Vibration Energy Reduction	Torque Ripple Increase
$\Omega^* = 200$ r/min	36.93%	6.07%
$\Omega^* = 400$ r/min	35.21%	4.52%
$\Omega^* = 600$ r/min	54.22%	3.54%
$\Omega^* = 800$ r/min	47.44%	5.4%

Table 4-2 Performance comparison for different loads and a reference speed of 600 r/min.

Load	Vibration Energy Reduction	Torque Ripple Increase
$T_L = 2$ N·m	54.22%	3.54%
$T_L = 4$ N·m	54.81%	2.89%
$T_L = 6$ N·m	53.82%	4.81%
$T_L = 8$ N·m	56.08%	2.55%

#### 4.2.4 Transient State Experiments

In the previous section, the proposed control method is compared to a traditional one (TMC) considering aspects related to vibration, acoustic noise and torque ripple when the

speed has reached the steady state. The transient periods when there are sudden changes in the reference speed or load torque are also important if we consider urban driving conditions. Thus, this section investigates the dynamic response of the proposed method under reference speed and load torque variations.

#### 4.2.4.1 Reference Speed Variation

Figure 4.22 and Figure 4.23 present the experimental results of TMC and DFC&RCA when the reference speed is increased from 200 r/min to 600 r/min at 5 s with a load torque of 2 N·m. As shown in the two figures, the phase current increases at the moment the reference speed changes. This is necessary so that the SRM can provide a higher torque in order to accelerate the rotor and to catch up with the new reference speed. According to the comparison, the transient period of the speed for both controllers is the same about 0.5 s.

The corresponding acoustic noise measurement results are given in Figure 4.24. The noises around 500 Hz are mainly from the power supply and MPB, which have been investigated in Section 4.2.2.2 and 4.2.2.3, respectively. The acoustic noise becomes more serious with the increase of the speed. However, DFC&RCA has always better acoustic performances than the traditional control method (TMC) whenever the speed is stable or is increasing.

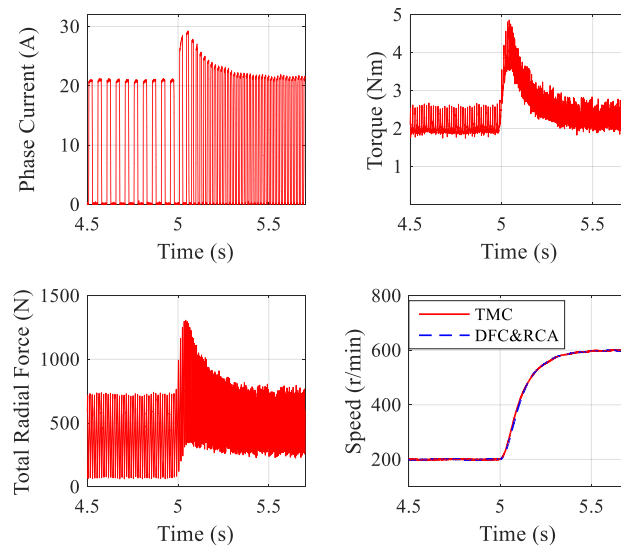


Figure 4.22 TMC: transient curves for a step-change in the reference speed from 200 r/min to 600 r/min and a load torque of 2 N·m.

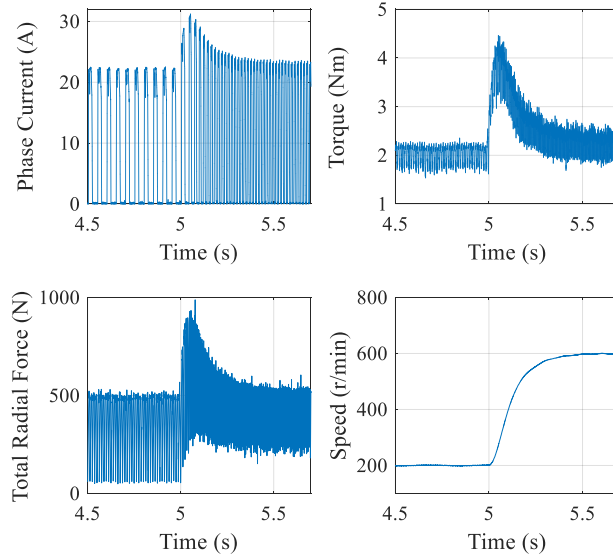
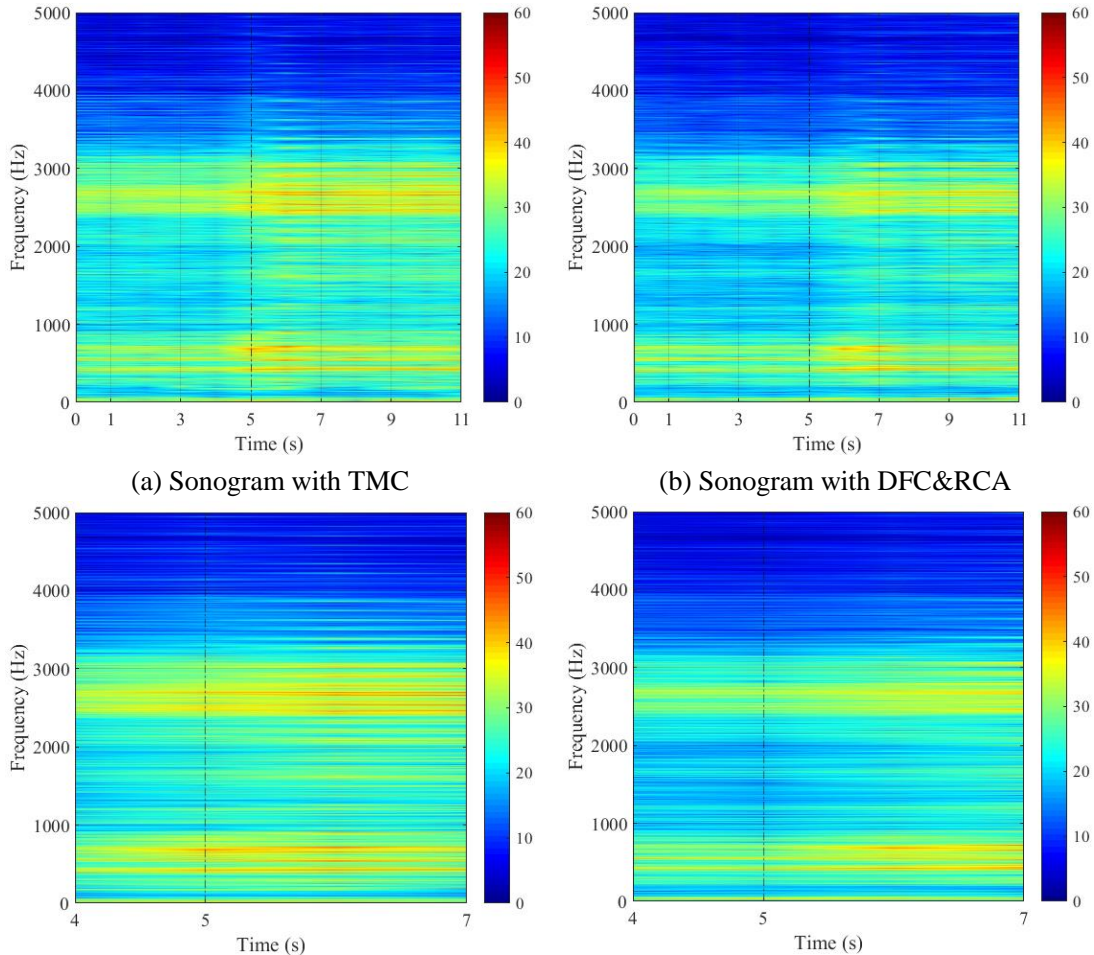


Figure 4.23 DFC&RCA: transient curves for a step-change in the reference speed from 200 r/min to 600 r/min and a load torque of 2 N·m.



(a.1) Partial zoom-in of (a) for the transient period (b.1) Partial zoom-in of (b) for the transient period

Figure 4.24 Experimental sonogram of acoustic noise for a step-change in the reference speed from 200 r/min to 600 r/min and a load torque of 2 N·m.

Figure 4.25 and Figure 4.26 present the experimental results of TMC and DFC&RCA when the reference speed is increased from 200 r/min to 600 r/min at 5 s with a higher load torque ( $T_L = 6 \text{ N}\cdot\text{m}$ ). Similar conclusions can be obtained as in the case with a light load of  $2 \text{ N}\cdot\text{m}$ .

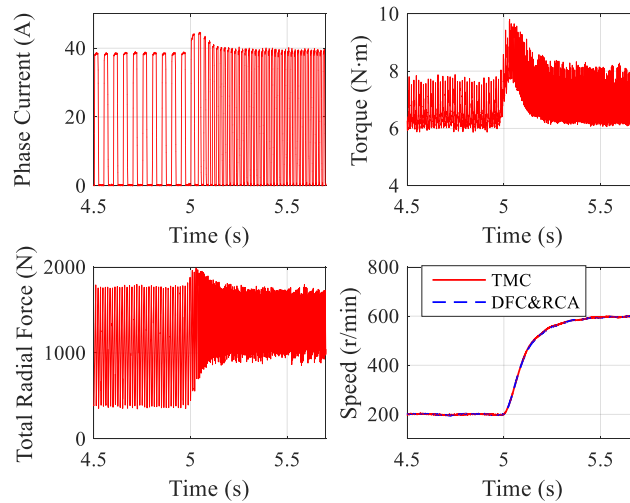


Figure 4.25 TMC: transient curve for a step-change in the reference speed from 200 r/min to 600 r/min and a load torque of  $6 \text{ N}\cdot\text{m}$ .

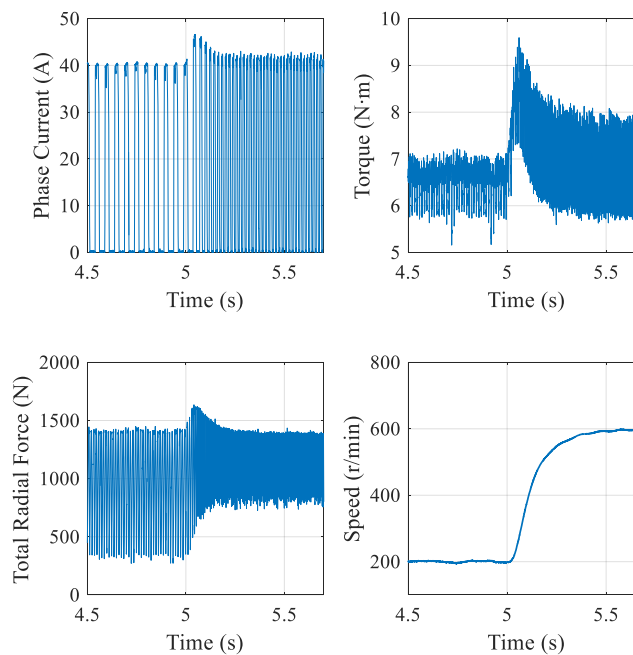


Figure 4.26 DFC&RCA: transient curve for a step-change in the reference speed from 200 r/min to 600 r/min and a load torque of  $6 \text{ N}\cdot\text{m}$ .

The corresponding acoustic noise measurement results are given in Figure 4.27. The noise from the power supply has a dominant frequency that changes from 420 Hz to 450 Hz

with a SPL amplitude increase of 10 dB. However, DFC&RCA has lower SPL than TMC both in stable and transient period.

Comparing Figure 4.24 with Figure 4.27, the SPL is higher with a load of 6 N·m than with a load of 2 N·m at the same speed. Besides, the noise from the power supply is more serious when the load torque is added.

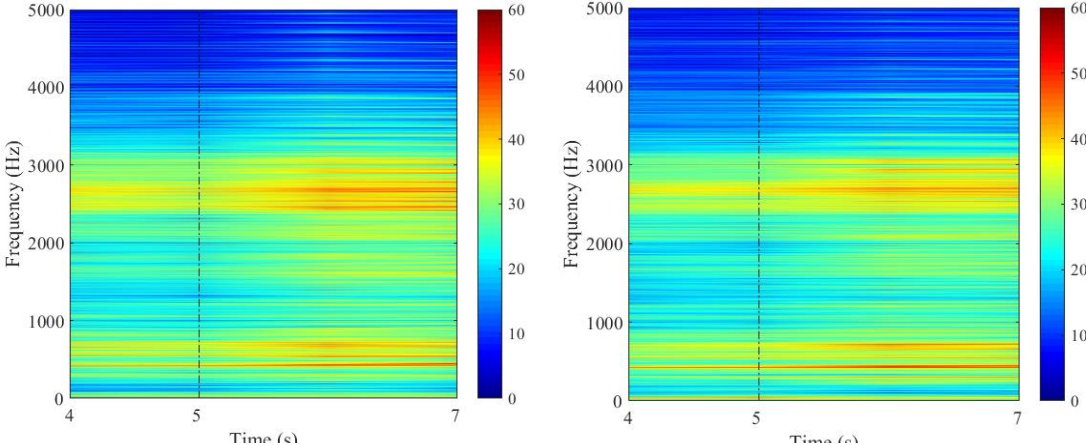
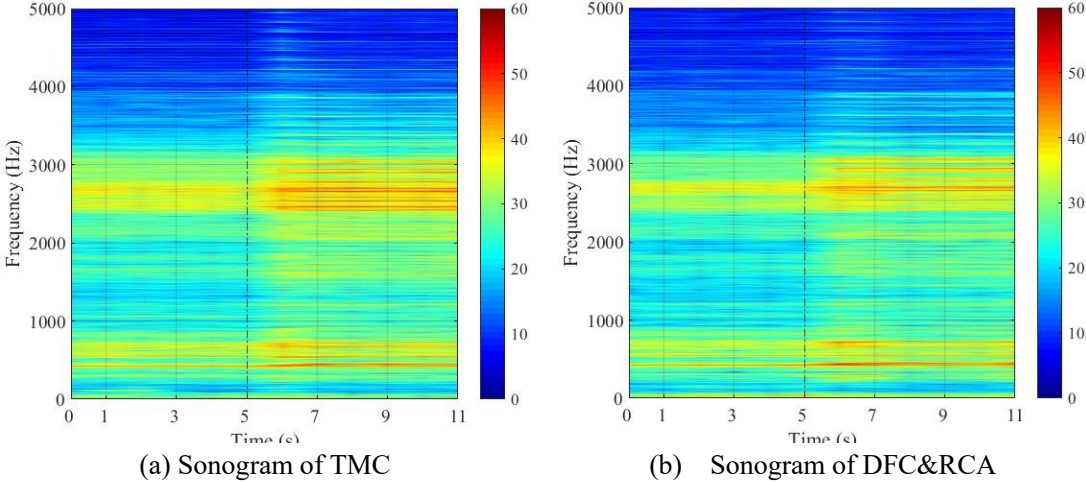


Figure 4.27 Experimental sonogram of acoustic noise for a step-change in the reference speed from 200 r/min to 600 r/min and a load torque of 6 N·m.

**4.2.4.2 Torque Load Variation**

Figure 4.28 and Figure 4.29 show the experimental results of TMC and DFC&RCA when the load torque is increased from 2 N·m to 6 N·m at 5 s with a reference speed of 600 r/min. As expected, the phase current increases at the moment the load torque is modified, so that SRM provides a higher torque to maintain the same speed. However, there exists a period

when the speed is smaller than the reference value because the output torque is lower than the load torque at the moment the load changes. However, both control methods assure a closed-loop response time within 0.5 s. The corresponding acoustic noise measurement results are given in Figure 4.30. The high-order acoustic harmonics are increased in Figure 4.30 (red dash line region) at the moment the load torque is increased (the current increases to maintain the reference speed). DFC&RCA has lower SPL than TMC at steady state and during transients.

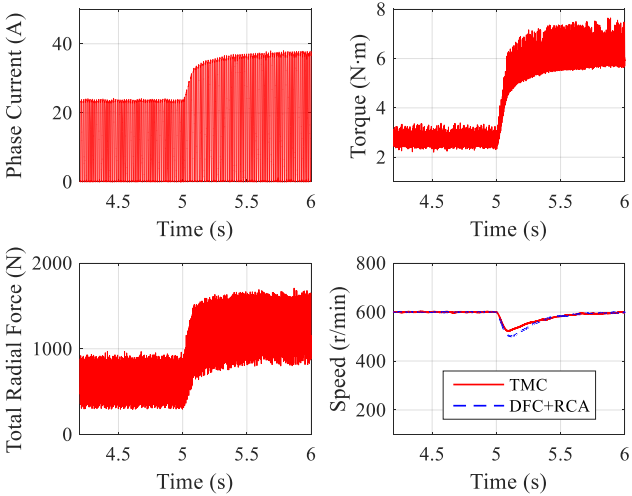


Figure 4.28 TMC: transient curves for a step-change in the load torque from 2 N·m to 6 N·m at constant reference speed  $\Omega^* = 600$  r/min.

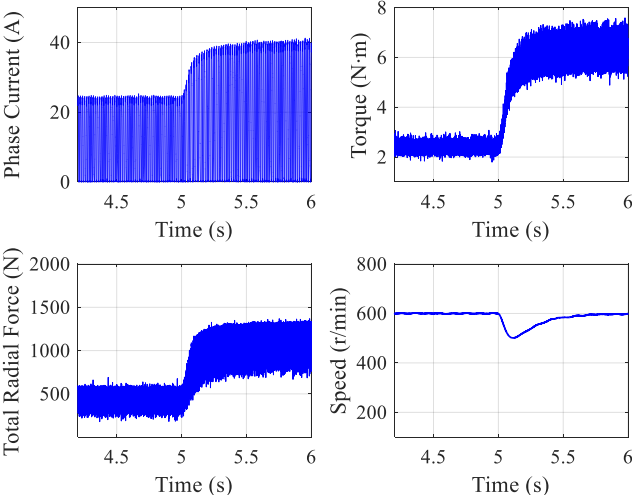
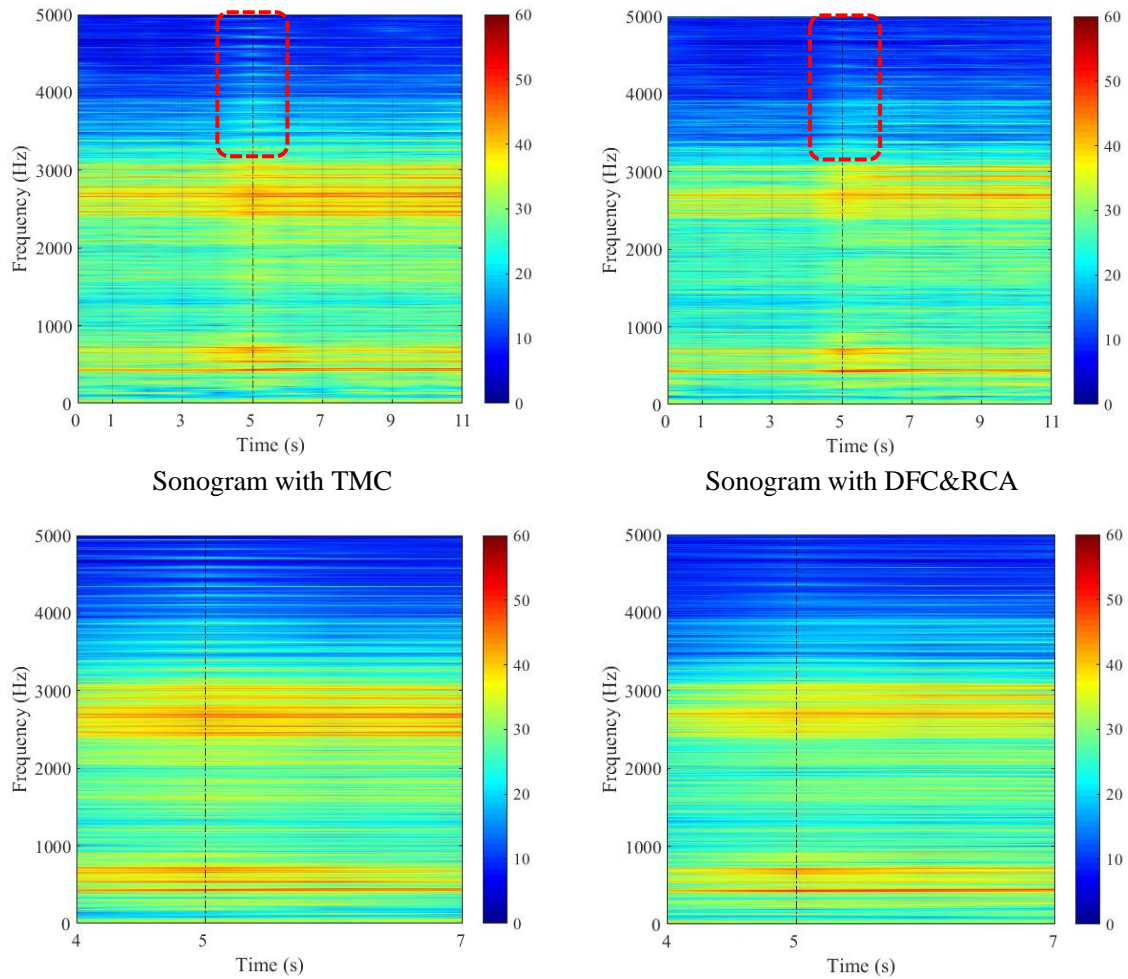


Figure 4.29 DFC&RCA: transient curves for a step-change in the load torque from 2 N·m to 6 N·m at constant reference speed  $\Omega^* = 600$  r/min.



(a.1) Partial zoom-in of (a) for the transient period (b.1) Partial zoom-in of (b) for the transient period  
 Figure 4.30 Experimental sonogram of acoustic noise for a step-change in the load torque from 2 N·m to 6 N·m at constant reference speed  $\Omega^* = 600$  r/min.

The falling edge of the step variation of the load torque is shown in Figure 4.31 and Figure 4.32. The closed-loop system has a response time about 0.5 s for both control methods and a speed overshoot around 17% because the output torque is higher than the load torque at that moment.

Figure 4.33 illustrates the corresponding sonogram of the acoustic noise obtained with TMC and DFC&RCA. The latter has lower SPL than the former at steady state and during transients the near the natural frequency. However, when the load-step occurs (shown in Figure 4.33 within a red dash line region), the high-order acoustic harmonics of DFC&RCA are higher than the ones of TMC, because the current reducing period is longer than TMC, which also explains the higher speed overshoot. After this transient period the high-order acoustic harmonics of TMC become higher than DFC&RCA ones. Moreover,

due to the sudden variation in the load torque, the noise from the MPB increases when the applied current is increased suddenly.

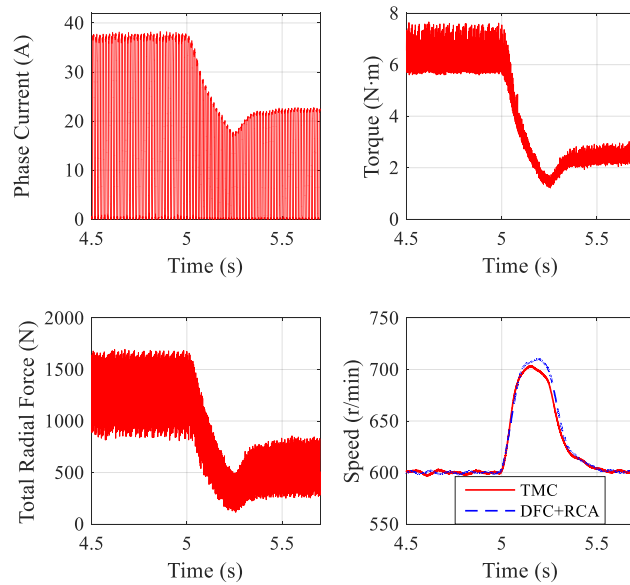


Figure 4.31 TMC: transient curves for a step-change in the load torque from 6 N·m to 2 N·m at constant reference speed  $\Omega^* = 600$  r/min.

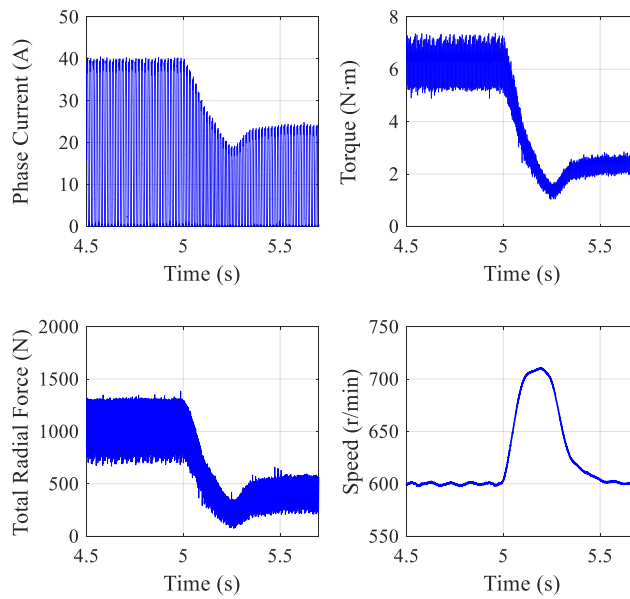


Figure 4.32 DFC&RCA: transient curves for a step-change in the load torque from 6 N·m to 2 N·m at constant reference speed  $\Omega^* = 600$  r/min.

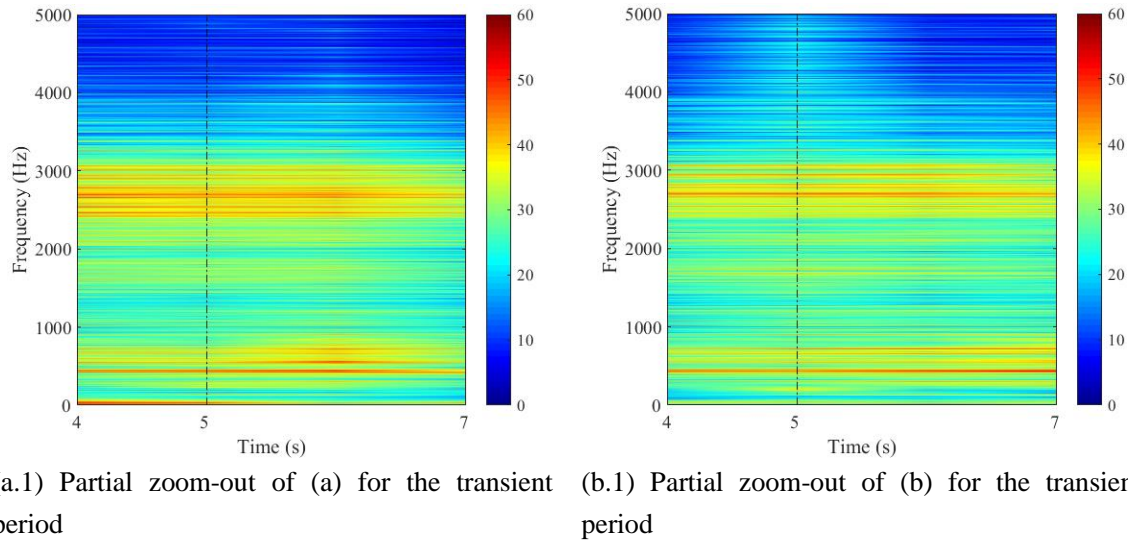
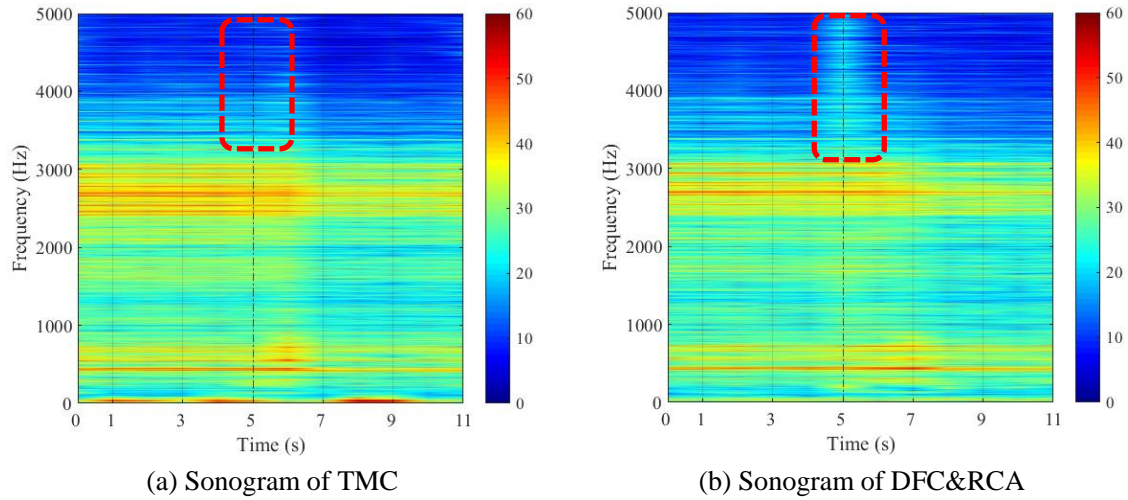


Figure 4.33 Experimental sonogram of acoustic noise at  $\Omega^* = 600$  r/min with the load torque decreasing from 6 N·m to 2 N·m.

### 4.3 Conclusion

In this chapter, a hardware/software partitioning solution is presented for the proposed vibration reduction control strategy (DFC&RCA) of a SRM. This solution of implementation is proposed considering the system performance, the resource consumption and the design flexibility. Next, experimental validation is carried out on a 8/6 pole 4-phase SRM prototype. To distinguish the SRM noise from the background noise, the acoustic noise from the environment, MPB, and power supply are measured respectively. Their dominant frequencies and distributed frequency range are determined, which yields that the dominant frequency of acoustic noise from the power supply increases with the increase of the current output. Thus,

different operating points have been tested under steady state and during transients. At steady state, the proposed method is compared to the traditional TMC analyzing the vibration, the torque ripple, the efficiency and the acoustic noise. According to the comparison results, the vibration energy can be reduced up to 67.4% without important penalizing the torque ripple and sacrificing the efficiency. The reduction of maximum SPL near the natural frequency is up to 13.7 dB. Regarding transients, both the speed mutation and load mutation are tested. The results show that the proposed method improves the acoustic performance of the SRM and maintains the dynamic response of it, which proves the potential of the DFC&RCA strategy.

# General Conclusion and Prospective

## Conclusions

This thesis analyzes the vibratory behavior of Switched Reluctance Machine (SRM) associated to its drives using both simulation and experimental approaches. At first, a semi-analytical electromagnetic/structural model to simulate the vibration acceleration based on transfer functions is introduced, where radial force is the output of the electromagnetic model and the input for the structural model. Then, the built model is used to develop and evaluate two vibration reduction methods: Improved Variable Turn-off angle Control (IVTC) and Direct Force Control with Reference Current Adapter (DFC&RCA). Finally, the second vibration reduction strategy DFC&RCA is evaluated by experimental tests using an 8/6 SRM prototype. A hardware/software partitioning solution is proposed to implement this control algorithm, where a FPGA board is used combined with a Microprocessor.

### **Main results regarding the semi-analytical electromagnetic/ structural model**

For SRMs, the radial force between the stator and rotor is the dominant sources of vibration and noise. It generates stator vibrations, which radiate airborne sound. Besides, the radial force produced is non-linear due to saturation effects. Usually, the radial force is expressed as a function depending on current and rotor position. Thus, the Finite Element Method (FEM) is adopted to calculate the radial force profile of the SRM. To predict the transient curve of the radial force, the dynamic current curve is required. Therefore, an inverse magnetization model for the current prediction is presented by the expression of flux linkage and rotor position. This flux-linkage profile is obtained by the static computation of FEM. Since the phases of an SRM can usually be regarded as magnetically independent, only one phase needs to be simulated and the results can be duplicated with adequate time shifts for the others. With the radial force obtained in the electromagnetic model, the vibration acceleration of several different modes on one excited phase can be calculated by the transfer function from radial force to vibration acceleration, and the vibratory behavior of the SRM

when several phases are excited can be calculated as the superposition of the contribution of corresponding phases coupled by the coupling factors. Moreover, considering the asymmetric structure of the investigated SRM stator, the transfer functions are categorized as self-transfer function and mutual-transfer function to improve the accuracy of the model. The major benefit of the simulation model developed in this thesis is the fact that all static characteristics (torque, flux-linkage and radial force profiles) of the machine can be pre-calculated and stored in look-up tables so that they do not need to be computed repeatedly during run-time, which leads to very low computational resource requirements and short simulation time.

### **Main results regarding SRM control strategies**

Based on the multiphysics model built, two vibration control strategies are developed in this thesis: IVTC and DFC&RCA. The main idea of IVTC is to vary the turn-off angle of the SRM, since the turn-off angle is the key variable related to the vibration. A random-variation-frequency sinusoidal function is adopted to make the turn-off angle vary with time. The mean frequency of the sinusoidal function is determined by the property of the transfer function between the radial force and the acceleration. It is the frequency corresponding to the local minimum amplitude of the transfer function to avoid the excitation of vibration modes. Then, a uniformly random-distributed function is introduced to the sinusoidal function as the variation of the mean frequency, so that it can avoid the concentrated harmonic component near the mean frequency and its multiple. The vibration can be reduced significantly, especially for the low speed, which can reduce the vibration energy up to 60.5% comparing to the traditional Average Torque Control (ATC) without sacrificing the efficiency and penalizing the torque ripple too much. However, its function decays when the speed is high. The increase of the magnitude of turn-off angle variation gives a possibility to improve the IVTC efficiency regarding such limitation.

The aim of the second controller -- DFC&RCA is to control the radial force in the teeth of the stator, since the dynamic of the radial force has a large impact on the vibratory performance. However, the DFC cannot be used alone because it increases the torque ripple due to the absence of the current limitation. Thus, a Reference Current Adapter (RCA) is

proposed to assess the torque and radial force variations, so as to manage the tradeoff between two objectives: torque ripple minimization and vibration reduction by updating the current reference. Different operating points are simulated with the DFC&RCA, the maximum vibration energy reduction is up to 72.2% which proves its potential. Besides, the secondary evaluation aspects such as torque ripple and efficiency are investigated. The simulations show that the DFC&RCA can reduce the torque ripple when the speed is low but deteriorates the torque ripple when the speed is high because the DFC works during the commutation periods. However, at high speed the torque ripple has a high frequency and could be filtered by the moment of inertia of the drive train. The efficiency is considered since it directly correlates with battery cost in traction applications which are not fed by a stationary grid. The DFC&RCA decreases the flux-linkage amplitude so that iron losses are reduced, and it can increase machine efficiency at low speed with heavy load by decreasing all the losses. On the downsides, the converter efficiency is usually lower compared to the Torque Minimization Control (TMC). This is attributed to the fast response of the hysteresis controllers in DFC. This shortcoming can be compensated by the iron losses reduction and sometimes copper losses reduction, which make the DFC&RCA competitive with that of TMC.

### **Main results regarding experimental implementation**

A hardware/software partitioning solution of experimental validation is presented for the proposed vibration reduction control strategy (DFC&RCA) of a SRM. The speed control is implemented in the microprocessor, while the current control and direct force control are implemented in the FPGA. This provides high dynamic response especially needed to control the force and the currents. Different operation points are evaluated under both the stable state and transient state. During the stable state, the proposed method is compared to the traditional TMC from the aspects of vibration, torque ripple, efficiency and acoustic noise. According to the comparison results, the vibration energy can be reduced up to 67.4% without penalizing the torque ripple and sacrificing the efficiency. Regarding noise emission, the reduction of maximum SPL near the natural frequency is up to 13.7 dB. Regarding to the transient state, both the speed mutation and load mutation are tested. The comparison results show that the

proposed method both improves the acoustic performance of the SRM and maintain the dynamic response of it, which proves the potential of the DFC&RCA coupling.

## **Prospective**

Several perspectives of this work can be envisaged, in the following they are divided into two parts: the short-term work and long-term work.

### **Short-term work**

- The IVTC has been validated by the simulation results, the experimental evaluation on the prototype SRM is necessary for the future work.
- The DFC&RCA has been tested on a SRM under different operating points, which are mainly the low-power output points, this method need to be further validated for the high speed and high torque region in experiments.
- A semi-analytical multi-physics model used to predict the vibration behavior of SRM is presented, which lowers the computational resource requirements and need short simulation time. Based on that, the acoustic noise model can be developed so that the acoustic behavior of this machine can be simulated directly.
- As investigated in Chapter 4, the vibration reduction capacity of IVTC is limited when the speed is high, and the solution is to increase the value of the turn-off angle variation. The problem is how much it should be increased, the relationship between the magnitude of turn-off angle variation and the speed need to be investigated further.

### **Long-term work**

- In the DFC&RCA, the speed-torque plane is divided into five regions to define the value of the control parameters, the commutation strategy between different regions need to be studied.
- The two vibration reduction methods have been verified on a small 8/6 4-phase SRM, whose rated power is 1.2kW. The characteristics of the SRM varies with the structure (i.e. different pole pairs, different phase) and the power capacity. Thus, more attention needs to be paid to the application of such control on other,

particularly for motors adapted to vehicle traction.

- The structural model presented in this work, extended with the acoustic part, could also be used to consider other vibration/acoustic control strategies, such as model-based predictive control.

## Bibliography

- [1] “A European Strategy for Low-emission Mobility”, European Commission, Brussels, Jul. 2016, <https://eur-lex.europa.eu/legal-content/en/TXT/?uri=CELEX%3A52016DC0501>
- [2] “Annual European Union greenhouse gas inventory 1990-2015 and inventory report 2017”, European Environment Agency, May 2017, <https://www.eea.europa.eu/publications/european-union-greenhouse-gas-inventory-2017>
- [3] “Electric Vehicles in Europe - 2016”, Transport & Environment, Oct. 2016, <https://www.transportenvironment.org/publications/electric-vehicles-europe-2016>
- [4] “These Countries Want to Ditch Gas and Diesel Cars”, CNN, Jul. 26, 2017, <http://money.cnn.com/2017/07/26/autos/countries-that-are-banning-gas-cars-for-electric/index.html>
- [5] “The Dutch Government Confirms Plan to Ban New Petrol and Diesel Cars by 2030”, Electrek, Oct. 2017, <https://electrek.co/2017/10/10/netherlands-dutch-ban-petrol-diesel-cars-2030-electric-cars/>
- [6] Cheng M., Chan C. C., “General requirement of traction motor drives”, *Encycl. Automot. Eng.*, pp. 1-18, 2014.
- [7] Chan C. C., Chau K. T., “An overview of power electronics in electric vehicles”, *IEEE Trans. Ind. Electron*, vol. 44, no. 1, pp. 3-13, 1997,
- [8] Zhu Z. Q., Howe D., “Electrical machines and drives for electric, hybrid and fuel cell vehicles”, *IEEE Proc.*, vol. 95, no. 4, pp. 746-765, 2007.
- [9] Rossi C., Casadei D., Pilati A. Marano M., “Wound rotor salient pole synchronous machine drive for electric traction”, *IAS Annual Meeting IEEE*, vo. 3, pp. 1235-1241, 2006.
- [10] Ehsani M., Gao Y., and Emami A., “Modern Electric, Hybrid Electric, and Fuel Cell Vehicles: Fundamentals, Theory, and Design”, 2nd. CRC Press, 2010.
- [11] Zeraouia M., Benbouzid M. E. H., and Diallo D., “Electric motor drive selection issues for hev propulsion systems: A comparative study,” *IEEE Transactions on Vehicular Technology.*, vol. 55, pp. 1756 – 1764, 2006.
- [12] Miura T., Chino S., Takemoto M., Ogasawara S., Chiba A. and Hoshi N., “A ferrite permanent magnet axial gap motor with segmented rotor structure for the next generation hybrid vehicle”, in *Proc. ICEM*, pp. 1-6, Sept. 2010.
- [13] Ozawa I., Kosaka T. and Matsui N., “Less rare-earth magnet-high power density hybrid excitation motor designed for hybrid electric vehicle drives”, in *Proc. EPE*, pp. 1-10, Sept. 2009.
- [14] Morimoto M., “Iron loss of non-rare earth traction motor for electric vehicle”, in *Proc. VPPC*, pp. 1-4, Sept. 2010.
- [15] Ito K., Sanada M. and Morimoto S., “Basic research on permanent magnet assisted synchronous reluctance motor with three-gap structure”, in *Proc. IPEC*, pp. 1348-1353, Jun. 2010.
- [16] Chiba A., Hoshi N., Takemoto M., Ogasawara S., Morimoto S., Sanada M. and Kosaka T., “Rare-earth-free AC motors—An alternative approach advances”, in *Proc. IEMDC*, pp. 1-5, May 2011.
- [17] Hilairet M., Hannoun H. and Marchand C., “Design of an optimized SRM control architecture based on a hardware/software partitioning”, in *Proc. IECON*, pp. 4053-4057, Nov. 2009.
- [18] Hannoun H., Hilairet M. and Marchand C., “Comparison of instantaneous and average torque control for a Switched Reluctance Motor”, in *Proc. ISIE*, pp. 675-680, Jul. 2008.
- [19] Hannoun H., Hilairet M. and Marchand C., “Design of an SRM speed control strategy for a wide range of operating speeds”, *IEEE Trans. Ind. Electron.*, vol. 57, no.9, pp. 2911-2921, 2010.

- [20] Hannoun H., Hilaiet M. and Marchand C., “Experimental validation of a switched reluctance machine operating in continuous-conduction mode”, *IEEE Trans. Veh. Technol.*, vol. 60, no. 4, pp. 1453-1460, 2011.
- [21] Timar P. L., Fazekas A., Kiss J., Miklos A. and Yang S. J., “Noise and Vibration of Electrical Machines”, New York: Elsevier, 1989.
- [22] Gieras J. F., Wang C. and Lai J. C., “Noise of polyphase electric motors”, Boca Raton: CRC press, 2005.
- [23] Krishnan R., “Switched reluctance motor drives: modeling, simulation, analysis, design and applications”, Boca Raton: CRC press, 2001
- [24] Anwar M., Husain I., “Radial force calculation and acoustic noise prediction in switched reluctance machines”, *IEEE Trans. Ind. Appl.*, vol. 36, no. 6, pp. 1589-1597, 2000.
- [25] Fiedler J. O., Kasper K. A. and De Doncker R. W., “Acoustic noise in switched reluctance drives: an aerodynamic problem?”, in *Proc. IEMDC*, pp. 1275-1280, May 2005.
- [26] Krishnan R., Vijayraghavan P., “State of the art: Acoustic noise in switched reluctance motor drives”, in *Proc. IECON*, pp. 929-934, Aug. 1998
- [27] Fiedler J. O., “Design of Low-Noise Switched Reluctance Drives”, PhD thesis, RWTH Aachen University, 2006.
- [28] Nakata K., Sanada M., Morimoto S. and Takeda Y., “Noise reduction for switched reluctance motor with a hole”, in *Proc. IPEC*, vol. 3, pp. 971-976, Apr. 2002.
- [29] Li J., Sun H. X. and Liu Y., “New rotor structure mitigating vibration and noise in switched reluctance motor”, in *Proc. ICINA*, vol.2, pp.80-84, Oct. 2010.
- [30] Gan C., Wu J., Shen M., Yang S., Hu Y. and Cao W., “Investigation of skewing effects on the vibration reduction of three-phase switched reluctance motors”, *IEEE Trans. Magn.*, vol. 51, no. 9, pp. 1-9, 2015.
- [31] Edamura K., Miki I., “Design of stator and rotor for noise reduction of SRM”, in *Proc. ICEMS*, pp. 1871-1874, Oct. 2014.
- [32] Kakishima T., Kiyota K., Nakano S. and Chiba A., “Pole selection and vibration reduction of Switched Reluctance Motor for hybrid electric vehicles”, in *Proc. ITEC*, pp. 1-4, Aug. 2014.
- [33] Hong J. P., Ha K. H. and Lee J., “Stator pole and yoke design for vibration reduction of switched reluctance motor”, *IEEE Trans. Magn.*, vol. 38, no. 2, pp. 929-932, 2002.
- [34] Besbes M., Picod C., Camus F. and Gabis M., “Influence of stator geometry upon vibratory behavior and electromagnetic performances of switched reluctance motors”, *IEE Proc.: Electr. Power Appl.*, vol. 145, no. 5, pp. 462-468, 1998.
- [35] Castano S. M., Bilgin B., Fairall E. and Emadi A., “Acoustic noise analysis of a high-speed high-power switched reluctance machine: Frame effects”, *IEEE Trans. Energy Convers.*, vol. 31, no. 1, pp. 69-77, 2016.
- [36] Li J., Cho Y., “Investigation into reduction of vibration and acoustic noise in switched reluctance motors in radial force excitation and frame transfer function aspects”, *IEEE Trans. Magn.*, vol. 45, no. 10, pp. 4664-4667, 2009.
- [37] Sun J. B., Zhan Q. H., Wang S. H. and Ma Z. Y., “A novel radiating rib structure in switched reluctance motors for low acoustic noise”, *IEEE Trans. Magn.*, vol. 43 no. 9, pp. 3630-3637, 2007.
- [38] Yasa Y., Tekgun D., Sozer Y., Kutz J. and Tylenda J., “Effect of distributed airgap in the stator for acoustic noise reduction in switched reluctance motors”, in *Proc. APEC*, no. 1, pp. 633-639, Mar. 2017.

- [39] Kiyota K., Kakishima T., Chiba A. and Rahman M.A., “Cylindrical Rotor Design for Acoustic Noise and Windage Loss Reduction in Switched Reluctance Motor for HEV Applications”, *IEEE Trans. Ind. Appl.*, vol. 52, no. 1, pp. 154-162, 2016.
- [40] Mademlis C., Kioskeridis I., “Performance optimization in switched reluctance motor drives with online commutation angle control”, *IEEE Trans. Energy Convers.*, vol. 18, no. 3, pp. 448-457, 2003.
- [41] Boukhobza T., Gabsi M. and Grioni B., “Random variation of control angles, reduction of SRM vibrations”, in *Proc. IEMDC*, pp. 640-643, Jun. 2001.
- [42] Wu C. Y., Pollock C., “Time domain analysis of vibration and acoustic noise in the switched reluctance drive”, in *Proc. IEMDC*, pp. 558-563, Sept. 1993.
- [43] Ahn J. W., Park S. J. and Lee D. H., “Hybrid excitation of SRM for reduction of vibration and acoustic noise”, *IEEE Trans. Ind. Electron.*, vol. 51, no. 2, pp. 374-380, 2004.
- [44] Chuang T. S., “Acoustic noise reduction of a 6/4 SRM drive based on third harmonic real power cancellation and mutual coupling flux enhancement”, *Energy Convers. Manag.*, vol. 51, no. 3, pp. 546-552, 2010.
- [45] Blaabjerg F., Pedersen J. K., “Digital implemented random modulation strategies for ac and switched reluctance drives”, in *Proc. IECON*, pp. 676-682, Nov. 1993.
- [46] Kang B. J., Liaw C. M., “Random hysteresis PWM inverter with robust spectrum shaping”, *IEEE Trans. Aerosp. Electron. Syst.*, vol. 37, no. 2, pp. 619-629, 2001.
- [47] Ojeda X., Gabsi M., Lecrivain M. and Mininger X., “Noise reduction using piezoelectric active control on high speeds switched reluctance drives”, in *Proc. IEEE IAS Anna. Meeting*, pp. 2204-2209, Sept. 2007.
- [48] Mininger X., Lefeuvre E., Gabsi M., Richard C. And Guyomar D., “Semiactive and active piezoelectric vibration controls for switched reluctance machine”, *IEEE Trans. Energy Convers.*, vol. 23, no. 1, pp. 78-85, 2008.
- [49] Ojeda X., Mininger X., Gabsi M., Kulcsar C., Raynaud H. F. and Lecrivain M., “Design of controllers: Vibration damping of switched reluctance machine by piezoelectric actuators”, in *Proc. ELECTROMOTION*, pp. 1-6, Jul. 2009.
- [50] Ojeda X., Mininger X., Gabsi M. and Lecrivain M., “Noise cancellation of 6/4 switched reluctance machine by piezoelectric actuators: Optimal design and placement using genetic algorithm”, in *Proc. PEMD*, pp. 611-615, Apr. 2008.
- [51] Ojeda X., Mininger X. and Gabsi M., “An active piezoelectric absorber for vibration control of electrical machine”, in *Proc. ICIT*, pp. 234-241, Feb. 2013.
- [52] Lin F. C., Yang S. M., “An approach to producing controlled radial force in a switched reluctance motor”, *IEEE Trans. Ind. Electron.*, vol. 54, no. 4, pp. 2137-2146, 2007.
- [53] Hofmann A., Al-Dajani A., Bösing M. and De Doncker R. W., “Direct instantaneous force control: A method to eliminate mode-0-borne noise in switched reluctance machines”, in *Proc. IEMDC*, pp. 1009-1016, May 2013.
- [54] Annegret K. H., Hofmann A. and De Doncker R. W., “Direct instantaneous torque and force control: a control approach for switched reluctance machines”, *IET Electr. Power Appl.*, vol. 11, pp. 935-943, 2017.
- [55] Takiguchi M., Sugimoto H., Kurihara N. and Chiba A., “Acoustic noise and vibration reduction of SRM by elimination of third harmonic component in sum of radial forces”, *IEEE Trans. Energy Convers.*, vol. 30, no. 3, pp. 883-891, 2015.
- [56] Kurihara N., Bayless J. and Chiba A., “Noise and vibration reduction of switched reluctance motor

- with novel simplified current waveform to reduce force sum variation”, in Proc. IEMDC, pp. 1794-1800, May 2015.
- [57] Anwar M. N., Husain I., “Radial force calculation and acoustic noise prediction in switched reluctance machines”, *IEEE Trans. Ind. Appl.*, vol. 36, no. 6, pp. 1589-1597, 2000.
- [58] Le Besnerais J., Lanfranchi V., Hecquet, M., Brochet, P. And Friedrich, G., “Prediction of audible magnetic noise radiated by adjustable-speed drive induction machines”, *IEEE Trans. Ind. Appl.*, 46, no. 4, pp. 1367-1373, 2010.
- [59] Lin C., Fahimi B., “Prediction of radial vibration in switched reluctance machines”, *IEEE Trans. Energy Convers.*, vol. 28, no. 4, pp. 1072-1081, 2013.
- [60] Dos Santos F. L., Anthonis J., Naclerio F., Gyselinck J. J., Van der Auweraer H. and Goes L., “Multiphysics NVH modeling: simulation of a switched reluctance motor for an electric vehicle”, *IEEE Trans. Ind. Electron.*, vol. 61, no. 1, pp. 469-476, 2014.
- [61] Torregrossa D., Peyraut F., Fahimi B., M'Boua J. and Miraoui, A., “Multiphysics finite-element modeling for vibration and acoustic analysis of permanent magnet synchronous machine”, *IEEE Trans. Energy Convers.*, vol. 26, no. 2, pp. 490-500, 2011.
- [62] Boisson J., Louf F., Ojeda J., Mininger X. and Gabsi, M., “Low Computational-cost determination of Vibrational Behavior: Application to Five-phase Flux-Switching Permanent-Magnet Motor”, *IEEE Trans. Magn.*, pp. 1, 2014.
- [63] van der Giet M., Lange E., Correa D., Chabu I. E., Nabeta S. I. and Hameyer K., “Acoustic simulation of a special switched reluctance drive by means of field-circuit coupling and multiphysics simulation”, *IEEE Trans. Ind. Electron.*, vol. 57, no. 9, pp. 2946-2953, 2010.
- [64] Lin C., Fahimi B., “Prediction of acoustic noise in switched reluctance machines”, in Proc. IECON pp. 3060-3065, Nov. 2013.
- [65] Lin C., Wang S. and Fahimi B., “Efficient multiphysics modelling of vibration and acoustic noise in switched reluctance motor drives”, in Proc. IECON, pp. 542-548, Oct. 2014.
- [66] Idkhajine L., Monmasson E., Maalouf A., “Fully FPGA-based sensorless control for synchronous AC drive using an extended Kalman filter”, *IEEE Trans. Ind. Electron*, vol. 59, no. 10, pp. 3908-3918, 2012.
- [67] Pinto S. J., Panda G., Peesapati R., “An Implementation of Hybrid Control Strategy for Distributed Generation System Interface Using Xilinx System Generator”, *IEEE Trans. Ind. Informat.*, vol. 13, no.5, pp.2735-2745, 2017.
- [68] Rodríguez-Andina J. J., Valdes-Pena M. D. and Moure M. J., “Advanced FEMtures and industrial applications of FPGAs—A review”, *IEEE Trans. Ind. Informat.*, vol. 11, no. 4, pp. 853-864, 2015.
- [69] Naouar M. W., Monmasson E., Naassani A. A., Belkhodja I. S. and Patin N., “FPGA-based current controllers for AC machine drives—A review”, *IEEE Trans. Ind. Electron*, vol. 54, no. 4, pp. 1907-1925, 2007.
- [70] Monmasson E., Cirstea M. N., “FPGA design methodology for industrial control systems—A review”, *IEEE Trans. Ind. Electron*, vol. 54, no. 4, pp. 1824-1842, 2007.
- [71] Bahri I., Idkhajine L., Monmasson E. and El Amine Benkhelifa M., “Hardware/software codesign guidelines for System on Chip FPGA-based sensorless AC drive applications”, *IEEE Trans. Ind. Informat.*, vol. 9, no. 4, pp. 2165-2176, 2013.
- [72] Senicar F., Dopker M., Bartsch A., Kruger B. and Soter S., “Inverter based method for measurement of PMSM machine parameters based on the elimination of power stage characteristics”, in Proc. IECON, pp. 702-708, Oct. 2014.

- [73] Kobravi K., Iravani R. and Kojori H. A., “Three-leg/four-leg matrix converter generalized modulation strategy—Part II: Implementation and verification”, *IEEE Trans. Ind. Electron.*, vol. 60, no. 3, pp. 860-872, 2013.
- [74] Multon B., “Les machines synchrones autopilotées”, Thèse de Doctorat, ENS Cachan, 2004.
- [75] Bösing M., “Acoustic modeling of electrical drives-noise and vibration synthesis based on force response superposition”, PhD thesis, RWTH Aachen University, 2014.
- [76] Coulomb J., Meunier G., “Finite element implementation of virtual work principle for magnetic or electric force and torque computation”, *IEEE Trans. Magn.*, vol. 20. no. 5, pp. 1894-1896, 1984.
- [77] Chang L., Eastham A. and Dawson G., “Permanent magnet synchronous motor: finite element torque calculations”, in *Proc. IEEE IAS Anna. Meeting*, pp. 69-73, Oct. 1989.
- [78] Hannoun H., “Etude et mise en œuvre de lois de commande de la machine à réductance variable à double saillance”, Thèse de Doctorat, Université de Paris-Sud, 2008.
- [79] Besnerais J. L., Lanfranchi V., Hecquet M. and Brochet P., “Characterization and reduction of audible magnetic noise due to PWM supply in induction machines”, *IEEE Trans. Ind. Electron.*, vol. 57, no.4, pp. 1288-1295, 2010.
- [80] Cremer L., Heckl M. and Petersson B. A. T., “Structure-Borne Sound. Structural Vibrations and Sound Radiation at Audio Frequencies”, 3rd ed., Berlin: Springer, 2005.
- [81] Tang Z., Pillay P. and Omekanda A. M., “Vibration prediction in switched reluctance motors with transfer function identification from shaker and force hammer tests”, *IEEE Trans. Ind. Appl.*, vol. 39, no. 4, pp. 978-985, 2003.
- [82] Fiedler J. O., Kasper K. A. and De Doncker R. W., “Calculation of the acoustic noise spectrum of SRM using modal superposition”, *IEEE Trans. Ind. Electron.*, vol. 57, no. 9, pp. 2939-2945, 2010.
- [83] Kuser K., “Analysis and Control of the Acoustic Behavior of Switched Reluctance Drives”, PhD thesis, RWTH Aachen University, 2011.
- [84] Yang S. J., “Low-Noise Electrical Motors”, Oxford: Clarendon Press, 1981.
- [85] Cai W., “Vibrations in Switched Reluctance Motors”, PhD thesis, Clarkson University, 2000.
- [86] Long S. A., Zhu Z. Q. and Howe, D., “Vibration behavior of stators of switched reluctance motors”. *IEE Proc.: Electr. Power Appl.*, vol. 148, no. 3, pp. 257-264, 2001.
- [87] Chowdhury I., Dasgupta S. P., “Computation of Rayleigh damping coefficients for large systems”, *Electron. J. Geotech. Eng.*, vol. 8, pp. 1-11, 2003.
- [88] Bolognani S., Peretti L. and Zigliotto M., “Parameter sensitivity analysis of an improved open-loop speed estimate for induction motor drives”, *IEEE Trans. Power Electron.*, vol. 23, no. 4, pp. 2127-2135, 2008.
- [89] Schulz S. E., Rahman K. M., “High-performance digital PI current regulator for EV switched reluctance motor drives”, *IEEE Trans. Ind. Appl.*, vol. 39, no. 4, pp. 1118-1126, 2003.
- [90] Sant A.V., Rajagopal K.R. and Sheth N.K., “Permanent Magnet Synchronous Motor Drive Using Hybrid PI Speed Controller with Inherent and Noninherent Switching Functions”, *IEEE Trans. Magn.*, Vol. 47, No. 10, pp. 4088 - 4091, 2011.
- [91] Ahmed F. I., El-Tobshy A. M. and Mahfouz A. A. and Ibrahim M. M. S., “P-I and I-P controllers in a closed loop for DC motor drives”, in *Proc. PCC'97*, vol. 2, pp. 613-618, Aug. 1997.
- [92] Ji J., Sul S., “DSP-based Self-tuning IP Speed Controller with Load Torque Compensation for Rolling Mill DC Drive”, *IEEE Trans. Ind. Electron.*, Vol. 42, No. 4, pp. 382-386, 1995.
- [93] Lin, F., “Real-time IP position controller design with torque feedforward control for PM synchronous motor”, *IEEE Trans. Ind. Electron.*, Vol. 44, No. 3, pp. 398-407, 1997.

- [94] Nandam P. K., Sen P.C., “Analog and Digital Speed Control of DC Drives Using Proportional-Integral and Integral-Proportional Control Techniques”, *IEEE Trans. Ind. Electron.*, Vol. IE-34, No. 2, pp. 227- 233, 1987.
- [95] Kaynak O., Abbaszadeh A.d. and Nazlibilek S., “Digital Speed Control System with Integral Proportional Control”, in *Proc. IFAC Contr. Power Electron. Electr. Drives*, pp.501-506, Sept. 1983.
- [96] Rain X., Hilairet M. and Bethoux O., “Comparative study of various current controllers for the switched reluctance machine”, in *Proc. VPPC*, pp. 1-6, Sept. 2010.
- [97] Blaabjerg F., Kjaer P. C., Rasmussen P. O. and Cossar, C., “Improved digital current control methods in switched reluctance motor drives”, *IEEE Trans. Power Electron.*, vol. 14, no. 3, pp. 563-572, 1999.
- [98] Hannoun H., Hilairet M. and Marchand C., “High performance current control of a switched reluctance machine based on a gain-scheduling PI controller”, *Control Eng. Practice*, vol. 19, no. 11, pp. 1377-1386, 2011.
- [99] Kolli A., Krebs G., Mininger X. and Marchand C., “Impact of command parameters on efficiency, torque ripple and vibrations for Switched Reluctance motor”, in *Proc. ICEM*, pp. 2975-2980, Sept. 2012.
- [100] Annegret K. H., Hofmann A. and De Doncker R. W., “Direct instantaneous torque and force control: a control approach for switched reluctance machines”, *IET Electr. Power Appl.*, vol. 11, no. 5, pp. 935-943, 2017.
- [101] Kim Y. S., Park J., Park T. W., Bang J. S. and Sim H. S., “Anti-jerk controller design with a cooperative control strategy in hybrid electric vehicle”, in *Proc. ICPE- ECCE Asia*, pp. 1964-1968, May 2011.
- [102] Klauz M., Dorrell D., “Eddy Current Effects in a Switched Reluctance Motor”, *IEEE Trans. Magn.*, vol. 42, no.10, pp. 3437-3439, 2006.

## A. Characteristic Data of the Investigated SRM

The technical parameters of the investigated 8/6 4-phase SRM are presented in Table A.1.

Table A.1: Characteristic data of investigated SRM

Nominal Power	1.2 kW
Nominal Speed	3000 r/min
Voltage Supply	24V
Number of Stator	8
Number of Rotor	6
Outer Diameter of Stator Poles	143 mm
Outer Diameter of Rotor Poles	67.8 mm
Active Stack Length	125 mm

## B. Investigation on Current Harmonic Removal related to the Vibration Excitation

The dominant vibration mode of the investigated SRM is mode 2, so that the main idea here is to eliminate the force harmonic components which are able to excite mode 2. Then, the relationship between the radial force harmonic components and corresponding current harmonic components needs to be determined. Finally, the determinate current harmonics can be removed by using a notch filter.

To determine the relationship between the radial force and the current harmonics, a simulation model to investigate the harmonic component variation after being filtered for both current and radial force is proposed, which is presented in Figure B.1. In this model, the speed and torque are regarded as the input and the output is the current  $I_f$  induced from the filtered radial force  $F_f$ . The unfiltered radial force  $F$  is predicted by the original current signal  $I$  from LUTS saving control parameters and rotor position  $\theta$ , which is computed from the given speed. An inverse look-up table of the radial force  $I(F_f, \theta)$  is adopted in the simulation, so that the current  $I_f$  can be predicted with the filtered radial force  $F_f$  and position  $\theta$ .

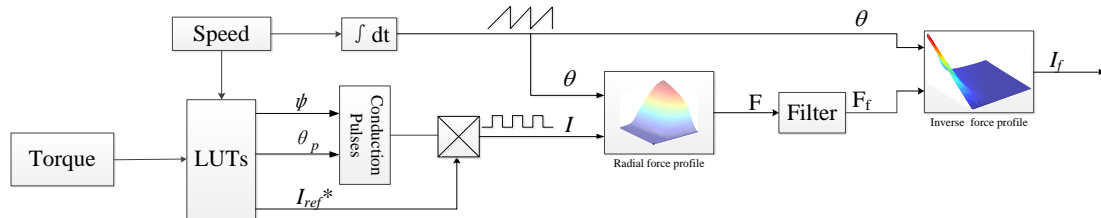


Figure B.1 Proposed model to investigate the relationship between the current and radial force harmonic components.

Thus, the harmonic component difference between the  $I$  and  $I_f$ , and the difference between  $F$  and  $F_f$  can be determined. That is to say, if the filter is designed to eliminate certain harmonic components of  $F$ , the corresponding current component variation can be determined by comparing the Fast Fourier Transfer (FFT) of original current  $I$  to the induced current  $I_f$ . In this way, the relationship between the current and radial force harmonic components can be determined.

In the simulation, the speed-up test is evaluated for different torques. Figure B.2

presents the comparison results for force harmonic component and current harmonic component when speed is up to 3000 r/min with a torque of 4 N·m. The definition of the force difference is the amplitude difference between the FFT of radial force  $F$  and the FFT of the filtered radial force  $F_f$ . The definition of the current difference is the amplitude difference between the FFT of the original current  $I$  and the FFT of the induced current  $I_f$ .

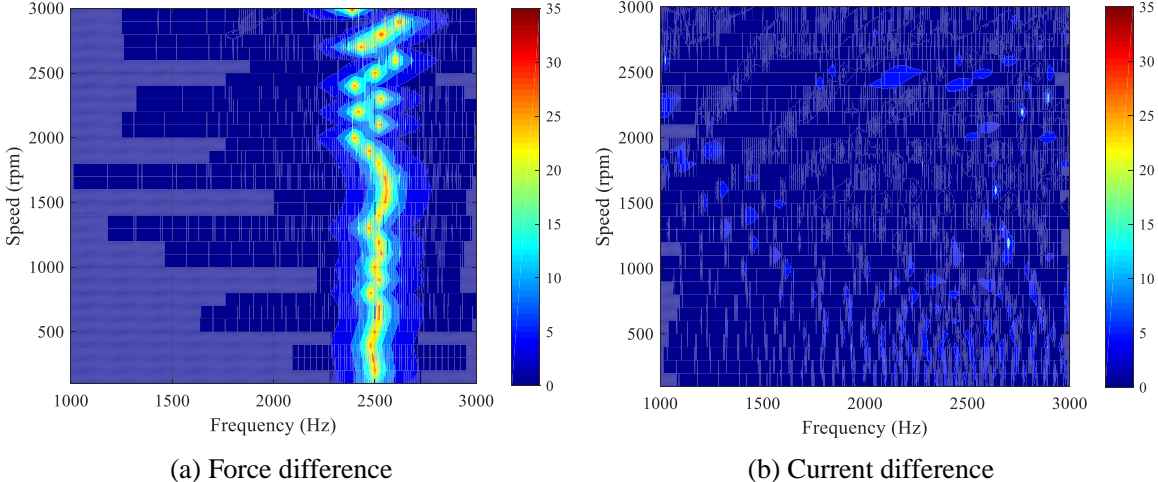


Figure B.2 Force and current harmonic component comparison when speed is up to 3000 r/min with a torque of 4 N·m.

It can be seen that if the radial force harmonics near the mode 2 are removed, the current harmonics need to be reduced in a wide range but relatively small amplitude. This means that a small current harmonic component variation may lead to a significant variation of the force harmonic components.

Moreover, Figure B.3 presents the comparison results for force harmonic component and current harmonic component when speed is up to 900 r/min with a torque of 18 N·m.

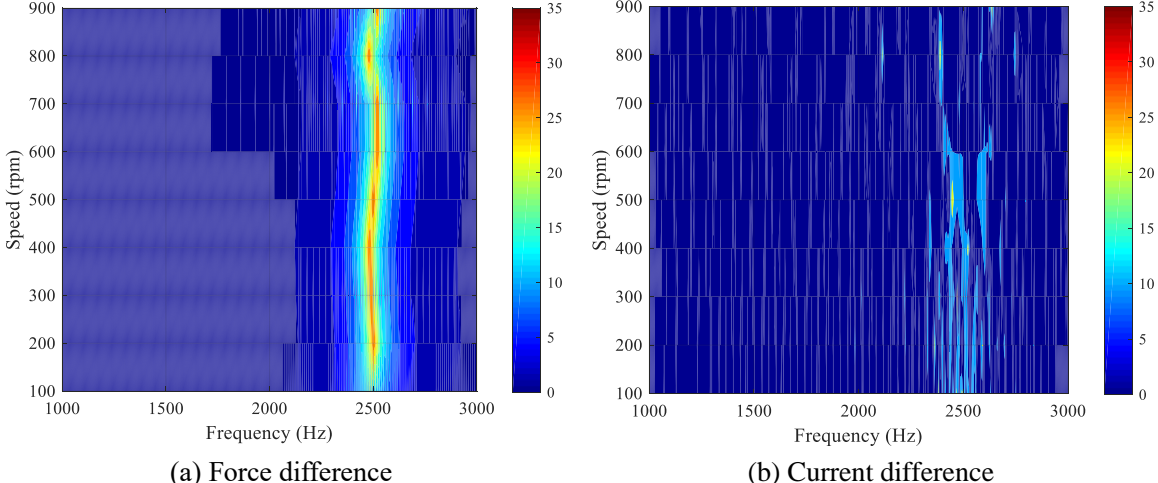


Figure B.3 Force and current harmonic component comparison when speed is up to 900 r/min with a torque of 18 N·m.

In this case, if the radial force harmonics near the mode 2 are removed, the current harmonic need to be reduced is also in that range, but the amplitude of the current difference is also rather small compared to that of the force difference.

In conclusion, the relationship between the current and its corresponding force harmonic component varies with both speed and load, and this study about force harmonic removal needs to be investigated further.

## C. Losses and Efficiency Computation of SRM drive system

Here we will introduce the computation of three major losses: the DC copper losses, the iron losses and the converter losses.

### Copper Losses Computation

The DC copper losses are dependent on the ohmic resistance and the phase-current trajectories. Assuming that the four-phase windings are symmetric, the DC-component loss can be calculated as:

$$P_{\text{copper}} = N_{ph} \cdot R \cdot I_{rms}^2 \quad (1)$$

where  $I_{rms}$  is the root mean square value of the phase current over one electrical cycle. It is expressed as:

$$I_{rms} = \sqrt{\int_0^{T_c} I_{ph}^2(t) dt} \quad (2)$$

where  $I_{ph}(t)$  is the transient phase current.

### Iron Losses Computation

The iron losses ( $P_{iron}$ ) are composed of the hysteresis losses ( $P_{hysteresis}$ ) and eddy-current losses ( $P_{eddy}$ ). The hysteresis losses are exclusively determined by the quality of the applied soft-magnetic steel. Eddy-current losses mainly depend on the thickness of the lamination sheets, but both of them strongly depend on frequency and flux density. They are calculated according to the following simplified relations:

$$P_{eddy} = K_e \left( \frac{dB}{dt} \right)_{rms}^2 \quad (3)$$

$$P_{hysteresis} = K_h f (\Delta B)^2 \quad (4)$$

where  $K_e$  and  $K_h$  are loss coefficients, which are given in the datasheet of the iron steel.  $B$  is the flux density in different parts of the SRM.  $\Delta B$  is the difference between the maximum flux density and minimum flux density during each electrical cycle in different parts of the

SRM.

## Converter Losses Computation

The converter losses ( $P_{conv}$ ) of the asymmetric half-bridge converter consists of conduction losses ( $P_c$ ) and switching losses ( $P_s$ ) of the power electronics devices. Conduction losses are similar to the DC copper losses aforementioned, and the switching losses are caused by the transition from conducting to blocking and vice versa.

The conduction losses of the adopted converter are divided into conduction losses from the MOSFET ( $P_{CM}$ ) and the anti-parallel diode ( $P_{CD}$ ). For the MOSFET, the losses arise during the period when the phase is magnetized. Nevertheless, the diode conduction losses occur when the converter is freewheeling or demagnetized.

Conduction losses  $P_{CM}$  caused by the power MOSFET can be calculated using an approximation with the drain-source on-state resistance ( $R_{DSon}$ ):

$$P_{CM} = \frac{1}{T_{sw}} \int_0^{T_{sw}} (R_{DSon} \cdot i_D^2(t)) dt = R_{DSon} \cdot I_{Drms}^2 \quad (5)$$

where  $i_D$  is the instantaneous MOSFET drain-source on-state current,  $T_{sw}$  is the switching period, and  $I_{Drms}$  is the root mean square (RMS) value of on-state current.

The conduction losses of the anti-parallel diode can be estimated using an approximation with a series connection for the DC voltage source  $u_{D0}$  representing the diode on-state zero-current voltage and a diode on-state resistance  $R_D$ . Then the diode conduction losses  $P_{CD}$  within a switching period are:

$$P_{CD} = \frac{1}{T_{sw}} \int_0^{T_{sw}} (u_{D0} \cdot i_F(t) + R_D i_F^2(t)) dt = u_{D0} I_{Fav} + R_D I_{Frms}^2 \quad (6)$$

where  $i_F$  is the instantaneous diode current,  $I_{Fav}$  and  $I_{Frms}$  are average value and RMS value of diode current respectively.

The circuit for the examination of the MOSFET switching losses is presented in Figure C.1. The MOSFET is driven from the driver circuit, providing a voltage  $u_{Dr}$  at its output. The idealized switching process of the power MOSFET is presented in Figure C.2. The uppermost part A presents the gate voltage ( $u_{GS}$ ) and the current ( $i_G$ ); the next one (part B) shows the drain-source voltage ( $u_{DS}$ ) and the drain current ( $i_D$ ) without taking the reverse recovery of

the free-wheeling diode into account. The part C gives a qualitative overview of the power losses, while the part D shows the reverse-recovery effects on the switching losses. According to Figure C.2-part C, the switching losses consists of switch-on losses and switch-off losses.

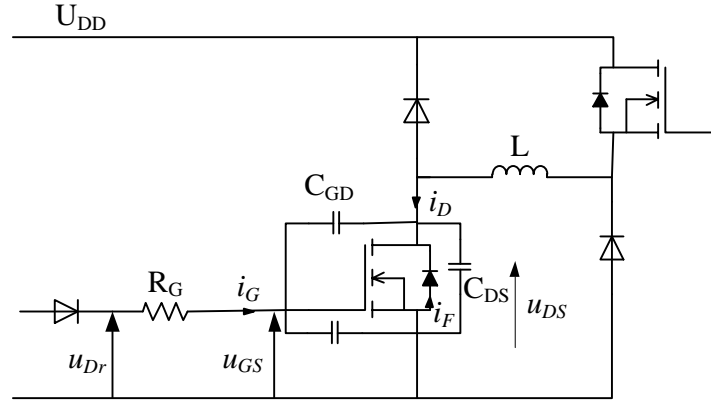


Figure C.1 MOSFET chopper with an inductance load.

During the switch-on transient period (within voltage fall time  $t_{fu}$ ), the gate current  $I_{Gon}$  can be calculated as:

$$I_{Gon} = \frac{u_{Dr} - U_{(plateau)}}{R_G} \quad (7)$$

where  $u_{Dr}$  is the drive circuit voltage of MOSFET, the  $U_{(plateau)}$  is the gate plateau voltage,  $R_G$  is the resistance connecting the drive circuit and the gate of MOSFET.

The voltage fall time  $t_{fu}$  can be calculated as a median of the fall times ( $t_{fu1}$ ,  $t_{fu2}$ ) defined through the gate current  $I_{Gon}$  and the gate-drain capacitances  $C_{GD1}$  and  $C_{GD2}$ .

$$t_{fu} = \frac{t_{fu1} + t_{fu2}}{2}$$

$$t_{fu1} = (U_{DD} - R_{DSon} \cdot I_{Gon}) \cdot R_G \cdot \frac{C_{GD1}}{(u_{Dr} - U_{(plateau)})} \quad (8)$$

$$t_{fu2} = (U_{DD} - R_{DSon} \cdot I_{Gon}) \cdot R_G \cdot \frac{C_{GD2}}{(u_{Dr} - U_{(plateau)})}$$

where  $C_{GD1} = C_{GD}(U_{DD})$  and  $C_{GD2} = C_{GD}(R_{DOn} \cdot I_{on})$ ,  $C_{GD}$  is a function depending on the gate-drain voltage, which is given in the MOSFET data-sheet.

During the switch-off transient period (within voltage rise time  $t_{ru}$ ), the gate current  $I_{Goff}$  can be calculated as:

$$I_{Goff} = -\frac{U_{(plateau)}}{R_G} \quad (9)$$

The voltage rise time  $tru$  can be calculated as a median of the fall times ( $tru1$ ,  $tru2$ ) defined through the gate current  $I_{Goff}$  and the capacitances  $C_{GD1}$  and  $C_{GD2}$ .

$$\begin{aligned} tru &= \frac{tru1 + tru2}{2} \\ tru1 &= (U_{DD} - R_{DSon} \cdot I_{Gon}) \cdot R_G \cdot \frac{C_{GD1}}{U_{(plateau)}} \\ tru2 &= (U_{DD} - R_{DSon} \cdot I_{Gon}) \cdot R_G \cdot \frac{C_{GD2}}{U_{(plateau)}} \end{aligned} \quad (10)$$

Thus, the switching losses in the MOSFET ( $P_{swM}$ ) and the diode ( $P_{swD}$ ) are:

$$P_{swM} = \underbrace{\left( U_{DD} \cdot I_{Don} \frac{tri + tfu}{2} \right)}_{E_{onM}} + \underbrace{\left( Q_{rr} U_{DD} \right)}_{E_{onMrr}} + \underbrace{\left( U_{DD} \cdot I_{Doff} \frac{tru + tfi}{2} \right)}_{E_{offM}} \cdot f_{sw} \quad (11)$$

$$P_{swD} \approx \underbrace{U_{DD} \cdot I_{Doff}}_{E_{onD}} \cdot \frac{tru + tfi}{2} \cdot f_{sw} \quad (12)$$

where  $E_{onMi}$  is the switch-on energy without considering the reverse recovery process;  $E_{onMrr}$  is the switch-on energy caused by the reverse-recovery of the free-wheeling diode;  $E_{onM}$  is the turn-on energy loss in the MOSFET;  $E_{offM}$  is the turn-off energy loss in the MOSFET;  $tri$  and  $tfi$  are the current rise-time and current fall-time respectively, which can be read from the MOSFET data-sheet;  $f_{sw}$  is the switching frequency;  $E_{onD}$  is the turn-on energy loss in diode (the switch-off losses in the diode are normally neglected).

Thus, the efficiency can be expressed as:

$$\eta = \frac{P_{out}}{P_{in}} = \frac{T_{em} \omega}{T_{em} \omega + P_{copper} + P_{iron} + P_{conv}} \times 100\% \quad (13)$$

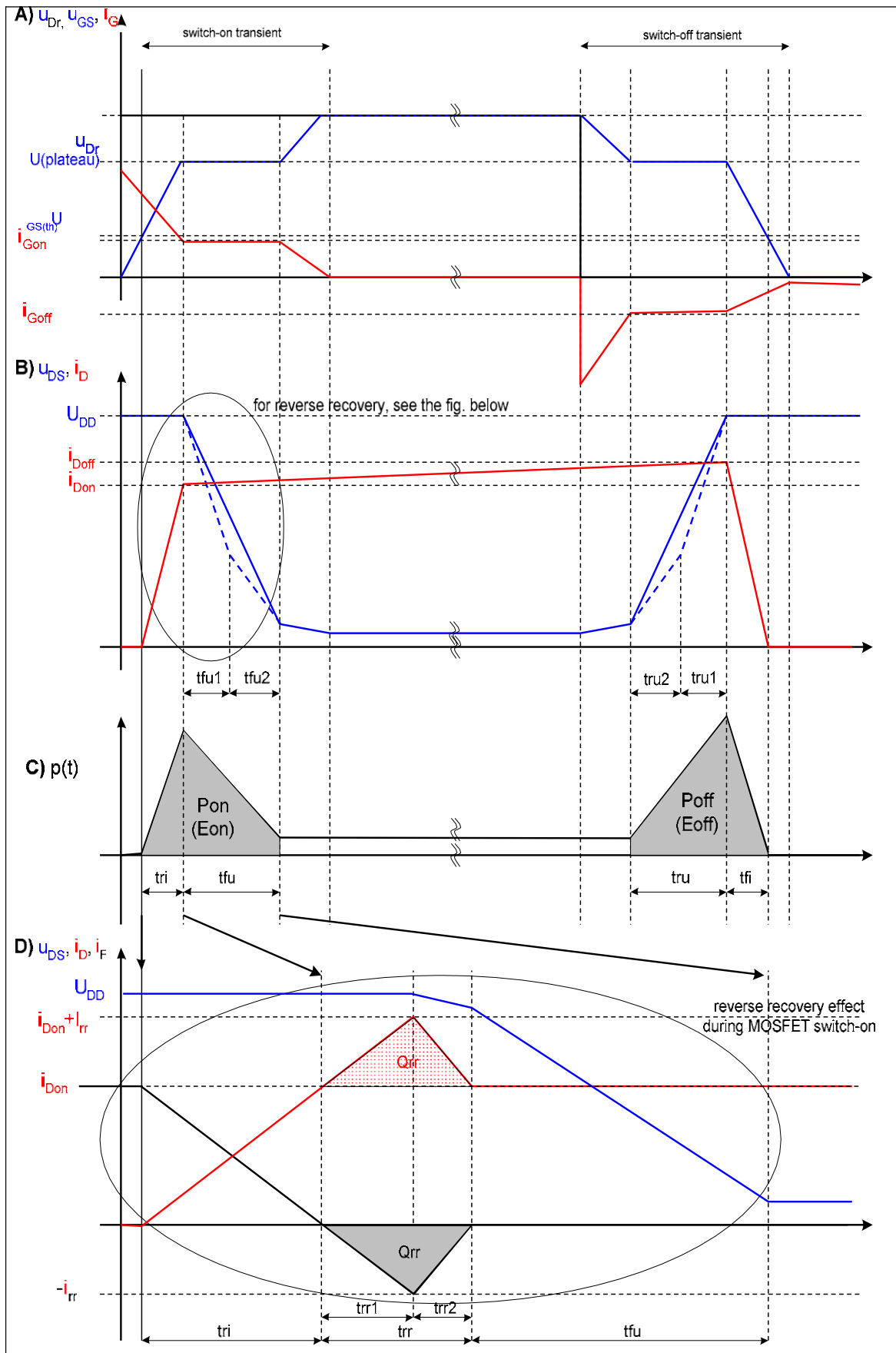


Figure C.2 Switching transients of the power MOSFET.

## D. Résumé

Le réchauffement climatique est aujourd'hui une préoccupation majeure en raison de l'augmentation des émissions de gaz à effet de serre (GES). En Europe, le transport représente près du quart des émissions de GES, le transport routier étant de loin le plus gros émetteur avec plus de 70% de cette part. Pour résoudre ce problème, l'Union Européenne cherche à rendre les consommations plus efficaces en ressources et sobres en émissions de carbone afin de réduire les émissions de GES, ce qui se traduit en particulier par les développements croissants autour des voitures hybrides et électriques.

En tant que composants de base des véhicules électriques, le moteur électrique et l'entraînement sont des éléments très importants. En raison des modes de fonctionnement particuliers du véhicule, un certain nombre d'exigences spécifiques pour le moteur électrique et les systèmes d'entraînement sont nécessaires, en particulier la gamme de vitesse atteignable, le couple développé, ou les émissions acoustiques. Au cours des dernières décennies, de nombreux types de moteurs électriques ont ainsi été analysés et évalués.

En raison de ses avantages inhérents comme la possibilité de fonctionnement en environnements difficiles, la tolérance aux pannes, la capacité de fonctionnement à grande vitesse et le faible coût, la machine à réluctance variable (MRV) est une solution attrayante pour l'industrie automobile. Il n'y a ni enroulement en cuivre ni aimant sur le rotor, ce qui augmente sa plage de fonctionnement en vitesse et diminue le coût. La structure saillante le rend facile à construire. La connexion indépendante entre les différents enroulements de phase apporte une grande tolérance aux pannes et une grande fiabilité. Cependant, la traction automobile est une application pour laquelle le comportement acoustique du groupe motopulseur doit être particulièrement considéré, dans l'optique de ne pas dégrader le confort des passagers.

Afin de rendre la MRV compétitive pour cette application automobile, le travail présenté se concentre sur plusieurs méthodes de contrôle cherchant à limiter les émissions acoustiques des MRV en réduisant les vibrations d'origine électromagnétique. L'objectif principal de cette

thèse est ainsi d'améliorer le comportement acoustique de la MRV du point de vue des stratégies de contrôle, et de mettre en application les solutions proposées sur une MRV 8/6.

En premier partie, les principales sources de bruit des MRV sont présentées : d'une part le bruit de structure causé par la vibration structurelle et d'autre part le bruit aérien lié à la rotation des ventilateurs de refroidissement ou du rotor, qui agissent sur la masse d'air environnante.

Ensuite, un état de l'art est proposé sur les thématiques des méthodes de réduction des vibrations, de la modélisation multi-physique et de la mise en œuvre expérimentale. Une vue d'ensemble des techniques de réduction des vibrations et du bruit est fournie sous deux angles : l'optimisation géométrique et le contrôle. Après quoi, les méthodes de modélisation multi-physique utilisées pour combiner modèles électromagnétique et structurel sont présentées. Trois approches de modélisation sont introduites, à savoir analytique, numérique et un modèle analytique-numérique. Enfin, différents systèmes d'application de contrôle sont introduits pour la mise en œuvre expérimentale, à savoir les solutions software, hardware et mixte hardware/software.

La contribution principale de la thèse concerne l'analyse du comportement vibratoire de la MRV associée à ses variateurs en utilisant à la fois des approches de simulation et expérimentales. Dans un premier temps, un modèle multi-physique électromagnétique/mécanique semi-analytique vibratoire, basé sur les fonctions de transfert, est introduit pour simuler l'accélération du rotor, la force radiale étant la sortie du modèle électromagnétique et l'entrée pour le modèle mécanique. Ensuite, le modèle construit est utilisé pour développer et évaluer deux méthodes de réduction de vibration : *Improved Variable Turn-off Control* (IVTC) et *Direct Force Control with Current Reference Adapter* (DFC&RCA). La première réduit la vibration en faisant varier l'angle de coupure du courant, la fréquence de la variation étant basée sur les propriétés mécaniques de la structure MRV. De plus, une fonction aléatoire uniformément distribuée est introduite pour éviter une composante fréquentielle locale de forte vibration. La seconde méthode est basée sur le contrôle direct de la force (DFC), qui vise à obtenir une force radiale globale plus douce pour

réduire les vibrations. Un adaptateur de courant de référence (RCA) est proposé pour limiter l'ondulation de couple introduite par le DFC, provoquée par l'absence de limitation de courant. Cette seconde méthode de réduction des vibrations appelée DFC & RCA est évaluée par des tests expérimentaux utilisant un prototype de MRV 8/6 afin de montrer sa pertinence. Une solution de partitionnement hardware/software est proposée pour implémenter cette méthode sur une carte FPGA utilisée en combinaison avec un microprocesseur.

## **Principaux résultats concernant le modèle électromagnétique/mécanique semi-analytique**

Pour les MRV, la force radiale entre le stator et le rotor sont les sources dominantes de vibration et de bruit. Elle conduit à la génération de vibrations du stator qui émettent un son aérien. En outre, la force radiale produite est non linéaire en raison des effets de saturation. Généralement, la force radiale est exprimée en fonction du courant et de la position du rotor. Pour limiter les hypothèses, la méthode des éléments finis (FEM) est adoptée pour calculer le profil de force radiale de la MRV. Pour prédire la courbe transitoire de la force radiale, le profil du courant dynamique est requis. Par conséquent, un modèle inverse pour la prédiction de courant est présenté à partir du flux et de la position du rotor. Ce profil de flux-linkage est obtenu par des calculs effectués en statique par FEM. Puisque les phases de la MRV peuvent généralement être considérées comme magnétiquement indépendantes, une seule phase doit être simulée et les résultats peuvent être dupliqués avec des changements de temps adéquats pour les autres. Avec la force radiale obtenue par le modèle électromagnétique, l'accélération vibratoire liée à plusieurs modes sur une phase excitée peut être calculée par la fonction de transfert considérant comme entrée le profil de la force radiale. Le comportement vibratoire de la MRV lorsque plusieurs phases sont excitées peut alors être calculé comme la superposition de la contribution des phases correspondantes couplées par les facteurs de couplage. De plus, compte tenu de la structure asymétrique du stator MRV étudié, les fonctions de transfert sont classées comme fonction d'auto-transfert et fonction de transfert mutuel pour améliorer la précision du modèle. Le principal avantage du modèle de simulation développé dans cette thèse est le fait que toutes les caractéristiques statiques (couple, liaison

de flux et profils de force radiale) de la machine peuvent être précalculées et stockées dans des tables afin de ne pas avoir besoin d'être calculées de façon répétée pendant l'exécution, ce qui entraîne des besoins en ressources de calcul très faibles et un temps de simulation court.

## **Principaux résultats concernant les stratégies de contrôle des MRV**

Basées sur le modèle multiphysique construit, deux stratégies de contrôle de vibration sont développées dans cette thèse : IVTC et DFC & RCA. Les stratégies de contrôle proposées sont considérées pour différents aspects de performance des MRV : le comportement vibratoire, l'ondulation de couple et le rendement.

### **✓ Principaux résultats concernant le contrôle IVTC**

L'idée principale de l'IVTC est de faire varier l'angle de coupure du courant de la MRV, puisque la vibration générée à cet instant est prépondérante. Une fonction sinusoïdale à fréquence de variation aléatoire est adoptée pour faire varier l'angle de déviation avec le temps. La fréquence moyenne de la fonction sinusoïdale est déterminée à partir de la fonction de transfert entre la force radiale et l'accélération vibratoire : il s'agit de la fréquence correspondant à l'amplitude minimale locale de la fonction de transfert, afin d'éviter l'excitation des modes de vibration. Par la suite, une fonction aléatoire uniformément distribuée est introduite dans la fonction sinusoïdale comme la variation de la fréquence moyenne, pour éviter d'avoir une composante harmonique concentrée près de la fréquence moyenne et de son multiple. Les vibrations peuvent être considérablement réduites, en particulier pour la basse vitesse, avec une réduction de l'énergie de vibration pouvant atteindre jusqu'à 60,5% par rapport au contrôle de couple moyen (ATC) traditionnel, sans sacrifier l'efficacité ni trop pénaliser l'ondulation du couple. Cependant, son efficacité décroît lorsque la vitesse est élevée. L'augmentation de l'amplitude de la variation de l'angle d'ouverture donne une possibilité d'améliorer l'efficacité de l'IVTC.

### **✓ Principaux résultats concernant le contrôle DFC&RCA**

L'objectif du second contrôleur, DFC & RCA, est de contrôler la force radiale localisée au niveau des dents du stator, car la dynamique de la force radiale a un impact important sur les performances vibratoires. Cependant, le DFC ne peut pas être utilisé seul parce qu'il augmente l'ondulation du couple en raison de l'absence de limitation de courant. Ainsi, un adaptateur de courant de référence (RCA) est proposé pour évaluer les variations de couple et de force radiale, afin de gérer le compromis entre deux objectifs : minimisation de l'ondulation du couple et réduction des vibrations par adaptation du courant référence. Différents points de fonctionnement sont simulés avec le DFC & RCA, la réduction maximale d'énergie de vibration est de 72,2%, ce qui prouve son potentiel. En outre, les impacts sur les aspects d'ondulation de couple et d'efficacité sont également étudiés. Les simulations montrent que le DFC & RCA peut réduire l'ondulation du couple lorsque la vitesse est faible mais détériore l'ondulation du couple lorsque la vitesse est élevée, car le DFC fonctionne pendant les périodes de commutation. Cependant, à grande vitesse, l'ondulation du couple a une fréquence élevée et peut être filtrée par le moment d'inertie de la chaîne cinématique. Le rendement est considéré car il est directement lié au coût de la batterie dans les applications de traction qui ne sont pas alimentées par un réseau fixe. Le DFC & RCA diminue l'amplitude du flux de sorte que les pertes de fer sont réduites, et il peut augmenter le rendement de la machine à basse vitesse avec une charge importante en diminuant toutes les pertes. Au niveau des inconvénients, le rendement du convertisseur est généralement inférieur à celui du contrôle de minimisation du couple (TMC). Ceci est attribué à la réponse rapide des contrôleurs d'hystérésis du DFC. Cette difficulté peut être compensée par la réduction des pertes de fer et parfois par la réduction des pertes dans les bobinages, ce qui rend le DFC & RCA compétitives par rapport à la solution TMC.

## **Principaux résultats concernant la mise en œuvre expérimentale**

Une solution de partitionnement hardware/software pour la validation expérimentale est présentée pour la stratégie de réduction de vibration proposée (DFC & RCA), appliquée à une MRV 8/6. D'un côté, le contrôle de vitesse est implémenté dans le microprocesseur, et de l'autre le contrôle de courant et le contrôle de force direct sont implémentés dans le FPGA.

Ceci fournit une réponse dynamique élevée spécialement nécessaire pour contrôler la force et les courants. Différents points de fonctionnement sont évalués à la fois en régime permanent et en transitoire. En régime permanent, la méthode proposée est comparée au contrôle TMC classique sur des aspects de vibration, d'ondulation du couple, de rendement et de bruit acoustique. Selon les résultats de la comparaison, l'énergie de vibration peut être réduite jusqu'à 67,4% sans pénaliser l'ondulation du couple ou sacrifier le rendement. En ce qui concerne l'émission de bruit, la réduction du SPL maximum près de la fréquence naturelle est de 13,7 dB. En régime transitoire, la variation de vitesse et les variations de charge sont testées. Les résultats de la comparaison montrent que la méthode proposée améliore les performances acoustiques de la MRV et maintient sa réponse dynamique, ce qui prouve le potentiel du couplage DFC & RCA.

**Titre :** Modélisation multiphysique du couplage électromagnétique/mécanique et développement de contrôles de vibration appliqués aux machines à réluctance variable

**Mots clés :** Machine à réluctance variable, Modèle de multiphysique semi-analytique, Réduction de vibration, Contrôle d'angle de déviation variable, Commande de force directe, Partitionnement hardware/software

**Résumé :** En raison de ses avantages inhérents, tels que son faible coût, sa fiabilité élevée, sa capacité de fonctionnement à grande vitesse et en environnements difficiles, la machine à réluctance variable (MRV) est une solution attrayante pour l'industrie automobile. Cependant, la traction automobile est une application pour laquelle le comportement acoustique du groupe motopropulseur doit être particulièrement considéré, dans l'optique de ne pas dégrader le confort des passagers. Afin de rendre la MRV compétitive pour cette application automobile, le travail présenté se concentre sur plusieurs méthodes de contrôle cherchant à améliorer le comportement acoustique des MRV en réduisant les vibrations d'origine électromagnétique.

Un modèle multi-physique électromagnétique / mécanique semi-analytique est proposé à partir de résultats de simulation numérique obtenus par la méthode des éléments finis. Ce modèle multi-physique est composé de modèles électromagnétiques et structurels, qui sont reliés par la composante radiale de la force

électromagnétique.

Deux méthodes de contrôle sont ensuite proposées. La première réduit la vibration en faisant varier l'angle de coupure du courant, la fréquence de la variation étant basée sur les propriétés mécaniques de la structure MRV. De plus, une fonction aléatoire uniformément distribuée est introduite pour éviter une composante fréquentielle locale de forte vibration. Une seconde méthode est basée sur le contrôle direct de la force (DFC), qui vise à obtenir une force radiale globale plus douce pour réduire les vibrations. Un adaptateur de courant de référence (RCA) est proposé pour limiter l'ondulation de couple introduite par le DFC, provoquée par l'absence de limitation de courant. Cette seconde méthode de réduction des vibrations appelée DFC & RCA est évaluée par des tests expérimentaux utilisant un prototype de MRV 8/6 afin de montrer sa pertinence. Une solution de partitionnement hardware/software est proposée pour implémenter cette méthode sur une carte FPGA utilisée en combinaison avec un microprocesseur.



**Title :** Modeling of Multiphysics Electromagnetic & Mechanical Coupling and Vibration Controls Applied to Switched Reluctance Machine

**Keywords :** Switched Reluctance Machine, Semi-analytical Multiphysics model, Vibration Reduction, Variable Turn-off Angle Control, Direct Force Control, Hardware/Software Partitioning

**Abstract :** Due to its inherent advantages Switched Reluctance Machine (SRM) are appealing to the automotive industry. However, automotive traction is a very noise sensitive application where the acoustic behavior of the power train may be the distinction between market success and market failure. To make SRM more competitive in the automotive application, this work will focus on the control one reduces the vibration by varying the turn-off angle, the frequency of the variable signal is based on the mechanical property of switched reluctance machine. Besides, an uniformly distributed random function is introduced to avoid local high vibration component. Another one is based on the Direct Force Control (DFC), which aims to obtain a smoother total radial force to reduce the vibration. An reference current adapter (RCA ) is proposed to limit the

strategy to improve the acoustic behavior of SRM by vibration reduction.

A semi-analytical electromagnetic/structural multi-physics model is proposed based on the simulation results of numerical computation. This multi-physics model is composed by electromagnetic and structural models, which are connected by the radial force.

Two control strategies are proposed. The first torque ripple introduced by the DFC, which is caused by the absence of the current limitation. The second vibration reduction strategy named DFC&RCA is evaluated by experimental tests using an 8/6 SRM prototype. A hardware/software partitioning solution is proposed to implement this method, where FPGA board is used combined with a Microprocessor.

